The electronic control of gyroscopes.

Johnson, Brian

Award date:
1985

Awarding institution:
University of Bath

THE ELECTRONIC CONTROL OF GYROSCOPES

Submitted by Brian Johnson for the degree of Ph.D. of the University of Bath

1985

COPYRIGHT

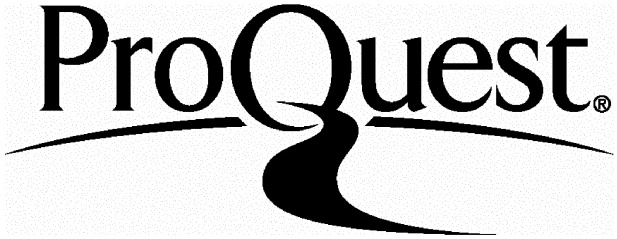

SUMMARY

The work reported in this thesis describes the design and implementation of three electronic controllers for a miniature two axis gyroscope. In particular the design is based upon the Microflex Gyroscope, which is manufactured by British Aerospace. Two variants of the Microflex gyroscope have been considered; the combined pickoff and torquer gyroscope and the separate pickoff and torquer gyroscope. These two gyroscopes are mechanically identical but feature different pickoff and torquer arrangements.

The thesis traces the history of the gyroscope from its origins to the development of small two axis rate sensors. It includes a detailed description of the Microflex gyroscope and develops mathematical models to describe its behaviour.

The electronic controllers are used to sense the angular displacement of the gyroscope, condition these signals then apply them as feedback to the gyroscope to null the displacement. The control is applied in the form of a type II servo system, hence the output from the system is a measure of the angular rate which is applied to the gyroscope.

The design of an analogue controller is developed for the combined pickoff and torquer gyroscope. The restrictions of the design of the controller due to this transducer configuration are identified. To overcome these restrictions and to increase the design options an analogue controller for the separate pickoff and torquer gyroscope was developed and implemented. This work lead into the design and implementation of a digital controller. The advantages of this design over a traditional analogue system are discussed.

Both modelled and practical results for all three systems are presented in the thesis. These show that design objectives can be achieved using simple design rules which have been developed as the designs progressed.

ACKNOWLEDGEMENTS

The Author would like to thank the Management of British Aerospace for their help and support in producing this thesis, members of the Microflex Development team for their help and assistance at various times, Nancy Hughes for typing the thesis, and his wife for putting up with him.

CONTENTS

CONTENTS (Contd.)

LIST OF FIGURES

LIST OF FIGURES (Contd.)

LIST OF FIGURES (Contd.)

CHAPTER I

INTRODUCTION

1.1 Introducing the Gyroscope

The Concise Oxford English Dictionary defines a gyroscope as:

"An instrument illustrating the dynamics of rotating bodies"

Basically, any spinning mass with freedom of movement of its spin axis is a gyroscope. However, the conventional gyroscope instrument usually consists of a driven flywheel, constrained in a Cardan suspension system, see Figure 1.1. This type of suspension allows freedom of movement in two axes. The Cardan suspension system was named after its inventor, Jerome Cardan (1501-1576), and until the advent of the gyroscope 300 years later, had no real application.

Figure 1.1

A Simple Gyroscope With Two Degrees of Freedom

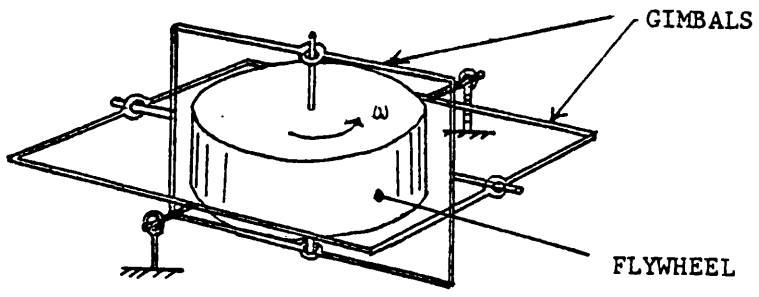

Gyroscopic devices are intriguing, as they appear to defy the normal laws of mechanics. In many cases gyroscopic motion is surprising and bizarre, but is actually a direct consequence

of the laws of conservation of angular momentum, which were first expounded by Newton (1687).

Gyroscopes occur in nature and embrace the scale of the universe. At the atomic level the intrinsic spin of particles gives them gyroscopic properties. The interaction of the gyroscopic properties of atomic particles and their magnetic and electrical properties, gives rise to some interesting and useful phenomena. The Zeeman effect and nuclear magnetic resonance (Finn 1975) are examples of this type of interaction; the latter effect is being developed for use in medical imaging (Morris 1980).

More classical gyroscopic behaviour is observed in the motion of the stars and planets. In the seventeenth century, Kepler, Galileo and Newton, formulated laws which describe the movement of the earth and the other planets. In particular, Newton supplied an explanation for the slow westward drift of the celestial sphere of 'fixed' stars. Newton showed that this phenomenon, the precession of the equinoxes, was due to the gyroscopic precession of the Earth. All astronomical bodies exhibit gyroscopic properties as a result of their spin and universal freedom.

Gyroscopes are not confined to the mechanics of the universe; nature has also made use of the gyroscope in the insect kingdom. Many species of insect (Diptera), including the

common housefly, are equipped with a tiny gyroscope. This device allows them to control their flight. This gyroscope is unconventional and consists of two rod-like weights called halteres which vibrate rather than rotate. These halters are driven by a muscular system; angular and linear motion are detected by a nervous system and used automatically to control the insects' wings. Gyroscopes occur in many forms in our world. For example, all machines which rotate, produce gyroscopic effects.

1.2 Gyroscopic Properties

The gyroscope demonstrates two fundamental properties: gyroscopic inertia and gyroscopic precession. Gyroscopic inertia is the property of a spinning mass to maintain its plane of rotation, unless acted upon by an external force. This is simply a manifestation of Newtons lst law of motion. Gyroscopic precession is the angular change of the plane of rotation under the action of an external force. The precessional motion occurs in an axis orthogonal to the axis to which the force was applied.

To understand the origins of gyroscopic precession consider the flywheel shown in Figure 1.2.

Figure 1.2

Gyroscopic Precession

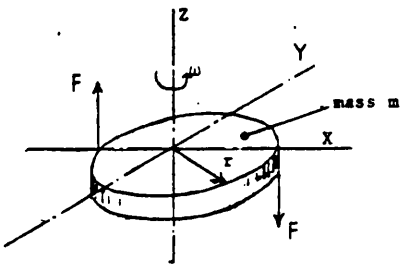

Figure 1.2.1

A flywheel with its centre of mass at centre of coordinate system X,Y,Z

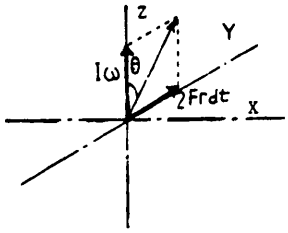

Figure 1.2.2

Angular momentum Vector Diagram

A flywheel of radius (r) and mass (m) is rotated about an axis (Z) with angular velocity (ω). The angular momentum (L_z) about the Z axis is given by:

$$L_z = I_z \omega \qquad 1.1$$

Where I_z is the moment of inertia of the flywheel about the Z axis. A force (F) applied to the flywheel in the plane (Z,X) produces a torque about the Y axis. This torque (M) is given by:

$$\underline{M}\underline{j} = -2r\underline{i} \wedge F\underline{k} \qquad 1.2$$

Where $\underline{i}$, $\underline{j}$, $\underline{k}$ are unit vectors corresponding respectively to the X, Y and Z axis. However, by Newtons second law, we know that torque is the rate of change of angular momentum thus:

$$\underline{M} = \frac{d\underline{L}}{dt}$$

Hence $d\underline{L} = (2 F \underline{k} \wedge r \underline{i})dt$

From the vector diagram of Figure 1.2.2 it can be seen that a force applied in the plane X, Z will result in motion in the plane Y, Z. This motion is gyroscopic precession. Now recalling that angular momentum is given by the product of angular frequency and moment of inertia, we have:

$$\underline{dL} = Id\,\underline{\omega} \qquad 1.3$$

The change in rotational frequency ($d\omega$) is given by the rate of change of the angle through which the spin axis rotates, ie. $d\theta/dt$. The rotation caused by precession is not about the spin axis, thus the total angular velocity of the flywheel is:

$$\underset{\text{(Total)}}{\underline{\Omega}} = \underset{\text{(Spin)}}{\omega\underline{k}} + \underset{\text{(Precession)}}{\dot{\theta}\underline{i}}$$

Thus angular momentum has two components, one due to the flywheel spin and the other to precession. If we apply Newtons second law we obtain:

$$M\underline{j} = \frac{d}{dt}(I_z\omega)\underline{k} + \frac{d}{dt}(I_x\dot{\theta})\underline{i} \qquad 1.4$$

I_x is the moment of inertia about a diametral axis of the flywheel. The rate of change of the resolved component of the flywheel's spin ω, is due entirely to the precession rate $\dot{\theta}$. I_z and I_x are time independent. Therefore Equation 1.4 becomes:

$$\underline{M}_j = -I_z \omega \dot{\theta}\ \underline{i} + \frac{d}{dt}(I_x \dot{\theta})\underline{j}$$

(Note $I_x = I_y$ for a disc)

Referring the vector components to the flywheels original axis X, Y and Z we obtain the Gyroscopic equation of motion:

$$M_y = -\dot{\theta}_x I_z \omega + \ddot{\theta}_y I_x \qquad 1.5$$

Thus, in the steady state a torque applied to the Y axis produces a rotation about the X axis. From this equation and Equation 1.2 we obtain the steady state precession rate as:

$$|\dot{\theta}| = \frac{2Fr}{I_z \omega} \qquad 1.6$$

A more detailed derivation of the gyroscopic equations of motion is given in Appendix 1. The equations of motion for the gyroscope were first established by Euler (1765).

An ideal gyroscope only precesses when subjected to an external torque. However, a practical gyroscope is influenced by a number of disturbances. The effects of friction and stresses in the suspension, shifts in the centre of mass, stability of the materials and magnetic effects all introduce parasitic torques which produce a drift precession. In general, this drift is used to define the quality of the gyroscope. The earth is a very good gyroscope and exhibits a drift of about 1×10^{-6} degrees hour^{-1}, whilst the drift of

man made gyroscopes ranges from 1000 degrees $hour^{-1}$ to 1×10^{-4} degree $hour^{-1}$.

1.3 Historical Development and Application of the Gyroscope

The theory of the gyroscope has its basis in Newton's laws. Newton also gave perhaps the earliest appreciation of gyroscopic motion. In book III of his 'Principia', he gave a dynamic explanation for the precession of the equinoxes. This astronomical phenomenon was first observed by Hipparchus, a Greek astronomer, about 130 BC. Newton's mechanics showed that the phenomenon was the result of gravitational torques between the Earths equatorial bulge and the moon. Order of magnitude calculations (French 1965) estimate a precession rate of 4×10^{-12} rad sec^{-1}. More detailed observation of the motion of the earth, revealed a second oscillation. This oscillation describes a cone of 26ft in diameter at the north pole, with a period of 428 days. This oscillation can also be explained by a gyroscopic phenomenon, which corresponds to the free oscillation, or nutation of a free gyroscope. This motion is known as 'Eulerian motion' after Leonhard Euler.

In his "Theoria Motus Corporam Solidorum Scurdorum" (1765), Euler laid the mathematical foundations of gyroscopic dynamics. Earlier, Euler was concerned with the motion of rigid bodies, and derived a set of dynamic equations relating torque, inertia, velocity and angular acceleration. This set of equations is known as Eulers equations, and are stated with reference to a fixed axis of the body. Later, Euler

established the independence of rotational and translational motion. He also devised a coordinate system, based upon angles, to define the axis of a body with respect to a fixed point. From this background, Euler was able to describe the motion of a rigid body with respect to a fixed point, free from external forces. Euler's later contributions to dynamics include concepts which led to the ideas of principal axis and moments of inertia.

Many other mathematicians investigated the subject of gyrodynamics, Clairaut in 1742 was the first to have noticed the force applied to a particle, when the axis along which the particle is moving is also rotating. This effect was much later credited to Coriolis.

After the death of Euler in 1783, little was added to gyroscopic theory until the nineteenth century. However, work by Poinsot (1851) and Silvester (1866) showed that interest in the subject had not ceased. Poisson (1781 - 1840) appears to have been the first to investigate the motion of a spinning top.

The first practical use of gyroscopic properties was to make a bullet spin as it flies through the air. The spinning bullet flies more accurately and further due to its gyroscopic properties. The inventor of this idea is unknown, but is thought to have preceeded the first experimental gyroscope by about 300 years. The next recorded application of the

gyroscope was made by Serson (Short 1752). He constructed a spinning rotor to indicate horizontal position. This rotor was suspended to be free of disturbance, caused by motion of a ship. This device was improved by Fleuriais, and later used by the French navy.

The earliest type of modern gyroscope was probably constructed by the German Bohnberger, in 1810. An improved type was built by Walter Rogers Johnson, of Philadelphia in 1832. He called his device a Rotascope and used it to demonstrate the dynamics of moving bodies (Scarborough, 1958).

In 1851 Jean Bernard Leon Foucault, using a simple swinging pendulum, successfully demonstrated the rotation of the earth. As the Earth rotates the plane of the swinging pendulum appears to change (Science Museum 1979). This simple demonstration is repeated daily at the Science Museum, using a model of Foucault's original pendulum. In order to confirm the results of this experiment by some independent means, Foucault devised a second experiment. For this experiment he mounted a spinning flywheel in a Cardan suspension. He called this device a Gyroscope deriving the name from the two Greek words gyros, meaning rotation, and skopeo, meaning to view. Foucault aligned the spin axis of his gyroscope parallel to the surface of the earth, so as the earth rotates the gyroscope is forced to precess. Foucault reported the results of this experiment to the Academy of Science in Paris in 1852.

Detailed analysis of the experiment by Hayward (1856) showed that an undamped gyroscope will oscillate about its equilibrium position (ie. with the spin axis aligned to the Earth's polar axis) like a circular pendulum, ie. precesses through 360 degrees.

The results of Foucaults experiment with the gyroscope were not totally conclusive, as measurement had to be made quickly because the rotation frequency was continually slowing down. A detailed description of Foucault's experiment is given by Bulgakov (1955) and Pearson (1964). Although Foucault's experiment was not entirely successful it established the gyroscope as a navigational instrument. A similar demonstration to that of Foucault was performed by Sang in 1836, however his results were inconclusive and he did not publish until 1856.

In the later part of the nineteenth century, several contributions were made to gyroscope theory by several mathematicians and physicists. Routh studied the stability of gyroscopic motion; Yait (1869) investigated gyroscope motion by vector methods and Lord Kelvin suggested using the gyroscope as a compass. George Hopkins, an American inventor, fitted an electric motor to a gyroscope in 1878, thus providing a simple means of driving the inertial element at constant speed.

Brennan in 1903, designed and patented a monorail. His monorail used a gyroscope to preserve its balance. However, Brennan's design suffered from several problems, which would have been overcome if resources had permitted (Maunder 1961). Schlick of Hamburg in 1904 used a gyroscope to reduce the rolling of a ship at sea. Schlick's stabiliser consisted of a gyroscope (weighing 0.5 tons) mounted with its spin axis vertical and with a pendulous weight attached to the bottom of the suspension, thus making the gyroscope gravitationally referenced (see Figure 1.3).

Figure 1.3

The Schlick Stabiliser

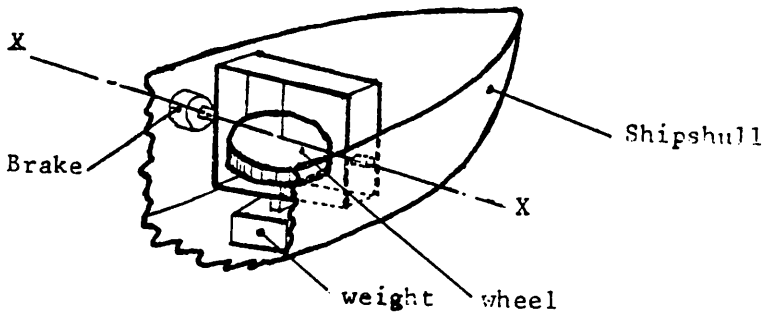

Rolling motion of the ship about the longitudinal axis will cause the gyroscope to precess about the axis, X,X. To limit the gyroscopes motion, a brake is applied to the axis and in this way the rolling of the ship is damped. A mathematical analysis of the Schlick stabiliser is given by Scarborough (1958). In the years to follow, the Schlick stabiliser was superseded by an active type of stabiliser.

At the beginning of the twentieth century, steel replaced wood as the material for building ships. This change had a detrimental effect upon the traditional magnetic ships compass. The advantages of using a 'gyro-compass' are summed up by the rhyme of an unknown navy officer:

"A compass of the spinning kind
Is also to the North inclined;
An iron ship doesn't mind
The axis of its spinning wheel
is quite oblivious to steel
In turret, funnel, deck or keel"

The first gyrocompass was designed and patented by Dr. Anschultz-Kaempfe. For the purpose of navigating, during a proposed trip to the north pole by submarine, he designed a gyroscopic device called an 'azimuthal top' (Bulgakov, 1955). This was intended as a directional indicator. Although Anschultz's early devices were unsuccessful, he became fascinated by the problem and in 1905 produced the first practical gyrocompass. Anschultz's first gyrocompass used only one floated gyroscope. In later designs, which were used by the Royal Navy before the first world war, he used three gyroscopes.

From 1904-1908 contributions were made to the theory of the gyrocompass by Foppl and Martienssen. Most early gyrocompasses usually operated by making the gyroscope's frame

pendulous with the spin axis horizontal. The rotation of the Earth forces the gyroscope to precess until the spin axis is aligned with the Earth's polar axis. Primarily gyrocompasses were intended for use at sea, although in practice a pendulous weight as a levelling element was found to be unsatisfactory in heavy sea's. However, the manufacturers devised some ingenious ways of overcoming this problem.

While developing his gyrocompass, Anschultz noted that it suffered from lack of accuracy during turns. Meanwhile, at this time, Martienssen published a paper which showed that a gyrocompass would develop large errors when subjected to north-south accelerations. Anschultz informed his cousin, Maximillan Schuler, of the problem. Schuler determined that the gyrocompass could be made insensitive to these accelerations, if the compass is made pendulous with a period of 84 minutes. This condition is known as 'Schuler tuning'.

Professor Andrew Gray (1909) published a paper in which he describes methods of analysing gyroscopic problems using Lagranges Equation of motion.

The Sperry Company in 1910 developed an active ship's stabiliser. A small gyroscope was used to sense the motion of the ship. This information was used to control a servo system, which forced a large gyroscope to precess. The sense of this precession was arranged to quell the rolling of the

ship. The Sperry stabiliser was fitted to many ships, at first mostly to pleasure yachts, but ultimately to the Italian liner S.S. Conte di Savica. Throughout a 29,000 mile cruise by a yacht of 3,000 tons displacement, a Sperry stabiliser kept the amplitude of roll below 1 degree using a gyroscope weighing 22 tons. The Sperry device was soon superseded by the Denny-Brown stabiliser. This stabiliser used a gyroscope to sense the motion of the ship, but used controlled fins, fitted to the ships hull to quelch the roll.

After a trip to France, Dr. Elmer Sperry studied the historic Foucault gyroscope, and in 1911 he invented a method for combining the effects of gravity with the rotation of the Earth, to keep the axes of a gyroscope aligned to true north. In mechanical construction, Sperry's gyrocompass was different to Anshultz's gyrocompass, but used the same principles of operation. To overcome the disadvantages of a heavy pendulous weight, Sperry used a fluid weight. Harrison and Rawling of the British Admiralty, in 1918 proposed an inverted fluid pendulum, and this scheme was developed as an improvement of the Sperry Compass.

With the advent of the aeroplane, it was inevitable that the gyroscope would find new applications. Lawrence Sperry, son of Elmer Sperry, established himself as a pioneer of aviation. He developed an interest in the possibilities of stabilised flight. The first Sperry stabiliser, or auto pilot was tested in 1912 at Hammondsport New York. In May 1914 Lawrence Sperry

won a French war department prize for a 'stable aeroplane'. To demonstrate the auto-pilot, while the aeroplane was flying low over a crowd, the passenger left his seat and walked along the wing. At the same time the pilot stood up and held his hands above his head. The aeroplane continued to fly on its level course, (Sperry Gyroscope Company, 1973).

In England in 1914, S. G. Brown and Professor Perry invented a gyrocompass, which in principle was similar to the Anschultz and Sperry gyrocompass. The main features of this compass were that, to reduce problems with friction the inertial element was supported upon a jet of oil and to level the compass a liquid level and pneumatic arrangement was used.

1.3.1 Significant Milestones

The following years saw the development of many devices which used gyroscopic principles for navigation or stabilisation. The individual devices are too numerous to mention in this paper and with the increasing application, the development branched into several specialised areas. Gyrocompassing was developed for both shipborne and airborne applications. Aircraft flight instruments formed another large development area, and included artificial horizons, stabilisers and auto pilots. From this point, the discussion will be limited to the milestones in the historical development of the gyroscope, and will trace the influences which lead to the development of

the miniature rate gyroscope, which is the subject of this thesis.

Inertial guidance is linked very closely with the development of miniature gyroscopes. Usually, an inertial guidance system involves using one or more gyroscopes in conjunction with other sensors to obtain directional information. Duncan (1964) assumed that the science of inertial guidance was born with the issue of a U.S. patent by Abbot in July 1924. However, the first airborne inertial navigation system did not emerge until 1949.

In 1925 Michelson and Gale performed an experiment to measure the rotation of the Earth. Unlike the Foucault experiment which used a spinning fly wheel, the Michelson-Gale experiment (Post, 1967) used an optical sensor. Using a 'Sagnac' interferometer (with dimensions of about 1km), Michelson and Gale successfully measured the rotation of the Earth. This early experiment was the forerunner of the Laser gyroscope. No further significant progress was made in this field until 1962.

The famous Stern-Gerlach experiment (Finn, 1968) of 1924 showed the interaction of the intrinsic spin of an electron and its magnetic field. This experiment linked gyrodynamics to atomic particles, and formed the basis of the nuclear gyroscope.

In America, the gyroscope was being developed for flight instruments. In 1929 Jimmy Doolittle, using instruments designed by the Sperry Company, made the first 'blind' flight relying only on flight instruments (Sperry Gyroscope 1973).

In the early 1920's there were three main manufacturers of gyroscopes, the Anschultz company, the Sperry company and the Arma-Bosch company. After the first world war a clause in the "Treaty of Versailles" prevented Germany from building battleships larger than 10,000 tons. This was intended to be a tactical disadvantage. However it prompted German scientists to develop stabilised platforms and guns for their ships. This development effort gave Germany a significant lead in gyroscope technology. During this time, Johann Maria Boykow, a German actor and naval officer, made a substantial contribution to inertial technology. Boykow conceived the principle of a stabilised platform, stabilised with three single axis gyroscopes and two accelerometers. According to Duncan (1964) Boykow took out a U.S. patent for his platform in 1938.

The contributions of Johannes Gievers have been documented by Kliens and Stieler (1979). Givers made very substantial contributions to Gyroscope technology and inertial navigation. Gievers headed teams of scientists, and engineers in Germany, before and during the second world war. The achievements of Gievers include: a miniature gyrocompass for use in submarines (the performance of this instrument is still considered

remarkable even by todays standards); attitude and heading reference systems with direct gyroscope stabilisation; stabilised gun platforms with direct and servoed gyroscope stabilisation and finally the guidance system for the V2 rockets. After the war, Gievers worked for the Russians then the British, before settling in America. Whilst working for the 'Chrysler' corporation, Gievers obtained a patent in 1972 for a type of laser gyroscope. Kliens and Stieler conclude that Gievers work had a traceable effect upon the development of the inertial navigation in the guidance system for the Apollo launcher.

In 1953 the Sperry Gyroscope Company introduced the concepts of the 'tuning fork' gyroscope. This gyroscope operates on the same principle as the halteres of the house fly.

Throughout the 1950's, improvements were made of a practical nature. Improvement in precision manufacturing techniques improved the 'quality' of the gyroscopes produced. The requirements for gyroscopes, tended to be for smaller gyroscopes, thus there was a trend to adopting gyroscopes without gimbals.

During the 1960's much work was done to improve the stability of gyroscopes. The most notable achievements are outlined by Maunder (1964). These are mostly the identification and

understanding of the mechanisms which affect gyroscope performance.

Stratten in the 1964 James Clayton lecture presented the requirements for gyroscopes which are to be used for inertial navigation. The lecture also reviews the gyroscope technology available at that time. Many of the developments made since 1964 are hidden by company and military secrecy. However, since about 1962 the main new areas of development are laser and nuclear gyroscope.

1.3.2 Development of Gyroscope Suspensions

After the second world war, much effort was devoted to solving the engineering and manufacturing problems encountered in making a practical gyroscope. Most early gyroscopes consisted of a fly-wheel mounted in a Cardan suspension. In 1946 Philpott and Mitchell (Bonfield, 1977) introduced the concept of the dynamically tuned Hooks joint gyroscope. In this type of gyroscope the Cardan suspension is replaced by a Hook's joint (torsional springs). This joint is dynamically tuned so that at a specific rotation frequency the joint impresses no torques upon the gyroscopes wheel. In recent years there has been a growth of interest in this concept. In 1963 the Arma Company patented a gyroscope based upon this principle (Howe and Savet, 1963).

In the 1950's, largely due to the work of Draper at the Massachusetts Institute of technology (M.I.T.), a floated

gyroscope was developed. In this type of gyroscope, the gimbal takes the form of a cylindrical shell which encloses the rotor. A second shell surrounds the gimbal supporting it with pivot bearings. This shell is completely filled with fluid. The fluid gives buoyancy to the gimbal and reduces unpredictable torques. Depending upon its design, this type of gyroscope can take the form of a rate gyroscope (senses rate of change of angle) or a rate integrating gyroscope (for angular input this gives an angular output). This type of gyroscope will be discussed in detail later. In the years to follow, the floated gyroscope was developed into a gas bearing gyroscope, where the floatation liquid was replaced by a gas jet (Savet, 1966).

In the search for high accuracy gyroscopes many unconventional designs were investigated. Two of these designs produced noteable performance, both designs are very similar in concept and operation.

The first of these designs was the cryogenic gyroscope invented about 1950. The name cryogenic is a little misleading as the cryogenic state is only a means of achieving suspension and stability. Basically a cryogenic gyroscope consists of a spherical rotor which is floated on a repulsive magnetic field. The flotation is achieved by cooling the rotor to a superconducting state. In this state the rotor material is almost perfectly diamagnetic. An external

magnetic field produces an oppositely directed field within the rotor. The result of this is to cause the rotor to float on a magnetic cushion. The cryogenic gyroscope was developed by the General Electrical Company of Pittfield Massachusetts. In 1962 the accuracy of this device was quoted as 0.0001 deg/hr (Corneretto 1962). Although a great amount of energy is required to maintain the cryogenic state on Earth, in space only a temperature differential of 15K needs to be overcome. The second type of 'field' supported gyroscope has elecrostatic suspension. This type of gyroscope consists of a spherical shell rotor suspended by a non uniform attracting electrostatic field in a high vacuum. To centralise the rotor an elaborate servo system is used. The electrostatic gyroscope was invented in 1950 by Nordsieck.

One other type of floated gyroscope which has produced good performance is the gas supported gyroscope. This gyroscope can take two forms; hydrodynamic where the wheel is lubricated by its own gas, or hydrostatic when the wheel is lubricated by an external gas supply. The gas supported gyroscope is used for Ships Inertial Navigation (S.I.N.) and is used on the Ethan class of Polaris submarines (Corneretto 1962). To achieve very high accuracy and stability it is necessary to operate the gyroscope at cryogenic temperatures.

1.4 Contemporary Miniature Rate Gyroscopes

Over the past twenty years much effort has been devoted to developing miniature gyroscopes. To achieve small size, designers have dispensed with the Cardan suspension system and adopted less bulky types of suspension. Usually the suspension system adopted limits the angular freedom of the gyroscopes inertial element. To overcome the angular limitation the gyroscope is operated in the 'rate' mode. In this mode the gyroscope is used to measure angular velocity. It offers the advantage that its mode of operation, the angular deflection of the inertial element, relative to the suspension, is nulled.

Figure 1.4

A Simple Rate Gyroscope

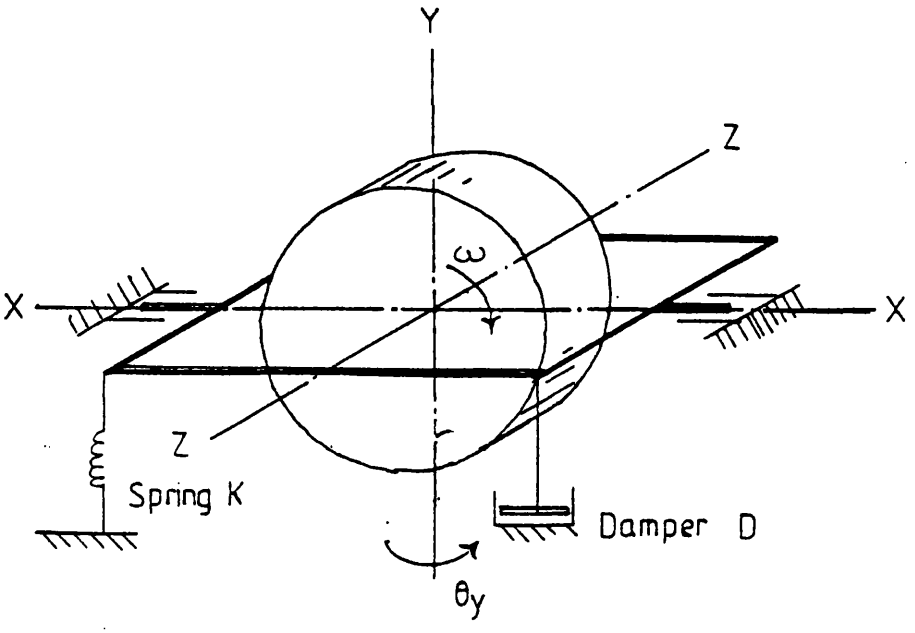

The simple rate gyroscope shown in Figure 1.4 consists of a flywheel with a single degree of freedom about the X axis. However, a spring of stiffness (K), and damper with damping

(D) are employed to restrain rotation about this axis. Any torques applied about the Y axis will produce a precession motion about the X axis. The spring and damper will produce torques to oppose the precessional torque. Thus for small angles (by inspection of Figure 1.4)

$$M_x = -K\theta_x r - D\dot{\theta}_x r \qquad 1.7$$

similarly as seen from Equation 1.5 the precession torque is given by:

$$M_x = \dot{\theta}_y I_z \omega + \ddot{\theta}_x I_x \qquad 1.5a)$$

If the equations 1.5a) and 1.7 are combined and the Laplace transform taken, assuming zero initial conditions at (t=0) the transfer function for the gyroscope can be shown to be:

$$\frac{\bar{\theta}_x}{s\bar{\theta}_y} = \frac{-I_z\omega}{s^2 I_x + sDr + Kr} \qquad 1.8$$

Where s is the Laplacian operator

$\bar{\theta}$ notation denotes the Laplace transform of θ

From this it is clear that in the steady state, angular 'rates' about the Y axis cause the gyroscopes gimbal to be displaced by an angle θ_x about the X axis. This angle gives a direct measure of the angular 'rate' applied to the gyroscope. This type of gyroscope is known as a spring restrained gyroscope.

For low accuracy application the spring restrained gyroscope will mechanically resemble the arrangement shown in Figure 1.4. However for more accurate application, the gyro gimbal will be sealed and floated in a liquid.

The gimbal is aligned to the case by a pair of bearings. Floating the gimbals provides partial buoyancy and reduces the load upon the bearing. This reduces the friction and attendant parasitic torques which cause the gyroscope to drift. The floatation liquid may also be used to provide viscous damping. Eddy current damping is another common form of damping used in the spring restrained gyroscope. The spring restrained gyroscope is manufactured by, for instance, Smiths Industries (Simons, 1964).

The rate integrating gyroscope is mechanically similar to the floated spring restrained gyroscope. In this type of gyroscope the spring restraint is eliminated and the damping increased. Proceeding as for the spring restrained gyroscope it can be shown that the transfer function for this type of gyroscope is:

$$\frac{\overline{\theta}_x}{\overline{\theta}_y} = \frac{-I_z\omega}{I_x s + Dr} \qquad 1.9$$

The symbols have their previous meaning (refer to Figure 1.4). The transfer function shows that at low frequencies, an angular displacement θ_y about the Y axis will produce an angular displacement θ_x about the X axis. The rate

integrating gyroscope can be operated as a displacement gyroscope, or with the use of an external feedback loop the gyroscope can be operated as a 'rate' gyroscope. The basic principle of how this is achieved is shown in Figure 1.5.

Figure 1.5

The Rate Integrating Gyroscope with Feedback

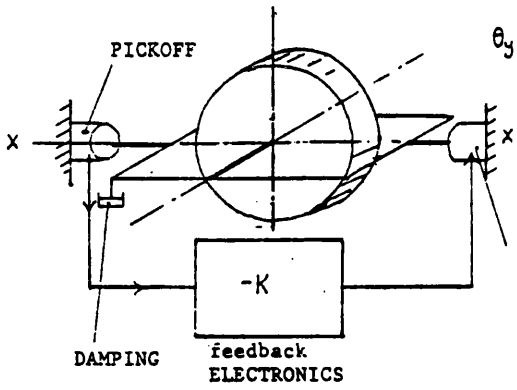

Figure 1.5.1 Schematic

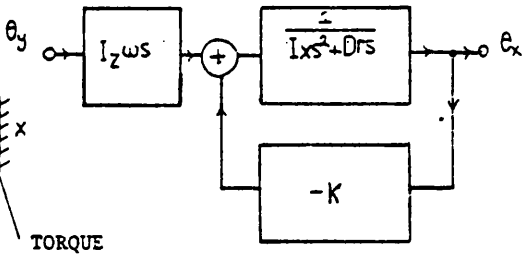

Figure 1.5.2 Block Diagram

From the schematic of Figure 1.5.1 it can be seen that the angular displacement θ_x is detected with a pick off. The angular displacement is appropriately scaled and used to drive a torquer motor. The motor is used to rotate the gimbal, and in conjunction with the displacement feedback acts like a spring and restrains the gimbal. From the block diagram of Figure 1.5.2, it can be seen that the transfer function for the rate integrating gyroscope with feedback is identical to that of a spring restrained gyroscope.

The rate integrating gyroscope was developed in the 1950's by Draper, and is manufactured by many companies. For some applications the floatation liquid is replaced by a gas bearing (Wrigley and Hollisler, 1965).

1.4.1 Low Cost Rate Sensors

For low accuracy applications there are a number of rate sensors. These use a number of different concepts, and include the tuning fork gyroscopes, a vibrating wire sensor, a gas jet sensor and a magneto hydrodynamic sensor. The stimulus for the development of the numerous devices is to achieve a low grade sensor at a minimal cost.

Figure 1.6

The Tuning Fork Rate Gyroscope

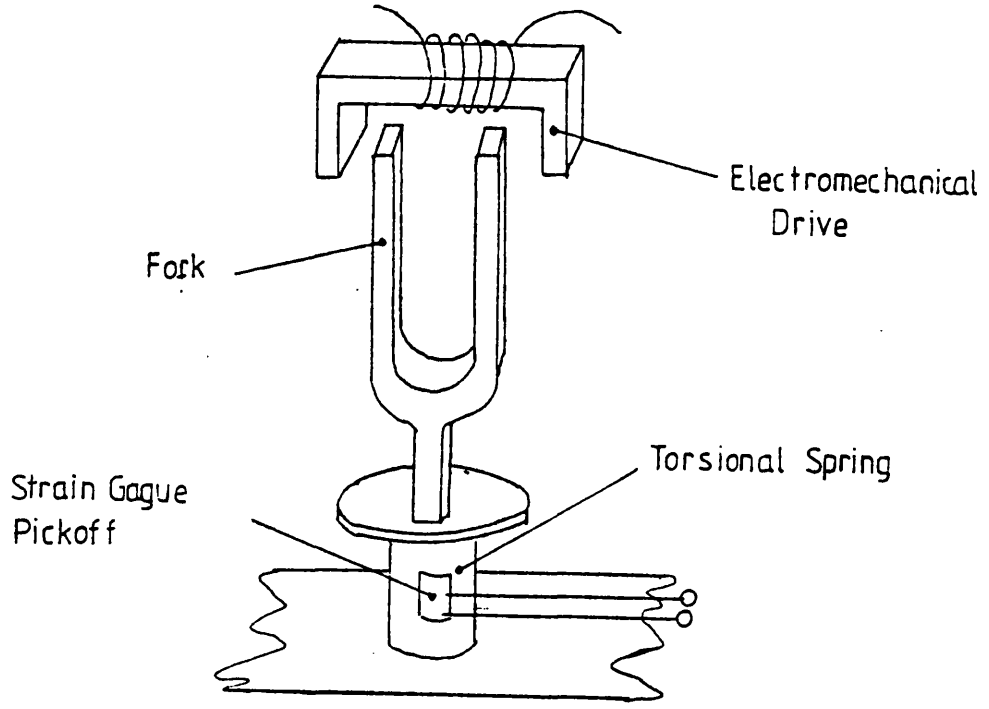

Figure 1.6 shows the basic tuning fork sensor, the sensitive element is essentially a tuning fork mounted upon a torsioral spring. The fork is vibrated using an electromechanical system. Rotation about the torsional axis produces coriolis forces on the arms of the fork. The arms of the fork are driven in opposition, this acts with the coriolis forces to produce a harmonic couple about the torsional axis. This motion is detected by the pickoff, and when demodulated gives a measure of the angular rate applied to the gyroscope (Smith 1977).

The vibrating wire sensor consists of a wire which is vibrated by an electromechanical drive. The plane of vibration tends to remain fixed. When the case of the gyroscope is rotated the vibration of the wire is detected in the other axis.

The gas jet sensor relies on the apparent deflection of a laminar flow of gas when the sensor is rotated. The deflection of the gas is sensed by hot wires. Sensing the current required to keep the wires at constant temperature gives a measure of the angular rates applied to the device.

Currently two hydrodynamic rate sensors are manufactured. The British Aircraft Corporation manufacture a Dual Axis Rate Transducer (D.A.R.T.). This sensor consists of a fluid filled body which is rotated at high speed. The fluid tends to retain its axis of rotation when its case is moved. However the fluid is subject to both geometric and gyroscopic torques.

The geometric torques tend to cause the rotation of the fluid to align to the case, while the gyroscopic torques precess the fluid. The torques applied to the liquid are sensed by a pair of paddles mounted as cantilevers, attached to a piezoelectric device. A detailed description of the D.A.R.T. is given by Naylor (1977). The second hydrodynamic sensor is manufactured by Honeywell. This is a single axis angular accelerometer, which is comutated to give two axes information. The angular accelerometer is a toroid of mercury, electrically coupled to the outside world by transformer action.

1.4.2 Two Degree of Freedom Gyroscope

Two degree of freedom gyroscopes can also be used as rate sensors. To convert the basic two degree of freedom gyroscope to a rate gyroscope, feedback must be applied to the gyroscope. In modern gyroscopes feedback is applied electrically. Size is an important criterion in the design of rate sensors, this usually means a suspension system using gimbals is undesirable . One type of suspension system which allows small size to be obtained is the dynamically tuned Hookes joint. This suspension consists of two orthogonal sets of torsional springs. When the rotor is driven at a 'tuned' rotational frequency, it is effectively decoupled from its shaft (Bonfield, 1977). Another suspension that also achieves small size, uses a flex pivot. The flex pivot gyroscope has the advantage of not being tuned. The flex gyroscope will be described in detail later. The basic gyroscope equations were

derived earlier, Equation 1.5 gives the basic equation of motion. A similar equation can be derived for the other gyroscope axis. These form a set of two equations which describe the gyroscope's behaviour:

$$M_x = \dot{\theta}_y I_z \omega + \ddot{\theta}_x I_x \qquad 1.5\,a)$$

$$M_y = -\dot{\theta}_x I_z \omega + \ddot{\theta}_y I_x \qquad 1.10$$

Rearranged, these equations are described by the model shown in Figure 1.7.

Figure 1.7

Two Degree of Freedom Gyroscope Model

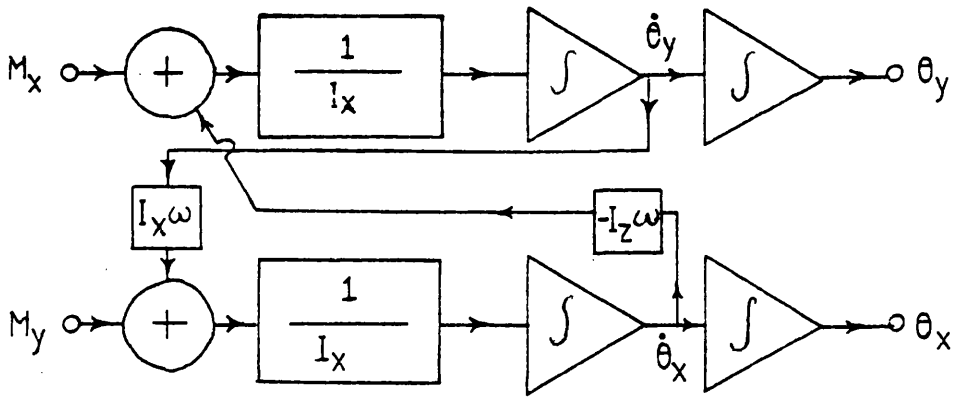

This model can be simplified to a pair of integrators, ie. a torque applied to the X axis is integrated, and produces a displacement in the Y axis, and vice versa. Feedback is usually applied by sensing the angular displacement of the gyroscopes wheel.

This information is then processed and fed back via a torquer, to precess the gyroscopes wheel and null the angular displacement. Normally the gyroscope is operated as a type II servo system, and consequently the feedback processing is basically an integrator. Sensing the torque required to precess the gyroscope gives a measure of angular rate. The theory of controlling a two degrees of freedom gyroscope will be discussed in detail later. Figure 1.8 shows a simplistic model of the servo loop for control of one of the gyro axes.

Figure 1.8

A Simple Model of a Rebalance Gyroscope

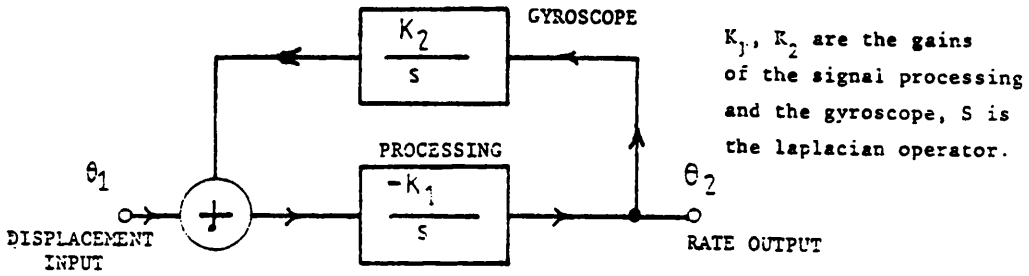

From this it can be shown that the output $\bar{\theta}_2$ is:-

$$\bar{\theta}_2 = \dot{\theta}_1 \frac{K_1}{s^2+K_1K_2}$$

One major problem with two degrees of freedom is that as the two axes are interactive, the gyroscope exhibits a natural resonance called nutation. Nutation does not introduce a severe limitation and will be discussed later.

1.4.3 Digitally Controlled Gyroscopes

The devleopment of gyroscopes with digital controllers has not yet progressed to the stage where they are commercially available. Potentially a digital controller offers many

advantages; it allows the use of digital processing with the advantages of high volume production, repeatability and stability of the design, small size and low cost, and for many applications a sensor with a digital output would be very attractive. The output could then be directly processed by a digital computer, without the need for a complex analogue to digital converter such as the converter described by Geen and Johnson (1985). Several authors have described modulated pulse torquing schemes for gyroscopes aimed at providing a digital output, but to date, all the reported configurations use analogue controllers. A good example of the design of a pulse torquing scheme is given by Coffman (1974). A detailed description of the implementation and testing of a pulse rebalance loop designed for use with the Microflex gyroscope is given by Johnson and Smith (1984). A theoretical design of a digital controller was presented as a subject for a PhD thesis by Puri (1979). This thesis presents a new design method to provide the control algorithms for the rebalance loop controller. The design is based upon a non-interactive controller, and explores the sensitivity of the system to parameter variations and processing time with regard to reducing the controller complexity.

One of the main objectives of the work presented in the following chapters is to progress the design of a digital controller and implement a simple digital control element. To examine the practical problems of a digital rebalance loop.

1.5 Outline of Thesis

This thesis discusses the control of a miniature rate gyroscope. In particular it will discuss the problems associated with the electronic control of a two degree of freedom gyroscope. The thesis explores control using both analogue and digital techniques. The gyroscope used is the 'Microflex' gyroscope, developed and manufactured by British Aerospace.

Chapter II describes the Microflex gyroscope in detail and examines the electrical sensing of the angular displacement of the inertial element. Also described is the electro-mechanical system for torquing the gyroscope's inertial element.

Chapter III develops the detailed mathematical model of the gyroscope which is used in the analysis of the various control loops.

Chapter IV reviews the control theory related to the design of the analogue control loop. Also this chapter details the design of the analogue electronic circuits.

Chapter V reviews the control theory and problems associated with the design of a digital control loop. The chapter also details the design of the electronics necessary to implement the digital control loop.

Chapter VI presents and discusses the results obtained for the various control loops.

Chapter VII presents the conclusions and recommendations of the work outlined in this thesis.

REFERENCES USED IN CHAPTER I

Bonfield, D.G. (1977). The Dynamically Tuned Gyroscope - A Sensor for Low Cost Attitude References and Navigation Systems. In: Applications of Modern Gyro Technology. Royal Aeronautical Society.

Bulgakov, B.V. (1955). Applied Theory of Gyroscopes. 2nd ed. Moscow Translated by J. Schorrekon by the Israel Programme for Scientific Translation 1960. Jerusalem.

Coffman, D.E. (1974). Feasibility Study of a Digital Rebalance Loop for a Dry Tuned Gyroscope (NASA-CR-144089), University of Tennessee.

Corneretto, A. (1962). Novel Gyros Promise Long Life, Accuracy. Electronic Design. (March 1962) 4-7.

Duncan, R.C. (1964). 1964 State of the Art Navigation, Guidance and Control. 1st AIAA Annual Meeting, Washington DC June 29 - July 2 1964, paper 64.500.

Euler, L. (1765). Theoria motus corporum solidorum seu rigidorum, through Maunder, Gyrodynamics and its engineering applications, (1961).

ALONSO-FINN, A (1975). Fundamental University Physics, London. Addison-Wesley.

French, A.P. (1971). Newtonian Mechanics, London. Thomas Nelson and Sons Ltd.

Geen, J.A., Johnson, B. (1985). Analogue to Digital Converter, European Patent No. 85304837.9.

Gray, A. (1909). On Lagranges Equations of Motion and on Elementary Solution of Gyrostatic Problems. Proceedings of the Royal Society of Edinburgh reprint Vol XX1X part IV. Robert Grant and Sons.

Harrison, G.B., Rawlings, A.L. (1915). British patent No. 137059. Through Bulgalov B.V. (1955). applied theory of gyroscopes.

Hayward, R.B. (1865). Onadirect method of estimating velocities, accelerations, and all similar quantities with respect to axes moveable in any manner in space, with applications. Cambridge Philosophical Trans, Vol X, part 1.

Howe, E.W., Savet, P.H. (1962). The dynamically Tuned Free Rotor Gyro reprinted from Control Engineering, McGraw Hill.

Johnson, B., Smith, C.F. (1984). Final Report on Contract A85c/2244 for Pulse Torquing the Microflex Type 507 Gyro. British Aerospace (for RAE Farnborough). TR3018, December 1984.

Kliens, G., Stieler, B. (1979). Contribution of late Dr. Johannes Gievers to Inertial Technology - some aspects on the history of inertial navigation. In: Symposium of Gyro Technology - DEON - Deutse Gesellschaft fur ortung und Navigation E.U. Special Committee Gyro Technology Stuttgart. Institute of Mechanics, University of Stuttgart.

Maunder, L., Arnold, R.N. (1961). Gyrodynamics and its Engineering Applications, London Academic Press.

Maunder, L. (1964). Recent developments in Gyrodynamics. Proceedings of the Institute of Mechanical Engineers 1964-65, vol 179, part 3E, pages 12-24.

Morris, P.G. (1980). Medical Imaging by Nuclear Magnetic Resonance. Physics Bulletin. Vol 31, 306-307.

Naylor, G.A. (1977). A Miniature Two Axes Rate of Turn Sensor for Advanced Missile and Stabilisation Systems. In: Applications of Modern Gyro Technology. Royal Aeronautical Society.

Newton, I. (1687). Principia, Through French, A.P. (1971). Newtonian Mechanics, London. Thomas Nelson and Sons Ltd.

Poinsot, L. (1851). Theorie nouvelle de la rotation des corps. Journal de Louisville, 16, through Arnold, R.N. and Maunder, L. Gyrodynamics and its engineering applications 1961. London Academic Press.

Poisson, S. (1833). Traite de Mecanique, 2nd ed. Paris through Arnold, R.N. and Maunder, L. Gyrodynamics and its Engineering Applications 1961. London Academic Press.

Pearson, E.B. (1964). An introduction to the gyroscope: an historical instrument. Proceedings of the Insititute of Mechanical Engineers 1964-65, vol 179, part 3E, pages 1-11.

Post, E.J. (1967) Sagnac Effect. Review of Modern Physics. Vol 39, No. 2, pages 475-493.

Puri, S.N. (1979). Direct Digital Control of Inertial Guidance Sensors, Phd Thesis, University of Aston in Birmingham, August 1979.

Savet, P.H. (1966). Gyroscopes. International Science and Technology, Jan. 1966, pages 50-57.

Sang, E. (1856). Trans. Roy. Scot. Soc. Arts, 4, 416.

Scarborough, J.B. (1958). The Gyroscope Theory and Applications. London Interscience Ltd.

Science Museum. The Foucault Pendulum.

Short, J. (1752). An account of an horizontal top invented by Mr. Serson. Phil. Trans. Roy. Soc. London 47, 1752.

Simmons, W.R. (1964). Miniature Rate Gyroscopes. Proceedings of the Institute of Mechanical Engineers. 1964-65, Vol 179, Part 3E, pages 95-105.

Sylvester, J.J. (1866). Phil. Trans. Roy. Soc. London.

Smith, S.G. (1977). The Effect of Modern Technology on Gyros. In: Applications of Modern Gyro Technology. Royal Aeronautical Society.

Sperry Gyroscope Company (1973). The gyroscope through the ages.

Stratton, A. (1964). Gyroscopes for Inertial Navigation, James Clayten lecture. The Institute of Mechanical Engineers.

Tait (1868). On the Rotation of a Rigid Body about a Fixed Point. Proc. Roy. Soc. Edinburgh, session 1867-68.

Wrigley, W. and Hollister, W.M. (1965). The Gyroscope: Theory and Application. Science Aug. 1965, Vol 149, pages 713-721.

CHAPTER II

THE MICROFLEX GYROSCOPE

2.1 A Brief History of the Microflex Gyroscope

The Microflex gyroscope is manufactured by British Aerospace at Bracknell, England. It is a highly miniaturised, two degree of freedom flex gyroscope. The Microflex gyroscope derives its name from its small size and unique flexure suspension. This suspension consists of a flexible strut pivot and radial spider. The flexure suspension system was developed in the United States by the Sperry Rand Corporation; its origins can be traced to a patent issued to Wing (1955). In his patent Wing describes a Rate of Turn Gyroscope, which features a flexure suspension. For a pivot Wing used a simple wire and a thin diaphragm acted as the radial spider. To convert this device to a rate gyroscope, Wing filled his gyroscope with liquid, and employed the hydrodynamic forces to provide the necessary restoring torques. Further development of flexure suspension can be traced through patents issued by the Sperry Rand Corporation. Querman (1970) describes a dry flexure suspension with a toggle strut to compensate for the torques introduced by flexing of the pivot. In 1976 Querman filed a patent which describes the current design of the suspension used in the Microflex gyroscope.

The very compact size of the Microflex gyroscope is achieved, in part, by the design of the pick-off and torquing scheme. This will be described in detail later in the chapter. The

development of the combined pick-off and torquer is documented in two U.S. patents filed by Querman. In 1971 he issued U.S. patent 3,557,629 which describes the operation of the torquer, and in 1976 he issued U.S. patent 741916 which describes the combined pick-off and torquer design. The design has been developed further to the state where the pickoff and torquing functions have been separated. This development will be described in more detail later.

The development of the Microflex gyroscope was transferred from the United States to the Sperry Gyroscope Company in England in 1975 (note: company changed to British Aerospace in 1983.) Initially, the Microflex gyroscope was operated as a displacement gyroscope. In this mode the gyroscope was suspended in gimbals. The angular displacement information provided by the gyroscope was used to servo the gimbals, to null the angle between the gimbal and gyroscope axes (Geary, 1977). The gyroscope has been successfully operated in the displacement mode as an attitude reference and as a north seeking gyroscope. However, operating the gyroscope in this mode does not exploit the advantage of the gyroscope's small size.

The small size of the Microflex gyroscope makes it highly suitable as a strapdown sensor. The generic term strapdown refers to a sensor which may be fixed to a surface, and be used directly to sense the motion of that surface. This type of operation excludes the use of gimbals. To overcome the

restrictions of limited freedom of the gyroscope's wheel, strapdown gyroscopes are normally operated in the rate mode (Napus, 1975). Recognising the potential of the Microflex gyroscope as a strapdown gyroscope, in 1978 the Sperry Gyroscope Company began the development of an electronic rebalance loop to use the Microflex gyroscope in a rate gyroscope mode. Since that time the development of the gyroscope has continued, resulting in two varients of the gyroscope :- the combined pickoff and torquer gyroscope (C.P.T.)and the separate pickoff and torquer gyroscope (S.P.T.).

2.2 The Mechanics of the Microflex Gyroscope

The mechanics of the C.P.T and the S.P.T. gyroscopes are identical. The description which follows refers to the C.P.T. gyroscope, the differences between to varients apply only to the pickoff and torquing arrangement. These differences will be decribed later in the chapter. The Microflex gyroscope, which is shown in Figure 2.1, is a highly compact two degree of freedom flex gyroscope. From Figure 2.1 it can be seen that the gyroscope comprises an angular wheel, mounted on a main shaft journalled by a pair of hard pre-loaded bearings, which is driven at synchronous frequency by a four pole hysteresis motor. The wheel is coupled to the main shaft by a flexible pivot and radial spider. An enlarged sketch of the flexible pivot and spider, which link the shaft to the wheel, is shown in Figure 2.2.

Figure 2·1 The Microflex Gyroscope

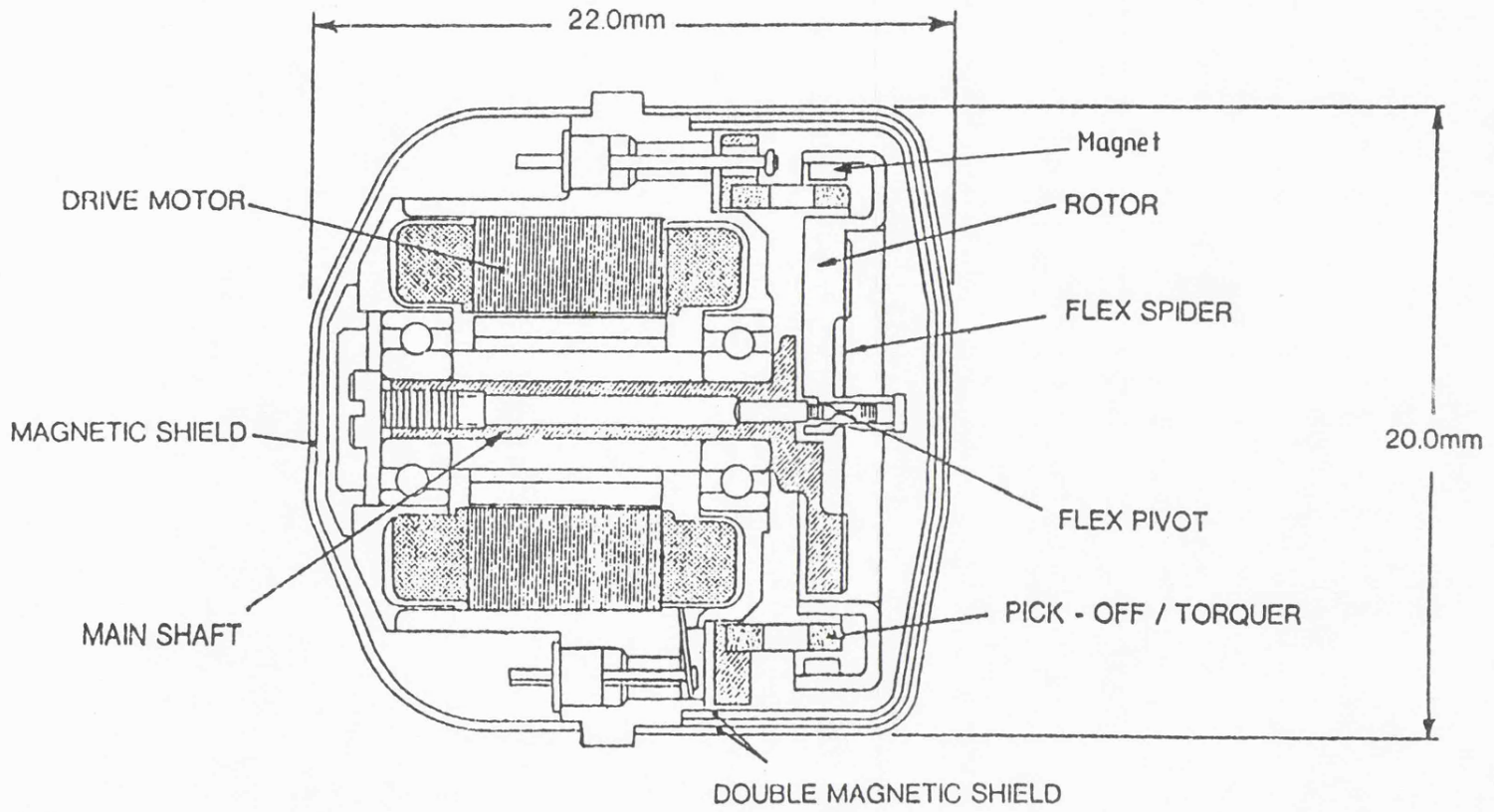

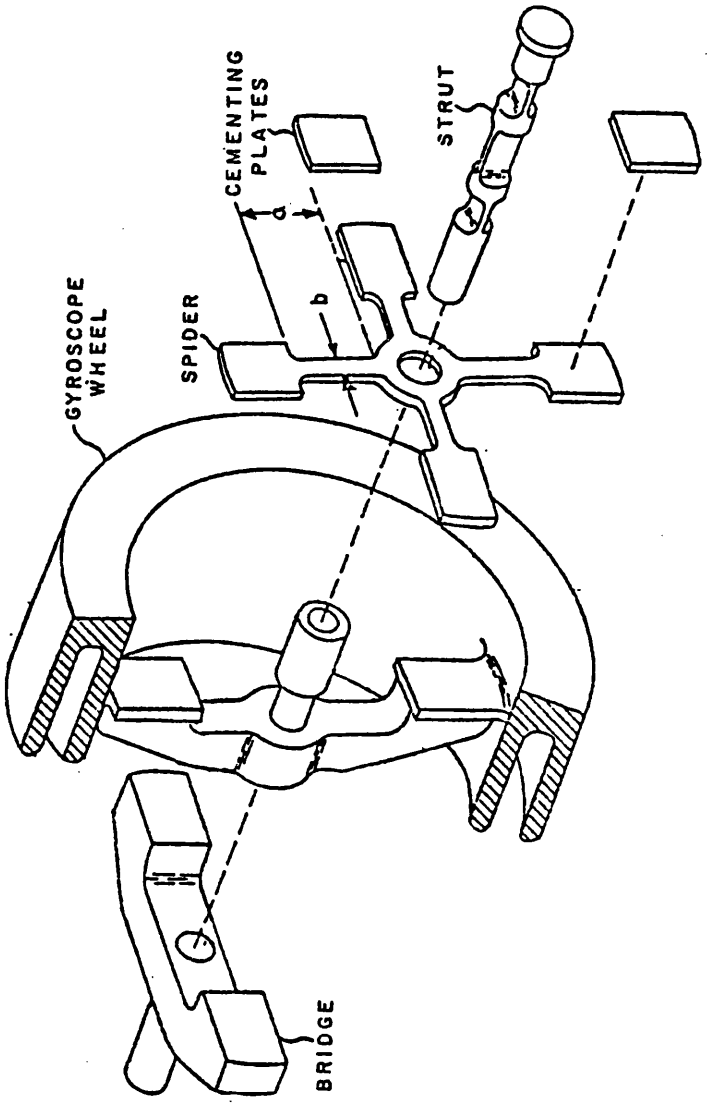

Figure 2·2 Microflex Gyroscope Suspension

The spider is fabricated from a thin, resilient, flat sheet of metal of thickness 0.001 inches. It is shaped as a cross with a central clearance hole. One diametric pair of radial arms is affixed to the bridge of the main shaft, while the other pair is affixed to the spoke of the gyroscope's wheel. The design is such that the tops of the bridge and the spoke of the wheel lie in the same diametric plane. The centre of the spider is unconstrained.

The flexible pivot consists of a cylindrical rod, with three flats ground in its active region. The centre flat is twice as long, and at right angles to the two end flats. This construction ensures that the centre of flexing is constant and that the pivot exhibits equal torsional stiffness in all directions. The flexible pivot is located inside the hollow tube at the centre of the wheel. One end of the pivot is affixed to the main shaft and the other end to the tube.

The flexure suspension provides translational rigidity in three mutually perpendicular axes, while exhibiting low torsional stiffness in the plane of the wheel. In operation, all radial and drive motor torques are carried by the spider. The spider allows angular tilt of the wheel with respect to the drive shaft by twisting deflection of its radial arms. In effect, the spider operates like a Hooke's joint. Hcwever, as the spider is mass balanced with respect to the pivot axis, it has inherently low sensitivities to the rotation frequency and vibrations. Axial loads are carried by the flexible pivot,

while angular tilt of the wheel is permitted by flexing of the pivot. Although the radial support of the pivot is soft, the extremely low mass of the suspension ensures that the aniso-elastic acceleration sensitivity is small. (Aniso-elasticity is the inequality of compliance of the structure in different directions).

The torques introduced by the flexing of the flex pivot act in a direction to restore the wheel to be orthogonal with respect to the shaft. To compensate for the pivot torques, use is made of the phenomenon of magnetic attraction. Figure 2.3 illustrates the scheme used.

Figure 2.3 Magnetic Compensation

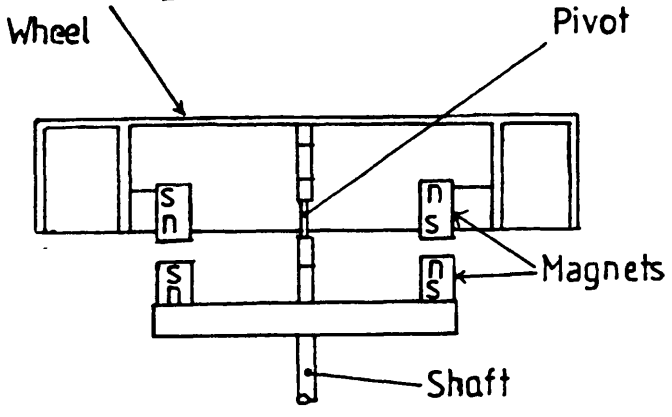

As shown in Figure 2.3, magnets are arranged in mutually attracting pairs. One magnet of each pair is attached to the rim of the wheel, while the other is attached to the shaft. Diametrically opposite pairs are arranged to have opposite polarity. This is in order to reduce torques due to stray magnetic fields. When the wheel of the gyroscope is orthogonal to the shaft the diametric torques acting upon it, due to the magnetic attraction, are equal and opposite. However, when

the wheel is tilted the gap between one pair of magnets increases, while the gap between a diametrical opposite pair decreases. This causes an inbalance in the torques acting upon the wheel. The resulting torque acts in a direction to increase the original displacement of the wheel. Although the change in magnetic attraction is non linear, over the small angular change it is sufficient to cancel the torques introduced by the flexing of the pivot. Adjustment of the compensation is achieved by adjusting the position of the shaft magnet. These are adjusted in preference to the wheel magnets in order to preserve the balance of the wheel.

The angular pickoff consists of a simple coil assembly, which projects into the annulus of the wheel. A continuous ring of magnet segments are attached inside the outer rim of the wheel, while eight magnetic segments are attached to the inner rim. This creates eight equally space zones of concentrated magnetic flux in the wheel anulus. To provide a good magnetic path the wheel is fabricated from a soft magnetic material. Rotation of the wheel subjects the coil assembly to an alternating magnetic flux. This generates an alternating voltage in the coil. The coil assembly is designed such that angular displacement of the wheel amplitude modulates this voltage. When this signal is synchronously demodulated it reproduces an electrical equivalent to the mechanical tilt of the wheel. The same coil assembly which is used to detect tilt of the wheel is also used to convert electrical signals

Figure 2,4 The Separate Pickoff and Torquer Gyroscope

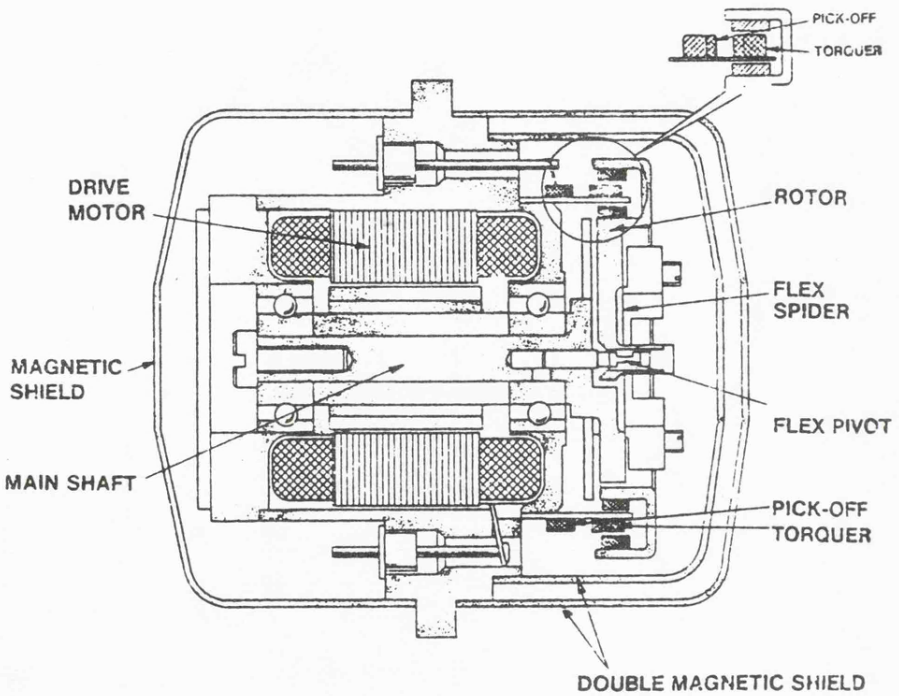

Pickoff and Torquer Coils

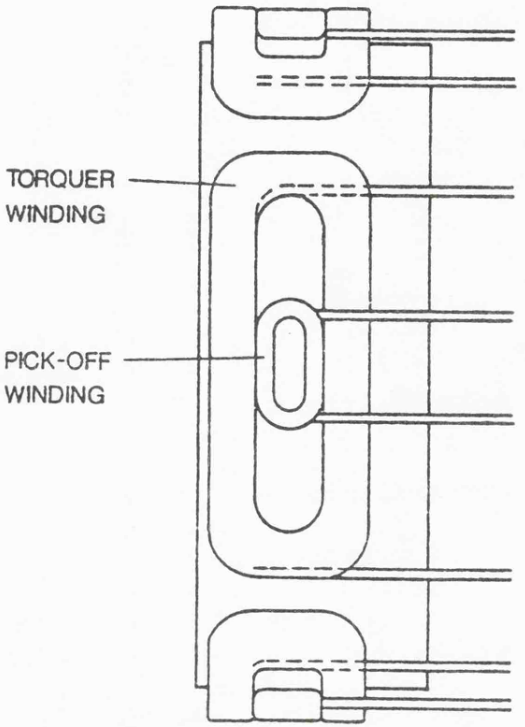

to torques to precess the wheel. This is achieved by driving a low frequency current through the coil assembly. The interaction of the magnetic flux of the wheel magnets and the flux established by the current in the coils, applies a torque to the wheel.

To reduce windage effects, the gyroscope is evacuated to a pressure of 20 torr. To screen against stray magnetic fields, the gyroscope is encased in a pair of soft magnetic covers.

2.2.1 Differences between the Gyroscope Varients

Figure 2.4 shows the separate pickoff and torquer gyroscope, with the details of the pickoff magnified for clarity. The principle of operation of the pickoff and torquer are identical to that described for the combined pickoff and torquer arrangement. The separation of the two functions is achieved by fitting four additional pickoff coils. As can be seen from figure 2.4 ,the new coils are cemented in the centre of the torquer coils. The reduction in size of the pickoff coil is such that the span of the new coil is equal to one magnet span. To gain additional benefit in the torquer, the coils are wound with fewer turns of heavier gauge wire, this allows higher angular rates to be attained, for a fixed voltage drive for the same power dissipation.

2.3 Electro-Mechanical Interfaces

The electro-mechanical interfaces of the gyroscope are, the drive motor, the angular displacement transducer (pick-off) and the torquing device (torquer). The principles of operation

apply to both the C.P.T. and the S.P.T. gyroscopes, however the practical implementation of these involves different geometrical and winding design for the tranducer coils.

The gyroscope drive motor is a four pole hysteresis motor. It is driven at synchronous speed by a two phase supply. The hysteresis motor was selected for its small size and stability of rotation frequency.

The pick-off provides angular displacement information. The limited angular freedom of the Microflex wheel (+/- 1 deg) restricts the use of the gyroscope to applications where feedback is applied to null the angular displacement of the wheel. When the gyroscope is operated in the displacement mode, it is usually mounted in gimbals and the pick-off signal is used to servo the gimbals. When operated in the rate mode, feedback is applied directly to the gyroscope via the torquer. Both these modes of operation require that the pick-off exhibits good null stability.

The torquer provides a means of applying control to the gyroscope. In the displacement mode, torques can be applied via the torquer to cancel the inherent drift torques of the gyroscope. In the rate mode, the torquer is the means by which feedback is applied to the gyroscope.

2.3.1 The Geometry of the Pick-off and Torquer

The design rules which are developed in the following section apply only to the C.P.T. gyroscope. The design of the S.P.T. gyroscope is only restricted by the following constraints:-

i) The pickoff coil span must be an odd integer of magnet spans.

ii) The torquer coil span must be less than 90 deg.

A sketch of the components involved in the pick-off and torquer is shown in Figure 2.5. The pick-off voltage is generated in the vertical windings of the coil, while the top windings are used for torquing.

Figure 2.5 The Pickoff and Torquer

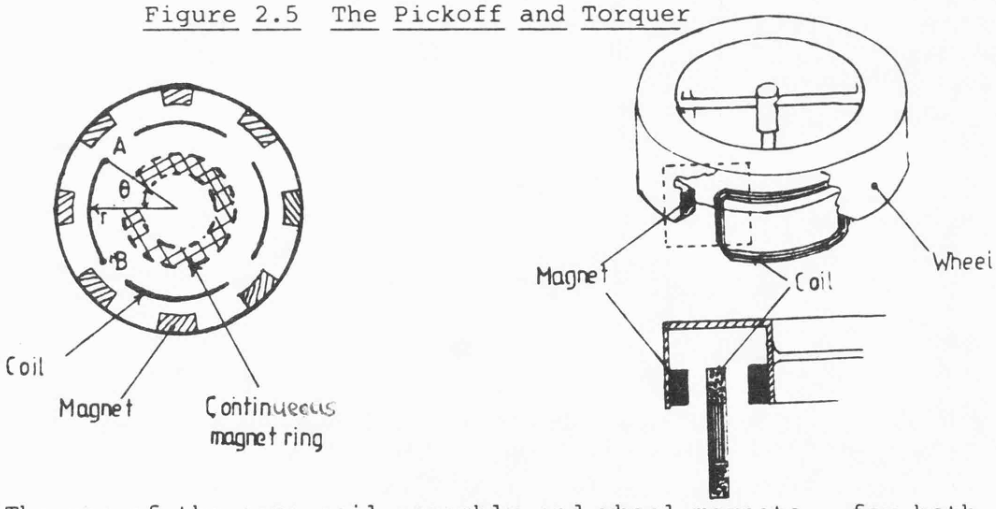

The use of the same coil assembly and wheel magnets, for both the pick-off and torquer, imposes restrictions on the geometry of the system. To obtain the maximum sensitivity of the pick-off, it is necessary to keep the span of the coils as short as possible. This can be explained by referring to Figure 2.5; as the pick-off points A and B are moved apart around the

circumference of the assembly, the linear displacement of the wheel (for a given tilt) reduces. As the pick-off is proportional to linear displacement, the sensitivity of the pick-off is reduced. Torquing however, requires the span of the coil to be as long as possible, as the force applied is proportional to the span of the coil. From Figure 2.5 it can be deduced that the pick-off sensitivity is proportional to cosine θ. It will be shown later that the torque (M) applied to the wheel is given by:

$$M = \frac{F\ r^2\ \sin\theta}{\pi}$$

Where F is the force applied per unit length of coil. Combining the two relationships, it can be shown that the maximum product of the torquer scale and pick-off scale factor occurs when $\theta = \frac{\pi}{4}$ rads.

To achieve a good pick-off signal, the spacing of the magnet must be such that when a magnet passes point A, a space must pass point B. To minimise the amount of harmonics generated, the magnet to space ratio must be unity. Since two axes are required, the coils are restricted to a maximum span of $\frac{\pi}{2}$. To ensure that the pick-off signals of each axis are in phase, an even number of magnets must be used. From these conditions two equations can be obtained which define the system's geometry. These are:

$$2\theta < \frac{\pi}{2} \qquad 2.1$$

$$2\theta = \frac{(n + \frac{1}{2})\ 2\pi}{m} \qquad 2.2$$

Where n is an integer, m is the number of magnets, and 2θ is

the span of the coil.

Eight magnets are used in the Microflex gyroscope's pick-off and torquer system. If this value is substituted in Equation 2.2 and ' Equation 2.1 is applied the maximum value of n = 1.5. The nearest integer value which satisfies Equation 2.1 is n = 1, this gives a coil span 3/8π (rads).

2.3.2 The Pick-off

Detection of the angular displacement of the gyro wheel is achieved using a method which employs electromagnetic induction. The four coils are fixed to the gyro case and are positioned around the rim of the wheel, as shown in Figure 2.5. Attached to the inner rim of the wheel are eight samarium cobalt rare earth magnets. The magnets are equally spaced with an angular separation of $\frac{\pi}{4}$ (rads). As the gyroscope's wheel rotates, the modulated magnetic flux pattern cuts the vertical edges of the coils and induces an e.m.f. in the coils. Figure 2.6 illustrates how the e.m.f. is induced, in an individual coil.

Figure 2.6

Pickoff Signal Generation

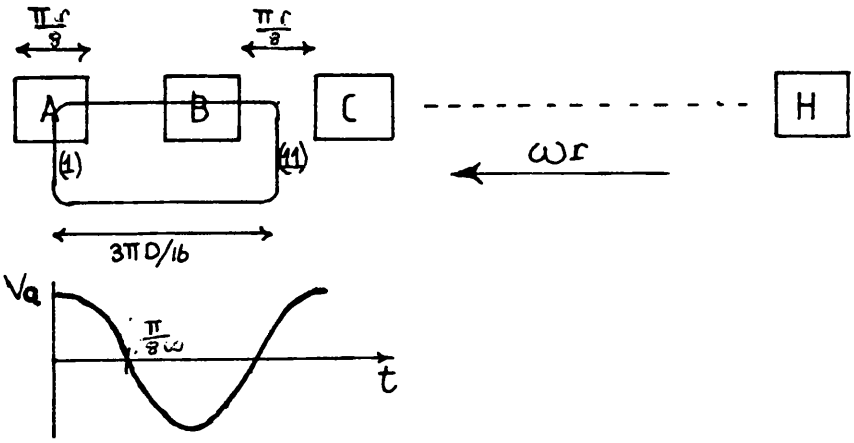

As magnet 'a' passes the edge (i) of the coil the magnetic flux cutting edge (i) passes through a peak and an e.m.f is generated in the coil. Let us assume that the induced e.m.f tries to drive a current in a positive sense, and that the magnitude of the e.m.f is 'Va'. The next magnet to pass an edge of the coil, and hence the next peak in the magnetic field, is magnet 'c'. This occurs after a rotation of the gyro wheel of $\pi r/8$. At this instant, magnet 'c' passes edge (ii) of the coil. The windings of this edge are in the opposite sense to edge (i), thus the e.m.f induced has magnitude '-Ve' and tries to drive current in a negative sense. Hence a voltage which is approximately sinusoidal is generated in a rotation of the $\pi r/4$. This means, that in one revolution of the gyro wheel (a displacement of $2\pi r$) eight cycles of pick-off signal are generated in the coil.

The distribution of the magnetic flux around the wheel may be approximated by a cosine distribution. This assumption will be examined later. It can be shown that the flux (B) experienced by one edge of a coil is given by:

$$B = Bm \left(\frac{1 + \cos 8wt}{2}\right) \qquad 2.3$$

Where Bm is the maximum flux density (tesla) and ω is the rotation frequency ($rad/_{s}$), t is time (seconds).

The geometry of the pick-off is such that the flux (B') experienced by the other edge of coil is delayed by half a cycle thus (B') is given by:

$$B' = Bm \left(\frac{1 - \cos 8wt}{2}\right) \qquad 2.4$$

The voltage (ε_c) generated in each edge of the coil is given by the flux cutting law (Duffin 1973):

$$\varepsilon = \int (\underline{V} \wedge \underline{B}).d\underline{\ell}$$

Where B is flux (tesla), V is the linear velocity ($msec^{-1}$), ℓ is the length of conductor in the magnetic field (m).

The voltage generated (ε) in each coil (assuming flux, motion and conductor mutually orthogonal) is given by the difference in the voltage generated in each edge of the coil, and is given by:

$$\varepsilon_c = \omega\ r\ B_m\ \ell\ n \cos 8wt \qquad 2.5$$

define $\varepsilon_o = \omega\ r\ B_m\ n$

Where n is the number of turns and r is the radius of coil assembly.

Angular displacement of the gyro wheel changes the length of coil which is cut by the magnetic field, and hence increases or decreases the voltage generated in the coils. To enhance this effect the coils are connected in diametrically opposing pairs (see Figure 2.7). The coils of a pair are electrically connected in antiphase, hence the output from a coil-pair is the difference between the voltages generated in each coil of the pair. When there is no angular displacement of the wheel, the magnitude of the voltage generated in each coil is equal, and the output from a coil-pair is zero.

Figure 2.7 Tilting of the Gyro Wheel

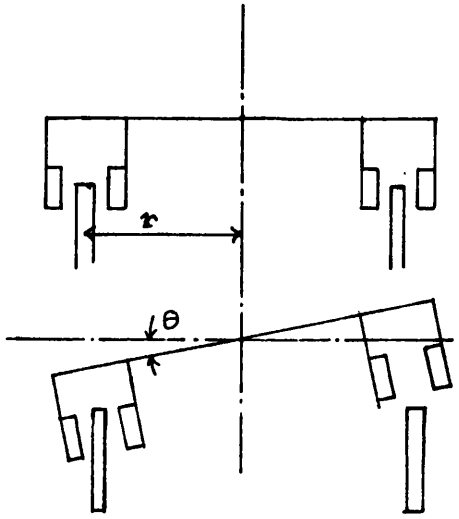

When the wheel is tilted, the length of one coil of the diametric pair of coils cutting the magnetic flux increases, while for the other the length decreases. This results in an unbalance in the magnitude of voltage generated in each coil. Referring to Figure 2.6 it can be shown that the difference in the voltage generated in a coil pair ε_ρ is:

$$\varepsilon_\rho = r\ \varepsilon_o \sin(2\theta) \cos(8wt) \qquad 2.6$$

Motion of the wheel modulates the angle say:

$$\theta = \theta_o \cos(\omega_m t)$$

If this is substituted in equation 2.6 we obtain:

$$\varepsilon_\rho = r\,\varepsilon_o \sin[2\theta_o \cos(\omega_m t)] \cos 8\omega t \qquad 2.7$$

Now $\sin[2\theta_o \cos(\omega_m t)] = 2J_1(2\theta_o)\cos\omega_m t - 2J_3(2\theta_o)\cos 3\omega_m t + \ldots$

Where $J_n(2\theta_o)$ are the zeros of the solution of Bessels equation hence:

$$\varepsilon_\rho = r\,\varepsilon_o \cos(8wt)\,[2J_1(\theta_o)\cos\omega_m t - 2J_3(2\theta_o)\cos 3\,\omega_m t + \ldots]$$

This result shows the pick-off signal to be a double-sideband-suppressed carrier signal, however this equation also generates sidebands about all the odd harmonics of carrier frequency. For small angles this equation reduces to a simpler form:

$$J_\ell(r_o) \sim \frac{r^\ell}{2\ell!}$$

$\lim r \to 0$

Maximum angular displacement for the Microflex gyro is 30 arc mins hence:

$$J_1(2\theta_o) \cong \frac{2\theta_o}{2} \cong \theta_o$$

$$J_3(2\theta_o) \cong \frac{(2\theta_o)^3}{2(2 \times 3)} \to 0 \text{ as } 2\theta_o \to 0$$

Higher terms of $J(2\theta_o)$ tend to zero thus the expression for the pick-off voltage ε_ρ becomes:

$$\varepsilon_\rho = 2\varepsilon_o\, r\, \theta_o \cos(8\omega t) \cos(\omega_m t) \qquad 2.8$$

To obtain Equation 2.8 it was assumed that the flux was distributed around the circumference of the gyroscope wheel in a cosine distribution. The basis of this assumption is as

follows, if the flux zones were restricted to the area of the magnets, the variation of the flux would be a squarewave. This can be represented by a fourier series of odd harmonics of the fundamental frequency (8ω). The fundamental is the largest component and is assumed dominant. However, in fact the flux zones are not restricted to the magnet area, fluxes from neighbouring magnets, and fringing due to the magnets shape, cause rounding of the squarewave. This rounding has the effect of reducing the higher frequency component and introducing even harmonics in the Fourier representation of the signal. This rounding of the flux zones enhances the dominance of the fundamental frequency and is the main justification of the cosine distribution.

The foregoing discussion also assumed that the coils are concentrated as a single turn. In practice, the coils will be distributed over a small area. Also, the corners of the coils are not perfect right angles but are radiused, these factors also influence the harmonic content of the pick-off signal.

Figure 2.8 Effects of Real Coils

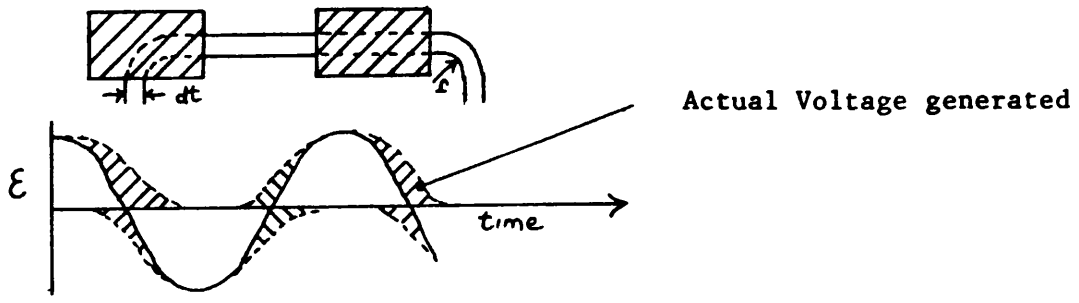

Figure 2.8 shows some of these effects upon the signal generated in a coil. These effects cause some cancellation of the signal. However, the pulse generated by an individual magnet passing a particular edge of one coil can be represented by a Fourier series of the form:

$$\varepsilon(t) = \varepsilon_o + \sum_{n=1}^{n=\infty} \varepsilon_n \cos n\,\omega t \qquad 2.9$$

Where ε_o, ε_n are the Fourier coefficients. For small time shift Δt in the origin of the pulse, corresponding to small positional errors in the location of the magnets 2.9 may be extended to:

$$\varepsilon\,(t \pm \Delta t) = \varepsilon_o + \sum_{n=1}^{n=\infty} \varepsilon_n \cos\,(n\,\omega t + \phi_n) \qquad 2.10$$

and $$\phi_n = \tan^{-1}\left[\frac{-\int_{-T}^{T} \varepsilon(t + \Delta t)\,\sin n\,\omega t\,dt}{\int_{-T}^{T} \varepsilon(t + \Delta t)\,\cos n\,\omega t\,dt}\right]$$

Where T is the time for one revolution of the gyroscope wheel and $\pm\Delta t$ is the maximum uncertainty due to any magnet's position relative to the pickoff coil.

If we now describe the voltage generated by a magnet passing an edge of a coil in the following manner:

$$\varepsilon(t) = G_{pq}(L)$$

This nomenclature represents the magnitude and shape of the voltage generated in a coil G by magnet p passing edge q at time L, G is a general label for a particular coil, p has associated functions which relate it to the field strength of magnet p, while q has associated functions which relate it to the distribution of turns of the coil and the length of conductor cut by the magnetic field. L describes the time when the centre of the magnet is aligned to centre of a coil

edge.

Referring to Figure 2.6 and using the above nomenclature, the voltage generated (ε_o) in a coil G is given by:

$$\varepsilon_c(t) = G_{ai}(0) - G_{cii}\left(\frac{T}{16} \pm \Delta t\right) + G_{bi}\left(\frac{T}{8} \pm \Delta t\right)$$

Δt is the uncertainty incurred by the positional tolerance of the magnets.

This can be extended to describe the voltage generated in a diametrically opposed pair, the other coil in the pair will be labelled F, thus:

$$\varepsilon_\rho(t) = [G_{ai}(0) - G_{cii}\left(\frac{T}{16} \pm \Delta t\right) + G_{bi}\left(\frac{T}{8} \pm \Delta t\right) \ldots] - [F_{ei}\ (\pm \Delta t) - F_{fii}\left(\frac{T}{16} \pm \Delta t\right) + F_{gi}\left(\frac{T}{8} \pm \Delta t\right) \ldots] \qquad 2.11$$

For simplicity consider only the voltage from t=0 to t=Δt.

$$\varepsilon_\rho\ (\pm \Delta t) = G_{ai}(o) - F_{ei}\ (\pm \Delta t)$$

Using the result of equation 2.10, we have:

$$\varepsilon_\rho\ (\pm \Delta t) = \varepsilon_o + \sum_{n=1}^{n=\infty} \varepsilon_n \cos\ (n\ \omega t) - \varepsilon_o' + \sum_{n=1}^{n=\infty} \varepsilon_n' \cos\ (n\ \omega t + \phi_n) \qquad 2.12$$

The dash notation has been used to distinguish between the two coils G and F.

Equation 2.12 gives a good representation of the pick-off signal, and contains terms which describe the effects of the small perturbations of a non ideal pick-off system. the terms (ε's) describe the magnitude of the voltage generated. These are functions of the magnetic field strength, the distribution of the coil and the length of coil in the magnetic field (and

hence the modulation). The cosine terms represent the frequency components of the pick-off signal. The term ϕn represents the effects of positional errors of the locations of the magnets. The pick-off signal consists of a series of terms similar to that of Equation 2.12 repeated every T/8 seconds, while the whole series is periodic every T seconds.

Consider the special case of when the gyroscopic wheel is orthogonal to the shaft, and the magnets evenly spaced, ($\Delta t=0$). Under these circumstances Equation 2.12 reduces to:

$$\varepsilon_\rho(0) = \varepsilon_o - \varepsilon_o' + \sum_{n=1}^{n=\infty} (\varepsilon_n - \varepsilon_n') \cos(n\,\omega t)$$

Ideally when the wheel is orthogonal the terms should be equal, thus $\varepsilon_\rho(t) = 0$. However, the terms depend on the individual magnetic field strengths, the distribution of the coils and the length of coil in the magnetic field. Differences in any of these parameters will result in a non zero value for $\varepsilon_\rho(t)$. Variations in the locations of the magnetic poles, as can be seen from Equation 2.12 will also result in a non zero value for $\varepsilon(t)$.

Figure 2.9a shows the pick-off signal after pre-amplification. In this signal we can see the largest frequency component is approximately 1600Hz, with many harmonics. Superimposed upon the signal is a 200Hz modulation. This is thought to be due to eccentricity of the rotation of the wheel and the coil assembly. Further evidence which suggests that this is the dominant effect, is seen after

Figure 2,9

The Pickoff Signal (after the preamplifier)

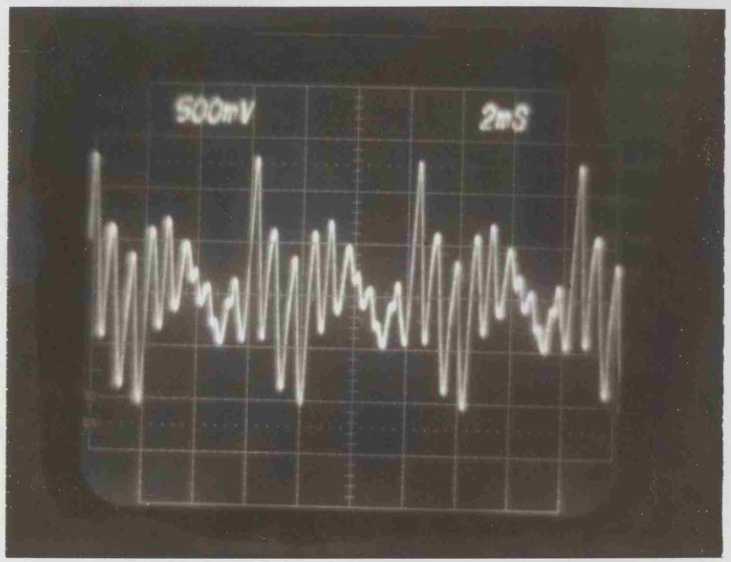

Figure 2,9a

Unmodulated

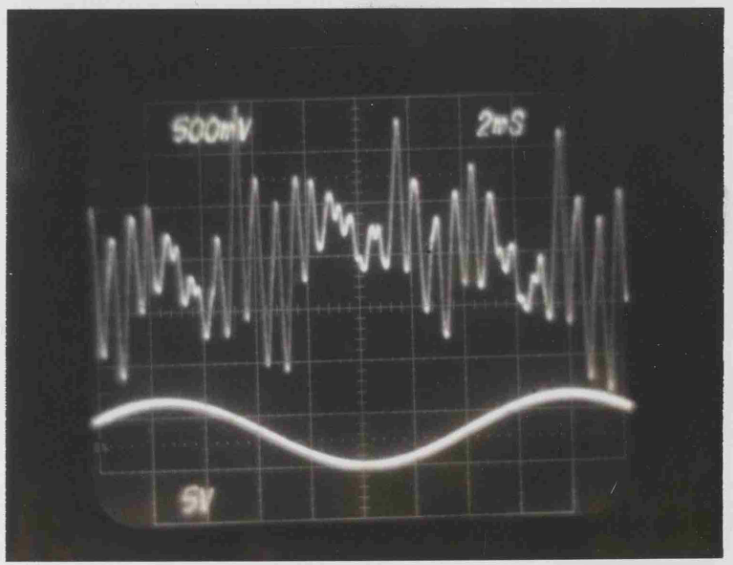

Figure 2,9b

Modulated

FIGURE 2.10

GYROSCOPE PICKOFF SPECTRUM (AFTER PREAMPLIFIER)

Separate Pickoff and torquer Gyroscope operating at 160Hz Wheelspeed

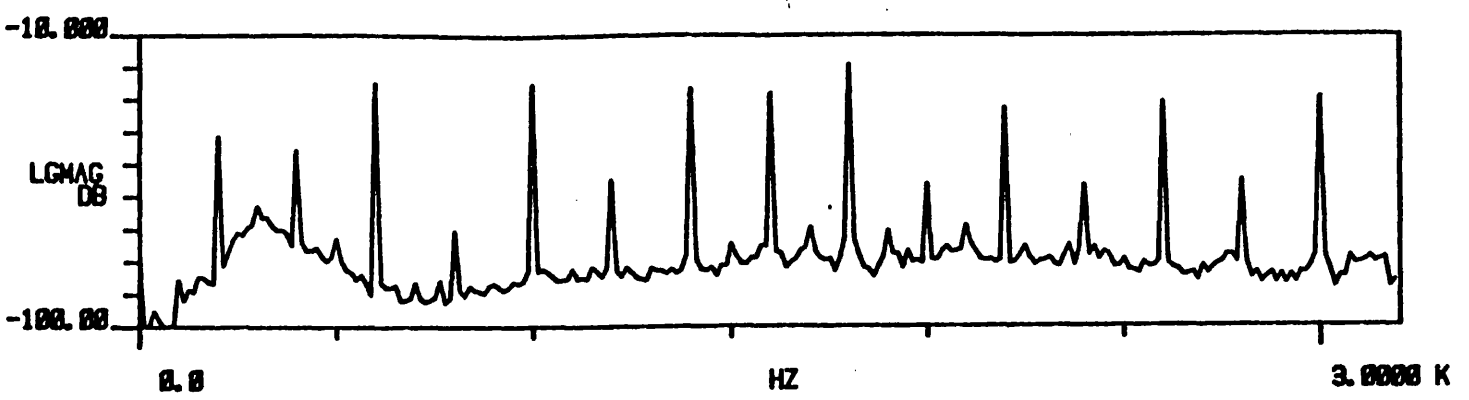

Combined Pickoff and torquer Gyroscope operating at 200Hz Wheelspeed

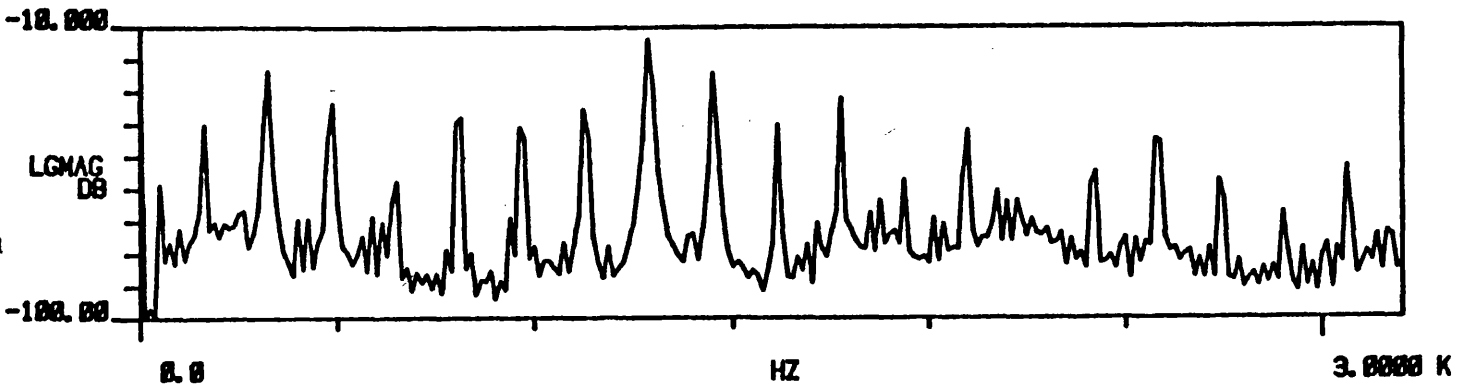

FIGURE 2.10

GYROSCOPE PICKOFF SPECTRUM (AFTER PREAMPLIFIER)

Separate Pickoff and torquer Gyroscope operating at 160Hz Wheelspeed

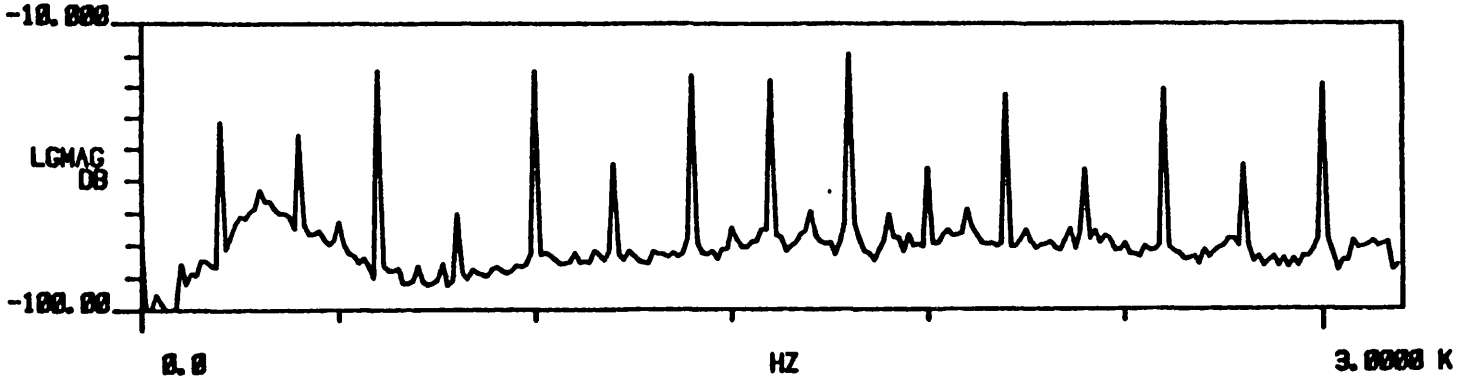

Combined Pickoff and torquer Gyroscope operating at 200Hz Wheelspeed

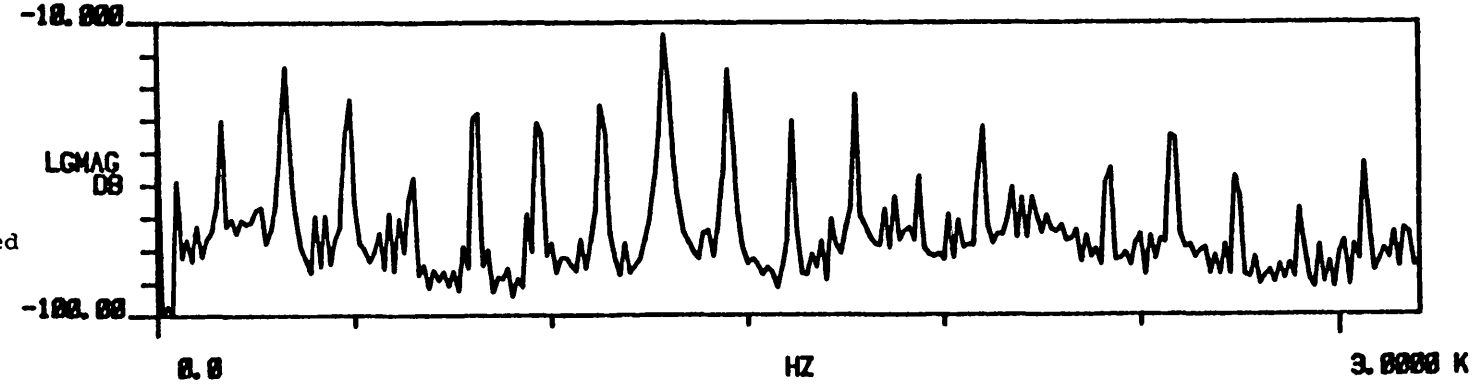

the signal is demodulated. After demodulation the 200Hz signals appear to be 90 deg out of phase when both axes of the gyroscope are compared. Figure 2.9b shows the pick-off signal when the angular displacement of the wheel is modulated. The lower trace of Figure 2.9b shows the modulating signal. The top trace shows the pick-off signal, it can be seen that the signal is amplitude modulated. However, all the side bands of the harmonics are also amplitude modulated. Figure 2.10 shows the typical spectrum analysis of the pickoff signal, this clearly shows the harmonics of wheel speed.

2.3.3 Torquer Motor

The conversion of electrical signals to mechanical torques is achieved by driving low frequency currents through the torquer coils. The coils used are the same coils which are used for the angular pick-off. The sensitive axes of the gyroscope are defined by a diametrically opposed pair of coils. The coils are electrically connected in anti-phase and are rigidly attached to the case of the gyroscope. When a current is driven through the coils, the flux established couples with the field of the wheel magnets and applies a force to the wheel. The couple of this force produces the torque necessary to precess the wheel.

Figure 2.11 The Torquer Motor

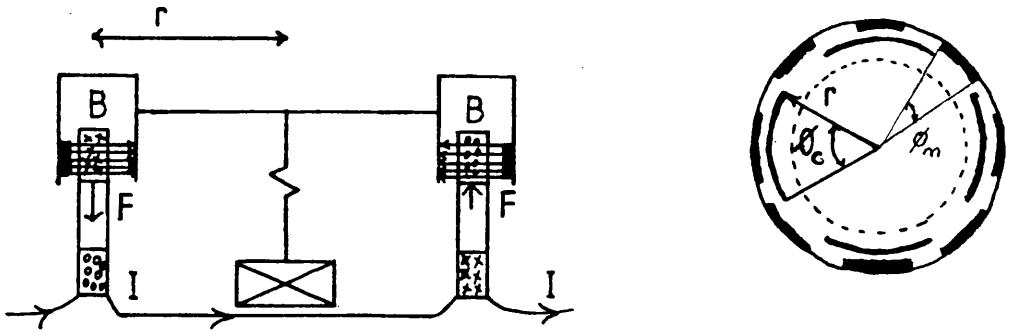

The basis of the torquer motor is shown in Figure 2.11, the coils are connected in antiphase thus the force acting upon each side of the wheel is in the opposite sense, ie. a positive/upward force acts at one side of the wheel while a negative/downward force acts upon the other side.

The force (F) applied to the wheel by current i is given by:

$$\underline{F} = \int i d\underline{\ell} \wedge \underline{B}$$

Where $d\underline{\ell}$ is an elemental length of the coil (metres) and is given by:

$$d\underline{\ell} = n\underline{r} \wedge \underline{d\phi_c} \qquad 2.13$$

Where n is the number of turns and $\underline{d\phi_c}$ is an elemental span of the coil (radians) B is the magnetic field, due to the wheel magnet, experienced by the coil. From Equation 2.3 we have:

$$B = B_m \frac{(1 + \cos 8\omega t)}{2} \qquad 2.3$$

Now $\omega t = \phi$, the angle through which the wheel moves in time t, thus Equation 2.3 becomes:

$$B = B_m \frac{(1 + \cos 8\phi_m)}{2} \qquad 2.14$$

Substituting the results of 2.14 and 2.13 in the expression for force we have:

$$\underline{F} = \int_0^{\phi_c} nir d\underline{\phi} \wedge \frac{(1 + \cos 8\theta_m)}{2} \underline{B}_m$$

$$|F| = \frac{nriB_m}{2} \frac{(\phi_c + \sin 8\phi_m)}{8} \qquad 2.15$$

Recalling the Equation 1.6 from Chapter 1 we have the precession rate given by:

$$\dot{\theta} = \frac{2Fr}{I_z \omega} \qquad 1.6$$

Combining Equation 2.15 and 1.6 we have:

$$\frac{\dot{\theta}}{i} = \frac{nr^2 B_m (\phi_c + \frac{\sin 8\phi_m}{8})}{I_z \omega} \qquad 2.16$$

This equation defines the torquer scale factor of the gyroscope.

Order of magnitude calculations of the gyro scalefactor and other parameters are given in Appendix 1.

REFERENCES USED IN CHAPTER II

Crangle, J. (1977). The Magnetic Properties of Solids, London, Edward Arnold Ltd.

Duffin, W.J. (1973). Electricity and Magnetion. 2nd ed., London, McGraw Hill.

Geary, M. (1977). Miniature Flex Gyros. In: Applications of Modern Gyro Technology. Royal Aeronautical Society.

Napus, G.A. (1975). Recent Advances in Strapdown Inertial Navigation. 1975 IEEE INTERCON.

Quermann, T.R. (1971). Sperry Rand Corporation. Pick-off and Torquing Device. U.S. Patent 3,557,629.

Quermann, T.R. (1970). Sperry Rand Corporation. Gyroscopic Rotor Suspension. U.S. Patent 3,529,477.

Quermann, T.R. (1976). Sperry Rand Corporation. Pick-off, Torquer, and Reference Signal Generator for Free Rotor Gyroscopes, U.S. Patent 7,419,16.

Wing, W.G. (1955). Sperry Rand Corporation. Rate of Turn Gyroscope, U.S. Patent 2,719,291.

CHAPTER III

THE DERIVATION OF A DETAILED MATHEMATICAL MODEL FOR THE MICROFLEX GYROSCOPE

3.1 Introduction and Foundations of the Model

The model described in this chapter is a general model for any two degree of freedom gyroscope, however it is selective of the parameters which are of particular importance when dealing with variants of the Microflex gyroscope. The Microflex gyroscope is unique in the sense that it is untuned and the suspension has a very simple dynamic behaviour.

The model used to describe the dynamics of the Microflex gyroscope is based upon the equations of motion of the gyroscope, which are derived in Appendix I. The Laplace transforms of these equations can be conveniently expressed in matrix form:

$$\begin{bmatrix} \bar{M}_x \\ \bar{M}_y \end{bmatrix} = \begin{bmatrix} sI_x & I_z\omega \\ -I_z\omega & sI_x \end{bmatrix} \begin{bmatrix} \bar{\dot{\theta}}_x \\ \bar{\dot{\theta}}_y \end{bmatrix} \qquad 3.1$$

Where s is the Laplacian operator, the bar notation denotes the Laplace transform, M_x and M_y are the precession torques applied to the x and y axes, $\dot{\theta}_x$ and $\dot{\theta}_y$ are the precession rates, ω is the rotational frequency of the gyroscopes wheel,

and I_z and I_x are the moments of inertia of the gyroscopes wheel about its spin axis and a diametric axis respectively. From these equations a mathematical model of the gyroscope can be obtained, this basic model is shown in Figure 3.1.

Figure 3.1

The Basic Gyroscope Model

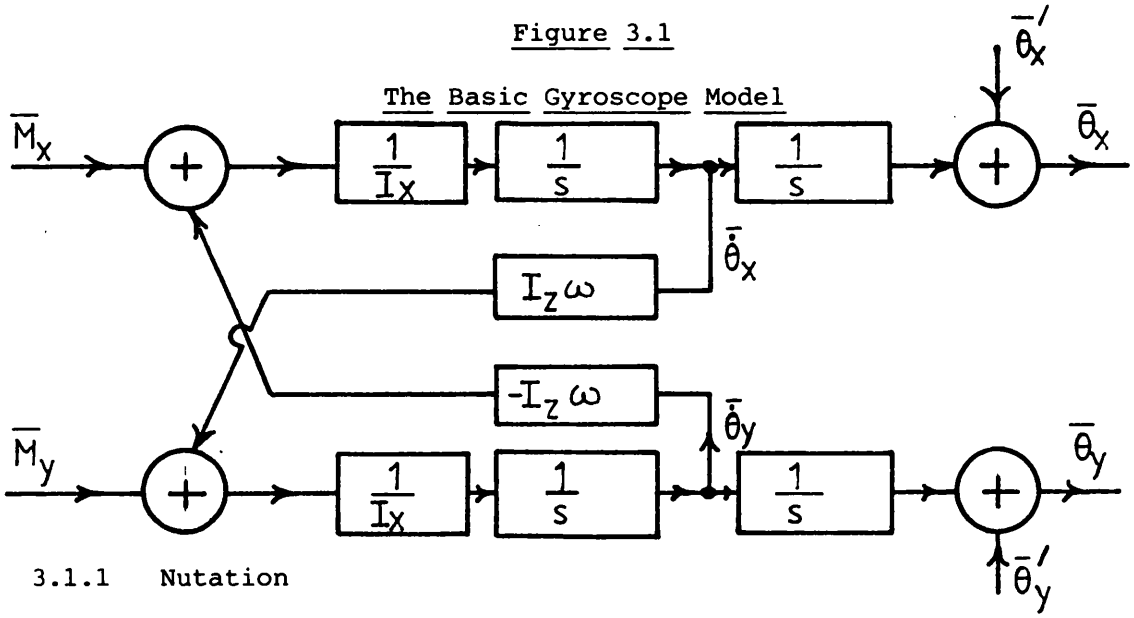

3.1.1 Nutation

Nutation is a feature of all two degrees of freedom gyroscopes. It arises from the interaction of the precessional torques. This coupling can be clearly seen from the model shown in Figure 3.1; a change of torque applied to the x axis, produces precession rates in both axes. This can be examined mathematically by solving Equation 3.1 for $\dot{\bar{\theta}}$. Recalling Equation 3.1, and applying Cramers rule (Weiss and Dubisch, 1962), we have

$$\bar{\dot{\theta}}_x = \frac{\bar{M}_x\, sI_x - \bar{M}_y\, I_z\omega}{s^2 I_x^{\,2} + I_z^{\,2}\omega^2} \qquad 3.2$$

Equation 3.2 can be re-arranged and separated into two separate transfer functions:

$$\left.\frac{\bar{\dot{\theta}}_x}{\bar{M}_x}\right|_{M_y=0} = \frac{s}{I_x\left(s^2 + \frac{I_z^{\,2}\,\omega^2}{I_x^{\,2}}\right)} \qquad 3.3$$

$$\left.\frac{\bar{\dot{\theta}}_x}{\bar{M}_y}\right|_{M_x=0} = \frac{-I_z\omega}{I_x^{\,2}\left(s^2 + \frac{I_z^{\,2}\,\omega^2}{I_x^{\,2}}\right)} \qquad 3.4$$

The pair of equations 3.3 and 3.4 represent the main axis and the cross axis transfer functions. From Equation 3.3 we can see that the precession rate $\bar{\dot{\theta}}_x$ results from the derivative of the precession torque, ie. for a constant torque (M_x) there is no precession motion. From Equation 3.4 it can be seen that a precession torque applied in the Y axis will produce a precession rate about in the X axis.

Both Equations 3.3 and 3.4 contain the term:

$$\frac{1}{s^2 + \frac{I_z^{\,2}\,\omega^2}{I_x^{\,2}}}$$

This term is unstable and will cause oscillation, the

frequency of the oscillation can be determined by taking the inverse Laplace transform of Equation 3.4 thus:

$$\mathcal{L}^{-1}\left\{ \left. \begin{matrix} \dot{\theta}_x \\ \overline{M_y} \end{matrix} \right| M_x = 0 \right\} = \frac{-1}{I_x} \sin\left(\frac{I_z \omega}{I_x}\right) \qquad 3.5$$

This oscillation is called nutation. (The term nutation is derived from the Greek word for nodding.) The nutation frequency is defined by the product of the rotation frequency and the ratio of the moment of inertia about the spin axis to the moment of inertia about a diameter of the gyroscope's wheel.

Taking the inverse Laplace transform of Equation 3.3 yields:

$$\mathcal{L}^{-1}\left\{ \left. \begin{matrix} \dot{\theta}_x \\ \overline{M_x} \end{matrix} \right| M_y = 0 \right\} = \frac{1}{I_x} \cos\left(\frac{I_z \omega}{I_x}\right)$$

This shows that when excited, nutation produces equal motion simultaneously in both axes of the gyroscope. Clearly nutation will limit the performance of the gyroscope. However, for a practical gyroscope a finite amount of damping is present which acts to reduce nutation. Also it will be shown that the application of feedback may not necessarily excite nutation.

3.2 Detailed Model of the Gyroscope

A detailed model of the Microflex gyroscope is shown in Figure 3.2 (Downton, 1979). This model contains the terms which significantly effect the gyroscopes performance and influence the design of the rebalance loop.

The model is based upon the gyroscopic equations of motion, as presented in Figure 3.1. The damping term D, which was introduced in the last section, is included. This term arises from the viscous and magnetic damping of the wheel. The viscous damping is mainly due to drag of the gas within the gyroscope. Magnetic damping arises from the coupling of stray fields from the torquer and pickoff system, inducing eddy currents in the gyroscope's case. The terms K and ρ arise from the residual spring stiffness and auto erection and will be discussed later. The damping (D) resists changes in angular velocity of the wheel and applies a resistance torque to the wheel. This torque is proportional to the angular velocity ($\dot{\theta}$) of the wheel and as it resists angular motion its sign is negative.

If terms of ϕ, K and ρ are neglected, inspection of Figure 3.2 shows that, to include the damping term, Equation 3.1 must be rewritten:

$$\begin{bmatrix} \bar{M}_x \\ \bar{M}_y \end{bmatrix} = \begin{bmatrix} (I_x s + D) & I_z\omega \\ -I_z\omega & (I_x s + D) \end{bmatrix} \begin{bmatrix} \bar{\dot{\theta}}_x \\ \bar{\dot{\theta}}_y \end{bmatrix} \qquad 3.6$$

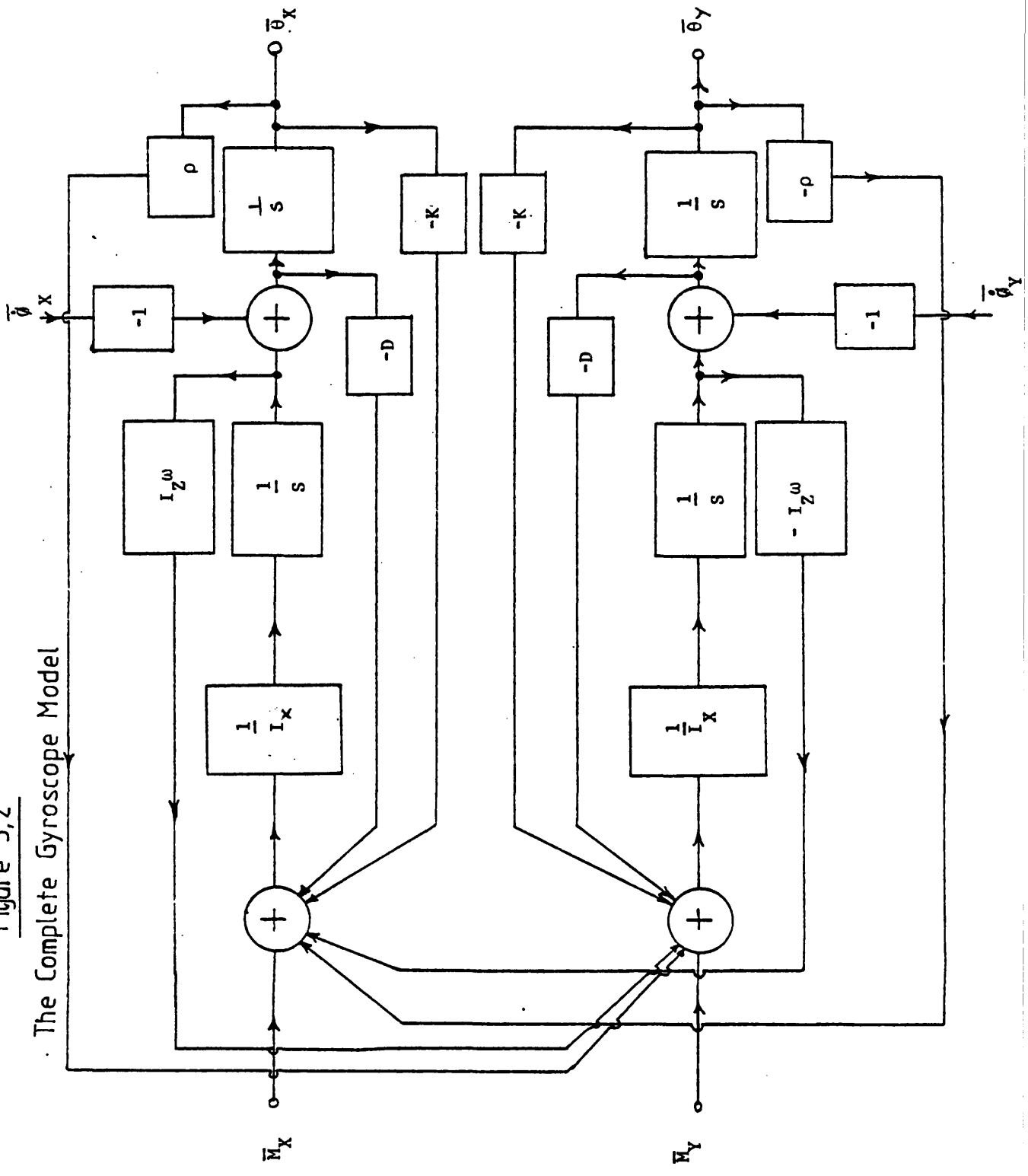

Figure 3,2

· The Complete Gyroscope Model

Applying Cramers rule, and taking the inverse Laplace transforms of Equation 3.6 it can be shown that for a step input:

$$\theta_x = M_x e^{\frac{-D}{I_x}t} \cos \omega_n t - \frac{M_y}{I_x} e^{\frac{-D}{I_x}t} \sin \omega_n t \qquad 3.7$$

$\omega_n = \frac{I_z}{I_x} \omega$ = the nutation frequency

A similar relationship to Equation 3.7 can be obtained for θ_y. This relationship shows clearly that the damping (D) acts to reduce the magnitude of nutation.

The model of Figure 3.2 has been configured to examine the effects of angular rates applied to the gyroscopes case. To simplify the model, vehicle rates ($\dot{\phi}$) have been summed with inertial rates. This simplification can be justified by returning to Figure 3.1, here the angular displacement of the wheel was summed with case displacement. However, for small angular displacement is the integral of angular rate, thus if angular velocities are summed instead of angular displacements the model is still correct. Provided all terms added to the basic model are case referenced the simplification of adding angular velocities is valid.

The term K in Figure 3.2 represents the residual uncompensated spring coefficient of the flexible pivot and the radial spider. This applies a resistance torque to the wheel which is proportional to the angular displacement of the wheel. If

the other terms arising from a practical gyroscope are neglected, the model can be represented by the matrix equation:

$$\begin{bmatrix} \bar{M}_x \\ \bar{M}_y \end{bmatrix} = \begin{bmatrix} (I_x s^2 + K) & I_z \omega s \\ -I_z \omega s & (I_x s^2 + K) \end{bmatrix} \begin{bmatrix} \bar{\theta}_x \\ \bar{\theta}_y \end{bmatrix} \qquad 3.8$$

Proceeding as before, using Cramers rule, we determine that:

$$\bar{\theta}_x = \frac{\bar{M}_x (I_x s^2 + K) - \bar{M}_y I_z \omega s}{I_x^2 s^4 + 2I_x K s^2 + K^2 + I_z^2 \omega^2 s^2} \qquad 3.9$$

If the approximations, $I_x^2 << I_z^2$ and $2I_x K << I_z^2 \omega^2$ are made, Equation 3.9 becomes:

$$\bar{\theta}_x = \frac{\bar{M}_x I_x (s^2 + \frac{K}{I_x}) - \bar{M}_y I_z \omega s}{I_z^2 \omega^2 (s^2 + \frac{K^2}{I_z^2 \omega^2})}$$

The term involving $\bar{M}_x$ will have a 'notching' effect while the term involving $\bar{M}_y$ will give rise to a cosine term of angular frequency

$$\frac{K}{I_z \omega}$$

The final term in the model of Figure 3.2 is the auto erection coefficient. This torque depends upon rotor deflection, the torque has a quadrature effect, ie. a deflection in the X axis produces a torque in the Y axis. These torques are due to the interaction of the spinning wheel and the flow of the surrounding gas. Kamich (1980) has

examined the origins of these torques. Quantatively Karnich has shown that the main mechanism for producing the erection torques is that shown in Figure 3.3.

Figure 3.3

Auto Erection Torques

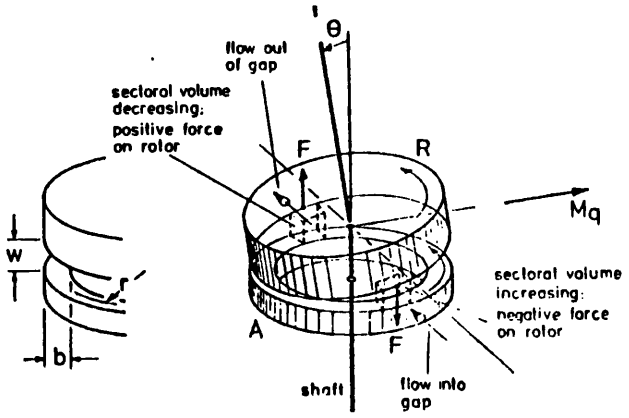

This mechanism operates in the following manner. Angular displacement of the wheel forms a wedge shaped change of volume about a diametric axis, between the wheel and the gyroscopes casing. The pumping of gas by the rotation of the wheel produces forces in the directions indicated in Figure 3.3. These forces are proportional to r b/w. The symbols have the meaning indicated in Figure 3.3. The auto erection effects can be represented by matrix equation.

$$\begin{bmatrix} \bar{M}_x \\ \bar{M}_y \end{bmatrix} = \begin{bmatrix} I_x s^2 & (I_z \omega s + \rho) \\ -(I_z \omega s + \rho) & I_x s^2 \end{bmatrix} \begin{bmatrix} \bar{\theta}_x \\ \bar{\theta}_y \end{bmatrix} \qquad 3.10$$

From Equation 3.10, proceeding as in the earlier cases, and neglecting the S^4 terms it can be shown that:

$$\bar{\theta}_x = \frac{\bar{M}_x I_x s^2}{I_z^2 \omega^2 \left(s + \frac{\rho}{I_z \omega}\right)^2} - \frac{\bar{M}_y}{I_z \omega \left(s + \frac{\rho}{I_z \omega}\right)} \qquad 3.11$$

Examining Equation 3.11 we can see that at low frequencies, the term containing $\bar{M}_y$ has a finite value. A fixed offset will produce a torque which precesses the gyroscope wheel to cancel the offset.

The complete model with all the terms is shown in Figure 3.2 and can be represented by the matrix equation:

$$\begin{bmatrix} \bar{M}_x \\ \bar{M}_y \end{bmatrix} = \begin{bmatrix} (I_x s^2 + sD + K) & (I_x \omega s + \rho) \\ -(I_x \omega s + \rho) & (I_x s^2 + sD + K) \end{bmatrix} \begin{bmatrix} \bar{\theta}_x \\ \bar{\theta}_y \end{bmatrix} \qquad 3.12$$

Using the usual rule of matrix algebra, Equation 3.12 can be re-arranged to give angular displacement as a function of applied torque, thus:

$$\begin{bmatrix} \bar{\theta}_x \\ \bar{\theta}_y \end{bmatrix} = \frac{\begin{bmatrix} (I_x s^2 + Ds + K) & -(I_z \omega s + \rho) \\ (I_x \omega s + \rho) & (I_x s^2 + Ds + K) \end{bmatrix} \begin{bmatrix} \bar{M}_x \\ \bar{M}_y \end{bmatrix}}{(I_x s^2 + Ds + K)^2 + (I_z \omega s + \rho)^2} \qquad 3.13$$

Equation 3.13 can be extended to include the angular rates applied to the gyroscopes case:

$$\begin{bmatrix} \bar{\theta}_x \\ \bar{\theta}_y \end{bmatrix} = \begin{bmatrix} \alpha & \beta \\ -\beta & \alpha \end{bmatrix} \begin{bmatrix} \bar{M}_x \\ \bar{M}_y \end{bmatrix} + \begin{bmatrix} \gamma & -\delta \\ \delta & \gamma \end{bmatrix} \begin{bmatrix} \bar{\dot{\phi}}_x \\ \bar{\dot{\phi}}_y \end{bmatrix} \qquad 3.14$$

$$\text{Where } \beta = \frac{-\left(I_z \omega s + \rho\right)}{\left(I_x s^2 + Ds + K\right)^2 + \left(I_z \omega s + \rho\right)^2}$$

$$\alpha = \frac{I_x s^2 + Ds + K}{\left(I_x s^2 + Ds + K\right)^2 + \left(I_z \omega s + \rho\right)^2}$$

$$\gamma = I_z \omega \beta - I_x s \alpha$$

$$\delta = I_z \omega \alpha + I_x s \beta$$

A model corresponding to Equation 3.14 is shown in Figure 3.4.

Figure 3.4

A Working Model of the Microflex Gyroscope

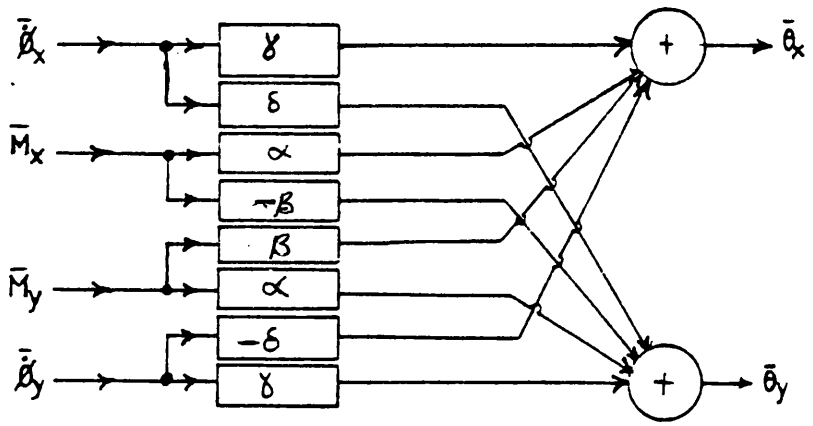

The model of Figure 3.4 is in a convenient form for design of the rebalance loop. The transfer function α (main axis) and β (cross axis) were modelled upon the computer (Downton 1979). The results of this modelling (for CPT gyroscope operating at a wheel rotation frequency of 200Hz) are shown in Figure 3.5. These results are presented in the form of Bode gain and phase plots. The most prominent feature of the gain plot of α is the nutation spike. This occurs at about 400Hz, the plot also indicates the effect of varying the rotor damping D. Clearly D controls the magnitude of nutation.

After the wheel has been tilted the spring pivot coefficient K causes the wheel to oscillate about its zero position, while the auto erection coefficient (ρ) causes this motion to spiral to the null position. The effects of ρ and K can be seen in the gain plot, these limit the one dc gain of the gyroscope to a finite value of $\frac{\rho}{\rho^2 + K^2}$

The gain plot of the cross axis shows the effect of varying the spring pivot at stiffness K. This has the effect of a notch at about 5Hz, and varying K, varies the extent of the notch. At dc the value of β is given by:

$$\frac{K}{K^2 + \rho^2}$$

The Bode plots shown in Figure 3.6 are measurements made upon an actual gyroscope. These plots also include the transfer functions of the voltage to current amplifier, the pre-amplifier and the demodulator. These have a similar response

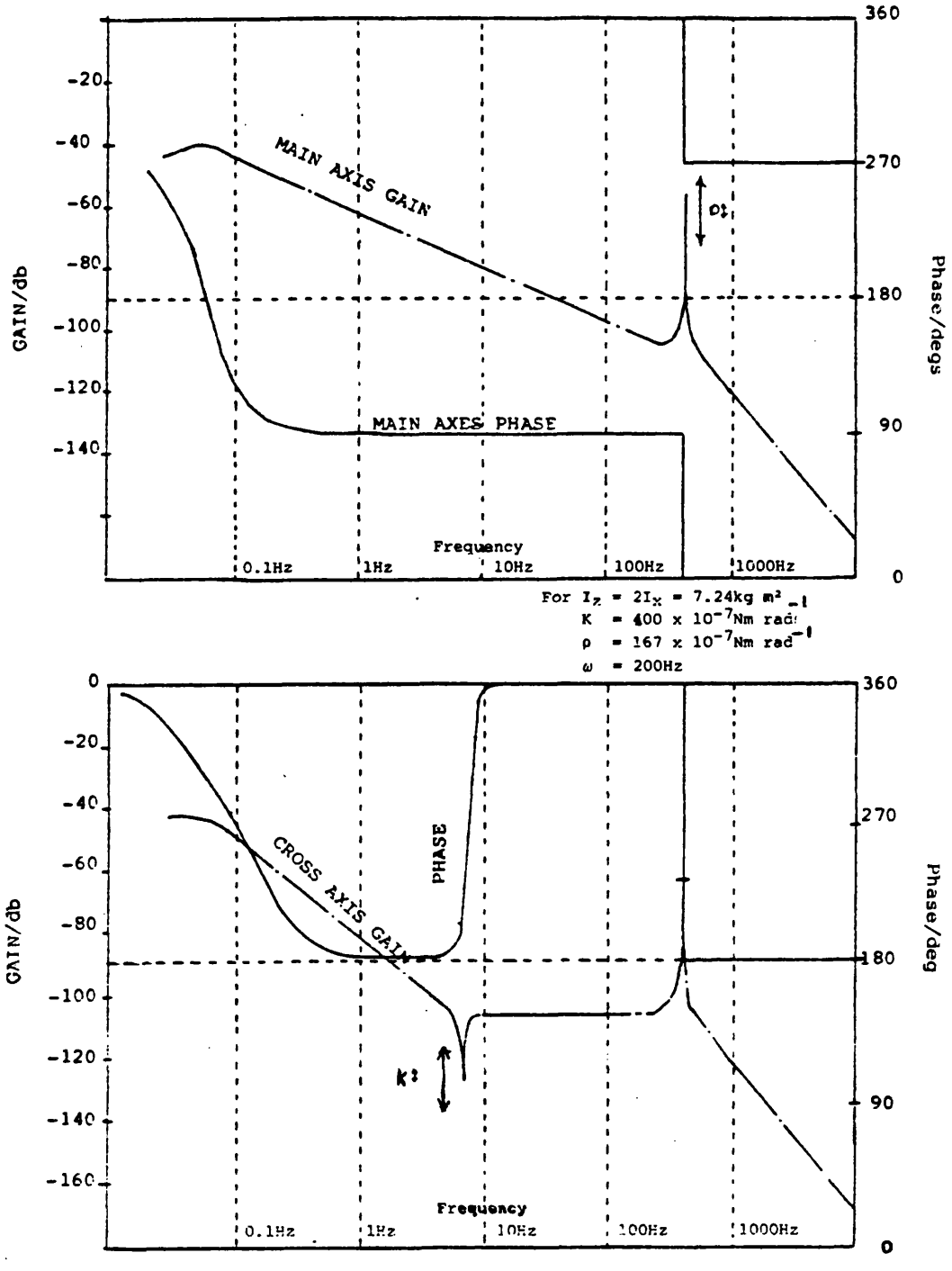

Fig. 3·5 - Theoretical Bode Plots of the CPT Gyroscope

Figure 3,5 Theoretical Bode Plots of the C.P.T Gyroscope

Figure 3,6 Simplified Model

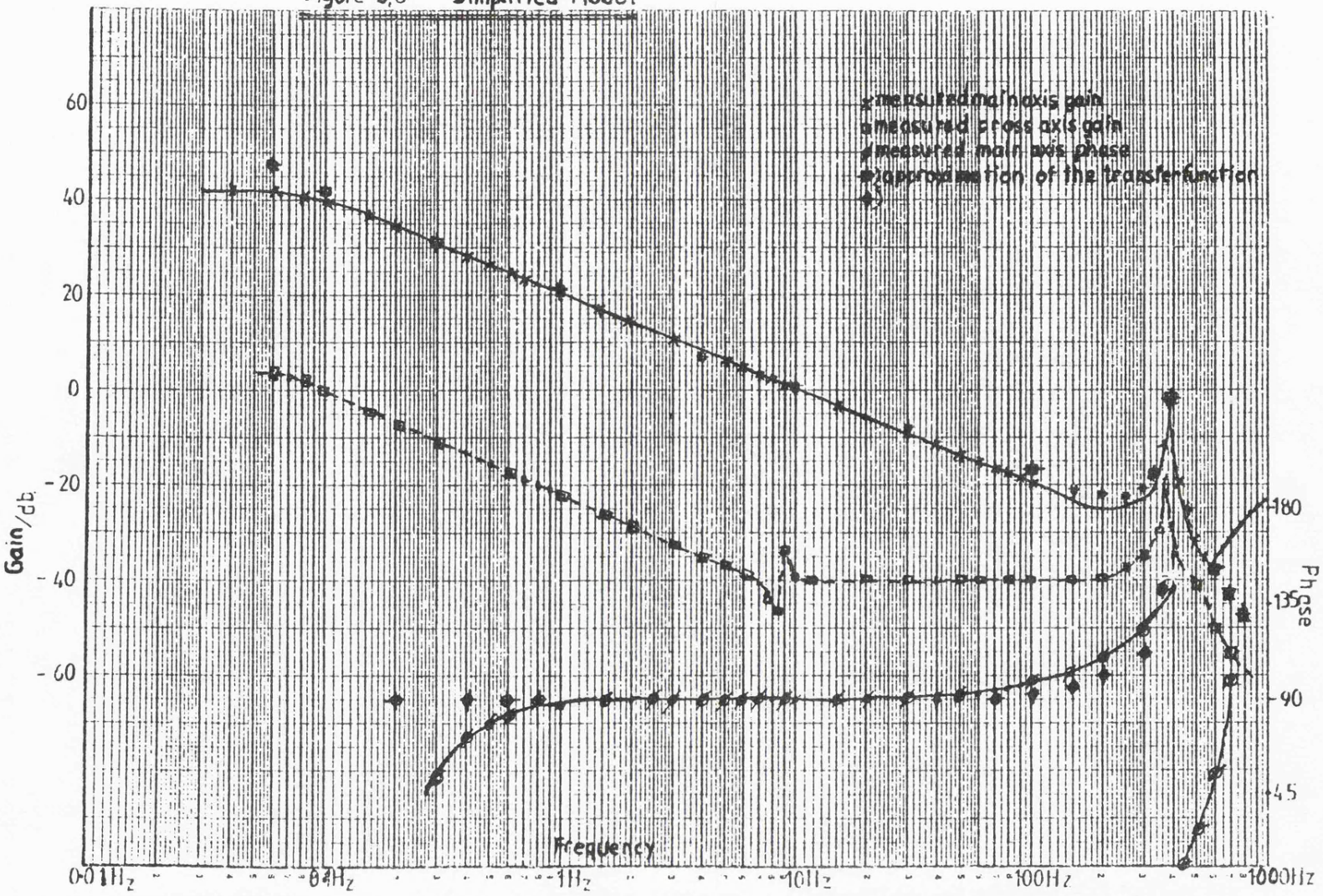

to the predicted plots of Figure 3.5. The main difference between the set of plots is the overall gain, but this is accounted for by the torquer scale factor, the pickoff scale factor and the gain of the electronics. From the plots of Figure 3.7 it can be seen that the main axis plot agrees well with the predicted plot up to frequencies of 600Hz, here the response deviates from the predicted response. This is due to a resistive path through the demodulator. The cross axis transfer function is almost as predicted, however a slight disturbance occurs at about 10Hz, this is thought to be due to an interaction between rotation frequency of the wheel and the nutation frequency.

From about 0.1Hz to 600Hz the main axis transfer function can be approximated by the transfer function:

$$\frac{K}{s} \quad \frac{1}{\frac{s^2}{\omega_n^2} + \frac{2\zeta s}{\omega_n} + 1} \qquad 3.15$$

The value of K can be determined from the scale factors of the gyroscope and associated electronics. Values have been substituted into the transfer function of Equation 3.15 and the results superimposed on the main axis plot of Figure 3.6. From this it can be seen that this transfer function gives a good approximation of the response of the gyroscope for the frequency range 0.1Hz to 600Hz. This provides a useful model for quickly testing and establishing a controller for the gyroscope.

REFERENCES USED IN CHAPTER III

D'Azzo J.J. (1960). Feedback Control System Analysis Synthesis, Second Edition, Tenden - McGraw-Hill.

Downton G.C. (1970) Sperry Gyroscope. Technical Note.

Di Steffano J.J., Stubberud A.R. and Williams I.J. (1976). Feedback and Control Systems, Schaums Outline Series, London, McGraw-Hill.

Karnich H. (1979). Experience based upon Experimental Dry Tuned Gyros. Symposium of Gyro Technology 1979 - DGON, University of Stuttgart.

CHAPTER IV

THE DESIGN OF THE ANALOGUE CONTROL ELECTRONICS

4.1.1 The Objectives

The concept of applying feedback to a two degree of freedom gyroscope to operate it as an angular rate sensor was introduced in Chapter I. The advantages of operating the gyroscope in the rate mode are twofold. Firstly, operating in the rate mode, the gyroscope directly measures the angular rates of the vehicle upon which it is mounted. Secondly, such a gyroscope can be used in a system that provides angular velocity information without the need for expensive, bulky gimbals.

The specification for the performance of a commercial rate gyroscope is determined by market demands. The dominant market for the microflex rate gyroscope is for use in strapdown navigation systems for airborne missiles. This market requires the measurement of rates in excess of 50 degrees per second and bandwidths greater than 50 Hertz. The particular gyroscope discussed in this thesis is the Microflex gyroscope. The basic Microflex gyroscope has been described in detail in Chapter II. The mathematical model used to represent the gyroscope has been detailed in Chapter III.

In general the design rules developed in this chapter apply to both the CPT and SPT gyroscopes. However the restriction of

the combined pickoff and torquer present a unique control problem which is colloquially referred to as the "figure of eight loop". This will be described in more detail later.

The objective of controlling the gyroscope is to operate it as a rate gyroscope which will meet the current market specification. The design of the rebalance loop is based upon the following criteria:

1. A minimum bandwidth of 50Hz (90 deg point) should be achieved.

2. The steady state angular hangoff of the gyroscope's wheel should be zero. (under constant angular velocity)

3. The feedback should not excite nutation.

4. The feedback should attenuate wheel rotation frequency components.

5. The performance of the rebalance loop shall be optimised with respect to acceleration transients.

6. The feedback loop will provide sufficient high frequency attenuation to avoid instability of the "figure of eight" loop. (In the case of the CPT gyroscope).

7. The control loop should be unconditionally stable.

The implications of design criteria 1, 3, 4 and 6 will be discussed in detail later. Criteria 2 and 7 determine that the rebalance loop will be a Type II servo system (Stefano, Stubard and William, 1967). A Type II servo system maintains the second derivative of the input constant, whilst the output is directly proportional to the first derivative of the input. Criterion 5 determines the minimum loop gain which is required to maintain an acceptable following error (D'Asso and Houpis, 1960).

Figure 4.1

Control Loop

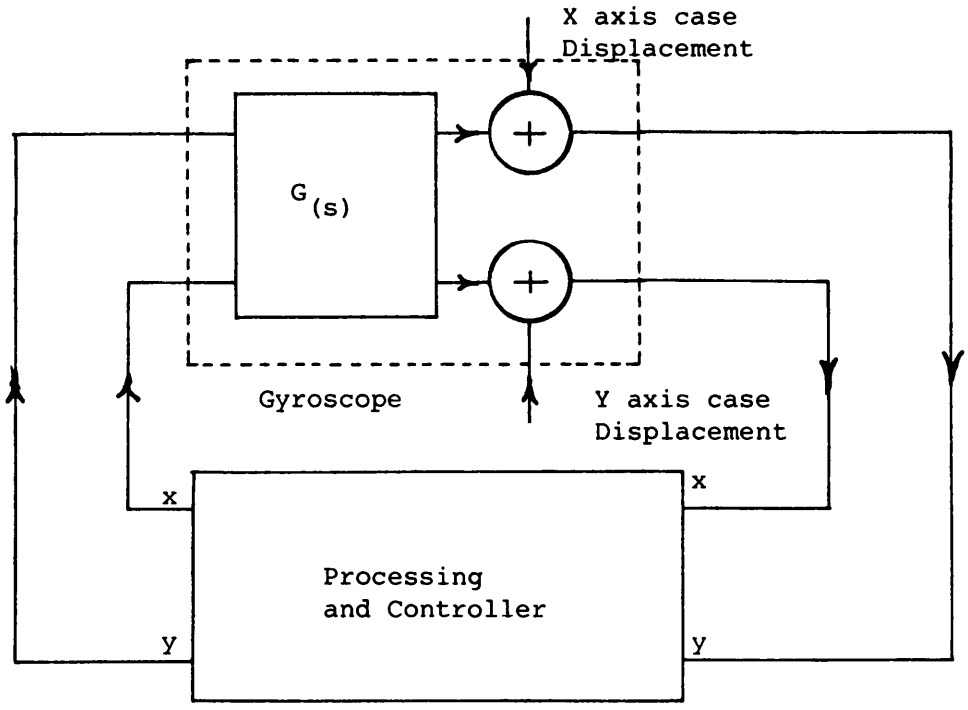

The control loop as shown in Figure 4.1 consists of the gyroscope and a controller. The gyroscope senses the angular displacement of its wheel. This displacement information is processed and converted to an electrical signal which is conditioned by an analogue controller to provide a feedback signal to precess the gyroscope. The sense of the precession is such that it nulls the relative displacement between the wheel and the case. The design of the controller determines the system performance.

4.1.2 Nutation Stability

All two degree of freedom gyroscopes exhibit nutation. This means that any design applying feedback to the gyroscope must take account of the lightly damped poles introduced by the phenomenon. The mechanism of nutation means that the output of each axis of the gyroscope is a combination of the dynamic inputs applied to both axes. The coupling mechanism is frequency dependant, with infinite separation of the two axes to steady continuous input, but equal contributions from each axis at the nutation frequency. Several design techniques can be applied to cancel the coupling effects; Lipman (1968) describes a complex root locus method to design a rebalance loop. However this type of design is difficult to implement and relies on notches or feedforward terms to cancel the effects of nutation. This type of design is highly dependant upon the stability of the elements on the control loop and is sensitive to noise and other disturbances.

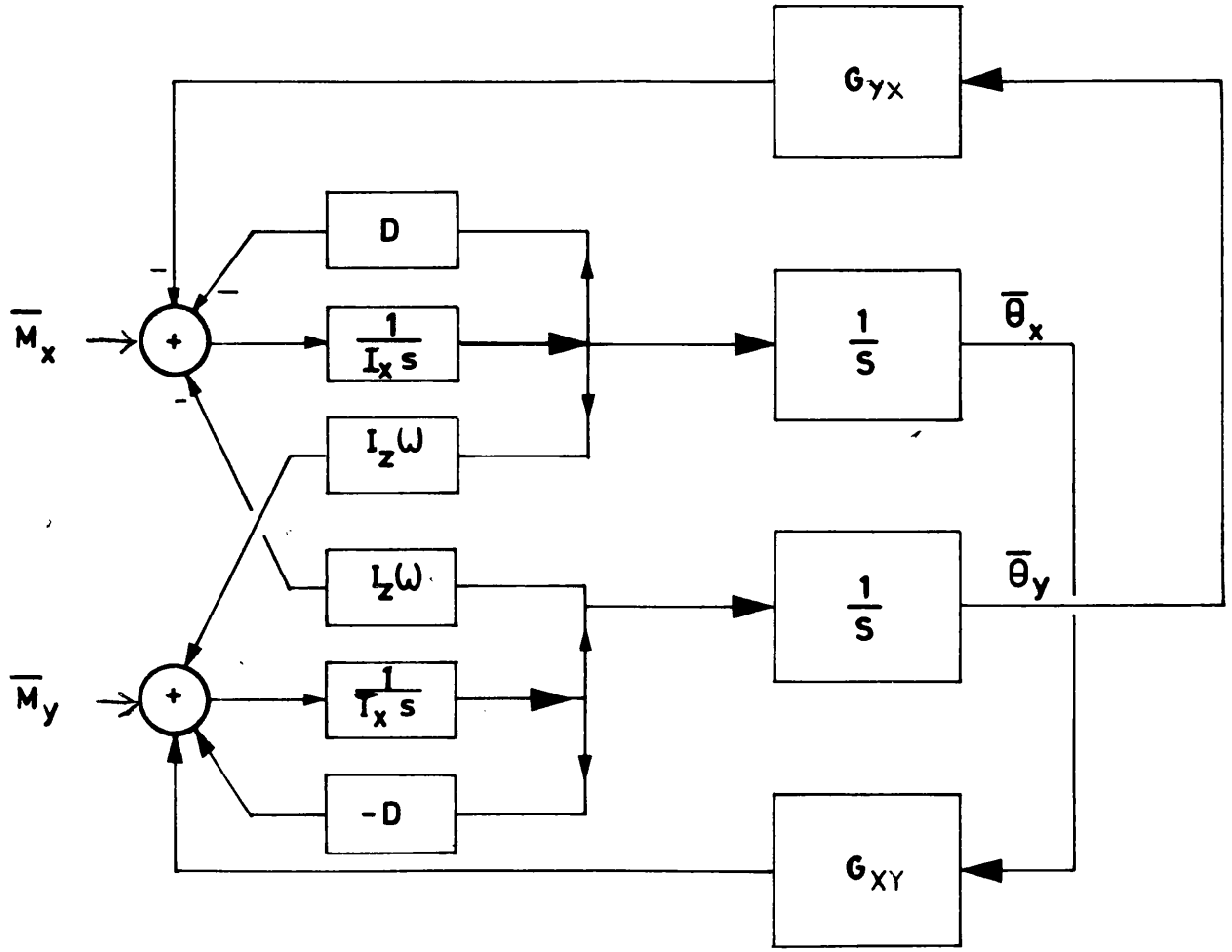

Fig 4·2 – THE BASIC GYROSCOPE MODEL WITH EXTERNAL FEEDBACK

Coffman (1974) describes a non-interacting loop. To achieve this he includes terms in series with the gyroscope to diagonalise the matrix of the gyroscopes transfer function. This method has the drawback that it needs an exact knowledge of the gyroscope parameters. If this is not achieved the cancelling effect turns the lightly damped poles into unstable zeros. Fortunately the nutation frequency of the Microflex gyroscope is sufficiently high for most applications to avoid the need for a non-interactive design. This leaves only the problem of ensuring the stability of nutation.

A method for examining the stability of a two degree of freedom gyroscope with external feedback has been described by Briggs, 1965. To apply this method to the particular case discussed here, Figure 3.1 is slightly modified and external feedback applied. This modified model is shown in Figure 4.2. A damping term D has been added to the model; this will be justified in the next section. The signs of the summing junctions have been chosen to apply negative feedback; the terms G_{xy} and G_{yx} are the external feedback terms. The model is simplified and shown in Figure 4.3 in the form of a block diagram.

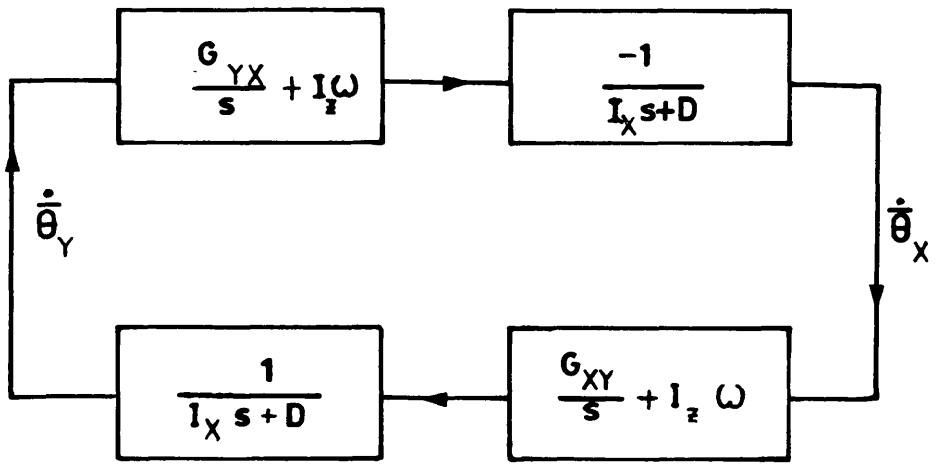

Fig 4.3 – SIMPLIFIED NUTATION LOOP

From these figures it can easily be shown if $G_{xy} = G_{yx} = G_f$ that the open loop transfer function is:

$$G = \frac{-(G_f + I_z \omega s)^2}{(I_x s^2 + Ds)^2} \qquad 4.1$$

Equation 4.1 can be re-arranged and expressed in the more convenient form:

$$G = G_1 (1 + G_2)^2 \qquad 4.2$$

Where $G_1 = \frac{1}{\alpha^2 \left(1 + \frac{s}{\alpha \omega_n}\right)^2}$, ω_n is the nutation frequency.

and $G_2 = \frac{G_f}{s} \frac{1}{I_z \omega}$ and $\alpha = \frac{D}{I_x \omega_n}$ and $\omega_n = \frac{I_z}{I_x} \omega$

It is interesting to note that G_1 is the open loop transfer function of the gyroscope without feedback, and when D = 0 $|G_1| = 1$ at an angular frequency ω_n. G_2 is the transfer function of the gyroscope with feedback, when cross coupling within the gyroscope is neglected.

The conditions for the stability of the gyroscope can be determined from Equation 4.2 provided that:

$$|G_1| \cdot |(1 + G_2)^2| < 1 \text{ for } \omega > \omega_n \qquad 4.3$$

The system will be stable if the phase margin θ_m is positive; as defined by the following inequality:

$$\theta_m = 180° + \theta_1 + \theta_2 > 0 \qquad 4.4$$

θ_1 is the phase angle of $G_1 = (-180 \text{ deg} + 2\tan^{-1}\alpha)$ and θ_2 is the phase angle of $(1 + G_2)^2\Big|_{s = j\omega_n}$

Thus 4.4 can be re-arranged to give:

$$\theta_2 > -2 \tan^{-1} \alpha \qquad 4.5$$

Equations 4.3 and 4.5 define the conditions for nutation to be stable when the gyroscope is operated with external feedback. Normally the damping D is low, therefore α is small. This implies that the stability conditions are met if θ_2 lies in the range -180 deg to -360 deg.

4.2.1 The Choice of Wheel Rotation Frequency

The bandwidth of the system is directly proportional to the wheel rotation frequency. The wheel rotation frequency dictates the carrier frequency of the pickoff signal. This in turn dictates the filtering which must be added to the loop to remove the unwanted demodulation products. In the case of the CPT gyroscope, the carrier frequency also determines the response of the "figure of eight" loop and consequently the filtering needed to attenuate it. The wheel rotation also determines the dominant noise components and hence the

filtering to attenuate them. As a rough rule of thumb, 25 percent of the wheel rotation frequency can be obtained as bandwidth with the "figure of eight" limited CPT gyroscope, while 50 percent of the wheel rotation frequency can be obtained as bandwidth with the SPT gyroscope.

The angular momentum of the wheel is proportional to rotation frequency, hence the torquer scale factor is inversely related to the wheel rotation frequency. Given that the current that can be supplied and dissipated within the gyroscope is limited, the maximum angular rate that can be balanced by the gyroscope is inversely proportional to the rotation frequency. Hence the choice of wheel speed is determined by assessing maximum bandwidth against maximum rate. However the wheel must have enough angular momentum to overcome the frictional and magnetic torques to ensure good gyroscopic properties. One other limiting factor in the choice of wheel rotation frequency is "gyro gain". Although changing the wheel speed does not change the product of pickoff scale factor and the torquer scale factor, it changes them each individually. As the wheel rotation frequency is increased, the pickoff scale factor increases and the torquer scale factor decreases. In a closed loop system this effects the noise and the points within the loop where saturation is likely to occur. In general the pickoff noise and its effect upon saturation within the loop increases quadratically with wheel rotation frequency. The pickoff noise and the mechanical stability of

the wheel materials limit the maximum wheel rotation frequency.

For the CPT application a bandwidth of 50Hz and a maximum rate of 300 degs per second is required; hence a wheel rotation frequency of 200Hz has been selected. The SPT application requires a bandwidth of 80Hz; hence a wheel speed of 160Hz has been selected.

4.2.2 Modelling of the Control Loops

All the control loops have been computer modelled using a British Aerospace modelling and simulation program called Organon. This program models the control loop in both the frequency and time domains. Listings of all the models used with a brief description of the structure of the model are given in Appendix 3.

4.3.1 The Design of the CPT Gyroscope Rebalance Loop

As the rebalance loop is to be used to measure angular velocity, it is desirable that a constant angular velocity input results in a zero steady state angular following error between the rotor and its null position. The 'rate' loop should be unconditionally stable, to ensure that the wheel will 'capture' upon switch on, or after the input range is momentarily exceeded. These two criteria determine that the rate loop will be a Type II servo system (Stefano et al, 1967).

From the Bode plots of Figure 3.7 it can be seen that there is a reasonable separation between the main axis and cross axis responses. These plots also show that nutation is well separated in frequency from the desired bandwidth point of 50Hz. These factors allow the design of the rebalance loop to be implemented without the need for control terms to decouple the axes. However, the criteria of Equations 4.3 and 4.5 must be met to ensure that nutation is stable and well controlled.

The design of the rebalance loop takes the simple approach of deriving the control terms to give the required response of the main axis, whilst using the criteria of Equations 4.3 and 4.5 to ensure that nutation is controlled. Nichols chart analysis is used as this gives the clearest method of displaying the open loop response, while indicating the closed loop behaviour.

Using the approximated transfer function of Equation 3.15 the modelled response of the gyroscope has been plotted upon the Nichols chart in Figure 4.4 (Plot I). To complete the control as a Type II servo system, a second integrator must be added to the loop. Clearly the addition of a second integrator will result in 180 deg phase shift when the gain exceeds 0db. This system is obviously unstable, thus more control terms are required to shape the low frequency response and ensure stability. The low frequency control terms must also ensure

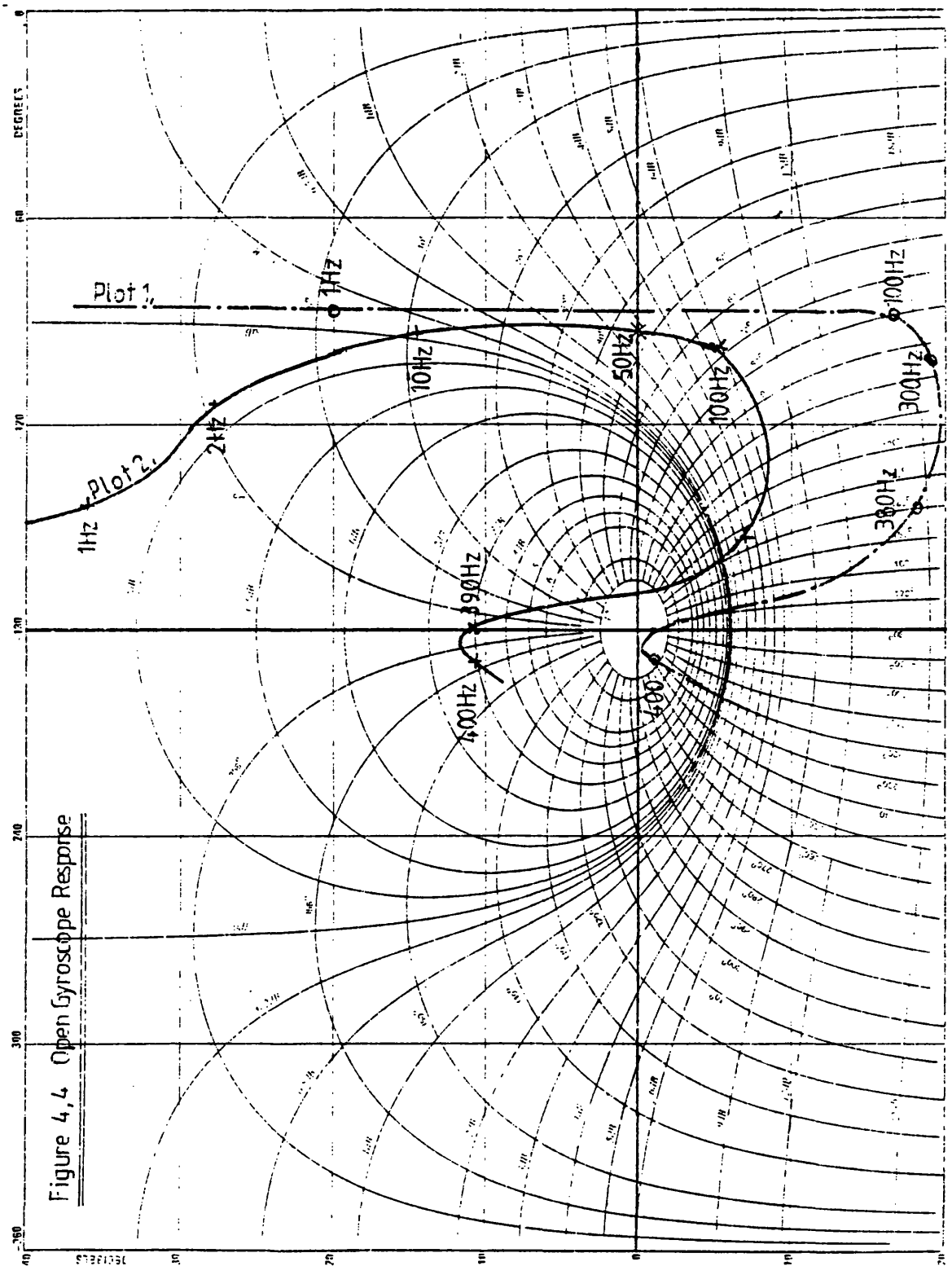

Figure 4,4 Open Gyroscope Response

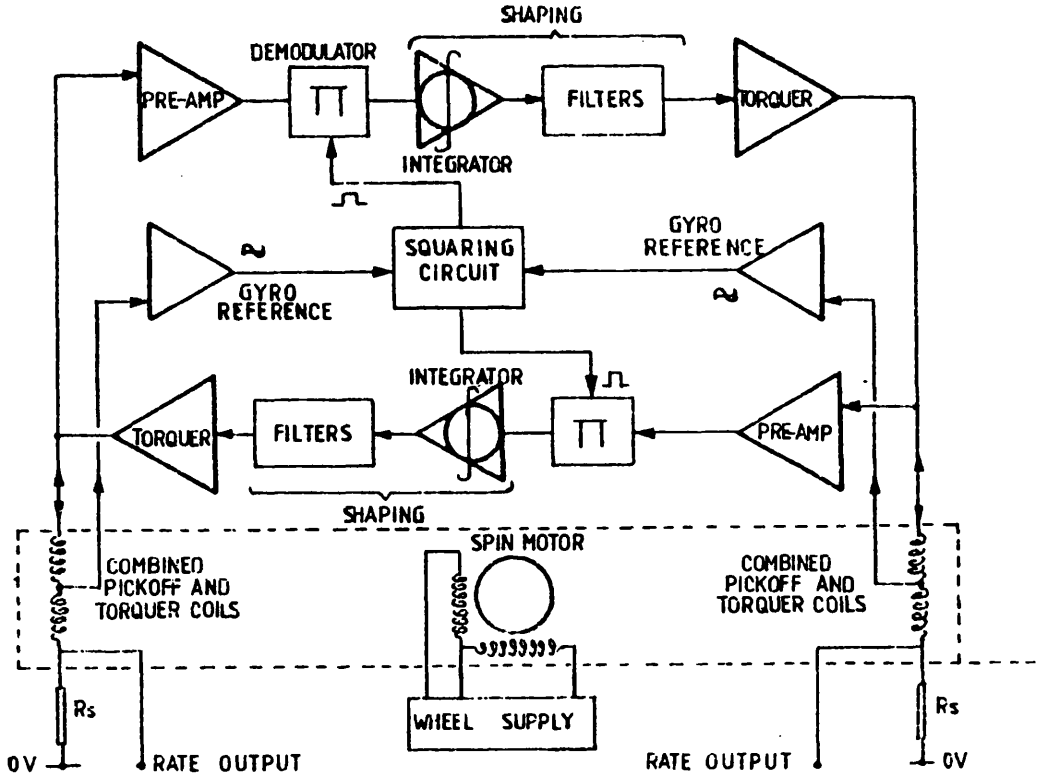

Figure 4,5,1 The C,P,T, Control Loop

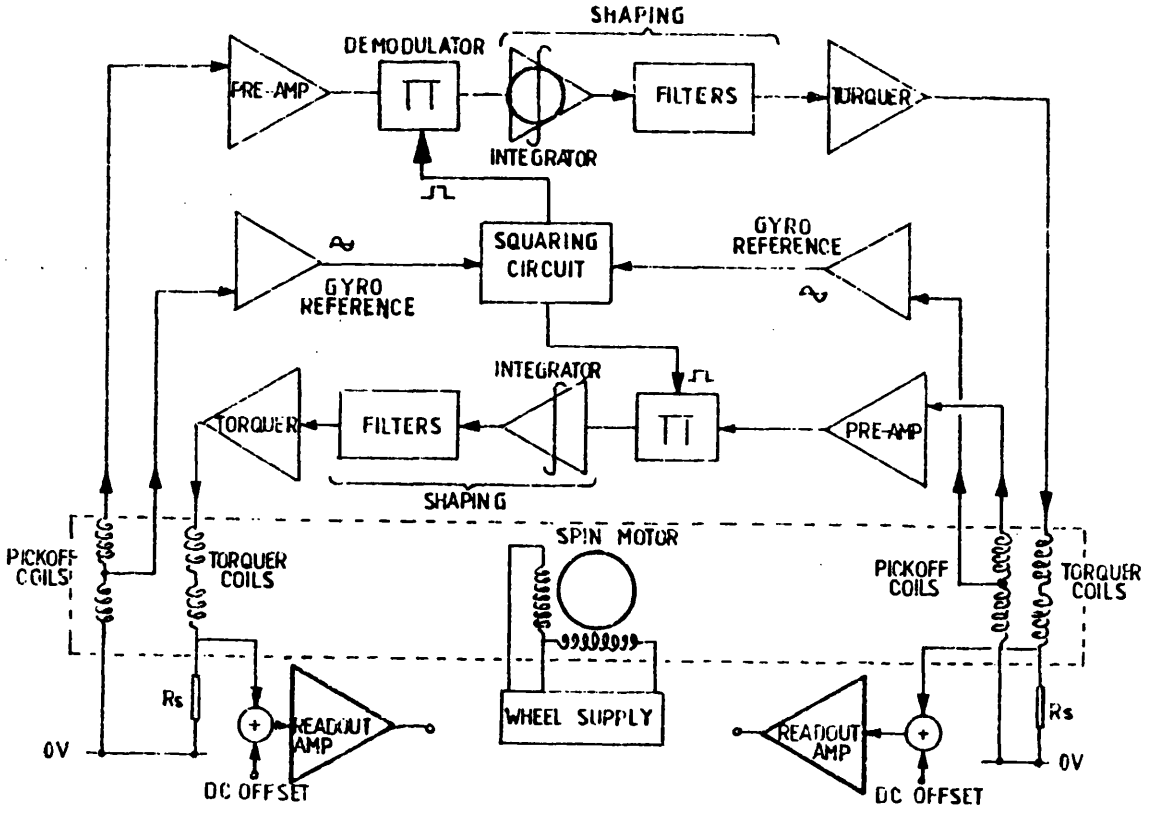

Figure 4,5,2 The S,P,T, Control Loop

stability. The low frequency control terms must also ensure that closed loop response is reasonably flat. The simplest control term that satisfies these requirements is:

$$\frac{K}{s}(sT_g + 1) \qquad 4.6$$

K is chosen initially to give 0db at 50Hz for T_g = 0.159. This term is cascaded with the transfer function of the gyroscope and plotted in Plot 2 of Figure 4.4. This is now stable at low frequencies, but nutation is likely to be unstable.

4.3.2 Figure of Eight Loop

From the previous section it would appear that to ensure complete stability it is only necessary to add control terms to stabilise nutation and adjust the loop gain to give the desired response. However, in practice, this was found not to be the case. As a result of using a combined pickoff and torquer gyroscope, the control electronics as can be seen from Figure 4.5.1 also form a closed loop. This is referred to as the "figure of eight loop". From Figure 4.5.2 it can be seen that the SPT gyroscope loop electronics are not directly coupled in this way.

The "figure of eight" loop is a frequency shifting loop, and contains two demodulators which act as multipliers. The demodulators are driven synchronously and frequency shift the response of the loop, modifying the normal transfer functions of the loop. The presence of this loop, and its stability

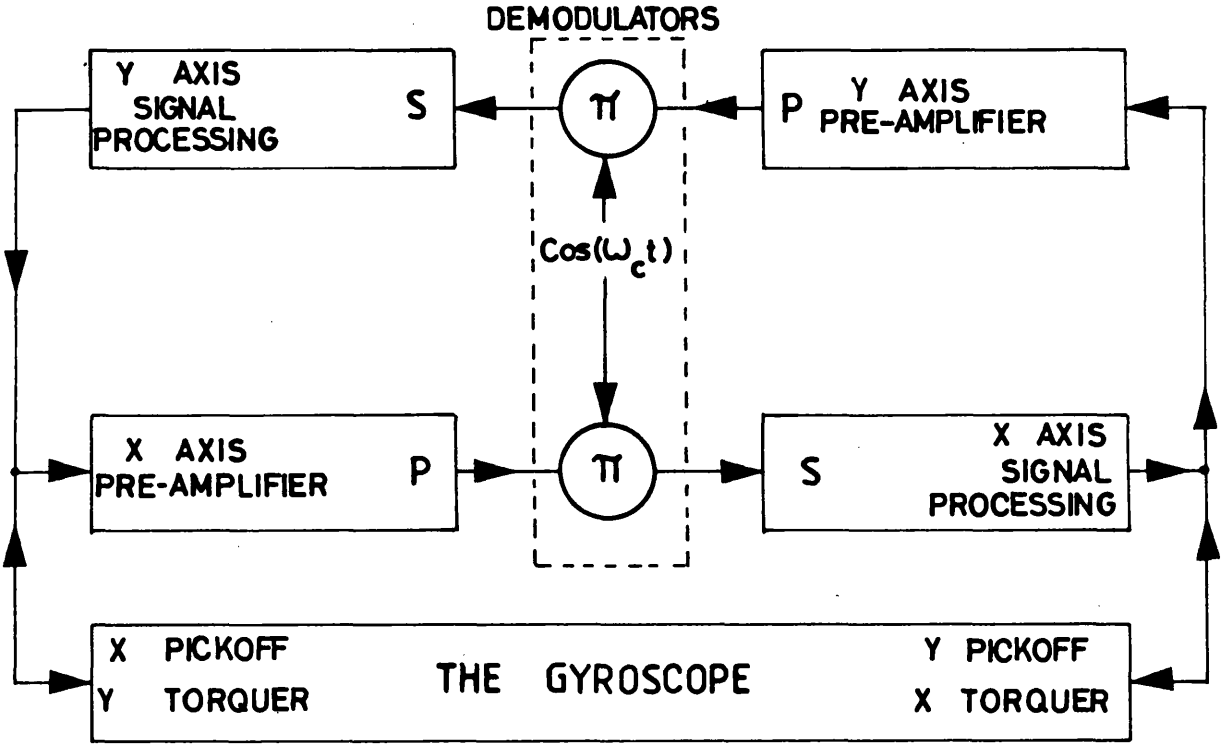

FIGURE 4·6 — THE "FIGURE OF EIGHT" LOOP

requirements, imposes further restrictions upon the design of the controller. As no direct summing of the "figure of eight" loop and the main gyroscope loop occur, the two loops can be treated as separate and can be superimposed. However, the controller must ensure that both loops are independently stable.

Examination of Figure 4.6 shows that the modulus of the open loop transfer function (G_8) of the "figure of eight" loop to be:

$$G_8 = |s\ P \cos(\omega_c t)|^2$$

Now put $s\ P = H$ and $G^1 = H \cos \omega_c t$

To analyse the stability of this loop it is easier to transfer the responses to the frequency domain by obtaining the laplace transform thus:

$$G^1(s) = \int H e^{-st} \cos \omega_c t\ dt$$

Expanding $\cos \omega_c t$ using De Moivres theorem gives:

$$G^1(s) = \int \frac{He}{2}^{-(s+j\omega_c)t} dt + \int \frac{He}{2}^{-(s-j\omega_c)t}\ dt$$

$$G^1(s) = \frac{H(s + j\omega_c)}{2} + \frac{H(s - j\omega_c)}{2}$$

$$\therefore |G_8(s)| = \left|\frac{H(s + j\omega_c)}{2} + \frac{H(s - j\omega_c)}{2}\right|^2 \qquad 4.7$$

This loop has a bandpass type response which is symmetrical about 800Hz. To reduce its gain, while not affecting the gyroscope loop, it is necessary to add attenuation at high frequencies. This loop is symmetrical about 800Hz. Any attenuation of this loop at frequencies above 800Hz will also be reflected as attenuation of frequencies less than 800Hz. To ensure complete stability of this loop the design must attenuate this loop such that its gain never exceeds -10db.

4.3.3 Actual Design

With so many criteria to satisfy, the design procedure was an iteration between theoretical modelling and practical tests. After several iterations the final controlling terms selected were:

(1) $\frac{26}{s}(0.159s + 1)$ — to shape the low frequency response

(2) $\frac{s^2 + \omega_1\zeta_1 s + \omega_1^2}{s^2 + \omega_1\zeta_2 s + \omega_1^2}$ — a 200Hz notch to attenuate the wheel rotation frequencies $\omega_1 = 2\pi \times 200$, $\zeta_1 = 0.01$, $\zeta_2 = 0.1$

(3) $\frac{1}{\frac{s^2}{\omega_1^2} + \frac{2\zeta_3 s}{\omega_1} + 1}$ — a 200Hz 2nd order lowpass filter $\omega_1 = 2\pi \times 200$, $\zeta_3 = 0.4$

(4) $\frac{1}{\frac{s^2}{\omega_2^2} + \frac{2\zeta_4 s}{\omega_2} + 1}$ — a 250Hz 2nd order lowpass filter $\omega_2 = 2\pi \times 250$, $\zeta_4 = 0.45$

(5) $\frac{1}{\frac{s^2}{\omega_3^2} + \frac{2\zeta_5 s}{\omega_3} + 1}$ — a 300Hz 2nd order lowpass filter $\omega_3 = 2\pi \times 300$, $\zeta_5 = 0.4$

(6) $\frac{5}{\frac{s^2}{\omega_4^2} + \frac{2\zeta_6}{\omega_4} + 1}$ — a 525Hz 2nd order lowpass filter $\omega_4 = 2\pi \times 525$, $\zeta_6 = 0.52$

(7) $\frac{1}{\frac{s}{\omega_5} + 1}$ — $\omega_5 = 570\text{Hz} \times 2\pi$

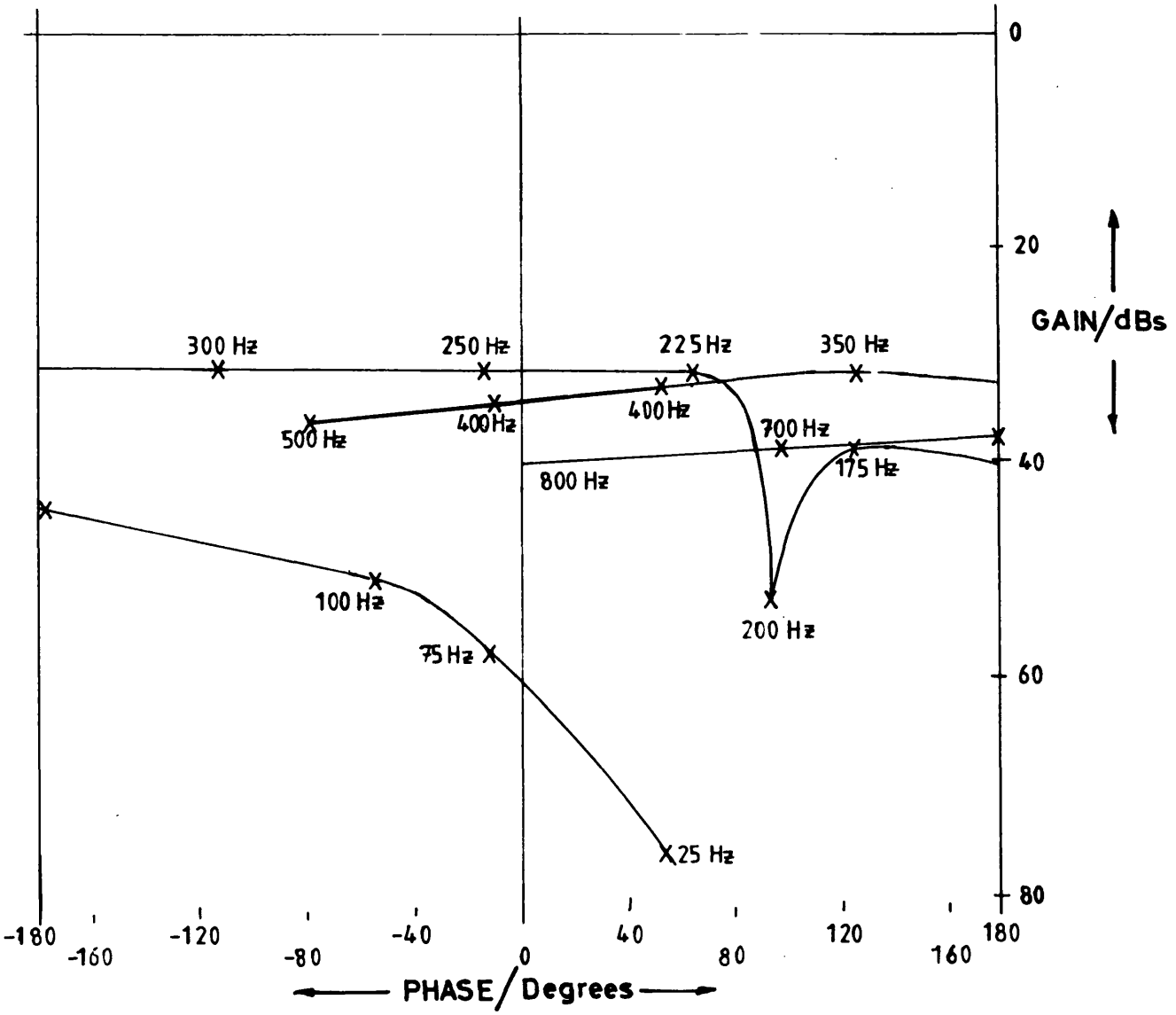

FIGURE 4·7 - OPEN LOOP PLOT OF THE "FIGURE OF EIGHT" LOOP

This controller satisfies all the criteria to ensure that the rebalance loop is stable. The criteria of Equations 4.3 and 4.5 are also satisfied and nutation is well controlled. The plot of the "figure of eight" is shown in Figure 4.7. From this it can be seen that this loop is also well attenuated and well separated from the gyroscope loop.

The Nichols plots of Figure 4.8 show the theoretical open loop response when the gyroscope is modelled using the transfer function of Equation 3.15 . The second plot of Figure 4.8 is the actual open loop of the complete rebalance loop. The two plots agree well up to 100Hz. The response exhibits three main characteristics:-

(i) the low frequency curve about the centre of the chart, which determines the low frequency response of the rebalance loop,

(ii) the "circle" of notch which is used to attenuate the rotation frequencies,

(iii) the resonance which is the nutation of the gyroscope.

The main departures of the practical plot from the theoretical occur between 280Hz and 380Hz. This is entirely due to the effect of the "figure of eight" loop.

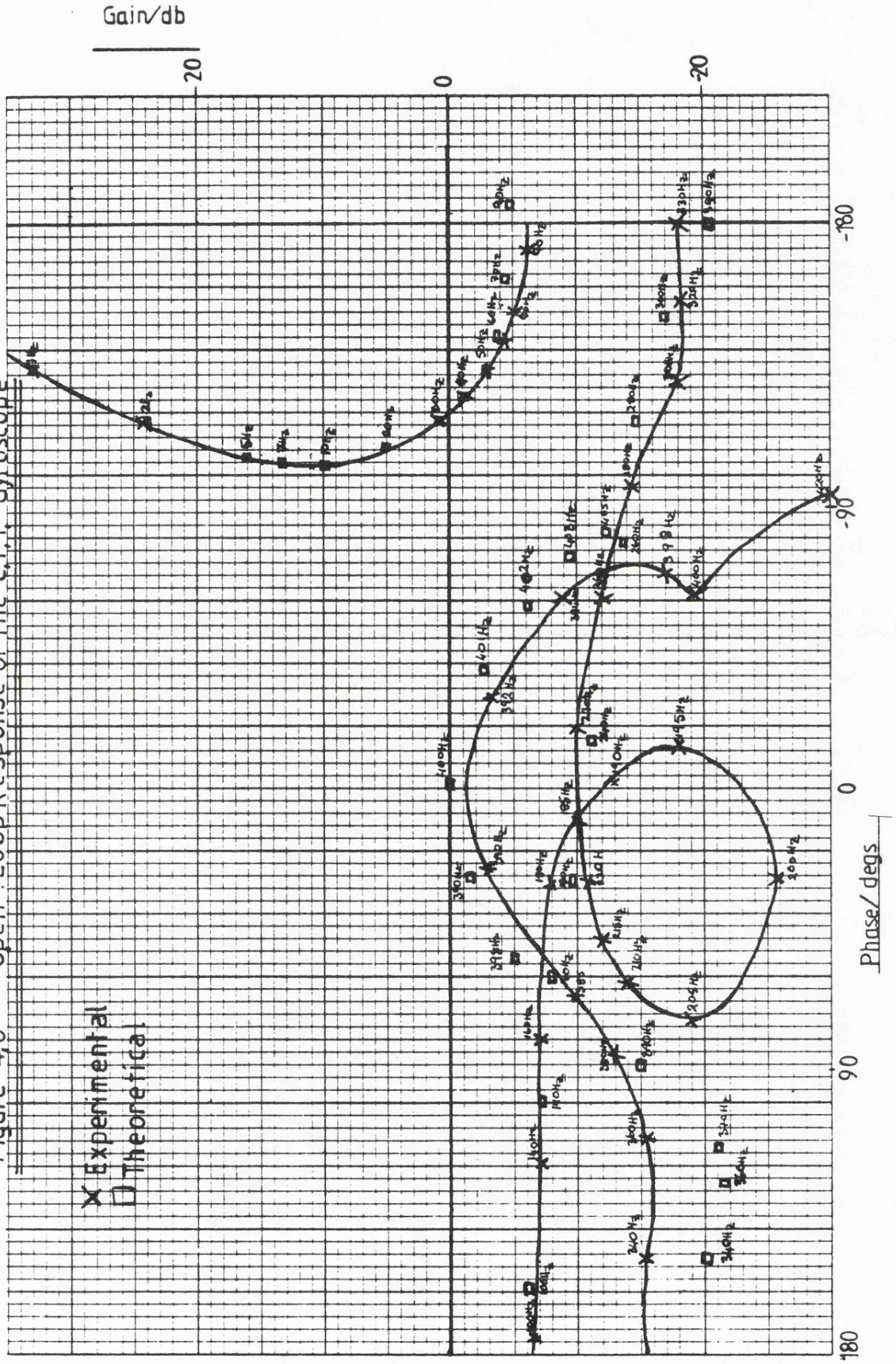

Figure 4.8 Open Loop Response of the C.P.T. Gyroscope

The closed loop response of the 'rate' loop is shown in Figure 4.9. This shows that the response of the loop is flat to within +/-0.5db and the -90 deg point bandwidth is 50Hz. The cross axis response is also plotted in 4.9; this is well separated from the main axis response; thus no further terms

are required to improve the dynamic separation of the response of the two axes.

4.4 The Design of the SPT Gyroscope Rebalance Loop

The design aims for the separate pickoff and torquer gyroscope are similar to those for the combined pickoff and torquer gyroscope. The gyroscope will be operated as a rate sensor employing a Type II servo loop. To avoid saturation of the loop, filters must be included to attenuate the unwanted demodulation signals as well as the rotation and twice rotation signals. The target for the 90 deg phase lag bandwidth has been set at 80Hz.

The basic model which was developed in Chapter 3 is used to describe the gyroscope. The parameters have been re-calculated for the new operating conditions. The change in design of the torquer coils has reduced the amount of eddy current damping provided, hence nutation is slightly more resonant.

Basically, the design of the separate pickoff and torquer gyroscope is similar to that of the combined pickoff and

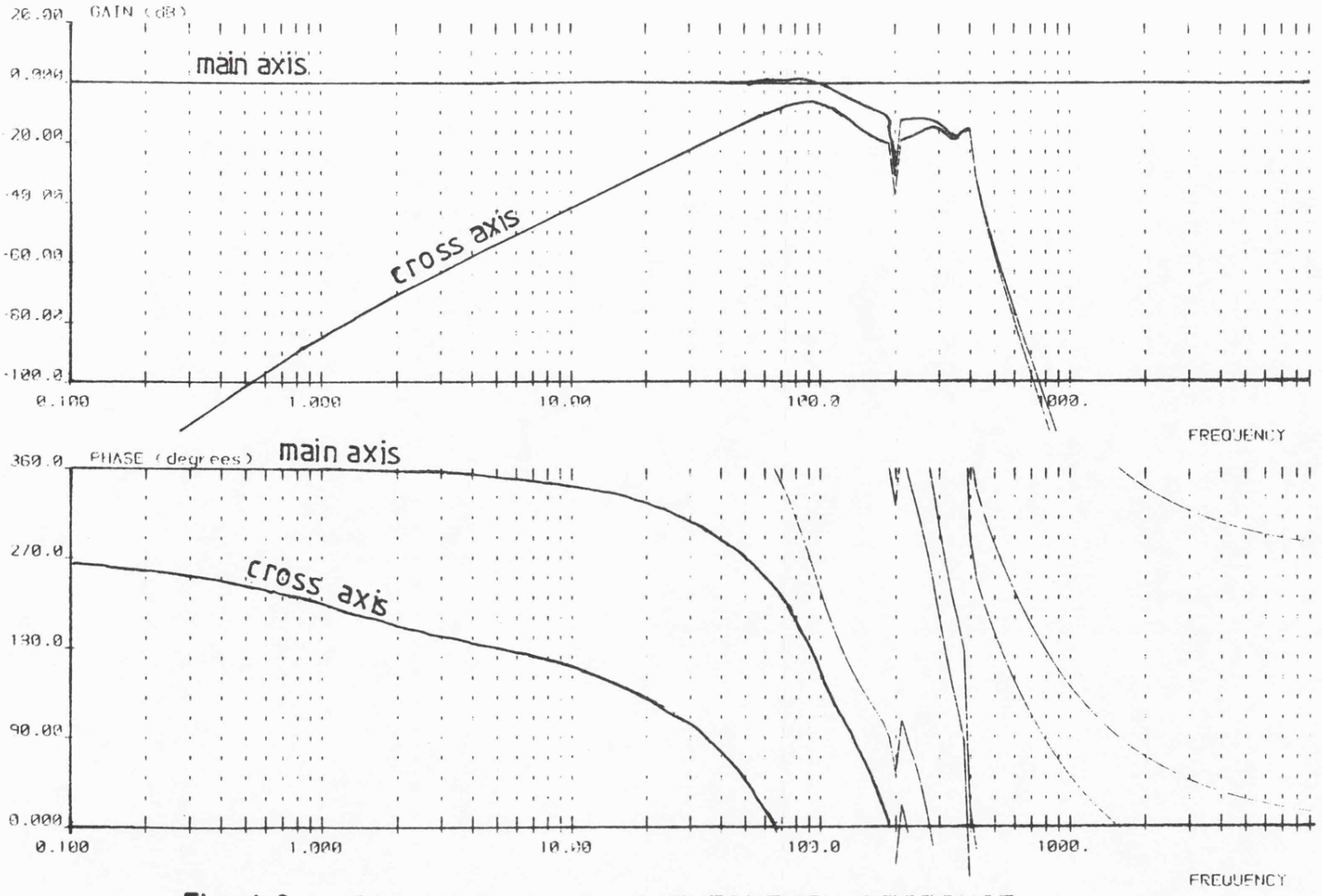

Fig. 4·9 – C.P.T. CLOSED LOOP FREQUENCY RESPONSE

torquer gyroscope. The design is based upon the design rules developed for the CPT gyroscope. To obtain the Type II servo loop the controller must include an integrator. To stabilise the loop a lead term is required. The break frequency of the lead is chosen to optimise the 'flatness' of the closed loop response. Typically this lead may lie between 0.5 and 10Hz. The 540Hz pole is retained in the torquer amplifier to stabilise this circuit. Two notch filters are included in the design to attenuate the rotation and twice rotation noise. These filters are designed to have effect mainly at their specific frequencies and are lightly damped to reduce their effects on phase shift at the closed loop bandwidth and nutation frequencies. A second order filter is used to attenuate the unwanted demodulation products. The demodulator operates by multiplying the pickoff signal by a square wave. This produces unwanted harmonics at twice the pickoff frequency and above. To provide reasonable attenuation of these signals, the natural frequency of this filter needs to be approximately 256Hz, ie. a frequency decade lower than the unwanted signal. However, by selecting the natural frequency of this filter carefully, the design rules developed in Section 4.1.2 for the control of nutation can be satisfied.

Using the simplified model of Equation 3.15 and several design iterations, the control loop shown in Figure 4.10 was optimised. The open loop plot of this is shown in Figure 4.11. This shows similar features to that of the combined

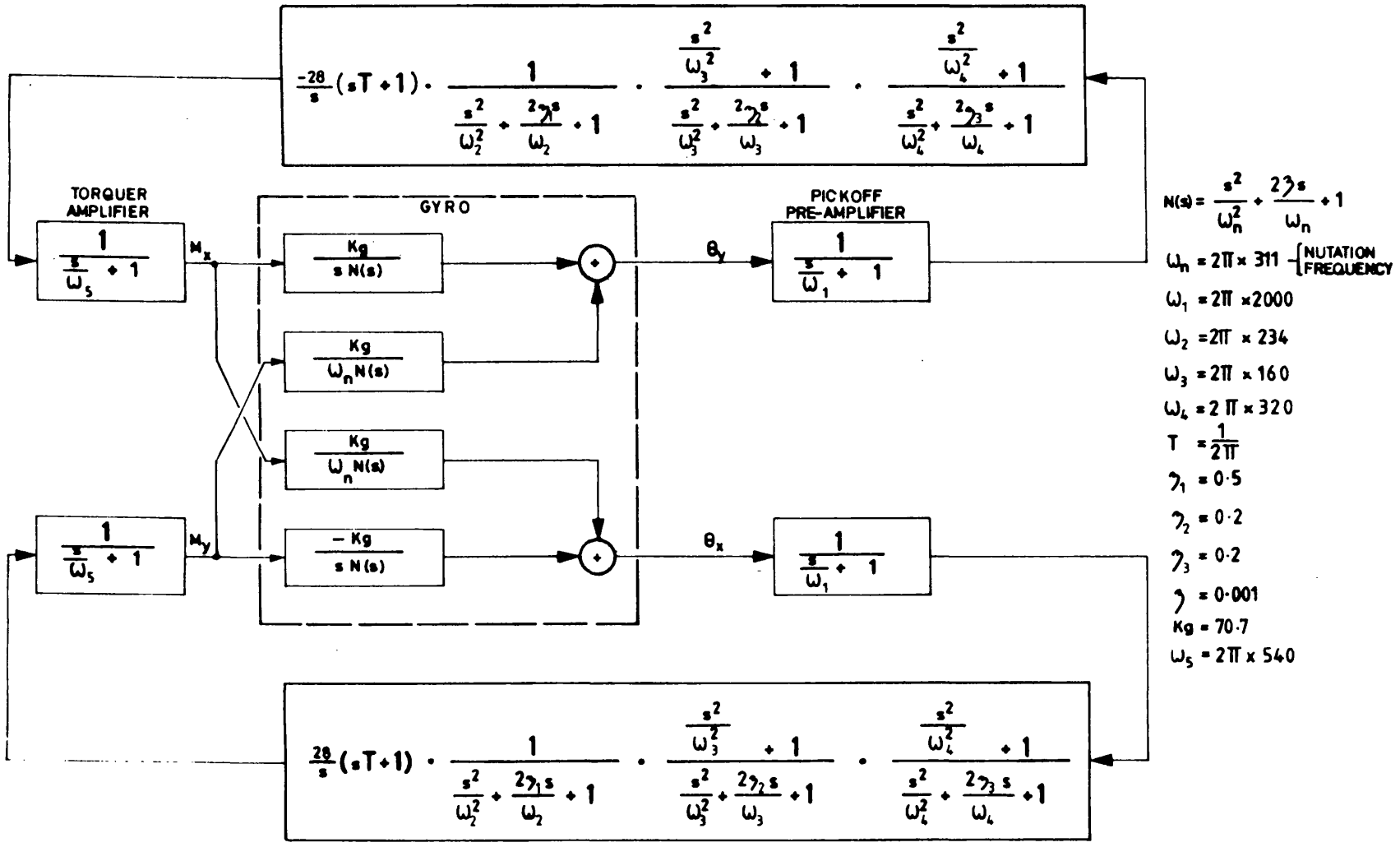

SEPARATE PICKOFF AND TORQUER GYROSCOPE CONTROL LOOP

Figure 4.10

Figure 4,11

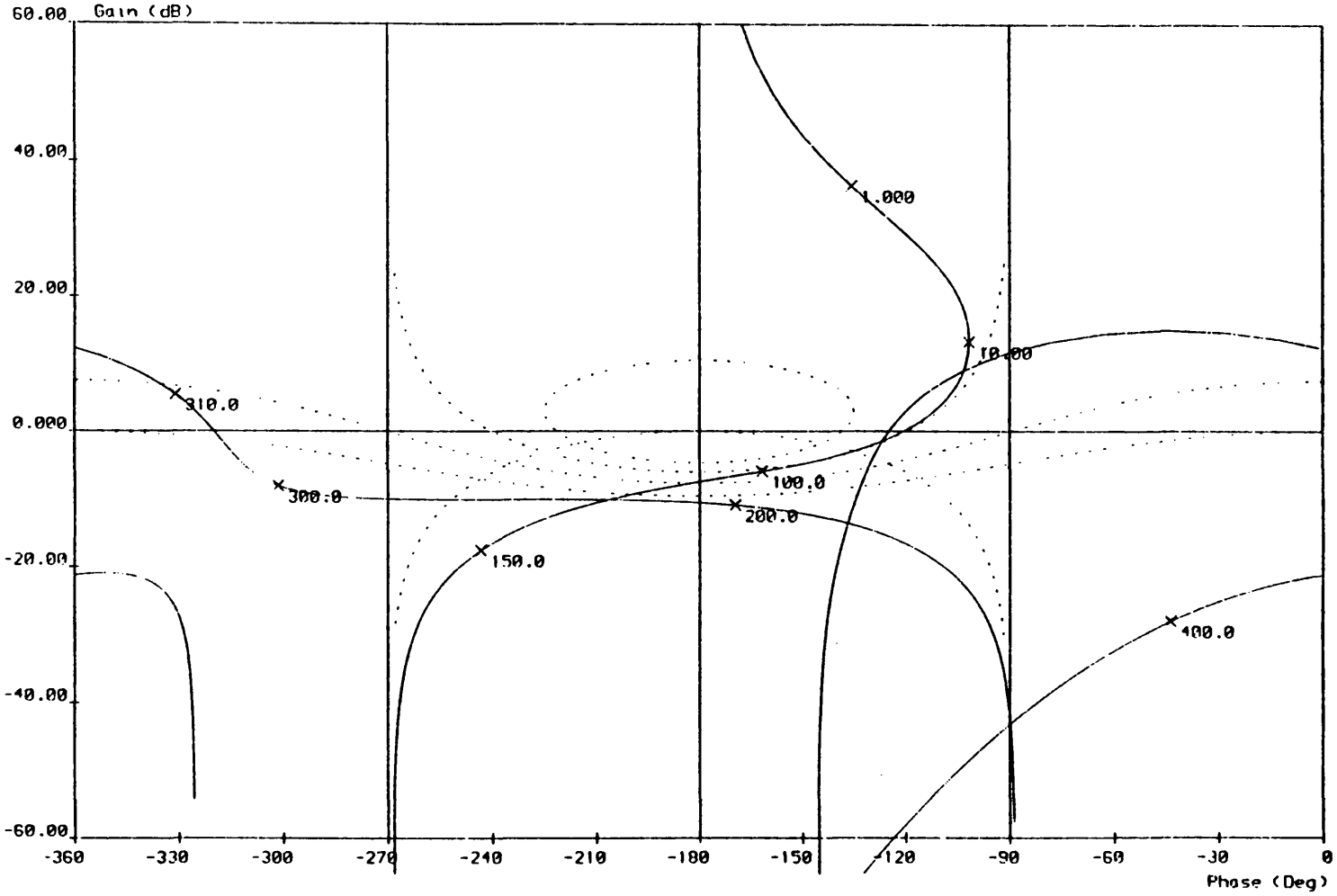

S.P.T. (OPEN) LOOP , ANALOGUE ELECTRONICS

pickoff and torquer loop with the exception of the 'figure of eight' loop effects. This plot has three distinct features at low frequencies. The effect of the gyroscope and the integral term can be seen. This shows approximately 180 degrees phase shift and high gain. At about 1Hz the effects of the lead term become significant. This increases the phase margin while the gyroscope and integral term attenuate the gain of the loop. At high frequencies the filtering and notches dominate the response, these introduce the two "circles" of the notches and ensure that nutation occurs, at 360 deg phase, thus ensuring its stability in the closed loop system. The modelled closed loop response of the system is shown in Fig 4.12. This design was performed as part of a research and development contract for the Royal Aircraft Establishment at Farnborough. Further details of this work are recorded in the final report TR1087.

4.5 Following Error

The steady state error of a Type II servo system is well defined in standard text books (D'azzo and Houpis, 1960) and is given by the formula:

$$\text{Steady state error } \theta_e = \frac{\ddot{\theta}}{K} \qquad 4.8$$

Where K is the open loop gain of the system.

The Microflex gyroscope has a limited amount of freedom hence the maximum steady state acceleration which the gyro can

Figure 4,12

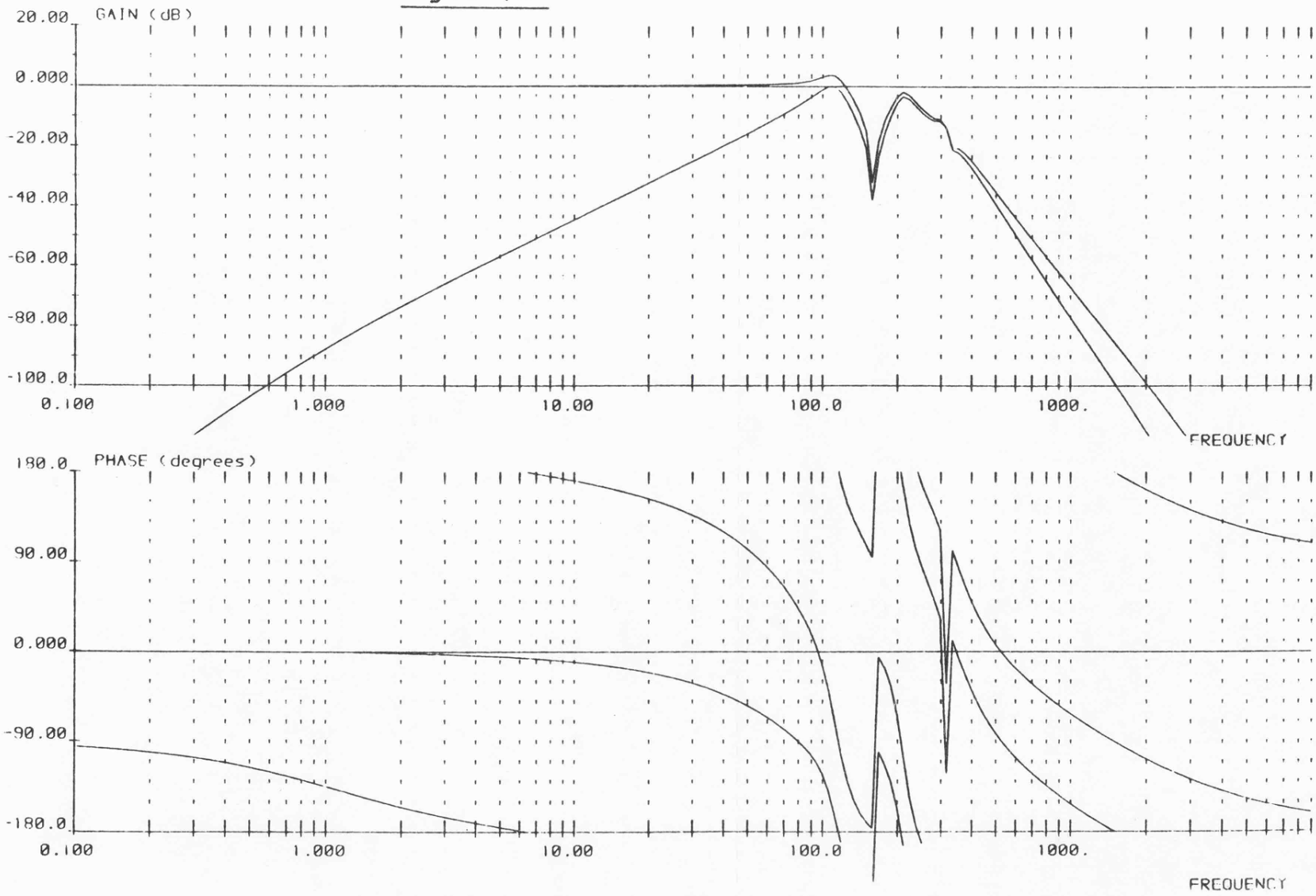

S.P.T. CLOSED LOOP , ANALOGUE ELECTRONICS

accommodate, and provide a representative output, is limited. Under steady angular acceleration conditions the rebalance loop will have a constant error as defined by Equation 4.8. Under dynamic conditions the following error is dependent upon the response of the loop. For the special case of sinusoidal input, a simple means of assessing the following error is demonstrated in Figure 4.13. From Figure 4.13 the following error for sinusoidal input can be determined to be:

$$\theta_e = \frac{\dot{\theta}_i}{s} \sqrt{1 + |G(s)|^2 - 2|G(s)| \cos (\angle G(s))} \qquad 4.9$$

FIGURE 4.13

SINUSOIDAL FOLLOWING ERROR

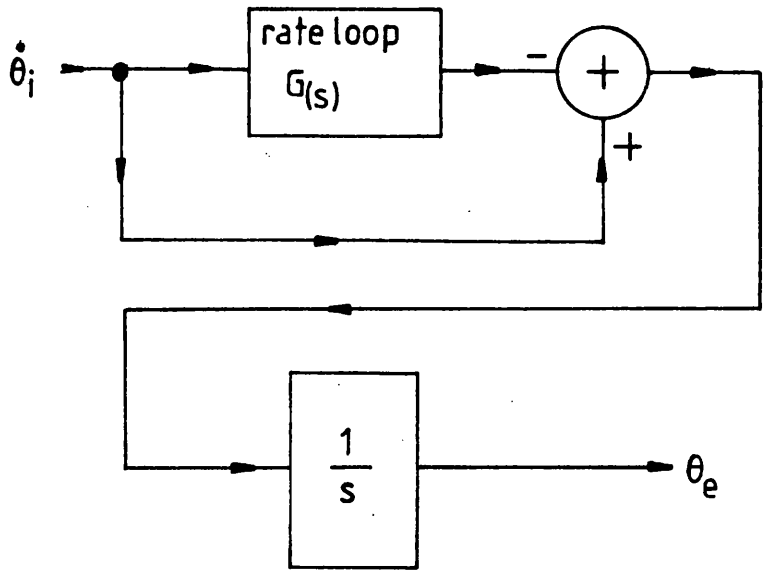

The parameters of the CPT Microflex rate system have been substituted into Equation 4.9 and the maximum angular rate, versus frequency (assuming 0.5 deg stops) has been calculated. The calculated results and actual measurements, are shown in Figure 4.14. From this graph it can be seen that the maximum sinusoidal rate under these conditions, which may be followed over a bandwidth of 50Hz, is 54 deg/sec r.m.s. At low frequencies the maximum rate agrees well with that predicted by the steady state equation (4.8). However, as the frequency increases the actual motion applied to the gyroscope reduces to less than the limits of the gyroscope stops, allowing greater acceleration to be accommodated but with greater error in the measured angular rate. The small differences between the measured and predicted response may be attributed to the actual freedom of the wheel and the errors incurred in the calculations.

The behaviour of the rate loop with other transients has been examined using computer models (see Appendix III). These transients and the response of the modelled loop to them are shown in Figure 4.15. These show that for short duration single transient that the following error is time dependent due to the response time of the control loop. They also show for short duration transients that the wheel may not hit its stops and saturate the control loop, and will provide a measured output albeit that the accuracy of the output is significantly degraded.

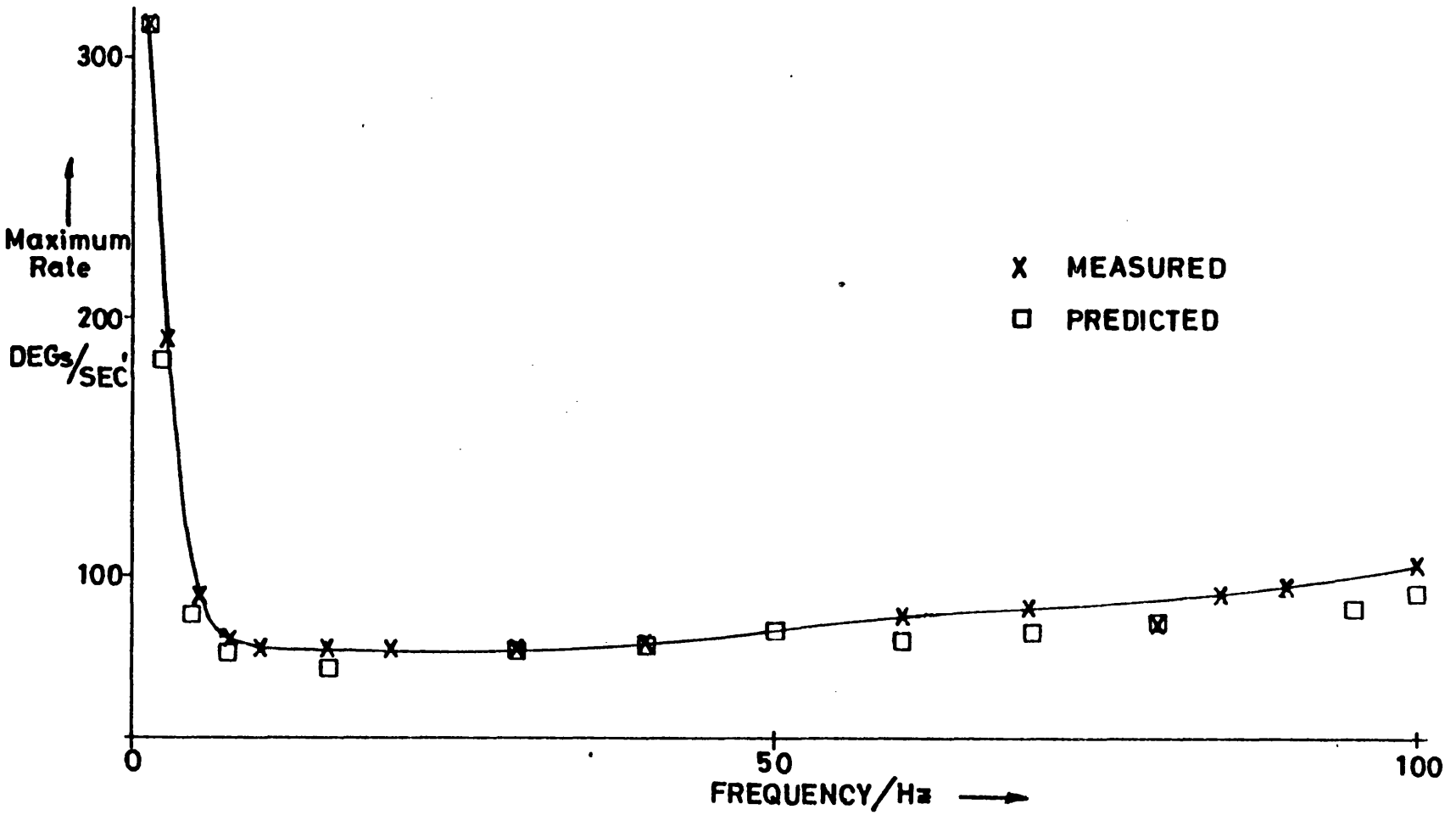

Fig. 4·14 — FOLLOWING ERROR

Figure 4,15

Modeled Transient Response

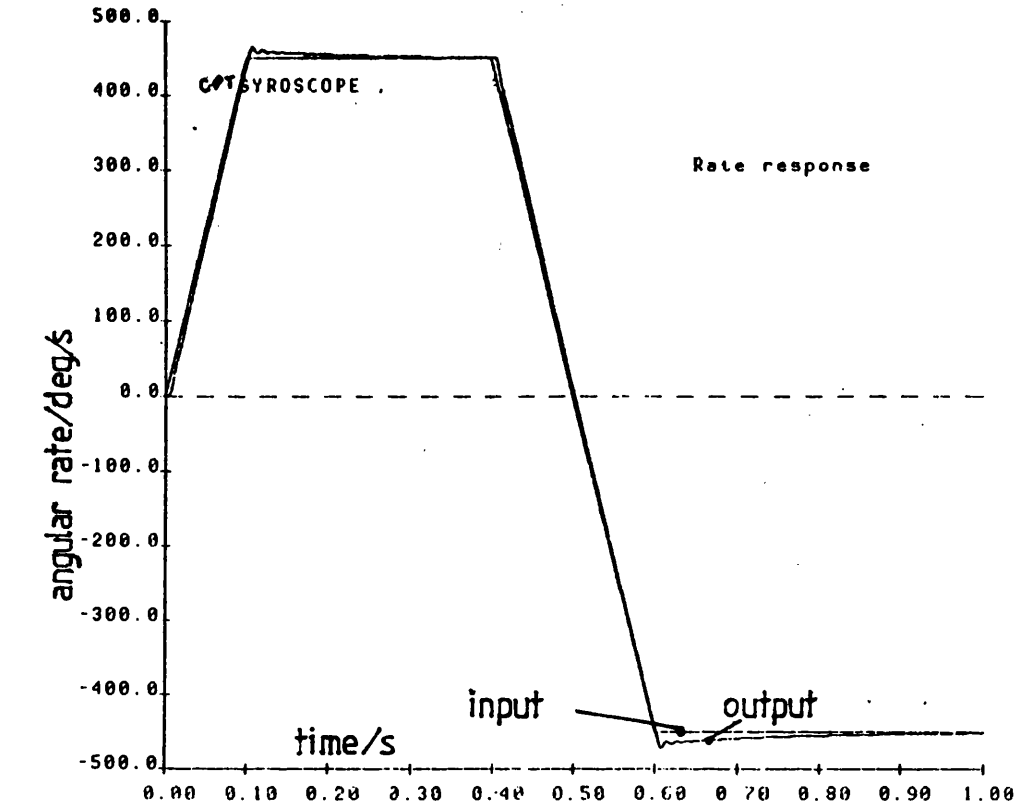

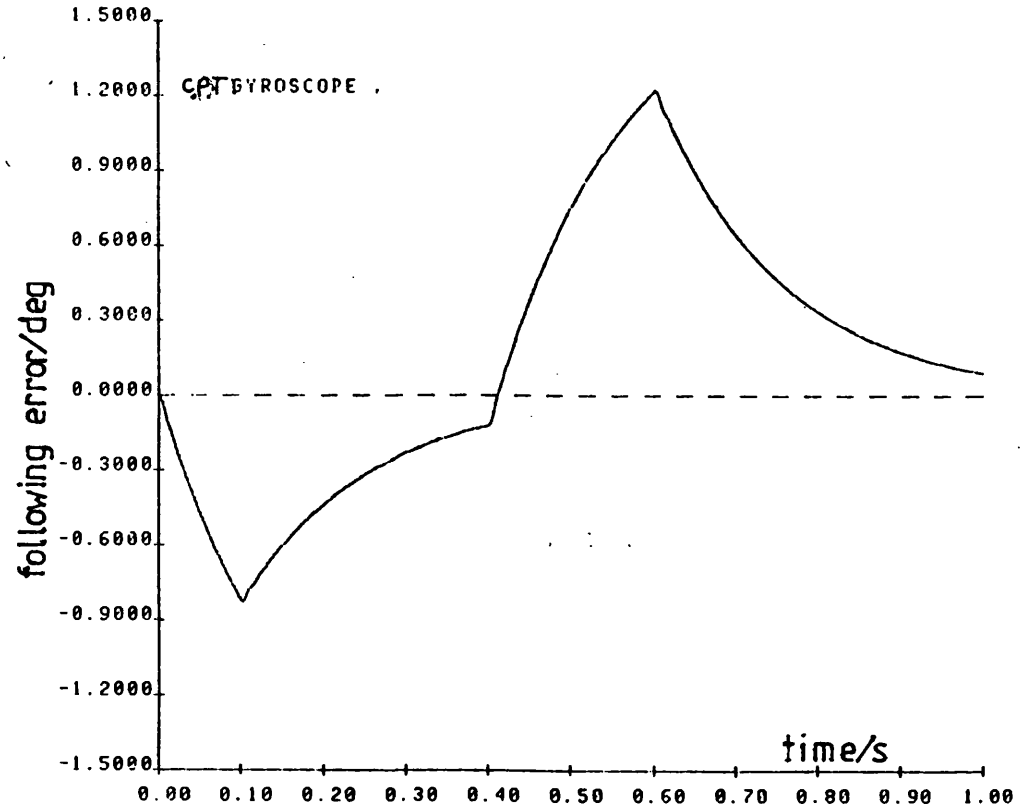

4.6 System Errors

The 'quality' of a rate gyroscope is normally determined by its drift performance. Although the Microflex rate gyroscope is a Type II servo system and ideally the steady state error is driven to zero, in practice both the electronics and gyroscope are not ideal. In general there are three sources of errors. Gyroscope errors, electronic errors and errors that result from the interaction of the electronics with the gyroscope.

The most significant gyroscope error is the stability or drift of the gyroscope. This drift is fundamental and represents the limit of performance if there were no other sources of error.

There are many sources of gyroscope drift, any effect which applies torque to the wheel results in drift. The most significant error associated with the electronics is the stability of the circuit element which is used to read out the rate information. Any offset or offset drift at this point will be seen as a drift in the output. As the datum signals are very small, a large proportion of these errors are due to thermal emfs.

The main drift errors due to the combined gyroscope and rebalance loop are associated with the gyroscope auto erection coefficient and residual spring coefficient of the flex pivot. Any offset between the electrical null and mechanical null of the gyroscope will cause the rebalance loop to slave the

gyroscope wheel to a position different from its mechanical null position. In this case the auto erection and spring mechanism apply torques which cause the gyroscope to precess and result in drift. The difference between mechanical and electrical null can be corrected for by adding an electronic null adjust (ENA) signal to the pick off signal. However, any offsets in the electronics before the control integrator, or any drift in the control integrator, will cause the output of the rebalance loop to drift. The other major interaction problem which is encountered is the coupling of twice wheel rotation frequency noise from the wheel supply electronics. This noise is rectified by the gyroscope's torquer and appears as gyroscope drift. The phase of the noise with respect to the rectification mechanism changes at each switch off / switch on of the rate system hence the gyroscope bias changes from switch on to switch on. Figure 4.16 shows the error model which is used to assess the drift performance of the loop.

Figure 4,16

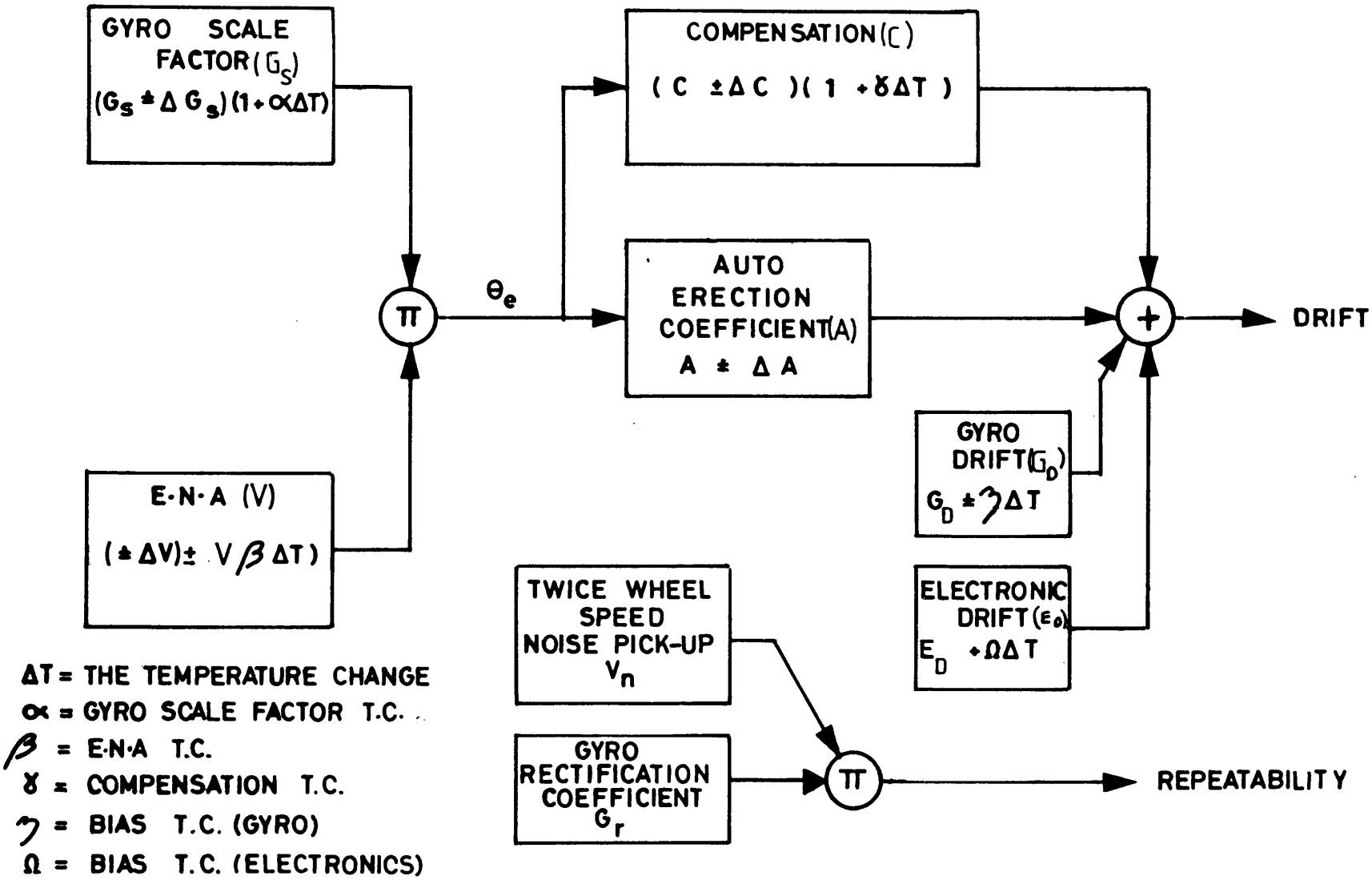

RATE LOOP ERROR MODEL

4.7 Implementation of the Analogue Rebalance Electronics

In general the electronics have to perform five main functions. These are:

i) To detect, amplify and demodulate the pick off signal to give an electrical representation of the gyroscopes wheel position.

ii) To implement the control terms and the filtering necessary to attentuate the noise within the rebalance loop.

iii) To convert the conditioned voltage signals to current signals to be applied to the gyroscopes torquer to precess the wheel.

iv) To provide the compensation to adjust for the mismatch between the mechanical and electrical null position of the wheel, the fixed rate bias error and the scale variations of the gyroscopes parameters.

v) To provide the two phase wheel motor drive signals.

These functions are common to both the CPT and SPT gyroscopes rebalance loop, although the implementation and complexity of the functions varies between the two schemes. In the sections which follow, the requirements and the implementation will be discussed in greater detail. The block diagrams of CPT and

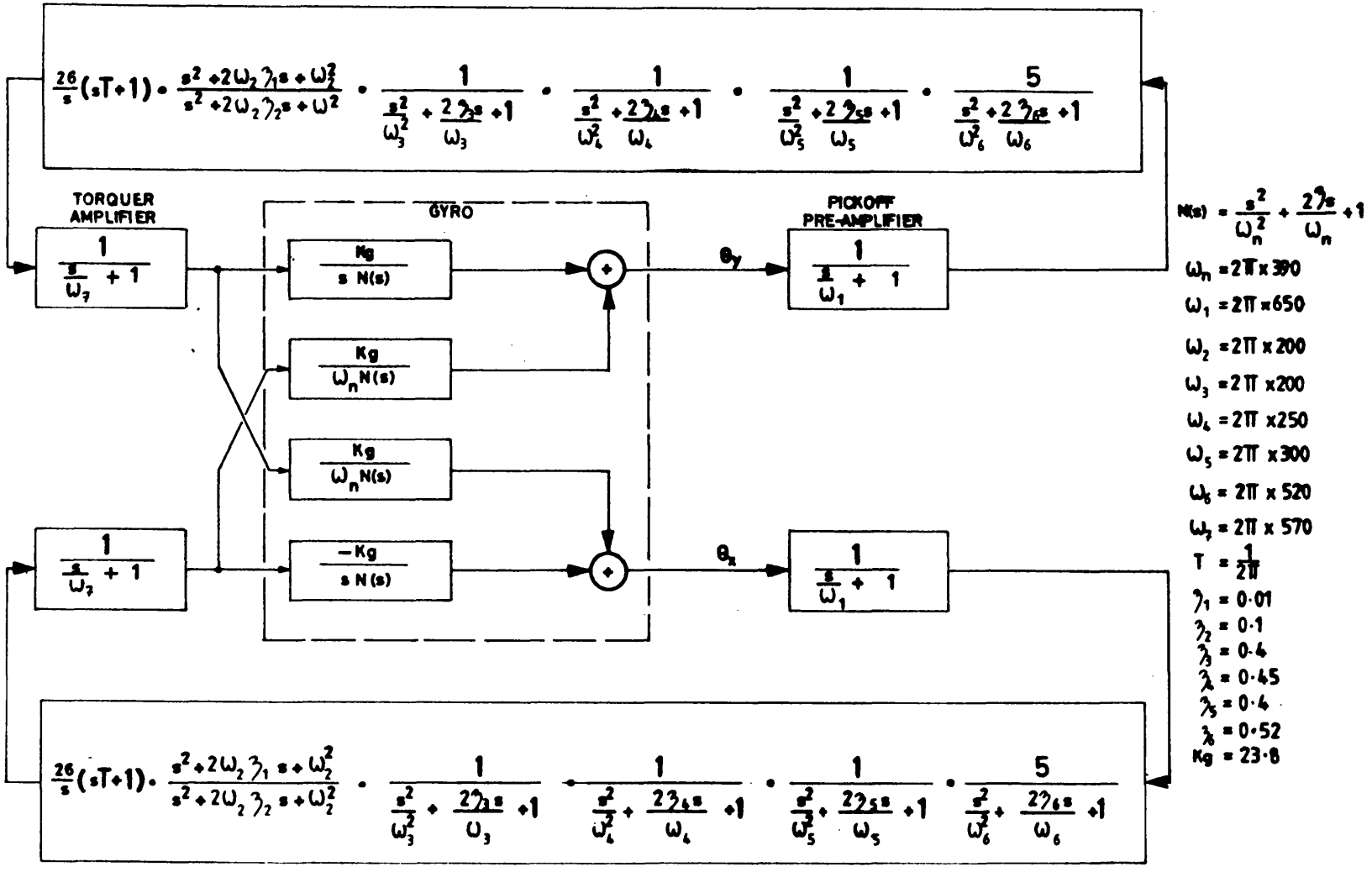

COMBINED PICKOFF AND TORQUER GYROSCOPE CONTROL LOOP

Figure 4.17

Figure 4,18

The C,P,T,Gyroscope Electronics

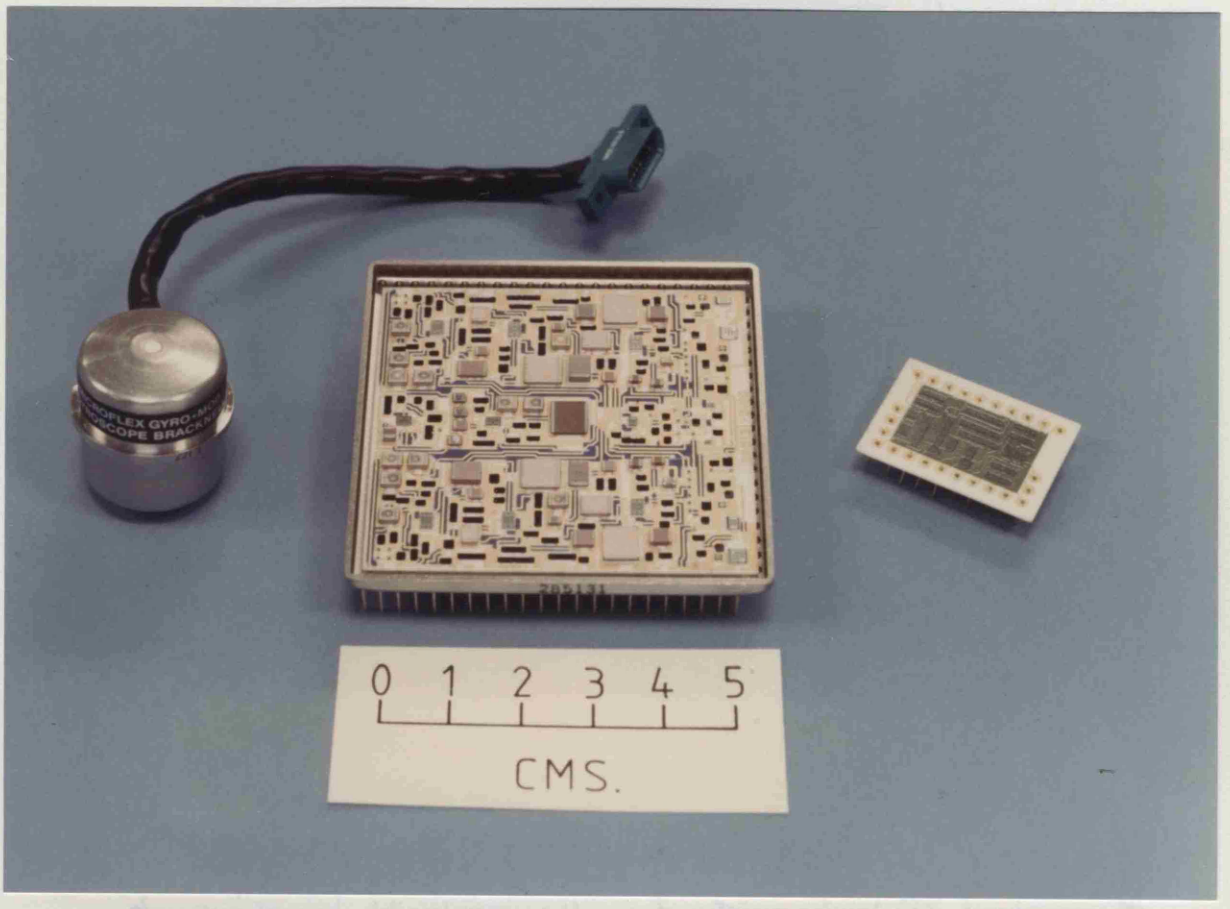

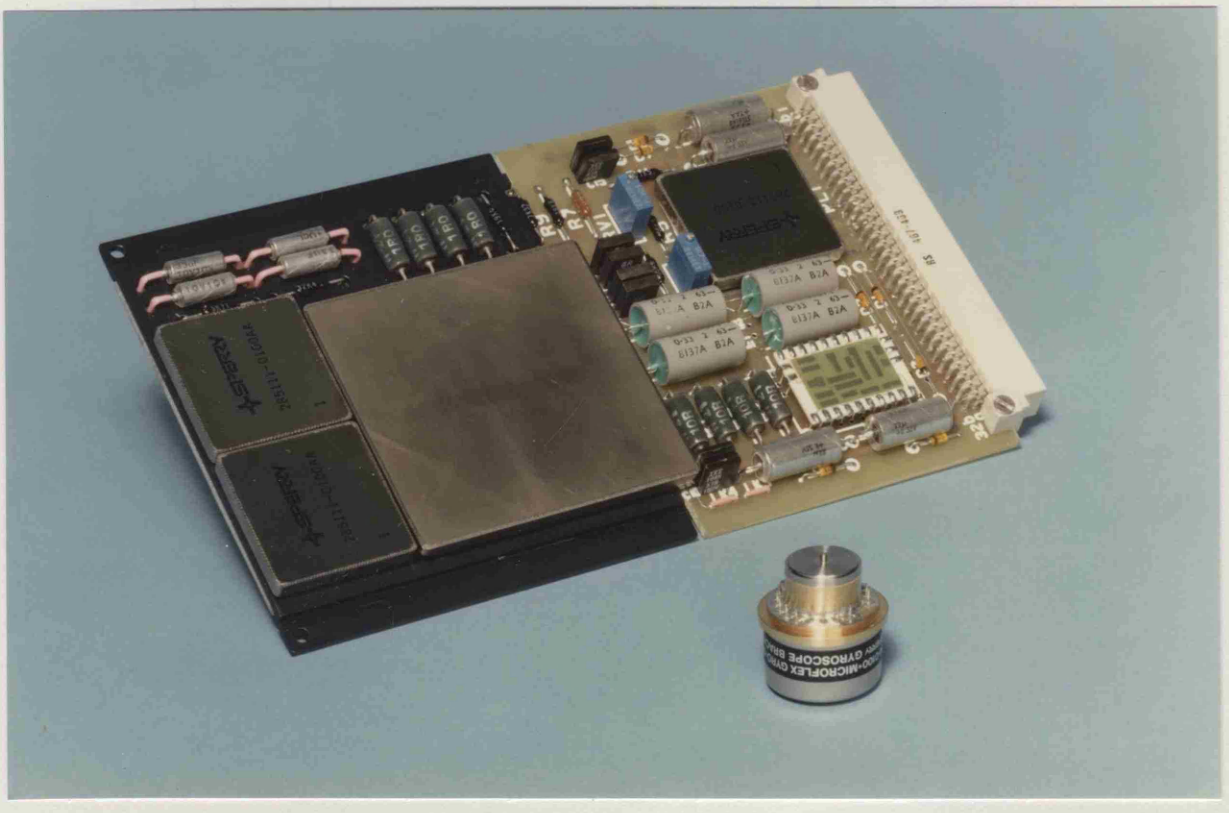

SPT are shown in figures 4.17 and 4.10 respectively. The block diagram gives the nominal transfer functions of the individual blocks. Currently the CPT electronics are manufactured using 'thick film chip and wire' technology. A photograph of the gyroscope and its electronics is shown in figure 4.18. The development of the SPT electronics is still at the breadboard stage.

4.7.1 Detection, Amplification and Demodulation of the Pickoff Signals

Figure 4.19

Detection Circuits Block Diagram

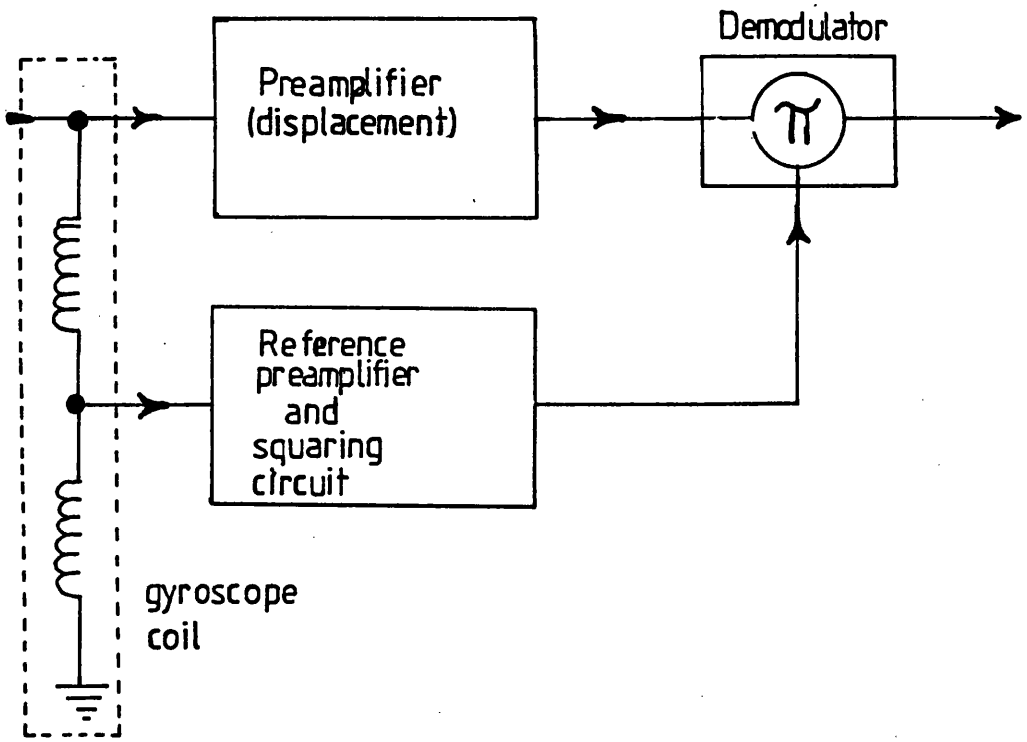

As shown in Figure 4.19 these functions are implemented as three sub-modules; the preamplifier, the demodulator and the reference generator. In the case of the CPT gyroscope, this circuitry has to detect the 1600Hz (typically 100microV pk) amplitude modulated pickoff signal in the presence of the low frequency (0 to 200Hz) signals which are used to torque the gyroscope (typically 2V pk). To achieve attenuation of the torquing signals while detecting and amplifying the pickoff signal, a preamplifier configured as a fourth order Buttertworth high pass filter with a gain of 100 is used. The choice of the break frequency is made to give a flat response to the pickoff signal while effectively attenuating the torquing signals. A high pass filter was chosen rather than a bandpass filter as this introduces less effective phase shift after the signal has been demodulated. This effect is analysed in Appendix IV. The analysis given in Appendix IV is also used to establish a single pole model of the effective frequency response of the preamplifier after demodulation for inclusion in the system model. The input impedance of the preamplifier is also important as it shunts the gyroscopes torquer coils and loads the pickoff signals. The noise introduced by the amplifier limits the resolution of the pickoff signal. (Typically resolution equivalent to 1 arc second is required).

Figure 4.20

Displacement Preamplifier

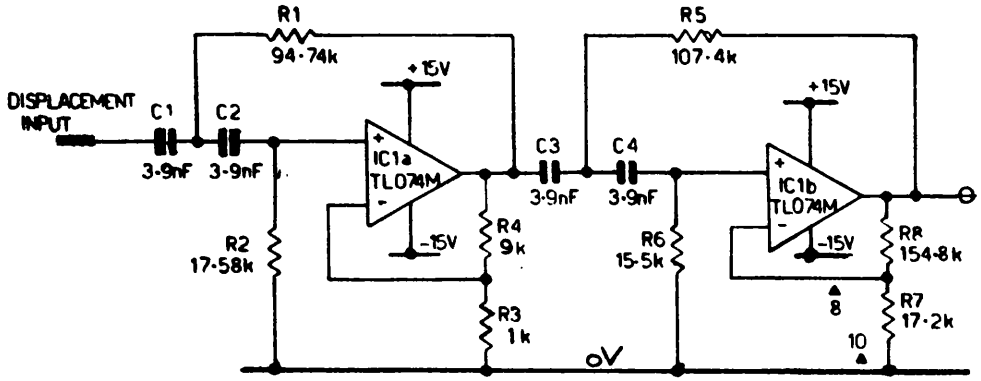

The preamplifier has been implemented using two cascaded filter sections of the type described by Sallen and Key (1954). The section used is shown in figure 4.20. This section achieves the required response and exhibits a high input impedance over the frequency ranges. A low noise operational amplifier has been selected to achieve a good resolution and null stability. The detailed design equation of the filter section is given in Appendix V. To provide a reference signal for the demodulator, it is necessary to recover the gyroscopes reference signal and convert it to a squarewave to drive the demodulators. The reference signal is available from the centre connection of the gyroscopes coils. This signal is a 1600Hz sinusoidal waveform; again the torquing signals are present and require attenuation. To

improve the signal to noise ratio and reduce the electronics needed, the reference signals from both axes are summed and a single reference generated. To optimise the sensitivity of the demodulation process, the phase response of the reference channel must match the phase response of the displacement channels. To achieve this a fourth order Butterworth filter is used with the same transfer function as the displacement channels. The filter section used as the input stage is shown in Figure 4.21. From this it can be seen that the filter has been divided into two sections.

Figure 4.21

Reference Preamplifier

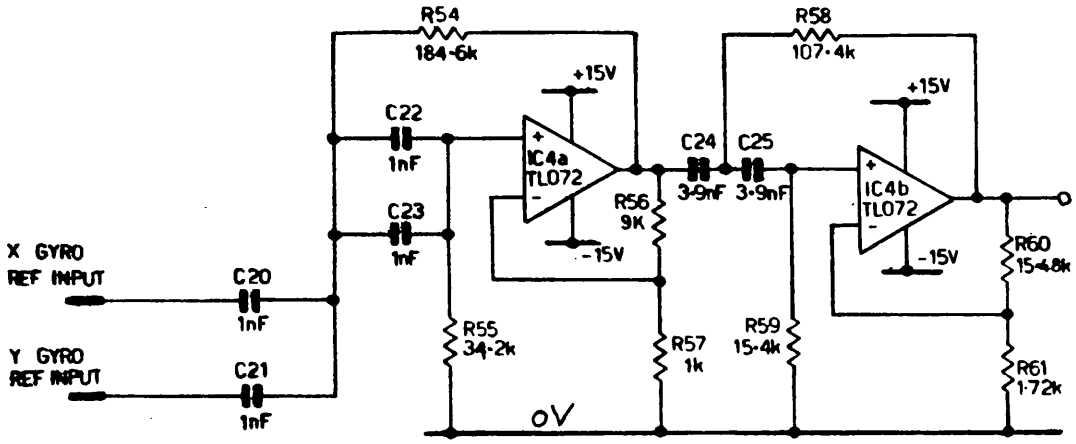

The first section has been designed to sum the voltages applied to its inputs. The detailed design equations for this section are given in Appendix VI. The second section is identical to that used for the second stage of the displacement channel. The reference signal is converted to a

squarewave by the use of the zero crossing detector and the associated circuitry which is shown in Figure 4.22.

Figure 4.22

Zero Crossing and Squaring Circuits

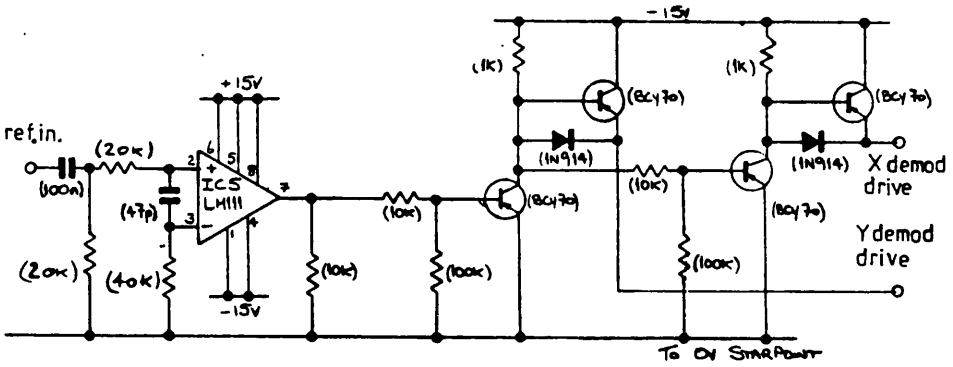

This is cascaded with a transistor switching arrangement which provides the in-phase and the anti-phase signals to drive the demodulators of the two displacment channels. The two channels are demodulated in anti-phase to correct for the sign inversion which occurs on one gyroscope axis.

The demodulator circuit is shown in Figure 4.23. This is a simple switching demodulator which, depending on the state of the FET, multiplies the input by +/-1

Figure 4.23

Demodulation Circuit

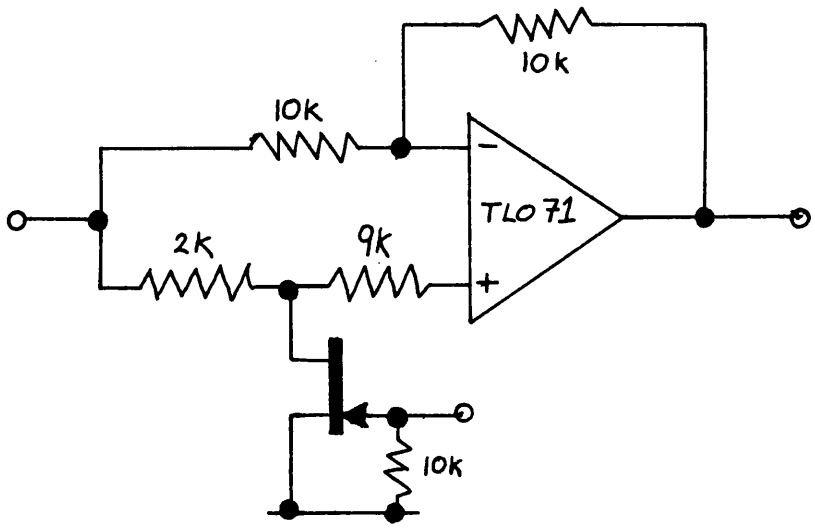

As detailed analysis of this circuit is given in Appendix VII, the dc offsets and offset drift of the stages before the demodulation are unimportant, due to the action of the demodulator which converts these to noise at 1600Hz. This noise is attenuated by the filtering action of the rebalance loop.

The SPT gyroscope has separate pickoff and torquer coils, hence the requirement for filtering the pickoff signals is less stringent and the preamplifier can be designed using cascaded amplifiers. To reduce the noise present the amplifier has been configured as a low 'Q' bandpass filter centred around the pickoff carrier frequency.

4.7.2 Control Terms, Filtering and Electronic Null Adjustment Summing Junction

The control terms are basically an integrator and lead. These are implemented using the circuit shown in Figure 4.24.

Figure 4.24

Integrator Circuit

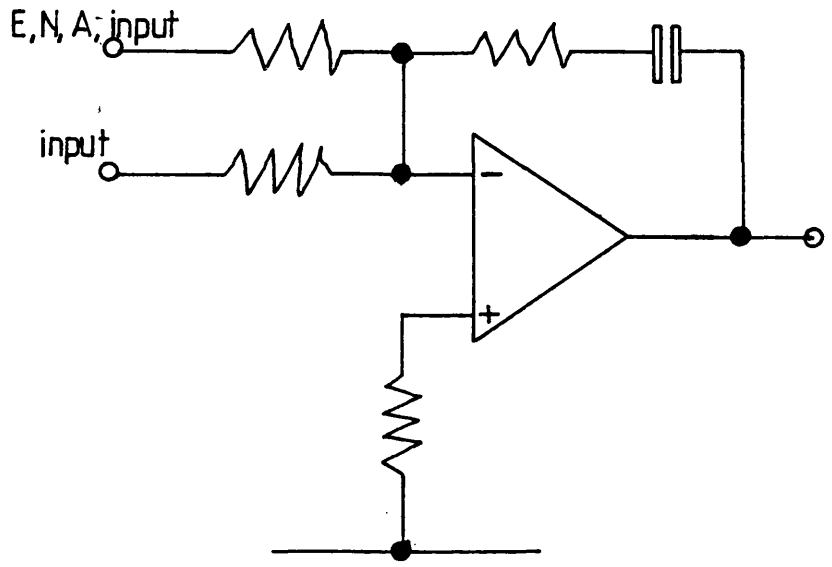

A detailed analysis of this circuit is given in Appendix VIII. The electronic null adjustment is a dc voltage which is summed into the loop at the demodulator output to cancel the electrical offset of the pickoff transducer when the wheel is orthogonal to the gyroscopes case. If this adjustment was not made, then the rebalance loop would servo the wheel to a non-orthogonal position. Any angular 'hang off' of the wheel results in a rate bias error due to the torques applied to the wheel by the residual stiffness of the suspension and the auto-erection mechanisms. It is therefore important that dc

offsets after the demodulator and before the integrator (ie. pseudo angular displacements) are kept to a minimum. This requires a careful choice of the parameters of the integrator amplifier.

The low pass filters are implemented using Sallen and Key sections, with and without gain. These sections are shown in Figures 4.25.1 and 4.25.2 respectively and the design details are given in Appendix IX. These filters appear after the integrator. This means that the dc offsets of these filters are attenuated by the dc open loop gain of the loop and hence resulting drifts are negligible. In the case of the CPT, many terms are cascaded. This requires that the individual transfer functions to have accurately defined to achieve the desired response of the overall loop. Also included within the filtering is a bandstop filter to attenuate noise components of the wheel rotation frequency. This is required to prevent these signals saturating the loop, and eroding the 'rate' capability of the loop. The circuit for this section is given in Figure 4.26, the design details are given in Appendix X.

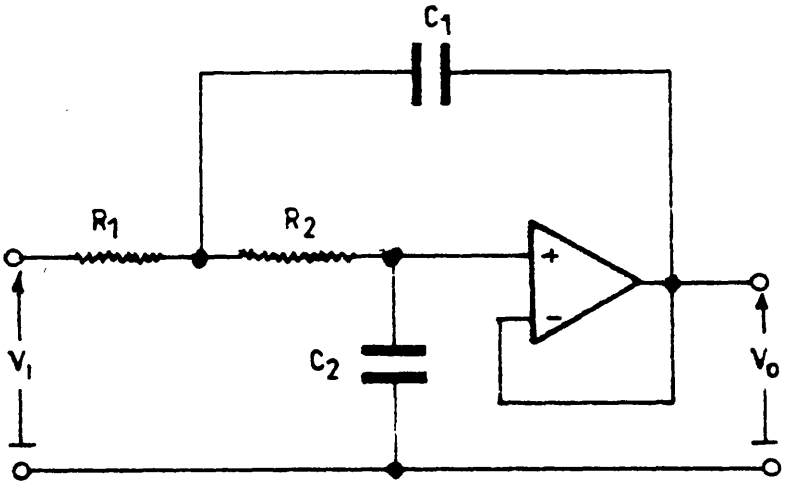

Fig. 4·25·1— UNITY GAIN 2nd ORDER LOW PASS FILTER SECTION

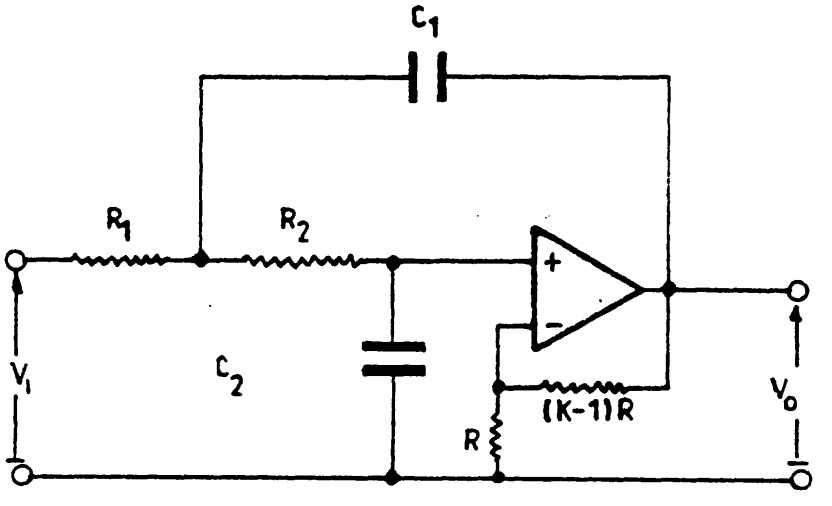

Fig 4·25·2— 2nd ORDER LOW PASS FILTER WITH GAIN

FIGURE 4·25— SECOND ORDER LOW PASS FILTERS

Figure 4.26

Band Stop Filter Section

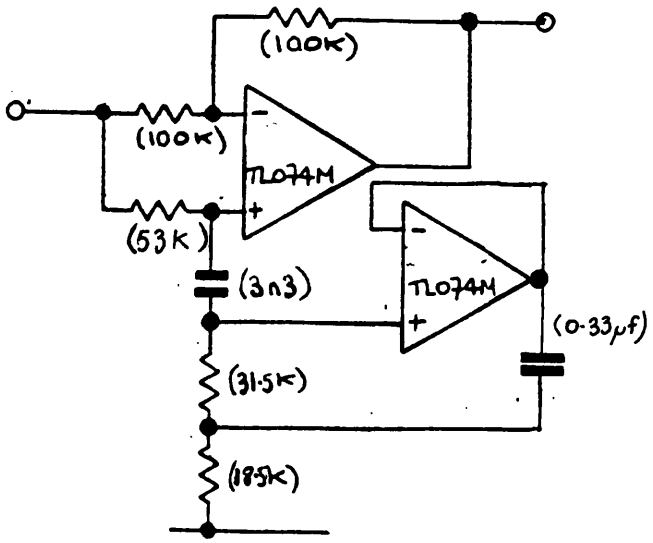

This filter has to be designed to have a stable natural frequency and high 'Q'. The filter has been designed to have a minimum effect upon the overall design of the loop. However, with the SPT gyro, the need for this filter becomes a limiting factor for the achievable bandwidth of the rebalance loop.

The SPT gyro also requires a notch filter at twice the wheel rotation frequency. This is implemented using the section shown in Figure 4.26. The need for this arises due to the fact that the gyroscopes torquer rectifies twice wheel speed noise which results in bias drift. This is not so critical in the design of the CPT gyroscope rebalance loop, because the filtering to attenuate the "figure of eight" loop also

provides attenuation at twice wheel speed. As this noise is phase related to the gyroscopes wheel it varies from switch on to switch on, and the rectification is manifest as a bias repeatability error.

4.7.3 The Voltage to Current Converter

This circuit is required to convert the voltage signals from the conditioning circuits to current signals to precess the gyroscopes wheel. The circuit diagram for the converter is shown in Figure 4.27. The converter consists of three stages. A push pull transistor amplifier to provide the output current, an operational amplifier to linearise the output stage and remove 'crossover distortion' and an operational amplifier to control the feedback to convert the voltage inputs to current outputs. The feedback signal is obtained by sensing the voltage developed across a precision 2.5 ohm resistor which is connected in series with the gyroscopes torquing coils. In the case of the CPT gyroscope, the output impedance of the converter shunts the torquer/pickoff coils. Thus it is important that the output impedance at the pickoff carrier frequency is much greater than the coils impedance. If this is not the case then the pickoff signal will be loaded and consequently attenuated. In the event that the output of the converter saturates, (ie. has insufficient voltage headroom to supply the demanded current) the output impedance becomes very low. This has the effect of attenuating the pickoff signal to a level where the rebalance loop can no longer operate. This

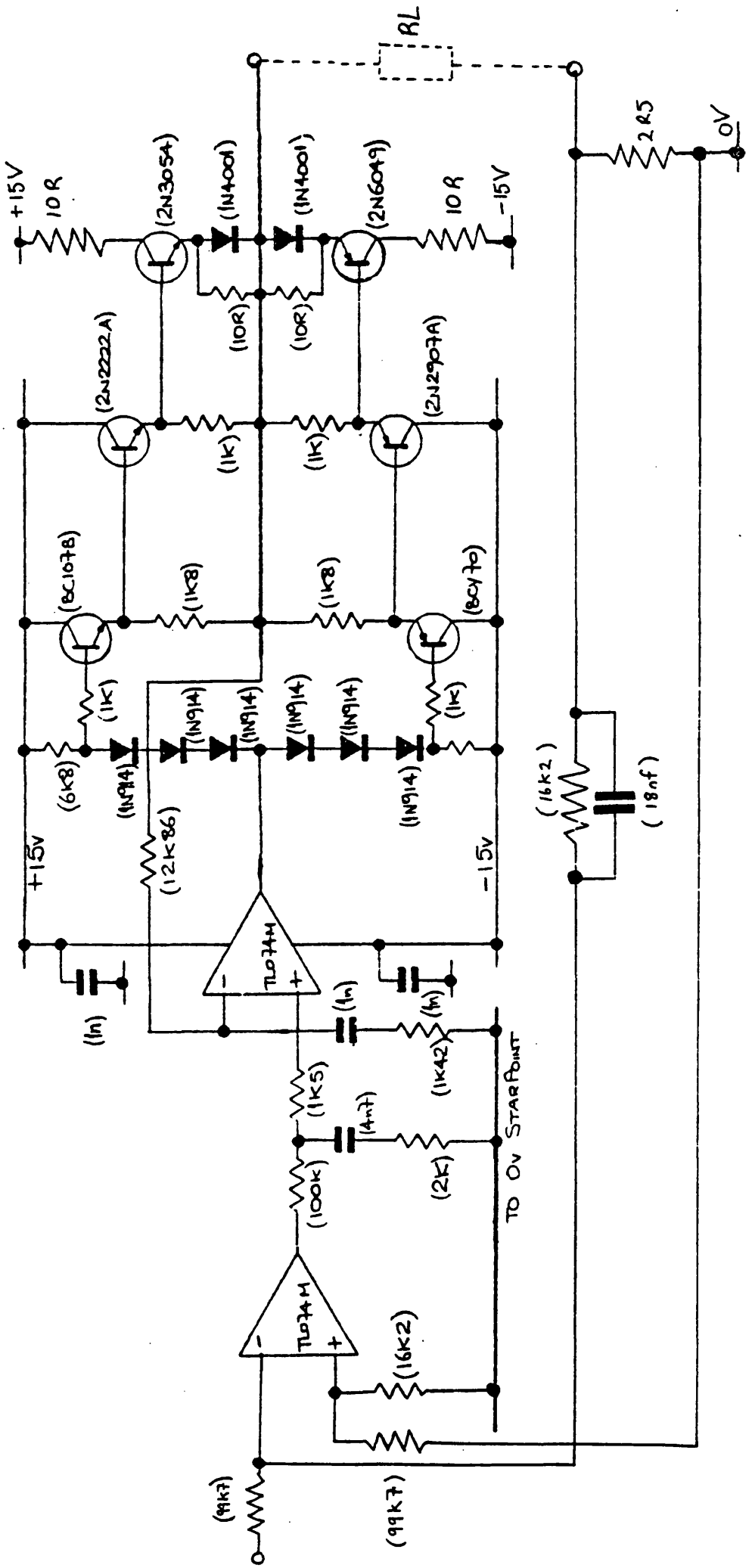

Figure 4·27 Voltage to Current Converter Circuit

has the effect of driving the voltage to current converter further into saturation and the rebalance loop cannot recover from this condition. To prevent this from occurring, the maximum input is clamped using a pair of zener diodes. The clamping level is chosen based on the voltage headroom and the maximum temperature that the gyroscope is likely to attain because the resistance of the coils is proportional to temperature and this determines the voltage required to supply the demanded current.

The output from the rebalance loop is measured by monitoring the current flowing in the gyroscopes coils. This is achieved by monitoring the voltage developed across the same sense resistor that is used to provide the feedback signal for the voltage to current converter. Any thermal emf generated at the terminals of this resistor appear directly as errors in the measured current and appear as gyroscope drift. Great care has been taken with the choice of materials and as far as possible thermal gradients in this circuit area have been minimised.

4.7.4 Compensation Trims

To adjust for variation in the gyroscopes parameters, an electrical trimming scheme is used. This scheme compensates for:-

(i) the variation in the product of pickoff and torquer scale factor (gyroscope gain),

(ii) the offset between the electrical and mechanical null positions,

(iii) the output scale factor and the gravity insensitive bias of the gyroscope.

To achieve the trims a series of resistor networks are used. The gyro gain is trimmed within the rebalance loop using a cascaded attenuator which is adjusted to trim the closed loop bandwidth. The output scale factor is adjusted by attenuating the output from the rate sensing system. To provide the electronic null adjustment (ENA) and a voltage signal, which is proportional to the electro-mechanical offset, two precision reference signals (+/-10V) are generated using the circuit shown in Figure 4.28. Adjustments of the ENA compensation signals are made using simple resistive potentiometers.

Figure 4.28

Reference Voltage Generator

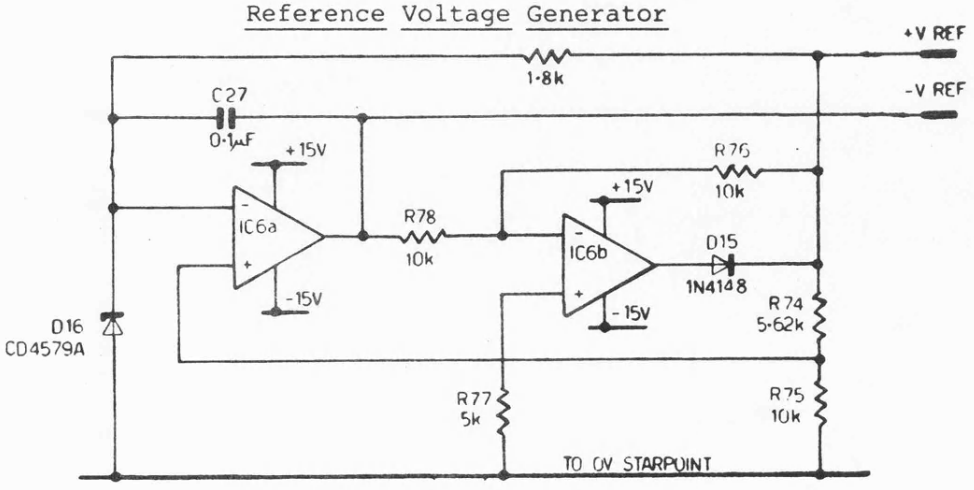

The voltage reference uses a compensated zener diode. The

circuit is arranged such that the reference voltage is used to control the operating current of the diode, thus ensuring low temperature coefficient of the reference voltage. The diode in the output of IC2 is to ensure that the circuit switches on with the correct polarity.

4.7.5 The Motor Drive Circuitry

The inertial element of the Microflex gyroscope is driven at a synchronous speed of 200Hz by a four pole hysteresis motor. The motor requires a two phase sinusoidal supply at a frequency of twice the rotation frequency of the motor. The two phases of the drive must be at a phase angle of 90 deg to each other (ie. sine and cosine).

The motor supply is provided by a phase shift oscillator which has sine and cosine outputs. These outputs are buffered by two power amplifiers which then drive the motor. The frequency stability of the oscillator is of prime importance as this defines the rotation frequency of the inertial element. Both the torquer and pickoff scale factors are proportional to wheel speed. Modulation of either of these will vary the gain of the rate system changing the dynamic performance and introducing unwanted noise. Variations of torquer scale factor are of particular importance as the torquer scale factor scales the output of the rate loop. Variations of the torquer scale factor under dynamic conditions appear as apparent changes in the angular rate

which is applied to the system.

A detailed analysis of the oscillator is given in Appendix XI.

REFERENCES USED IN CHAPTER IV

Briggs, R.W. (1965). Stability of a Two Degree of Freedom Gyro with External Feedback, IEEE Transactions on Automatic Control, pp 244-249, July.

Coffman, D.E. (1974). Feasibility Study of a Digital Rebalance Loop for a Dry Tuned T.D.F. Gyro. University of Tennessee, May 1974, Scientific Report S-28.

Cornwell, R.J., Mertens, M.J., Johnson, B. (1983). Final Report on Contract A81a/2048 for the Build of Two Temperature Compensated Type 507 Microflex Rate Gyros, TR1087, British Aerospace, Bracknell, England.

D'Azzo, J.J., Houpis, C.H. (1960). Feedback Control System Analysis and Synthesis, Second Edition, Tenden - McGraw-Hill.

Di Steffano, J.J., Stubberud, A.R. and Williams, I.J. (1976). Feedback and Control Systems, Schaums Outline Series, London, McGraw-Hill.

Lipman, J.S. (1968). Application of the Complex Method of Transform Analysis of Spinning Systems with Rotating Non-symmetries. Litton Systems Inc.

Sallen, R.P., Key, E.L.(1954). A practical Method of Designing RC Active Filters. IRE Transactions - Circuit Theory, pp 74-75, March.

CHAPTER V

DIGITAL CONTROL OF THE MICROFLEX GYROSCOPE

5.1 INTRODUCTION

The main applications for miniature rate gyroscopes are in 'strapdown' inertial navigation systems. In these types of systems the inertial sensors are directly 'strapped down' to the frame of the vehicle rather than mounted on gimbals or platforms as in traditional systems. Napus (1975) points out the advantages of strapdown systems over gimbal systems. The elimination of the gimbal structure reduces both size and cost, as well as offering the advantages of reduced complexity and increased reliability. In a strapdown system the platform and gimbals are replaced by a set of computation algorithms. These effectively perform mathematically the function of the platform and maintain an inertial reference in space. The main obstacle which has retarded the development of strapdown systems has been the need for a relatively large computer to implement the algorithms. Microprocessor technology has now provided small size, low cost and the computing power necessary to allow economical implementations of strapdown systems. The basic concept of the strapdown algorithms is described by Schmidt (1975). The basic block diagram of a strapdown system is shown in Figure 5.1.

Figure 5.1

Block Diagram of a Strapdown Navigation System

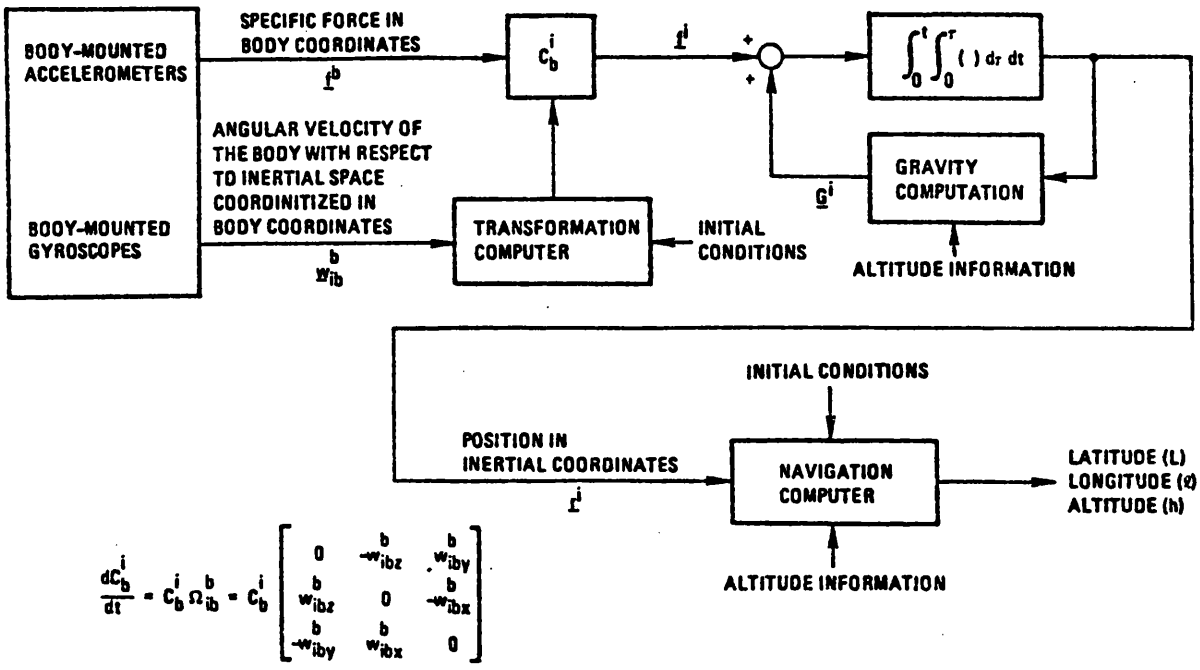

From the block diagram it can be seen that in such a system the angular velocity outputs from the gyroscopes are integrated. This is done to provide the angular information required to transform the acceleration inputs, from body referenced acceleration to inertial referenced acceleration. In practice, the strapdown algorithms are performed using a microprocessor, hence it is necessary to convert the gyroscopes outputs to digital signals. A typical strapdown application would require a bias stability/resolution of 5 deg/hr, and a peak angular rate demand of 300 deg/sec. This wide dynamic range requires an expensive and complex 'Analogue to Digital Converter' of typically 20 bits range of the type

described by Geen and Johnson (1985). One technique which can be used to generate a direct digital output from force rebalance sensors is to provide the rebalance forces using a Binary Pulse Width Modulated Scheme (Coffman 1974). This provides a wide range conversion of the sensors output in a form which is particularly suitable for processing by the strapdown algorithms. In this form the output is quantised in angular increments, and any error or fractional quanta are actually stored within the system and corrected on the next data transfer. Hence, when the output is time averaged (integrated) a very accurate measure of angle is obtained. A block diagram showing the elements of a Binary Pulse Width Modulated Control Loop is shown in Figure 5.2.

Figure 5.2

Binary Pulse Width Modulated Control Loop

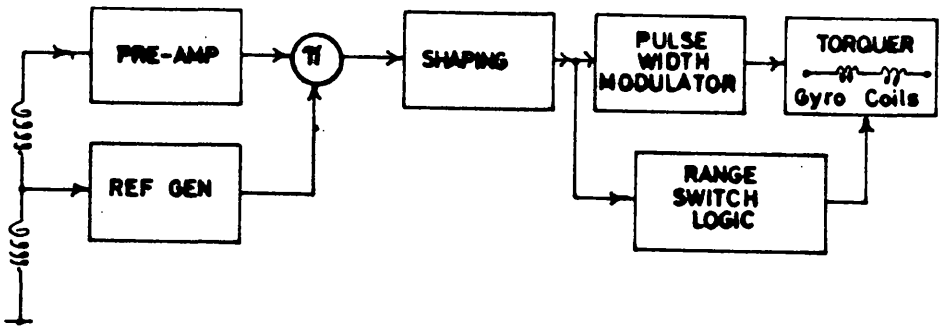

The feasibility and practicality of a Pulse Width Modulated rebalance loop based upon the Microflex Gyroscope has been studied and demonstrated by Johnson and Smith (1984). The pulse width modulation and drive circuit can readily be implemented in digital form. To be able to configure the remaining electronics in digital form offers the opportunity to reduce the electronics to a single custom silicon integrated circuit. This approach has many size and cost advantages over traditional electronic technology, as well as being easy to manufacture in large quantities. Digital processing offers the advantage that more precise implementation of control functions can be obtained, because the accuracy of the circuits response does not depend upon individual component tolerances. This means that a design can be produced more reliably and repeatedly.

The objective of the work described in this chapter was to examine the feasibility of using a digital controller, and to demonstrate the practicality by producing a simple working digital controller design. This design was used to examine the practical problems which may arise from a more complex arrangement.

5.2 DIGITAL CONTROL

There are several design methods which can be used to determine the form of a digital controller. These various general approaches are described in detail by Franklin and Powell (1980). A design technique specific to controlling two

degree of freedom gyroscopes has been developed by Puri (1979). Puri's design method is based upon achieving minimum settling time, and eliminating the cross coupling within the gyroscope (nutation). However, for the purposes of this study, it is considered that actively suppressing nutation is too complex to be easily realised in a simple practical design.

One of the objectives of the work described in this chapter is to develop a digital control loop which is comparable with analogue control loops described in the earlier chapters. To achieve this, the design of the SPT gyroscope analogue control loop was converted for digital implementation. To allow the design to be easily implemented, only the basic controller was converted to digital form. To convert the analogue signal to digital signals and vice versa, two 12 bit converters and a sample and hold circuit were used within the loop.

5.2.1 Basic Controller

As a starting point the SPT Gyroscope's Analogue Controller was examined for its suitability as the basis of a digital controller. The transfer function of the controller in the frequency domain is described by Equation 4.6. The transfer function to be used for controlling both axes of the gyroscope is given by:

$$D(S) = \frac{kg}{s}\left(\frac{s}{\omega_o} + 1\right)\begin{bmatrix} 0 & 1 \\ -1 & 0 \end{bmatrix} \qquad 5.1$$

Using the Bilinear transform it can be shown that after mapping to the Z plane that the corresponding controller D(Z) is:

$$D(Z) = SG\,\frac{(\alpha Z - 1)}{(Z - 1)}\begin{bmatrix} 0 & 1 \\ -1 & 0 \end{bmatrix} \qquad 5.2$$

Where $SG = \dfrac{(1 - \frac{T}{2}\omega_o)\,kg}{\omega_o}$

and $\alpha = \dfrac{1 + \frac{T}{2}\omega_o}{1 - \frac{T}{2}\omega_o}$

Where T = sampling period

To ease the implementation of the controller in practical terms the lead , which for the analogue controller was chosen to break at 1Hz, will be chosen to break at 1.59 Hz. This has very little effect upon the design of the loop and only has a minor effect at low frequencies. Provided that the loop gain is increased to compensate for the loss in high frequency gain, this will not effect the closed loop bandwidth or the stability of nutation. However, to a small extent it will increase the gain ripple in the systems pass band and increase the loops ability to follow angular accelerations.

5.2.2 The Effects of Quantisation

In implementing the digital rebalance loop, two forms of quantisation are introduced into the control loop. The first of these is the quantisation due to the analogue to digital converter, the second occurs in the truncation of the numbers in the control algorithms. Both of these forms of quantisation make the loop non-linear and may cause limit cycles. Limit cycles are periodic oscillations which may exist in spite of there being no input to the system. The analysis of limit cycles has been studied by several authors, Gleb (1968) uses describing function analysis to predict limit cycles and determine their behaviour. Bertran (1958) examines the effects of quantisation in sampled data systems and develops a worst case analysis, while Slaughter (1964) develops an analysis for the steady state worst case. More recently, Franklin and Powell (1980) describe quantisation as a signal dependent gain. The following analysis is based on

that concept. Consider a first order system with characateristic equation:

$$Y(k+1) = Q\{\gamma\, y(k)\}$$

Where Q is the quantisation function

γ is a linear function

Figure 5.3 shows plots of the trajectories of the unquantised and quantised signals. Note the quantised signal is delayed by one sample period, and remains fixed over that period. The next value is dependent upon the previous quantised value hence the error tends to grow. Suppose y is positive and has a value a, and the input is removed, and then this is traced to point b, the next value of y will be c. Hence if this process is continued it can be seen that the system will achieve equilibrium at y=0. Now suppose y is negative, clearly the trajectory reaches equilibrium at point s, ie. at the intersection of the two plots. By inspection of Figure 5.3 we can see that the largest value for which y is stationary is $y = -Kq$, such that:

$$|Y| < \frac{q}{1-\gamma}$$

This gives the worst case bound as described by Bertram (1958). This is dependent upon both the quantisation level and the time constant of the system. This analysis can be

Figure 5,3

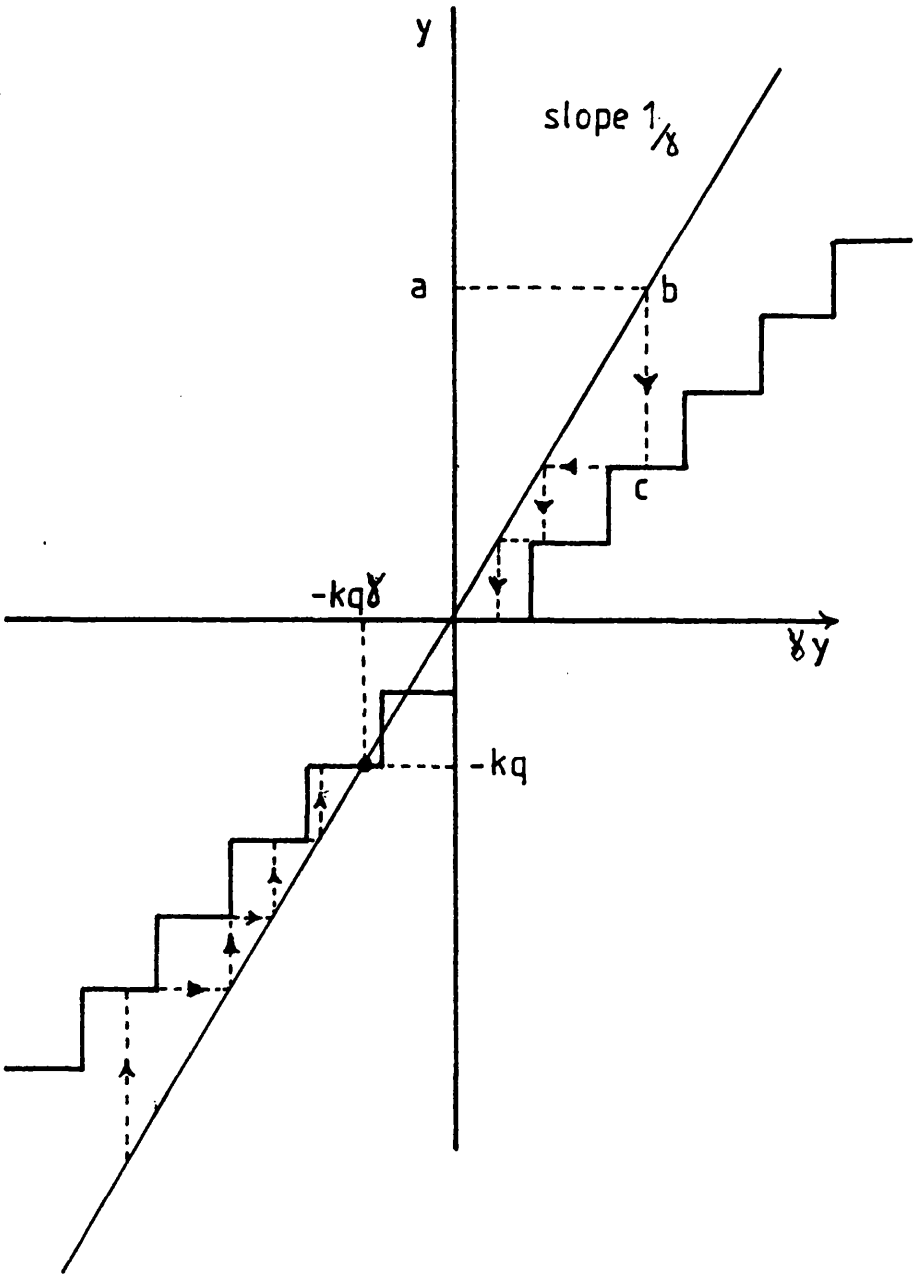

Trajectory of a First Order System with Quantisation

developed for higher order systems. By considering the quantiser as a variable gain, equilibrium occurs when the combined gain of the quantiser and system is unity, which in a linear system corresponds to a pole at Z=1. Applying this argument to high order systems leads to the supposition that the limiting motion will be no larger than the largest signal for which the linear system (with the resulting limiting gains) has a pole in the unit circle. This means that the amplitude is dependent upon any pole which may have a complex root on the unit circle. So each of these needs to be tested to determine the maximum amplitude of any limit cycling. The frequency of the limit cycle will be determined by the frequency response of the system. This model of limit cycling gives an insight as to how dither or zero mean value noise signals may be used to disturb the system and destroy the limit cycle, or remove large constant bias which may have resulted from quantisation. If a zero mean signal of amplitude greater than the limit cycle with a frequency beyond the bandwidth of system is added to the input, then the average value of the output signal will tend to drift towards zero, hence destroying the limit cycle.

In general the complexity of the gyroscope loop does not lend itself to algebraic analysis. To study the points at which limit cycling may occur, the computer model was used to plot the root locus of the system in the Z plane. Figure 5.4 shows the locations of the poles of the closed loop system with the

Figure 5,4 Location Of The System Poles

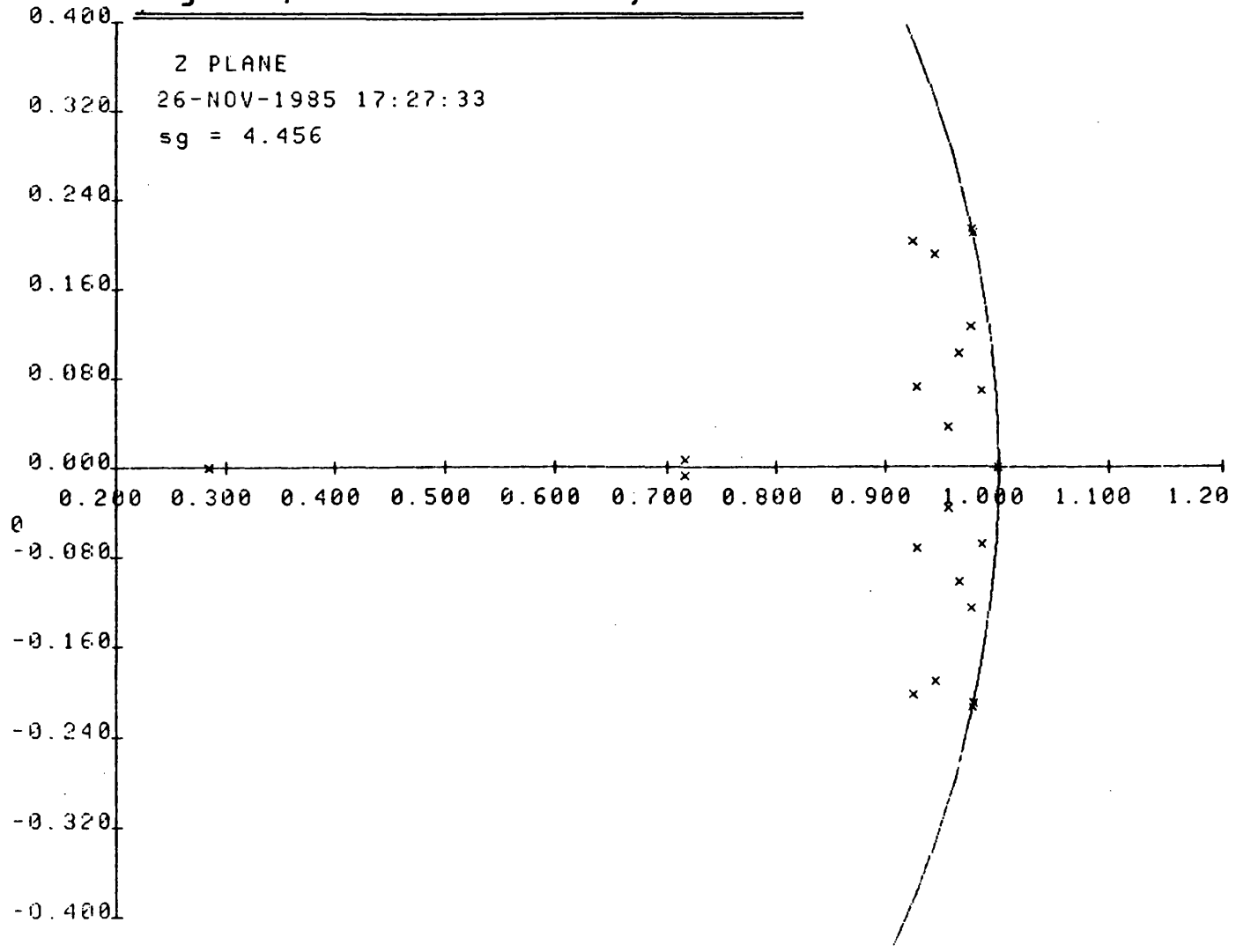

Figure 5,5 Pole Migration

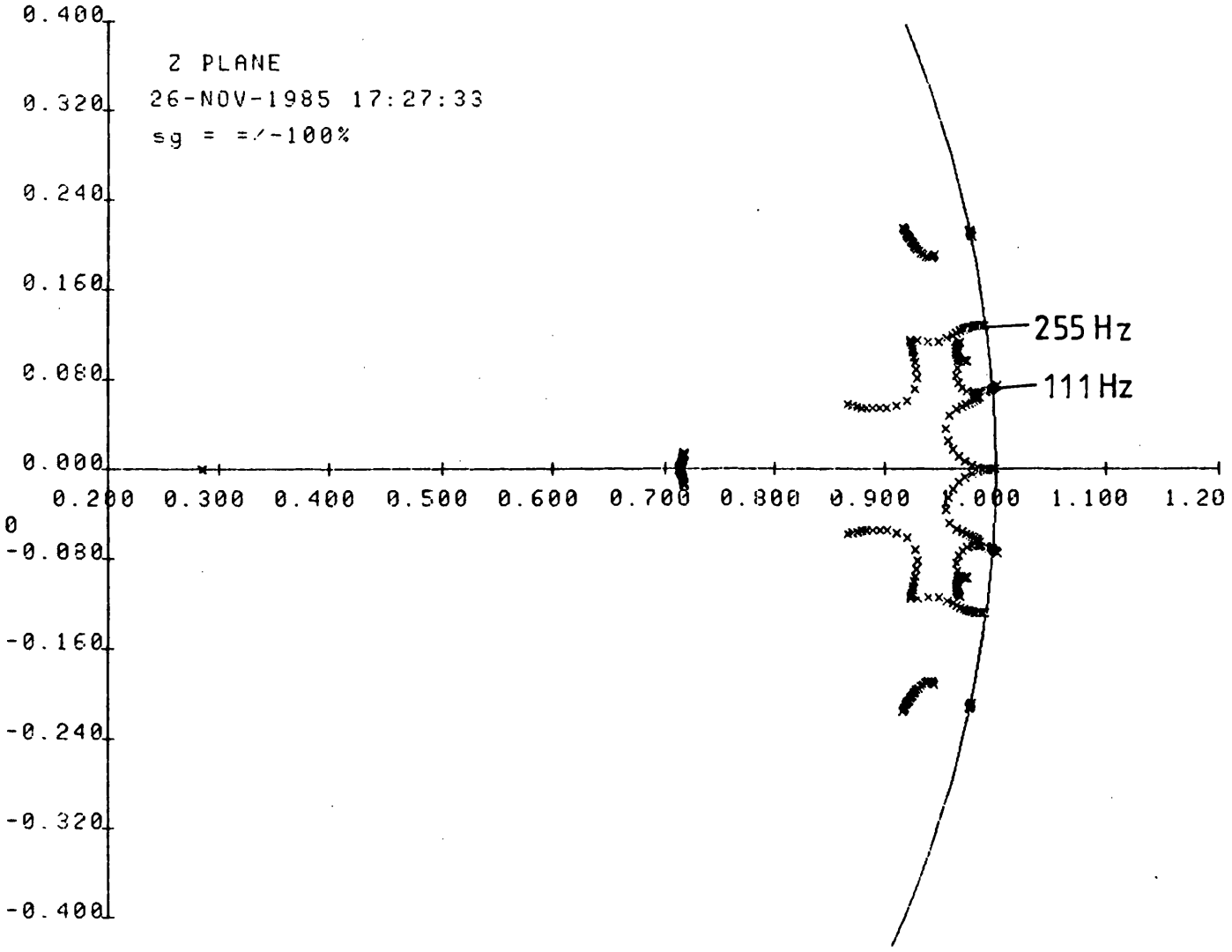

Table 5,1

TIME ROOTS RESULTS Z DOMAIN
RUN NO. 3 28-NOV-1985 08:28:21

GAIN VARIABLE SG = 4.4560E0

REAL	IMAG	MODULUS	PHASE
2.8461E-1	2.0405E-5	2.8461E-1	4.1078E-3
2.8461E-1	-2.0405E-5	2.8461E-1	-4.1078E-3
7.1540E-1	6.8712E-3	7.1543E-1	5.5029E-1
7.1540E-1	-6.8712E-3	7.1543E-1	-5.5029E-1
9.2333E-1	2.0283E-1	9.4535E-1	1.2390E1
9.2333E-1	-2.0283E-1	9.4535E-1	-1.2390E1
9.7783E-1	2.0987E-1	1.0001E0	1.2113E1
9.7783E-1	-2.0987E-1	1.0001E0	-1.2113E1
9.7668E-1	2.1362E-1	9.9977E-1	1.2337E1
9.7668E-1	-2.1362E-1	9.9977E-1	-1.2337E1
9.4315E-1	1.9037E-1	9.6217E-1	1.1411E1
9.4315E-1	-1.9037E-1	9.6217E-1	-1.1411E1
9.7534E-1	1.2641E-1	9.8350E-1	7.3846E0
9.7534E-1	-1.2641E-1	9.8350E-1	-7.3846E0
9.6465E-1	1.0223E-1	9.7005E-1	6.0495E0
9.6465E-1	-1.0223E-1	9.7005E-1	-6.0495E0
9.2731E-1	7.1693E-2	9.3007E-1	4.4209E0
9.2731E-1	-7.1693E-2	9.3007E-1	-4.4209E0
9.8527E-1	6.8238E-2	9.8763E-1	3.9619E0
9.8527E-1	-6.8238E-2	9.8763E-1	-3.9619E0
9.5479E-1	3.6289E-2	9.5548E-1	2.1766E0
9.5479E-1	-3.6289E-2	9.5548E-1	-2.1766E0
9.9990E-1	0.0000	9.9990E-1	0.0000
9.9990E-1	0.0000	9.9990E-1	0.0000

are given in Table 5.1. Figure 5.5 shows the effect of varying the loop gain from 10% to 200% of its nominal value. This shows that the nutation poles are stable and migrate around the unit circle as the gain is increased. It also shows that two limit cycles are possible at 111Hz and 255Hz. Both these frequencies are beyond the bandwidth of the system. According to Franklin and Powell (1980) the maximum magnitude (Kq) of the limit cycle

$$Kq < \frac{1}{2}\frac{q}{1-|a|}$$

Where q is the quantisation level and a is the starting value complex root that migrates to the unit circle. Hence the system limit cycles will have maximum amplitude of 30 least significant bits (LSB) of the quantiser. However, this is very pessimistic, as can be seen from the trajectory of the poles in Figure 5.5, the gain of the system has to be increased by a large amount before the pole migrates to the unit circle. In practice it is likely that the limit cycles will be destroyed by the system noise.

5.2.3 The Effects of the Gyroscopes Pickoff Noise

As described in Chapter II the self generating pickoff transducer produces noise components at harmonics of wheel speed. The presence of these noise components affects the choice of sampling frequency. Care must be taken to avoid aliasing of these signals. However, the presence of these

noise signals may have a beneficial effect. As described in the previous section, the presence of the noise may destroy any limit cycles which may exist. Another benefit of the noise is the effect it has on the resolution of data conversion and processing when averaged by the integrating properties of the gyroscope. A typical error plot for an analogue to digital converter is shown in Figure 5.6.

Figure 5.6

ADC Error Distribution

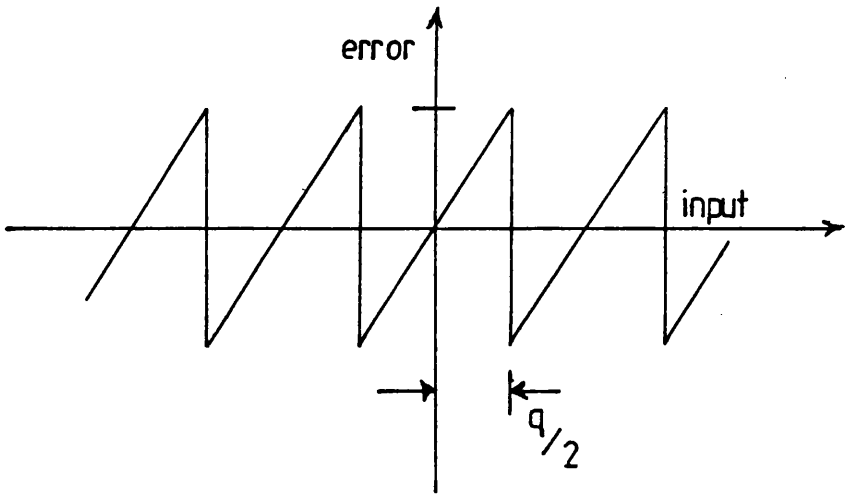

The error distribution shown in Figure 5.6 can be described by the Fourier series:

$$e(x) = \frac{2q}{\pi} \sum_{n=1}^{\infty} \frac{(-1)^{3n-1}}{n} \sin \frac{(n \pi x)}{q} \qquad 5.3$$

If the input is assumed to be of the form:

$$x = V(t) + A \cos(\omega t + \phi)$$

Where V(t) is the signal of interest, A is the amplitude of the noise, ω is a harmonic of the gyroscopes noise and ϕ is a random phase variable, it can be shown that:

$$e(x) = \frac{2q}{\pi} \sum_{n=1}^{n=\infty} \frac{(-1)^{3n-1}}{n} [\sin(n\,\alpha\,V(t))\, J_0(n\,\alpha\,A) + \sum_{i=1}^{\infty} \{\sin(n\,\alpha\,V(t))\,(-1)^{-i}\, J_{2i}(n\,\alpha\,A).\cos(2i\beta) + (-1)^{i+1}\, J_{2i-1}(n\,\alpha\,A)\cos(n\,\alpha\,V(t))\cos((2i-1)\beta)\}] \quad 5.4$$

Where $J_n(Y)$ are the solutions of Bessel equation

$$\alpha = \frac{\pi}{q} \quad \text{and} \quad \beta = \omega t + \phi$$

When this signal is time averaged by the integrators within the loop the average error $(e(x)_{av})$ is given by:

$$e(x)_{av} = \frac{2q}{\pi} \int_0^T \sum_{n=1}^{\infty} \sin(n\,\alpha\,V(t)\, J_0(n\,\alpha\,A)\, \frac{(-1)^{3n-1}}{n} \quad 5.5$$

Equation 5.5 shows that the noise causes the average error to be decreased and that a relatively small amount of noise can greatly improve the resolution of the system. In practice, the bit errors of an analogue to digital converter are not evenly distributed and errors occur in patterns as the input is increased. A similar analysis can be carried out to examine the effects of this, but for this particular system,

where the ADC input is servoed to a null, the operating range of the ADC can be assumed linear.

5.2.4 Selection of the Sampling Frequency and Word Length

The selection of the sampling frequency and word length are important as they have a significant effect on the response and stability of the loop. To avoid effects of aliasing the noise within the system, the sampling frequency needs to be as high as possible. One effect of sampling is to cause the frequency response of the digital part of the system to repeat at multiples of half the sampling frequency. This distorts the response of the loop, hence the sampling frequency must be chosen to have minimal effect within the frequency range of the controller, so allowing the required bandwidth to be obtained. In the particular case of the gyroscope, special attention must be paid to the response of the loop near the nutation frequency. However, to maximise the computation time available, it is necessary to have the largest sampling period. The prime consideration for the selection of the minimum sampling period for this particular design is the stability of nutation. The effects of sampling can be examined by introducing a "sample and hold" term; which is represented in the frequency domain by:

$$SH_{(s)} = \frac{1-e^{-sT}}{s} \qquad 5.6$$

Where T is the sampling period

The term e^{-sT} can be estimated using Padé approximants . As the system is essentially second order a second order approximate was chosen.

$$e^{-sT} \cong \frac{1 - \frac{1}{2} sT + \frac{1}{12} (sT)^2}{1 + \frac{1}{2} sT + \frac{1}{12} (sT)^2} \qquad 5.7$$

Substituting Equation 5.7 in Equation 5.6 yields:

$$SH_{(s)} \cong \frac{T}{1 + \frac{sT}{2} + \frac{(sT)^2}{12}} \qquad 5.8$$

Basically, Equation 5.8 represents a second order low pass filter with break frequency equivalent to the sampling frequency divided by the square root of 12. Provided that this break frequency is higher than the nutation frequency, only the phase effects of the sample and hold need to be considered. The phase (Ø) of the filter can be shown to be represented by:

$$\emptyset = \tan^{-1} \left[\frac{\omega T/2}{1 - \frac{\omega^2 T^2}{12}} \right] \qquad 5.9$$

Using the relationship of Equation 5.9, if the maximum increase in phase at the nutation frequency is to be kept at less than 6 deg, then a sampling frequency of 10kHz is required. This sampling rate was selected as, in addition to satisfying the nutation stability requirements, it is

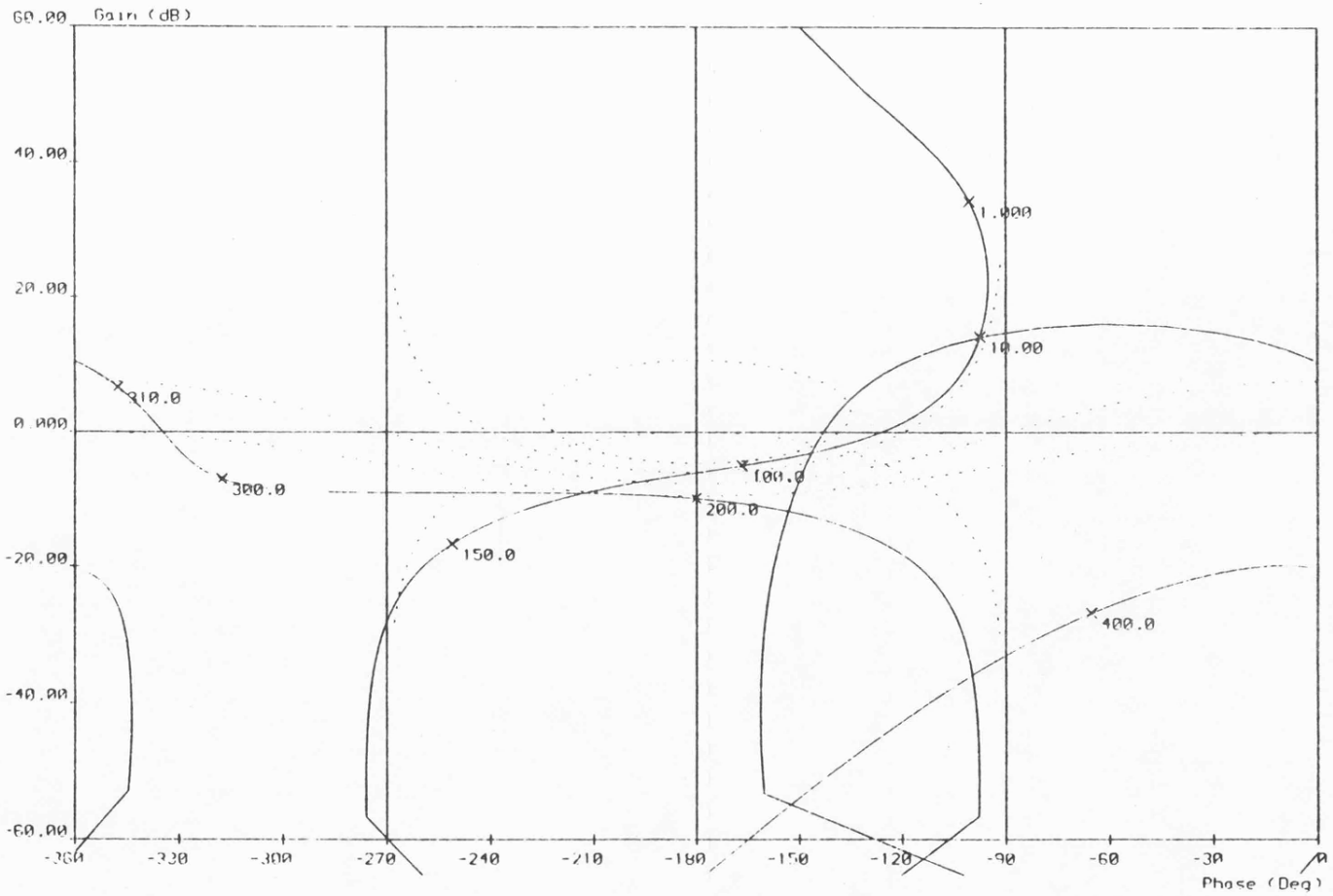

Fig 5.7 – S.P.T. (OPEN) LOOP DIGITAL INT & LEAD . Fs=10000Hz

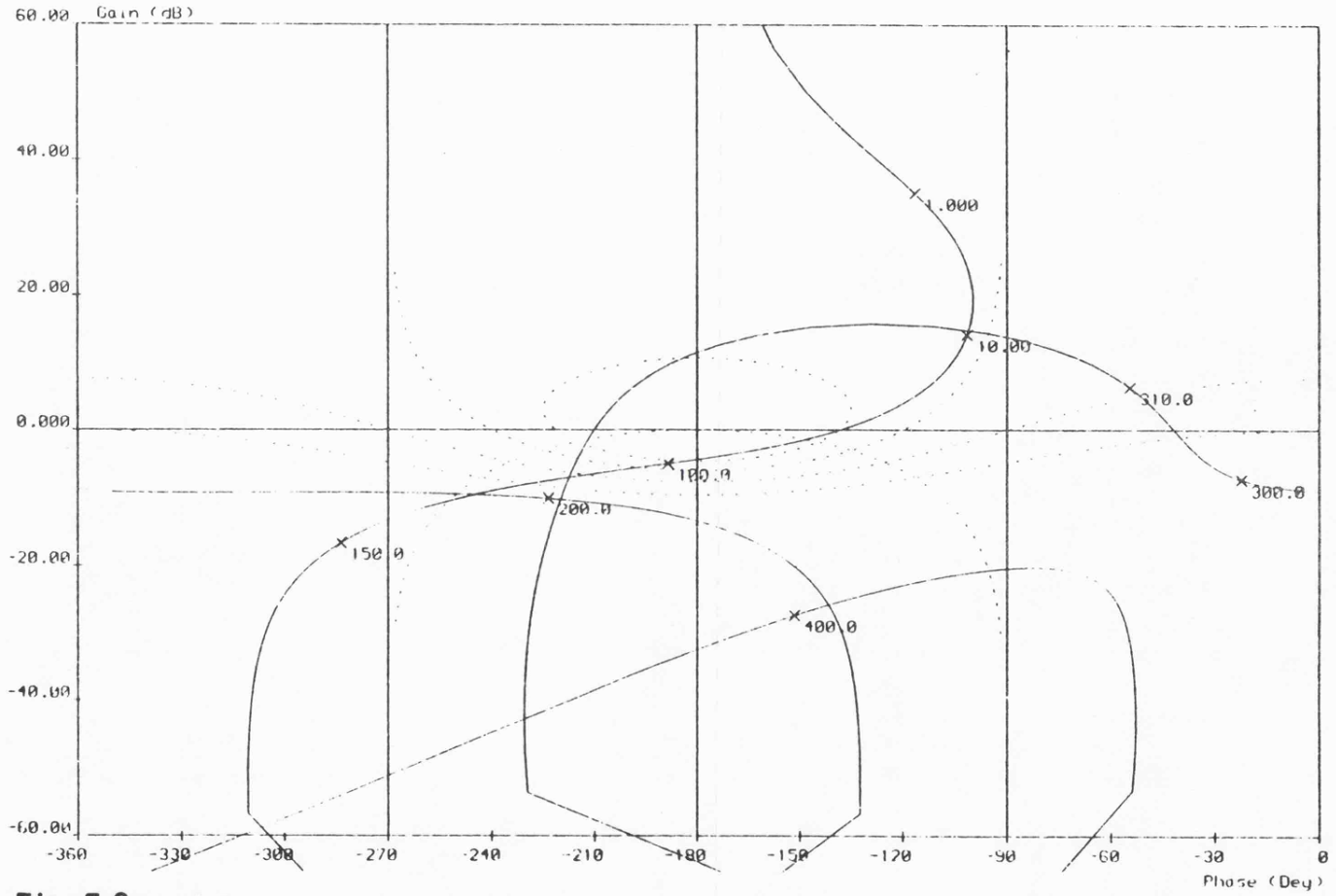

Fig. 5·8 – S.P.T. (OPEN) LOOP , DIGITAL INT & LEAD . Fs=2000Hz

allowing sufficient time for computation of the control algorithms. Figure 5.7 shows the open loop response of the digital control loop sampling at 10kHz. This can be compared directly with the open loop response of the analogue control loop which is shown in Figure 4.11. Apart from the difference at low frequencies which is due to the controller lead term breaking at 1.59Hz in the case of the digital controller these two plots have similar responses and nutation is well controlled. Figure 5.8 shows the effect of reducing sampling frequency to 2kHz while using the same control terms. Clearly in this instance the sampling has a significant effect and nutation has become unstable, as the response in the region of nutation results in positive feedback. Hence, if a longer sampling period is required different shaping terms are required.

The selection of word length effects the resolution and stability of the system. In the previous section the effects of quantisation and rounding errors with respect to limit cycling were discussed. In practice, limit cycling is not the only criterion which determines word length. In general, the requirement to control the wheel position to within fixed limits determines the resolution of the analogue to digital converter, ie. to control the wheel null to within 6 arc seconds with a 2 deg range requires a 12 bit word length. However, to a certain extent this can be traded against sample time as the noise within the system will time average due to

the loop containing two integrators. If necessary this relationship can be determined using a similar analysis to that used in the previous section. Witting (1974) has shown that the word length required to maintain stability is proportional to the inverse of the sampling time and the order of the digital section which is to be implemented. He arrives at this conclusion by considering the effects of perturbing the coefficients of the controller polynomials. The working word length within the processor is also important. In this particular design all the coefficients are less than unity so that there is no arithmetic overflow in the multiplications. However, the controller is configured as an integrator and accumulation of the loop error signal occurs. To estimate the worst case working computer word length, the closed loop bandwidth of rate system is considered simply as a time delay, then with the maximum error input to the computer, the overflow is given by:

$$\text{Overflow} = \frac{\text{Sampling frequency (fs)}}{\text{Bandwidth of the system (BW)}}$$

ie. for 10kHz sampling fequency and a closed loop bandwidth of 80Hz a maximum overflow of 128, or seven bits, is required.

For the system described in this chapter a sampling frequency of 10kHz with an analogue to digital converter range of 12 bits and a computer word length of 32 bits was chosen. (Note

Figure 5,9 Digital Control Loop

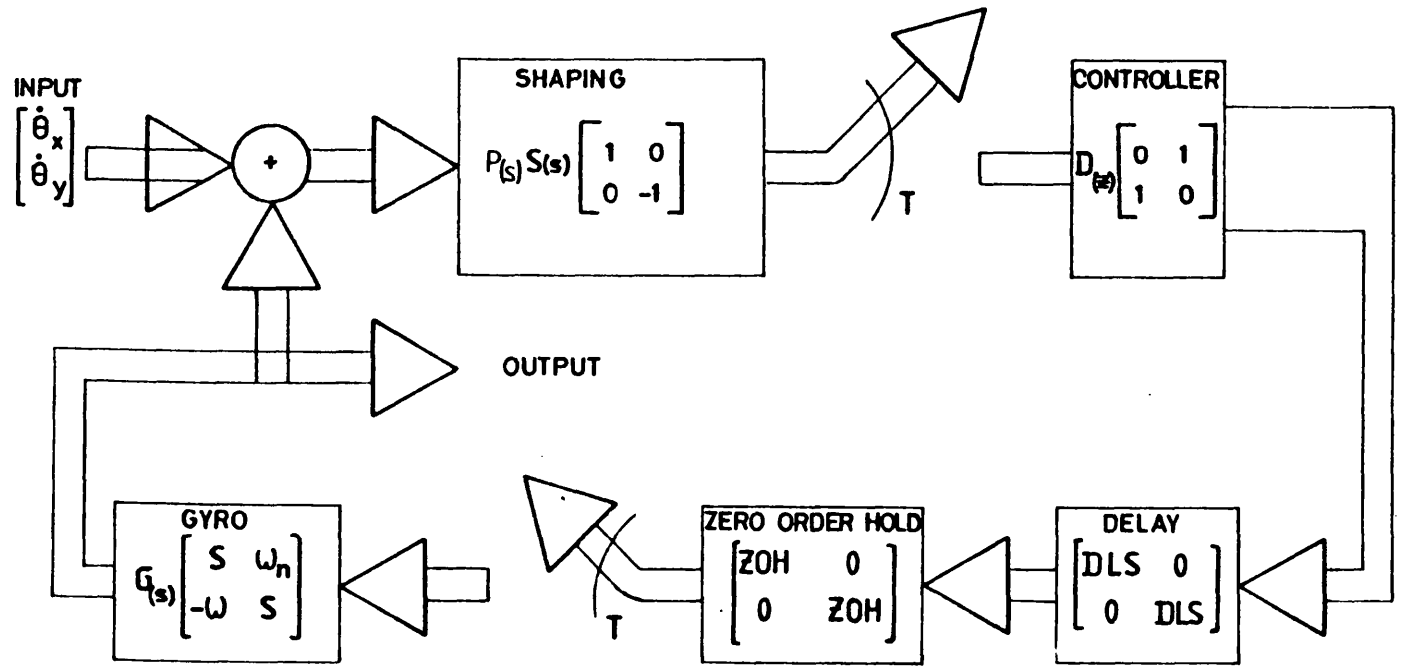

$\omega_n = 311 \times 2\pi$
$K = 4{\cdot}46$
$\alpha = 1{\cdot}00097$
$Kg = 70$
$\zeta = 0{\cdot}001$
$\omega_1 = 2\pi \times$
$\omega_2 = 2\pi \times 160$
$\omega_3 = 2\pi \times 320$
$\omega_4 = 2\pi \times 570$
$\omega_5 = 2\pi \times 2000$

$\zeta_1 = 0{\cdot}5$
$\zeta_2 = 0{\cdot}2$
$\zeta_3 = 0{\cdot}2$

$$N_{(s)} = \frac{s^2}{\omega_n^2} + \frac{2\zeta s}{\omega_n} + 1 \qquad P_{(s)} = \frac{1}{\frac{s}{\omega_5} + 1}$$

$$D(Z) = \frac{K(Z\alpha - 1)}{Z - 1}$$

$$G(S) = \frac{Kg}{\omega_n N_{(s)} S}$$

$$S_{(s)} = \frac{1}{\frac{s^2}{\omega_1^2} + \frac{2\zeta_1 s}{\omega_1} + 1} \cdot \frac{s^2 + \omega_2^2}{s^2 + 2\zeta_2\omega_2 s + \omega_2^2} \cdot \frac{s^2 + \omega_3^2}{s^2 + 2\zeta_3\omega_3 s + \omega_3^2} \cdot \frac{1}{\frac{s}{\omega_4} + 1}$$

the computer word length was ultimately dictated by convenience of implementation on the processor used).

5.2.5 Digital Loop Configuration

Figure 5.9 shows the configuration used for both modelling and practical implementation of the control loop. The digital controller D(z) is placed in the loop after the analogue terms S(s). In this configuration, the analogue terms act as an anti-aliasing filter for the sampler. The loop also incorporates a sample and hold to model the digital to analogue converter and a delay to simulate computation time. In the model of the system the processing time has been examined by varying the delay. The results obtained agree with Puri (1979) in that delays of up to half the sampling time have no significant effect upon the response of the loop. The model actually computes the transform in the form:

$$T(s') = \prod_{1}^{n} (s \pm j_n \omega_s)$$

Where s = Laplacian operator

and ω_s = the sampling frequency

The number of passes through the loop n is set within the program. For all the models used in this chapter, n is set to 3. A listing of the model used is given in Appendix 3. The modelled open loop response of the digital rebalance loop is given in Figure 5.7 and the modelled closed loop response is given in Figure 5.10.

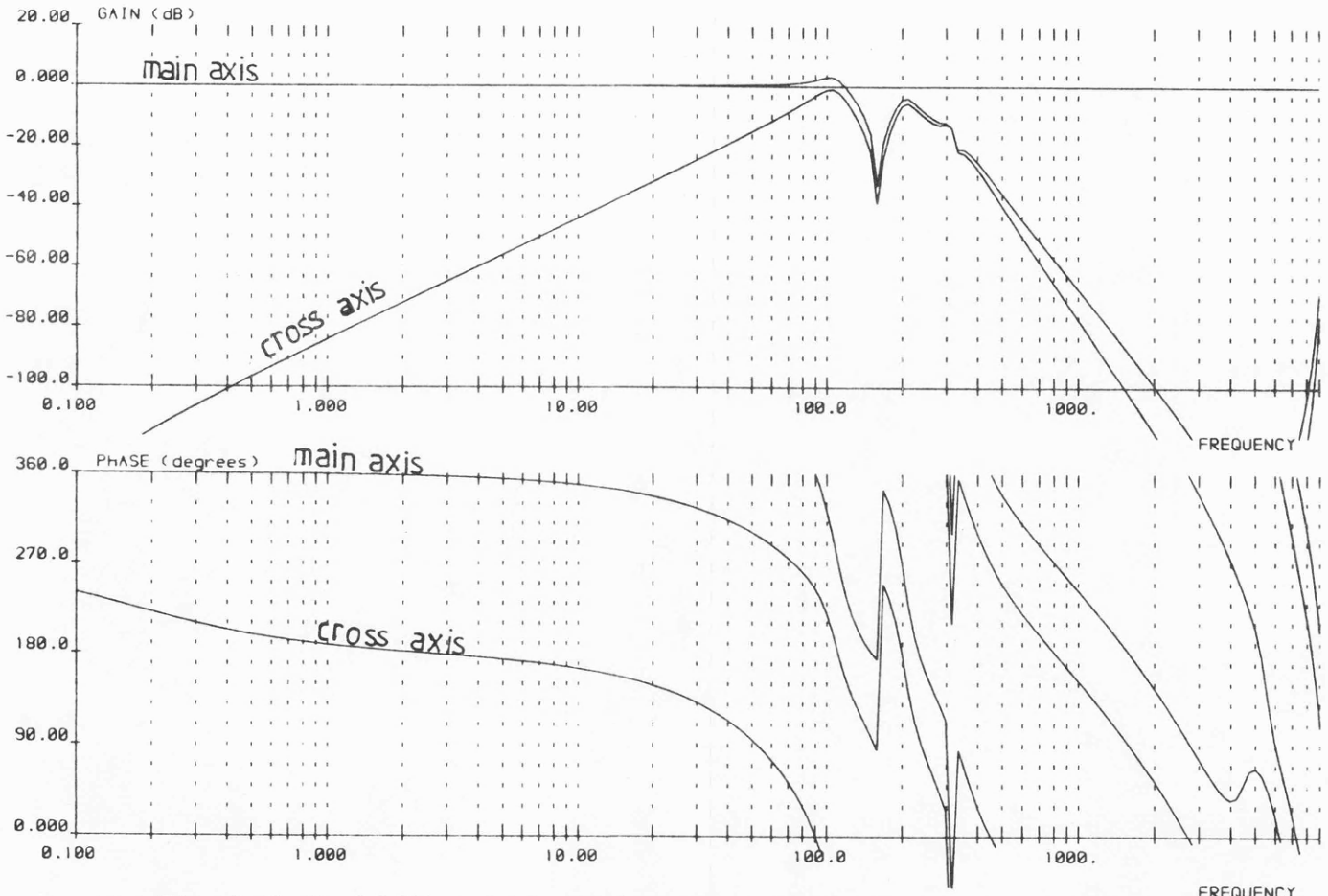

Fig. 5.10—CLOSED LOOP FREQUENCY RESPONSE Fs=10000Hz

5.3 Implementation

The majority of the electronics used to implement the digital control loop is identical to that used for the analogue system. However, the basic controller is replaced by a digital section. The following paragraphs describe the electronics and the software which have been used to implement the digital controller.

5.3.1 The Digital Controller Electronics

The block diagram of Figure 5.11 shows the hardware modules which were used to implement the controller. The controller consists of four main blocks; the Analogue to Digital Converter (ADC), the output Digital to Analogue Converter (DAC), the control logic and the processor. The processor used was the Z8002 operating at a clock frequency of 6MHz. The software was developed and run using a Tektronix 8540 development system and emulator. The circuit diagram for the ADC is shown in Figure 5.12. The converter is based upon AD578. This is a proprietary 12 bit device providing a two's complement output format. Incorporated around this device is an analogue multiplexer (AD7592) to select the input channel, a sample and hold (AD346) to hold the input over the conversion period of 10 μs and a twelve bit latch to interface the ADC to the processor. The input of the converter is scaled for a range of +/-10V.

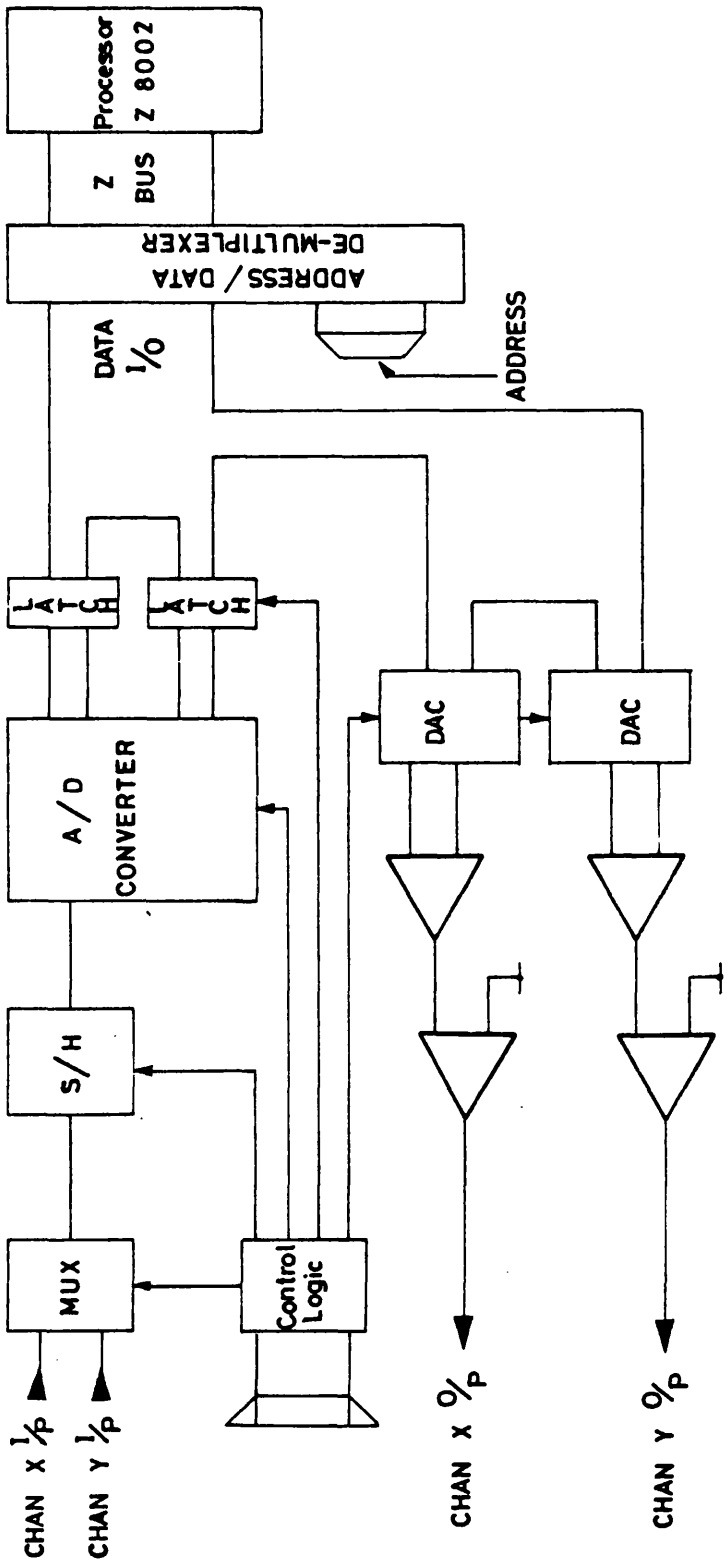

Fig. 5·11 – HARDWARE USED TO IMPLEMENT THE DIGITAL CONTROLLER

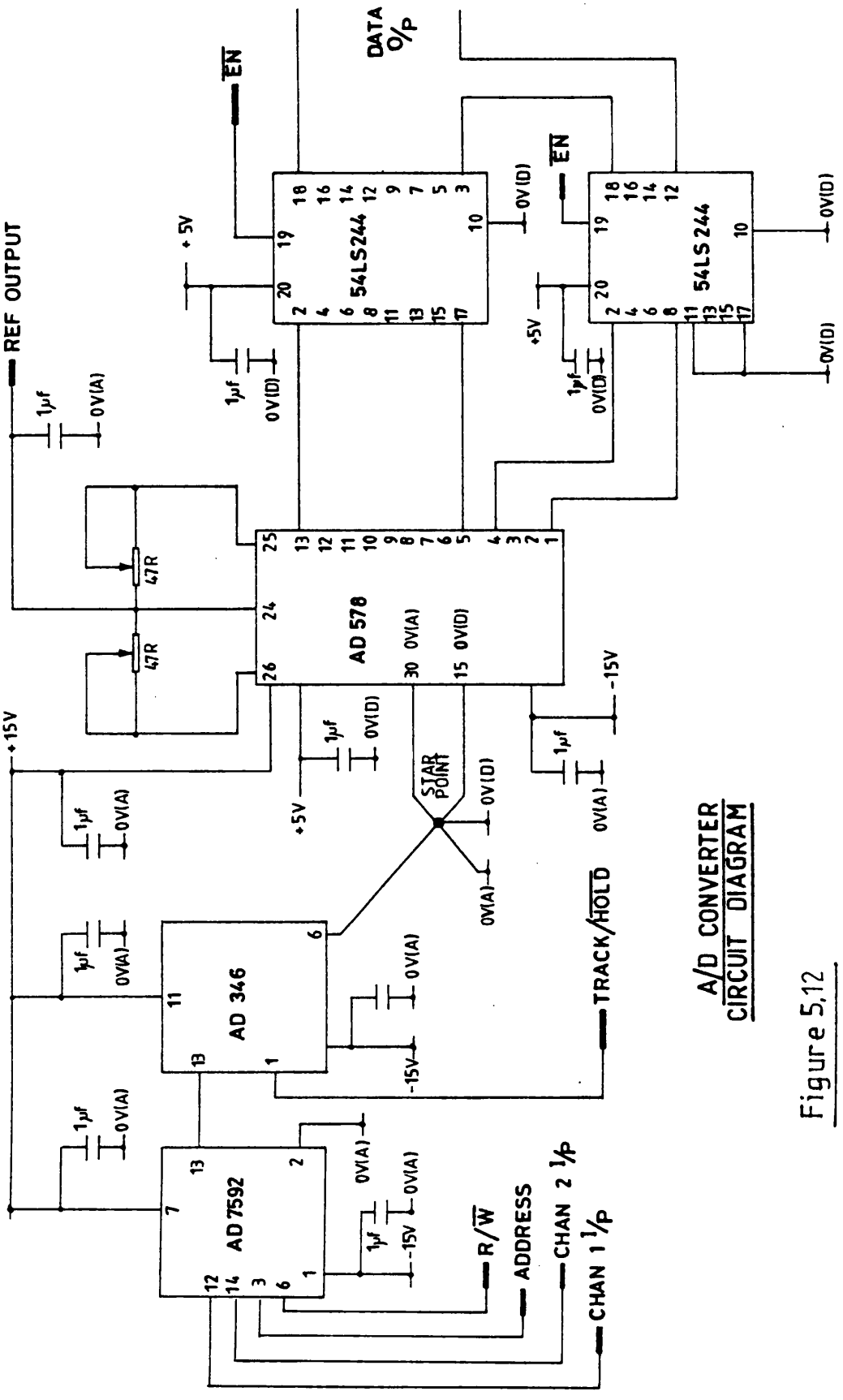

A/D CONVERTER
CIRCUIT DIAGRAM

Figure 5.12

Figure 5.13

Digital to Analogue Converter

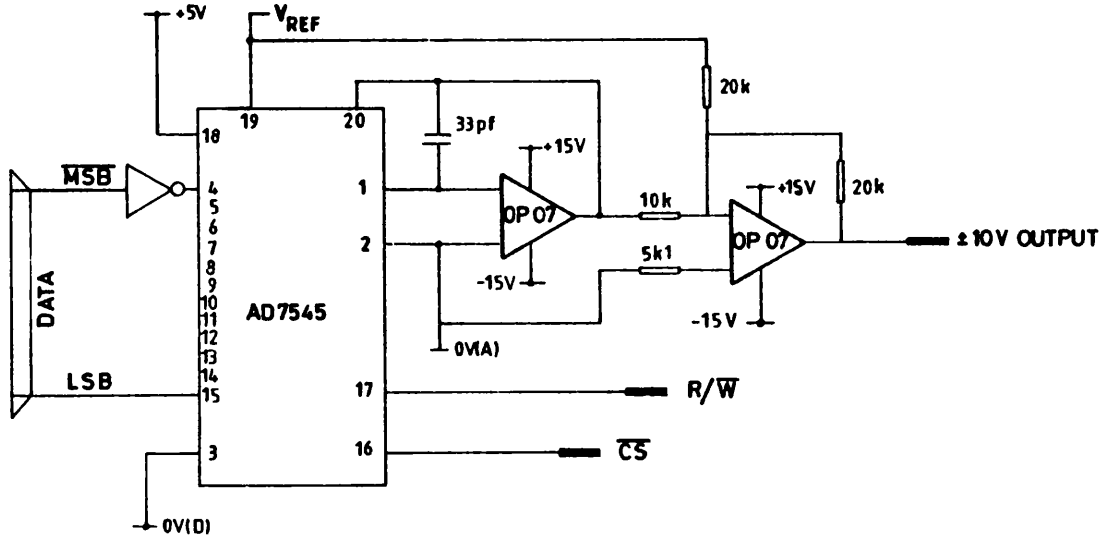

The circuit diagram for the DAC is shown in Figure 5.13. This circuit is based upon the AD7545, this is a proprietary 12 bit device, which can be interfaced directly with the processor. The circuit is configured to accept a 12 bit two's complement format. The output range is scaled to have a bipolar range of +/-10V.

Figure 5.14

Control Logic

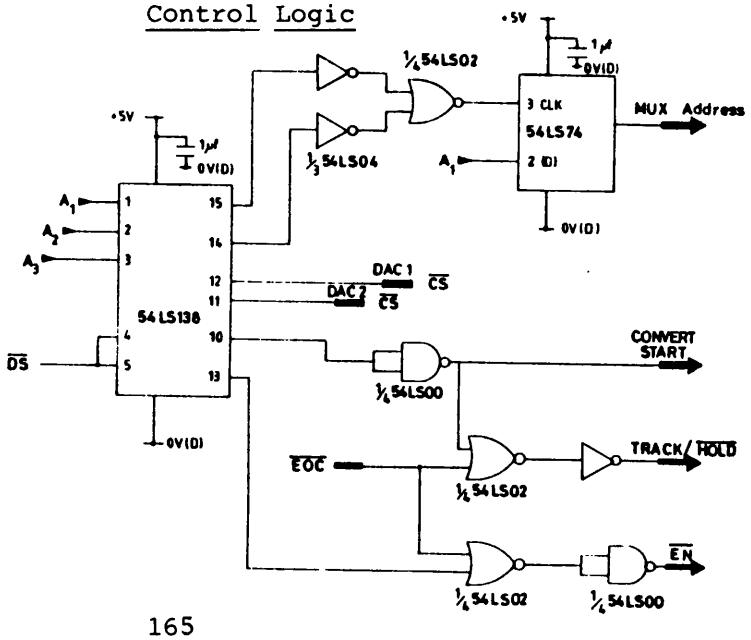

The control logic which is shown in Figure 5.14 is used to decode the unique addresses to select the hardware functions. A memory map for the control logic is shown in Table 5.2.

Table 5.2

Location in Hexadecimal	Function
9000	Select channel Y)
	) "Dummy write"
9002	Select channel X)
9004	Read ADC data
9006	Write to DAC1 (X)
9008	Write to DAC2 (Y)
900A	Start convert "Dummy write"

5.3.2 The Controller Software

The transfer function of the controller is given by Equation 5.2, this can be rearranged to give the active element as:

$$D(Z) = SG \frac{(1 - \frac{1}{\alpha} Z^{-1})}{1 - Z^{-1}} \qquad 5.10$$

This equation is implemented using the canonical form shown in Figure 5.15.

Figure 5.15

The Canonical Form of the Controller Terms

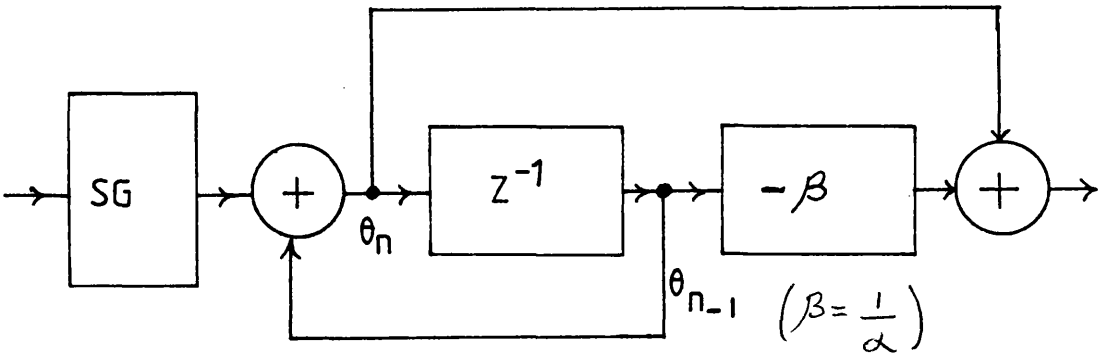

Arranging the filter in the canonical in this particular case ensures that all the coefficients of the controller are <1. The sample time is controlled by the controller program, a wait operation has been added after the control computations to set the sampling time. The control computations have been performed serially. This introduces time skewing of the controllers for each axis, but ensures that the computation delay is a minimum for each controller. A Z8002 assembly code listing of the program used is given in Table 5.3. The structure of the program is roughly the same as the carnonical form which is shown in Figure 5.15. The first part of the program clears the working registers. The main program loop begins at the label 'START'. The first program block selects the 'X' channel of the multiplexer and initiates the ADC to start conversion. While the ADC conversion process is taking place (approximately 10 micro sec) the program calculates the value of $\theta_{n-1} \times \beta$

Table 5,3

```
         asmid z8002
        global start
        clr r0
        clr r1
        clr r2
        clr r3
        clr r4
        clr r5
        clr r6
        clr r7
        clr r8
        clr r9
        clr r10
        clr r11
        clr r12
        clr r13
start   ld 9002h, £00h              ; select 'X' channel
        ld 900ah, £00h              ; start convert
        ldl rr6,rr4                 ; calculate theta(n-1)*beta
        ldl rr10,rr4                ; --------  ditto  --------
        sral rr10, £0ah             ; --------  ditto  --------
        subl rr6,rr10               ; --------  ditto  --------
        ld r1 ,9004h                ; read a/d data
         sra r1, £02h               ; adjust a/d data
        exts rr0                    ; extend input to 32 bits
        ldl rr2,rr4                 ; calculate theta(n)
        addl rr2,rr0                ; calculate theta(n)
        ldl rr4,rr2                 ; copy theta(n-1)
        ldl rr8,rr2                 ; calculate output
        subl rr8,rr6                ; calculate output
        slal rr8,£04h               ; shift for output
        ld 9006h,r9                 ; output to dac1
                                    ; START Y LOOP
        ld 9000h, £00h              ; select 'Y' channel
        ld 900ah, £00h              ; start convert
        ldl rr6,rr12                ; calculate theta(n-1)*beta
        ldl rr10,rr12               ; --------  ditto  --------
        sral rr10, £0ah             ; --------  ditto  --------
        subl rr6,rr10               ; --------  ditto  --------
        ld r1 ,9004h                ; read a/d data
        sra r1, £02h                ; adjust a/d data
        exts rr0                    ; extend input to 32 bits
        ldl rr2,rr12                ; calculate theta(n)
        addl rr2,rr0                ; calculate theta(n)
        ldl rr12,rr2                ; copy theta(n-1)
        ldl rr8,rr2                 ; calculate output
        subl rr8,rr6                ; calculate output
        slal rr8,£04h               ; shift for output
        ld 9008h,r9                 ; output to dac2
        ldb rl0, £12h               ; load wait count
wait1   dbjnz rl0, wait1            ; approx 32 usec wait
        jr start                    ; jump to start
        end start
```

The multiplication of the term - (0.999) is achieved by subtracting the stored value from itself right shifted 10 binary places. The next program block reads the converted value from the ADC and extends it to a 32 bit two's complement number. The next block of program calculates and stores it for the next sample period. The output is then calculated and the gain adjusted by a series of shifts. On completion of this operation the output is sent to the 'X' channel DAC. The process is then repeated for the 'Y' channel. On completion of this a wait period is introduced to adjust the sample time before the program is looped back to 'START'. The processing delay of each channel is approximately 35 micro secs.

REFERENCES USED IN CHAPTER V

Bertram, J.E. (1958). The Effect of Quantisation in Sampled Feedback Systems. Trans AIEE 77, pt 2, 177-182, 1958.

Coffman, D.E. (1974). Feasibility Study of a Digital Rebalance Loop for a Dry Tuned Gyroscope (NASA-CR-144089), University of Tennesse.

Franklin, G.F., Powell, J.D. (1980). Digital Control of Dynamic Systems. Addison-Wesley Publishing Company, Massachusetts, 1980.

Geen, J.A., Johnson, B. (1985). Analog to Digital Conversion. European Patent No. 85304837.9.

Gleb, A., Van der Velde, W.E. (1968). Multiple Input Describing Functions and Non-linear Systems, McGraw Hill, New York, 1968.

Johnson, B., Smith C.F. (1984). Final Report Contract A85c/2244 for Pulse Torquing the Microflex Type 507 Gyro, British Aerospace (for RAE Farnborough), TR3018, December 1984.

Napjus, G.A. (1975). Recent Advances in Strapdown Inertial Navigation, 1975, IEEE INTERCON.

Puri, S.N. (1979). Direct Digital Control of Inertial Guidance Sensors. Ph.D. Thesis, University of Aston in Birmingham, August 1979.

Schmidt, G.T. (1975). Strapdown Inertial Systems - Theory and Applications, Introduction and Overview. From AGARD-LS-95, the Advisory Group for Aerospace Research and Development. North Atlantic Treaty Organisation (1978).

Slaughter, J. (1964). Quantisation Errors in Digital Control Systems. IEEE Trans Aut Control AC-9, pg 70-74, 1964.

Witting, P.A. (1974). Finite Word Length Effects on Digital Processes. Electron, November 1974, pages 49-51.

CHAPTER VI

RESULTS AND DISCUSSION

6.1 Introduction

This chapter presents and discusses the results of a set of tests which examine the effectiveness of the three control systems which have been described in this thesis. The scope of the tests is limited to determining that the desired frequency response has been obtained, that the output has a useable working range and that the bias of the system is stable. Parameters of the design which are features of the gyroscope alone, eg. G sensitivity, magnetic sensitivity, etc. will be stated as typical figures for completeness where available. The test methods and detailed results used to obtain these parameters are beyond the constraints of the work described in this thesis.

6.2 Test Method

6.2.1 Open Loop Transfer Function

In practice, because the control loop contains two integrators, it is difficult to measure the open loop response by simply removing the feedback and measuring the response of the cascaded terms. To measure the response in this way it would be necessary to add a bias to the loop to exactly cancel the gyroscopes drift and any offsets in the controller circuits in order to prevent the system from drifting into saturation. To overcome the problem of the integrators drifting in to saturation, the technique used to obtain the

open loop transfer function operates with the control loop closed. Hence the drift is controlled by the system. The arrangement used to measure the open loop transfer function is shown in Figure 6.1. Basically a non-inverting unity gain summing junction is inserted in the loop. The summing junction is used to stimulate the rate loop allowing the transfer function from its output (the input to the loop) to the feedback return to be measured. The transfer function of the summing junction is not included in the measurement, hence a true open loop response is obtained. This method of obtaining the transfer function is also advantageous as it identifies and includes any interactions which may occur due to closing the control loop. In particular this method with the CPT gyroscope also includes the figure of eight loop. This would not be identified by measuring the open loop transfer function without the feedback being applied as only one demodulator would be included in the transfer function.

Figure 6.1

Method of Measuring the Open Loop Transfer Function

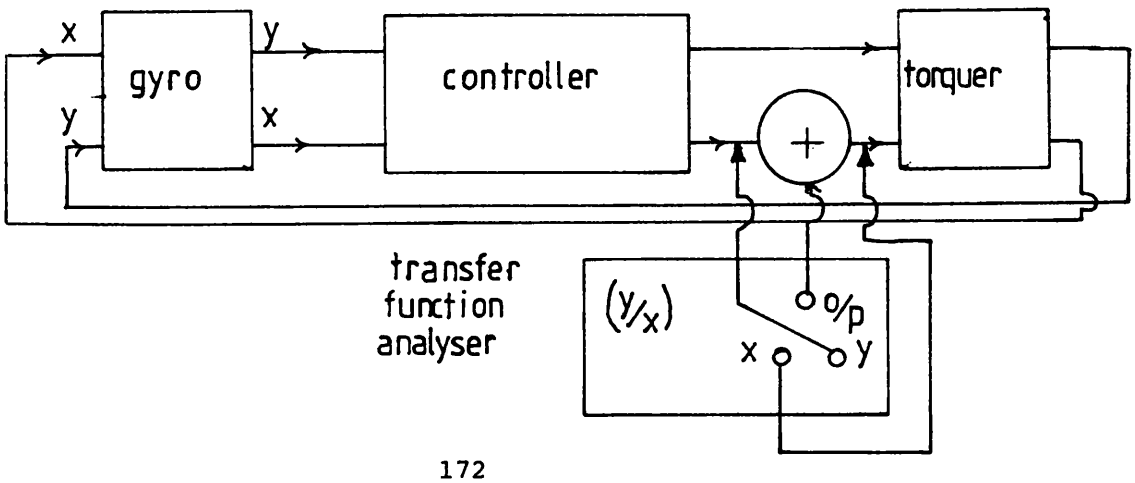

6.2.2 Closed Loop Transfer Function

The closed loop transfer function is measured using the arrangement shown in Figure 6.2.

Figure 6.2

Method Used to Measure the Closed Loop Transfer Function

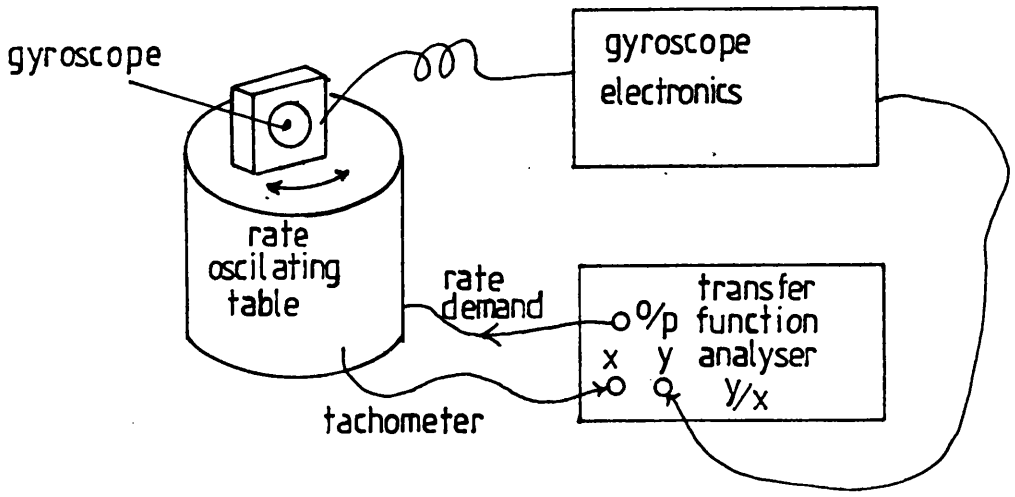

For these tests the gyroscope is mounted on a 'rate oscillating' table and oscillated about one of its sensitive axes. The frequency responses of the main axis and the cross axis are obtained by correlating the Tachometer output of the 'rate oscillating' table with the output from the gyroscopes control electronics, for a range of frequencies.

6.2.3 Torquer Scale Factor and Linearity Tests

These tests were performed using a computer controlled 'rate table'. The rate table was fitted with a diffraction grating. Using the output from the grating a very accurate measure of the average rates applied to gyroscope were obtained. The tests were performed by incrementing the applied rates in

steps of 10% of the maximum rate which was to be applied. These started with a -10% rate then increased in rate fully clockwise, followed by decrementing rate fully counter clockwise finishing at zero rate input. At each step the program allowed 5 seconds settling time followed by 10 seconds measurement time. During the measurement time the output of the control electronics was monitored and averaged using a digital voltmeter. The results obtained from these measurements were used to calculate, by the least squares method, the 'best fit' straight line of applied rate versus measured rate. The errors in the measured values from the value predicted by this relationship were then plotted.

6.2.4 Drift Measurements

These tests were performed by monitoring the output from the control electronics via a 3 seconds time constant filter. The output was monitored either using a computing digital voltmeter or a chart recorder.

6.3 CPT Gyroscope Results

Throughout this thesis actual results have been presented to clarify and justify the design rules which have been used to develop the controllers. Figure 2.10 shows the noise spectra of the CPT gyroscope. This was measured 'closed loop' at the output of preamplifier. The spectrum's main feature is the recurrence of the harmonics of the wheels rotational frequency (200Hz). The origin of these noise components is fully

discussed in Chapter II, and the spectrum shown in Figure 2.10 emphasises the need for a band stop filter to reject the fundamental harmonic component of wheel rotation frequency.

Figure 3.6 shows the frequency response of the gyroscope. This response was obtained using a similar technique to that described in Paragraph 6.2.2. This response was used to justify the use of the simplified gyroscope model in the computer simulation of the control loop. An interesting feature of the cross axis plot is the small resonance between 7 and 10Hz. This resonance was predicted from the detailed gyroscope model, and results from the residual stiffness of the gyroscopes pivot. This effect is described in Chapter III, Paragraph 3.2.

Figure 4.8 shows the comparison between the modelled open loop response and the actual measured open loop response. At low frequencies the model gives a good prediction of the response. The model does not include the 'figure of eight loop' and hence the agreement is not exact in the region 200 to 300Hz. However, provided that the stability requirements of the 'figure of eight' loop are satisfied, then the model gives a reasonable indication of the loop response. The modelled response also departs from the real measurements in the region of nutation, this is because the exact nutation frequency cannot be determined by calculation, and varies from gyroscope to gyroscope. The model in this region is still sufficiently good to determine the phase and stability of nutation. In

general the actual 'response' obtained agrees well with the anticipated response and major differences can be understood using the explanations described in Chapters III and IV.

Figure 4.14 presents the modelled and practical measurement of the following error for sinusoidal angular rate inputs. The theory agrees well with the practical situation, the major differences are within the limits set by the experimental method used to determine when the stop limits were exceeded.

The measured closed loop transfer function of the combined pickoff and torquer gyroscope is shown in Figure 6.3. If this is compared with the modelled response of Figure 4.9, it can be seen that the main axis gain and phase response, after normalisation (the measured response includes the gain of the rate table tachometer) agrees well with the modelled response up to 300Hz. At low frequencies the cross axis measured response levels at about -35db below the main axis. This is caused by the misalignment of the rate table axis to the gyroscope axis. This error corresponds to a misalignment of approximately 1.7 deg. At frequency near the bandwidth point the separation of the measured response is greater than that predicted by the model. This separation is determined by the nutation parameters. The values of the nutation parameters used in the modelled response do not match exactly the values encountered in practice. Also, due to the simplicity of the model used, the modelled response gives a pessimistic estimate

of the cross coupling. However, the model used to design the control loop is adequate to ensure that the design criterion of a minimum bandwidth of 50Hz is achieved and that the feedback does not excite nutation. The response shown in Figure 6.3 confirms that this is the case. From Figure 6.3 it can be seen that a -90 degree point bandwidth of 52Hz has been obtained and that the ripple within the passband of the system is less than 3db.

Tables 6.1, 6,2 and 6.3 and Figures 6.4, 6.5 and 6.6 show the results of the torquer scale factor and linearity test when the gyroscope and its electronics were subjected to temperatures of 23 deg C, -37 deg C and 65 deg C respectively. These tests were performed using the technique described in Paragraph 6.2.3. The principal feature of the error plot shown in Figures 6.4, 6.5 and 6.6 is the 'butterfly' nature of the curves. This is caused by the joule heating of the gyroscopes torquer coils. The 'butterfly' plots result from the thermal lag between the power being applied and temperature change of the gyroscopes torquer magnets. Hence the actual scale factor for applied rates varies with time, due to the effects of the thermal lag. Hence for a fixed time test which linearly increases and decreases the applied rate different scale factor profiles are seen which result in the 'butterfly' curve. The dynamic heating affects both bias and scale factor, but at high angular rates the effects caused by the scale factor changes are much greater than the bias change.

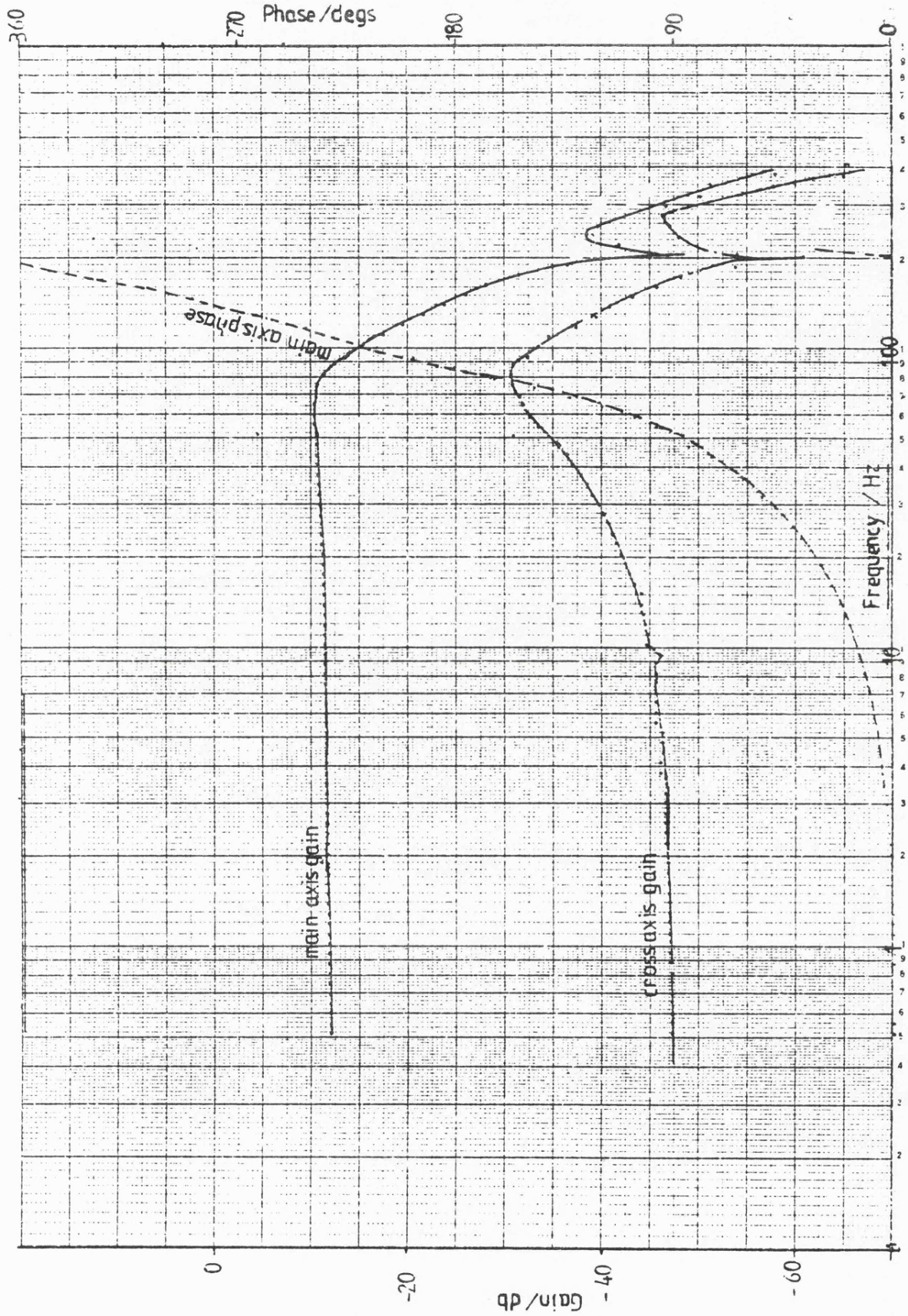

Fig. 6-3 - C P T Gyroscope Closed Loop Response

TABLE 6.1

RATE TRANSFER TEST M505-020 ANALYSIS

GYRO TYPE:-G/FLEX 505 SERIAL NUMBER:-E105 TEST NUMBER:-020 DATE OF TEST:-19/5/82
INPUT AXIS:-Y-UP OUTPUT AXIS:-Y ENGINEER:-DJ/RJC TIME OF TEST:-09HRS 50MINS 19SEC

INITIAL TEMP:- 22 MID TEMP:- 23.2 FINAL TEMP:- 24.4

RATE INPUT (DEG/SEC)	SENSOR OUTPUT (VOLTS)	ERROR (DEG/SEC)	ERROR %	
-.0048	.00002	.01780		*
-39.9859	-.03970	-.06405	-.32038	*
-59.9699	-.07959	-.13780	-.34458	*
-99.9734	-.11910	-.20383	-.33987	*
-79.9576	-.15880	-.26710	-.33905	*
-99.1922	-.19896	-.30697	-.30654	*
-119.1203	-.23877	-.32193	-.26799	*
-139.1136	-.27867	-.29193	-.20836	*
-159.0962	-.31863	-.22312	-.13937	*
-179.0719	-.35871	-.09222	-.05121	*
-200.0773	-.39901	.11634	.05815	*
-180.0712	-.35958	.34494	.19156	*
-160.0977	-.31979	.33431	.22151	*
-140.1154	-.27977	.26061	.18600	*
-120.1322	-.23972	.14926	.12424	*
-100.1471	-.19968	.04833	.04826	*
-79.9579	-.15929	-.02309	-.02887	*
-59.9752	-.11939	-.05668	-.09451	*
-39.9899	-.07955	-.05788	-.14474	*
-20.0045	-.03976	-.03610	-.18047	*
-.0048	.00003	.01269		*
-19.9645	.03970	.07303	-.36578	*
-39.9446	.07959	.13882	-.34754	*
-59.9264	.11969	.20323	-.33917	*
-79.9075	.15880	.26106	-.32673	*
-99.7895	.19836	.30005	-.30068	*
-119.7682	.23817	.30509	-.25674	*
-139.7477	.27805	.27933	-.19985	*
-159.7234	.31801	.20863	-.13062	*
-179.6917	.35809	.07084	-.03942	*
-199.6903	.39839	-.15034	.07529	*
-179.6918	.35896	-.06753	.20453	*
-159.7237	.31915	-.36448	.22819	*
-139.7462	.27914	-.27000	.19320	*
-119.7677	.23906	-.14089	.11764	*
-99.7877	.19904	-.04139	.04147	*
-79.994	.15926	.03151	-.03944	*
-59.9266	.11935	.07595	-.12670	*
-39.9457	.07951	.07992	-.20008	*
-19.9669	.03972	.06193	-.31018	*
-.0047	.00001	.02347		*

ANALYSIS

MEAN TEMP:- 23.2 DEGS

SCALE FACTOR:- -1.99333 mV/DEG/SEC
NON-LINEARITY,MAX:- -.36753 DEG/SEC
OCCURING AT:- -179.6918 DEG/SEC
EQUIVALENT TO:- .18376% OF MAXIMUM RATE
STD. DEVIATION:- .20261 DEG/SEC

ZERO CROSSING:- -.02264 DEG/SEC
ZERO OFFSET:- -.00587 DEG/SEC
ZERO HYSTERESIS:- .00002 DEG/SEC

RATE I/P (DEG/SEC)	HYSTERESIS (DEG/SEC)
20	-.02699
40	-.07992
60	-.14595
80	-.24432
100	-.36020
120	-.47509
140	-.55335
160	-.57893
180	-.43646
200	
-20	-.01319
-40	-.06000
-60	-.12753
-80	-.22876
-100	-.33963
-120	-.44549
-140	-.54783
-160	-.57341
-180	-.43846
-200	

RATE TRANSFER TEST A505-021 ANALYSIS

GYRO TYPE:-M/FELX SERIAL NUMBER:-E105 TEST NUMBER:-021 DATE OF TEST:-19/5/87
INPUT AXIS:-Y-UP OUTPUT AXIS:-Y ENGINEER:-BJ TIME OF TEST:-16HRS 56MINS 23SEC

INITIAL TEMP:--38.5 MID TEMP:--37.2 FINAL TEMP:--35.9

ERROR LIST

RATE INPUT (DEG/SEC)	SENSOR OUTPUT (VOLTS)	ERROR (DEG/SEC)	ERROR %	
-.0049	.00002	.01862		*
20.0090	-.03870	-.03976	-.19872	*
39.9963	-.07736	-.09906	-.24766	*
59.9839	-.11605	-.14774	-.24630	*
79.9721	-.15474	-.19113	-.23903	*
100.1607	-.19385	-.22214	-.22178	*
120.1508	-.23263	-.22674	-.18871	*
140.14	-.27143	-.22014	-.15709	*
160.1278	-.31030	-.17245	-.10770	*
180.1063	-.34923	-.08299	-.04608	*
200.1145	-.38833	.06130	.03063	*
180.1066	-.34984	.22699	.12603	*
160.1317	-.31113	.25296	.15799	*
140.1439	-.27225	.19963	.14244	*
120.1563	-.23332	.12494	.10398	*
100.1675	-.19443	.06588	.06577	*
79.9738	-.15515	.01638	.02048	*
59.9865	-.11632	-.01268	-.02113	*
39.9987	-.07752	-.01997	-.04992	*
20.01	-.03875	-.01470	-.07347	*
-.0048	.00003	.01588		*
-19.971	.03870	.05066	-.25369	*
-39.9539	.07740	.09032	-.22606	*
-59.9401	.11609	.13047	-.21767	*
-79.9211	.15479	.16855	-.21089	*
-99.8212	.19333	.20015	-.20051	*
-119.8084	.23209	.20765	-.17332	*
-139.7877	.27088	.19824	-.14181	*
-159.7656	.30975	.14643	-.09165	*
-179.7387	.34867	.05765	-.03207	*
-199.7393	.38774	-.08084	.04047	*
-179.7372	.34924	-.23918	.13307	*
-159.7656	.31052	-.25312	.15843	*
-139.7841	.27163	-.20274	.14504	*
-119.8019	.23272	-.11678	.09765	*
-99.8189	.19382	-.05109	.05118	*
-79.9295	.15510	.00642	-.00804	*
-59.9397	.11627	.03812	-.06360	*
-39.9553	.07748	.04896	-.12253	*
-19.9725	.03871	.04660	-.23331	*
-.0049	.00002	.02071		*

ANALYSIS

MEAN TEMP:- -37.2 DEGc

SCALE FACTOR:-	-1.94021 MV/DEG/SEC
NON-LINEARITY,MAX:-	-.25312 DEG/SEC
OCCURRING AT:-	-139.7656 DEG/SEC
EQUIVALENT TO:-	.12656% OF MAXIMUM RATE
STD. DEVIATION:-	.14240 DEG/SEC
ZERO CROSSING:-	-.02501 DEG/SEC
ZERO OFFSET:-	-.00724 DEG/SEC
ZERO HYSTERESIS:-	.00001 DEG/SEC

RATE I/P (DEG/SEC)	HYSTERESIS (DEG/SEC)
20	-.02546
40	-.05149
60	-.13767
80	-.20926
100	-.29481
120	-.35718
140	-.42367
160	-.42934
180	-.31028
200	
-20	-.00557
-40	-.04077
-60	-.09195
-80	-.16132
-100	-.24694
-120	-.32213
-140	-.39738
-160	-.39635
-180	-.29533
-200	

TABLE 6.2

TABLE 6.3

RATE TRANSFER TEST M505-022 ANALYSIS

GYRO TYPE:-M/FLEX505 SERIAL NUMBER:-E105 TEST NUMBER:-022 DATE OF TEST:-19/5/84
INPUT AXIS:-Y-UP OUTPUT AXIS:-Y ENGINEER:-RJC TIME OF TEST:-14HRS 41MINS 25SECS

INITIAL TEMP:- 68.4 MID TEMP:- 65.9 FINAL TEMP:- 63.4

RATE INPUT (DEG/SEC)	SENSOR OUTPUT (VOLTS)	ERROR (DEG/SEC)	ERROR %	
-.0049	.00012	-.04974		*
18.0141	-.03690	-.10099	-.56062	*
36.0148	-.07288	-.15185	-.42163	*
54.0163	-.10937	-.20011	-.37047	*
72.0179	-.14587	-.23957	-.33265	*
90.018	-.18241	-.26526	-.29295	*
108.2113	-.21937	-.27103	-.25046	*
126.2298	-.25605	-.24177	-.19153	*
144.2463	-.29279	-.17407	-.12068	*
162.2711	-.32973	-.02518	-.01552	*
180.2792	-.3668	.20539	.11398	*
162.2861	-.33060	.38839	.23933	*
144.2907	-.29400	.37146	.25744	*
126.3152	-.25724	.26279	.20805	*
108.3196	-.22037	.11272	.10406	*
90.1149	-.18314	-.00097	-.00107	*
72.1047	-.14638	-.07740	-.10734	*
54.0961	-.10976	-.08805	-.16275	*
36.1725	-.07326	-.12287	-.33967	*
18.0947	-.03657	-.09612	-.53121	*
-.0049	.00011	-.04684		*
-18.0904	.03668	.01083	-.05999	*
-36.13	.07327	.08170	-.22612	*
-54.201	.10986	.14612	-.26959	*
-72.2746	.14647	.20867	-.28872	*
-90.3446	.18310	.25355	-.28064	*
-108.3194	.21957	.25339	-.23347	*
-126.3944	.25634	.26636	-.21076	*
-144.4673	.29319	.20591	-.14293	*
-162.5381	.33013	.10249	-.06306	*
-179.6627	.36638	-.10097	.05620	*
-161.7116	.32925	-.29346	.18147	*
-143.7332	.29268	-.27872	.19392	*
-125.7535	.25592	-.17032	.13544	*
-107.769	.21920	-.08344	.07743	*
-89.8909	.18269	.00158	-.00176	*
-71.9117	.14605	.05292	-.07359	*
-53.9307	.10946	.07294	-.13524	*
-35.9496	.07295	.05767	-.16041	*
-17.9656	.03647	.02400	-.13359	*
-.0048	.00008	-.03419		*

ANALYSIS

MEAN TEMP:- 65.9 DEGC

SCALE FACTOR:- -2.03233 mV/DEG/SEC
NON-LINEARITY,MAX:- .38839 DEG/SEC
OCCURING AT:- 162.2861 DEG/SEC
EQUIVALENT TO:- .21577% OF MAXIMUM RATE
STD. DEVIATION:- .18365 DEG/SEC

ZERO CROSSING:- -.00209 DEG/SEC
ZERO OFFSET:- -.04649 DEG/SEC
ZERO HYSTERESIS:- .00001 DEG/SEC

RATE I/P (DEG/SEC)	HYSTERESIS (DEG/SEC)
18	-.08547
36	-.16668
54	-.19387
72	-.24896
90	-.35919
108	-.49205
126	-.58996
144	-.59193
162	-.42857
180	
-19	-.10397
-37	-.13637
-55	-.19711
-73	-.20715
-91	-.20174
-109	-.16156
-127	-.20420
-145	-.24947
-163	-.43054
-180	

The results in Tables 6.1, 6.2 and 6.3 show that the typical scale factor non linearity is 0.215% of maximum rate. It can also be calculated from the results in Tables 6.1, 6.2 and 6.3 that the bias temperature coefficient (zero offset) is 1.8 deg/hr/deg C. As this is less than that specified for the gyroscope alone (4.5 deg/hr/deg C) it can be assumed that the electronics contribution to the bias temperature coefficient is less than 2.7 deg/hr/deg C. Unfortunately because of the effects of thermal lag these tests do not give sufficient information to calculate the scale factor temperature coefficient. However, from other tests it has been shown to be typically 400 ppm/degCwhich is what is expected from the torquer magnets temperature coefficient. The temperature coefficient of the sense resistor used to measure the scale factor has a temperature coefficient of less than 10ppm/deg C.

Figure 6.7 shows the typical drift result for a combined pickoff and torquer gyroscope. The plots start at the switch on of the gyroscope. After an initial warm up the output soon converges to about 2 deg/hr. The warm up period is highly dependant upon the thermal characteristics of the gyroscopes mounting block.

Figure 6.4

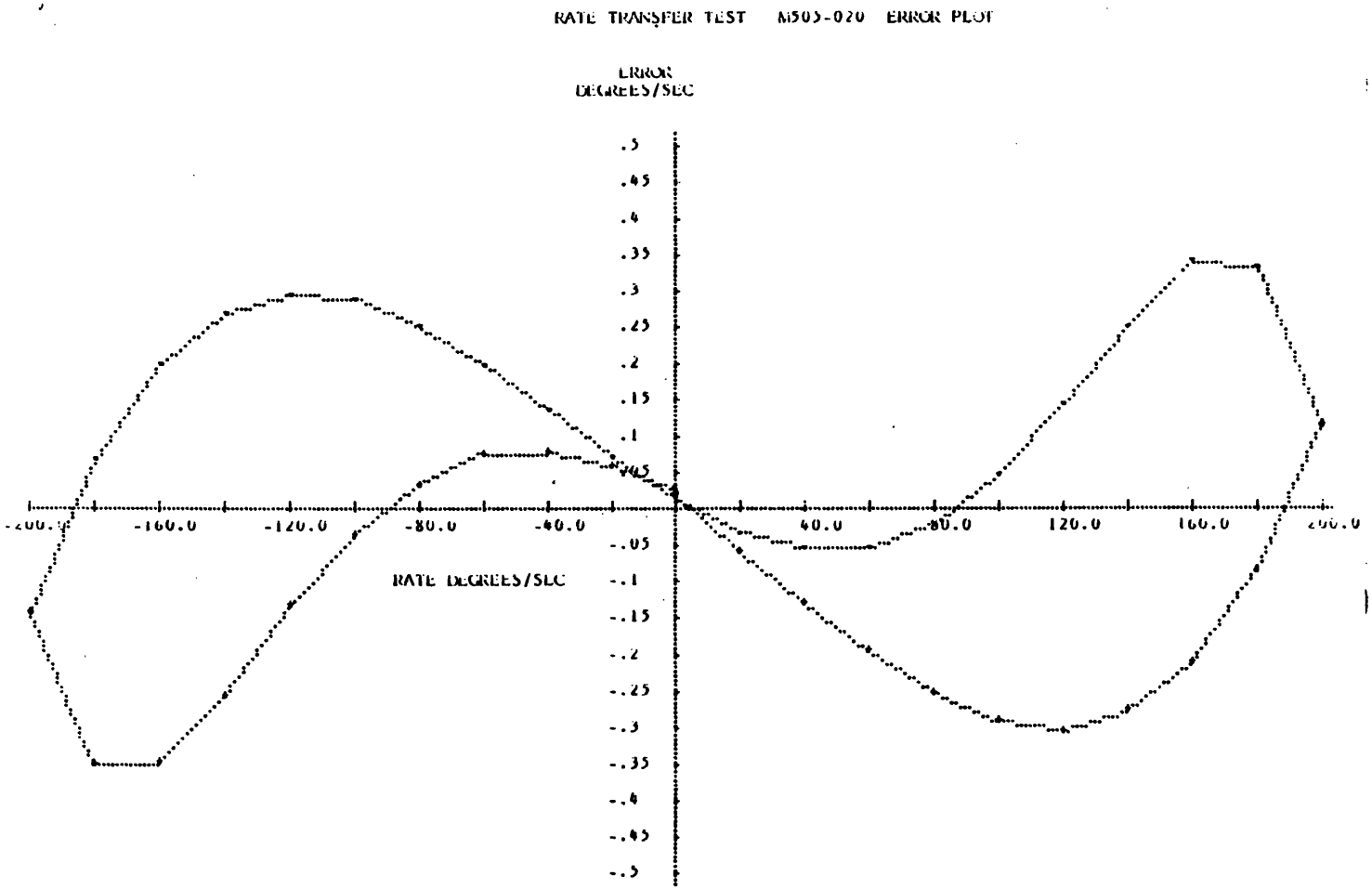
RATE TRANSFER TEST M503-020 ERROR PLOT
ERROR
DEGREES/SEC
.5
.45
.4
.35
.3
.25
.2
.15
.1
-160.0
-120.0
-80.0
-40.0
40.0
120.0
160.0
RATE DEGREES/SEC
-.05
-.1
-.15
-.2
-.25
-.3
-.35
-.4
-.45
-.5

Figure 6.5

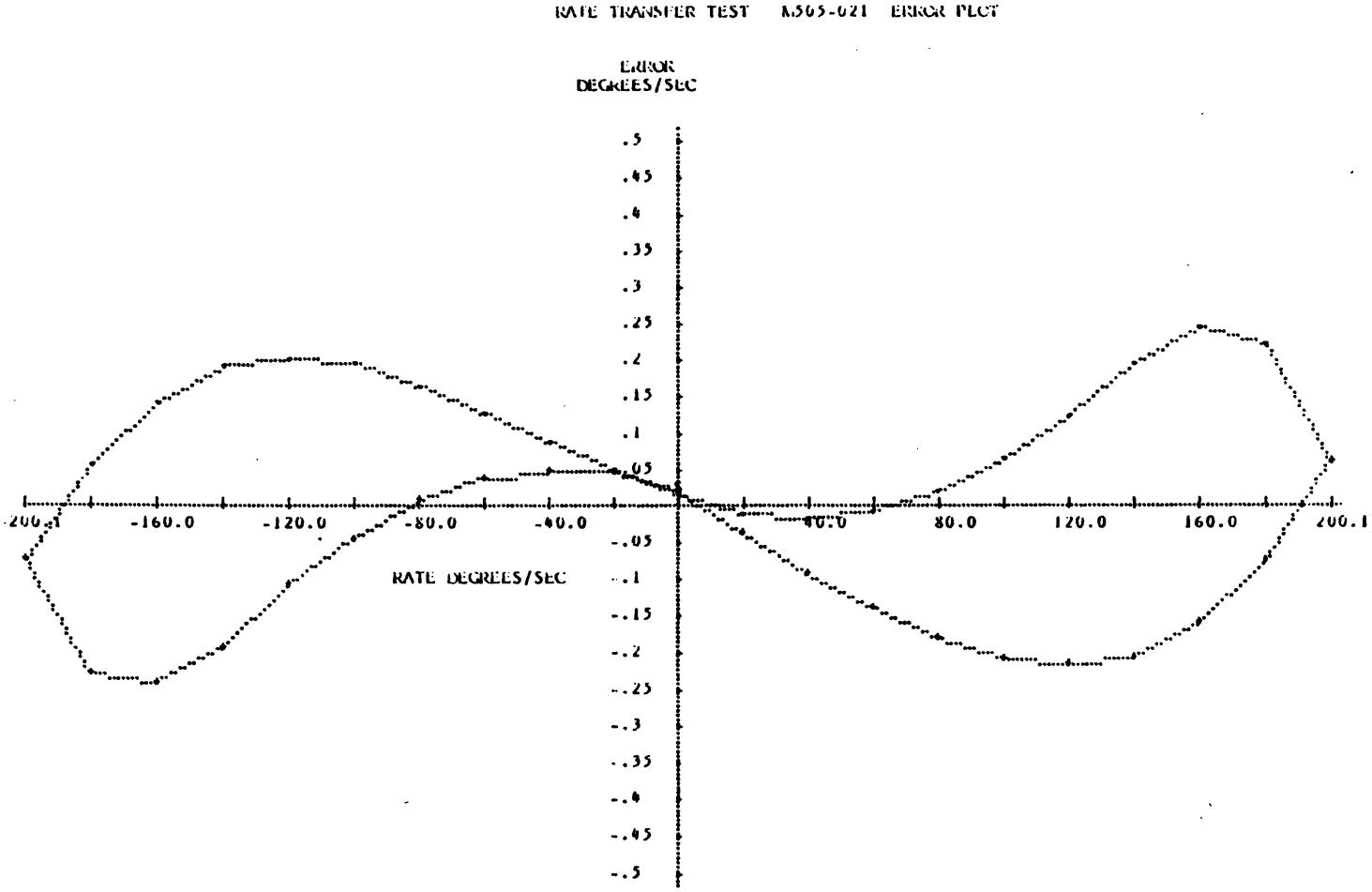
RATE TRANSFER TEST M505-021 ERROR PLOT
ERROR
DEGREES/SEC
.5
.45
.4
.35
.3
.25
.2
.15
.1
.05
-.05
-.1
-.15
-.2
-.25
-.3
-.35
-.4
-.45
-.5
-200.1
-160.0
-120.0
-80.0
-40.0
40.0
80.0
120.0
160.0
200.1
RATE DEGREES/SEC

Figure 6.6

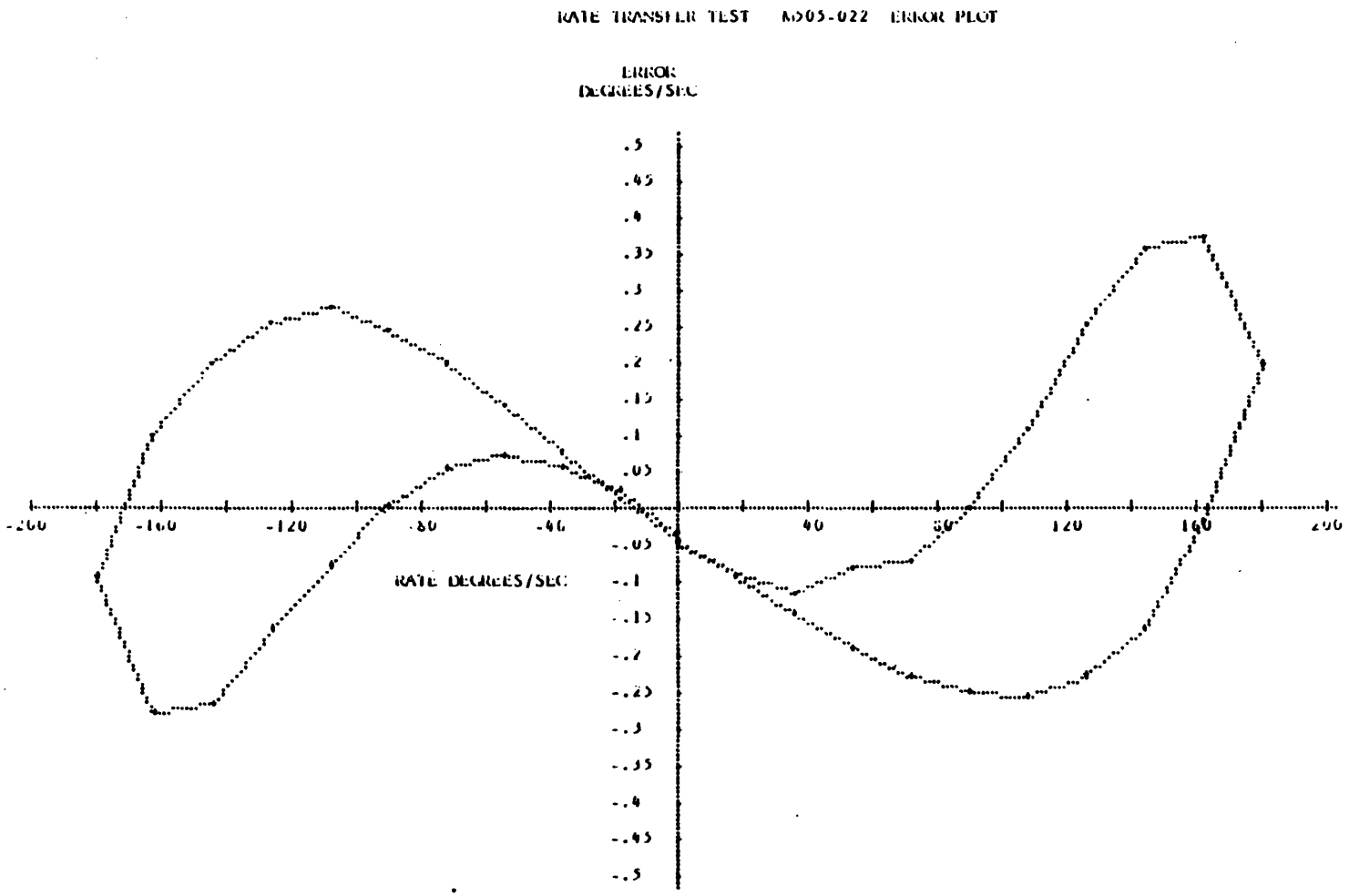
RATE TRANSFER TEST M505-022 ERROR PLOT
ERROR
DEGREES/SEC
.5
.45
.4
.35
.3
.25
.2
.15
.1
.05
-.05
-.1
-.15
-.2
-.25
-.3
-.35
-.4
-.45
-.5
-200
-160
-120
-80
-40
40
80
120
160
200
RATE DEGREES/SEC

Figure 6.7

The CPT Gyroscope Stability TEST

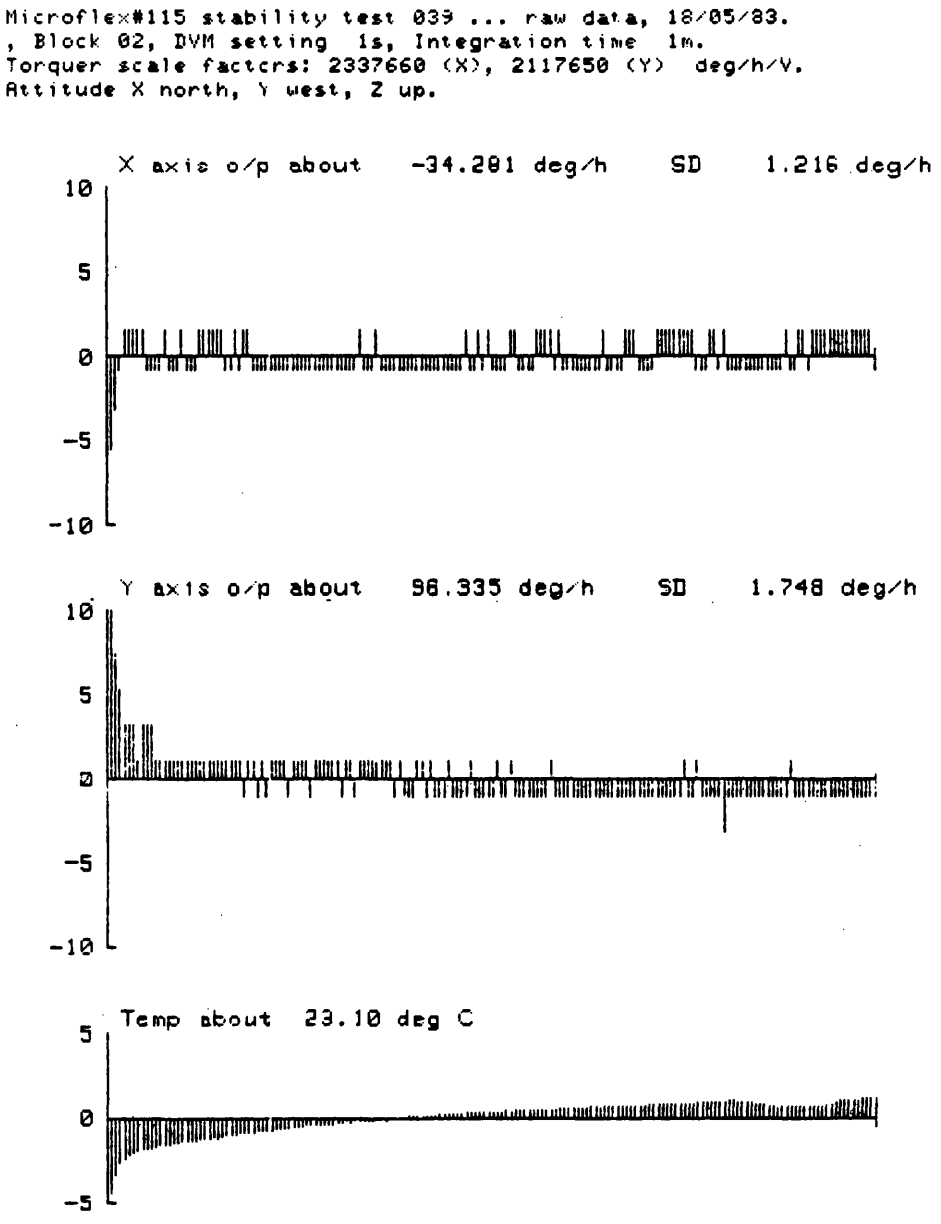

6.4 Results for the SPT Gyroscope Analogue Controller

The electronics for the SPT gyroscope have only been produced to breadboard standard and are not suitable for temperature cycling, therefore all the results reported in this section apply to ambient laboratory temperatures only.

Figure 6.8 and Table 6.4 present the results of the torquer linearity tests. These tests reflect the increase in rate capability of the SPT gyroscope and the rate demand is incremented to 450 deg/sec. As for the CPT gyroscope the characteristic 'butterfly' curve is observed. This test demonstrates the rate capability and linearity of the SPT gyroscope and shows that adequate control has been applied to null the position of the gyroscopes wheel.

Figure 6.9 shows the open loop plot of the system. Comparing this with the modelled response, Figure 4.11, it can be seen that the two plots agree well up to 80Hz. However in the region 80Hz to 200Hz the agreement is not so exact. Above 200Hz, given the imprecise knowledge of the nutation parameters, the plots agree well. The mismatch between the two plots in the region 80 to 200Hz is not yet understood, it may be a result of the simple model that is used to describe the effects of the displacement preamplifier. This requires further investigation. The effects of the discrepancy can be seen in the closed loop response which is shown in Figure 6.10. Comparing this with the modelled response of Figure 4.12 it can be seen that this has an effect between 50 and

Figure 6.8

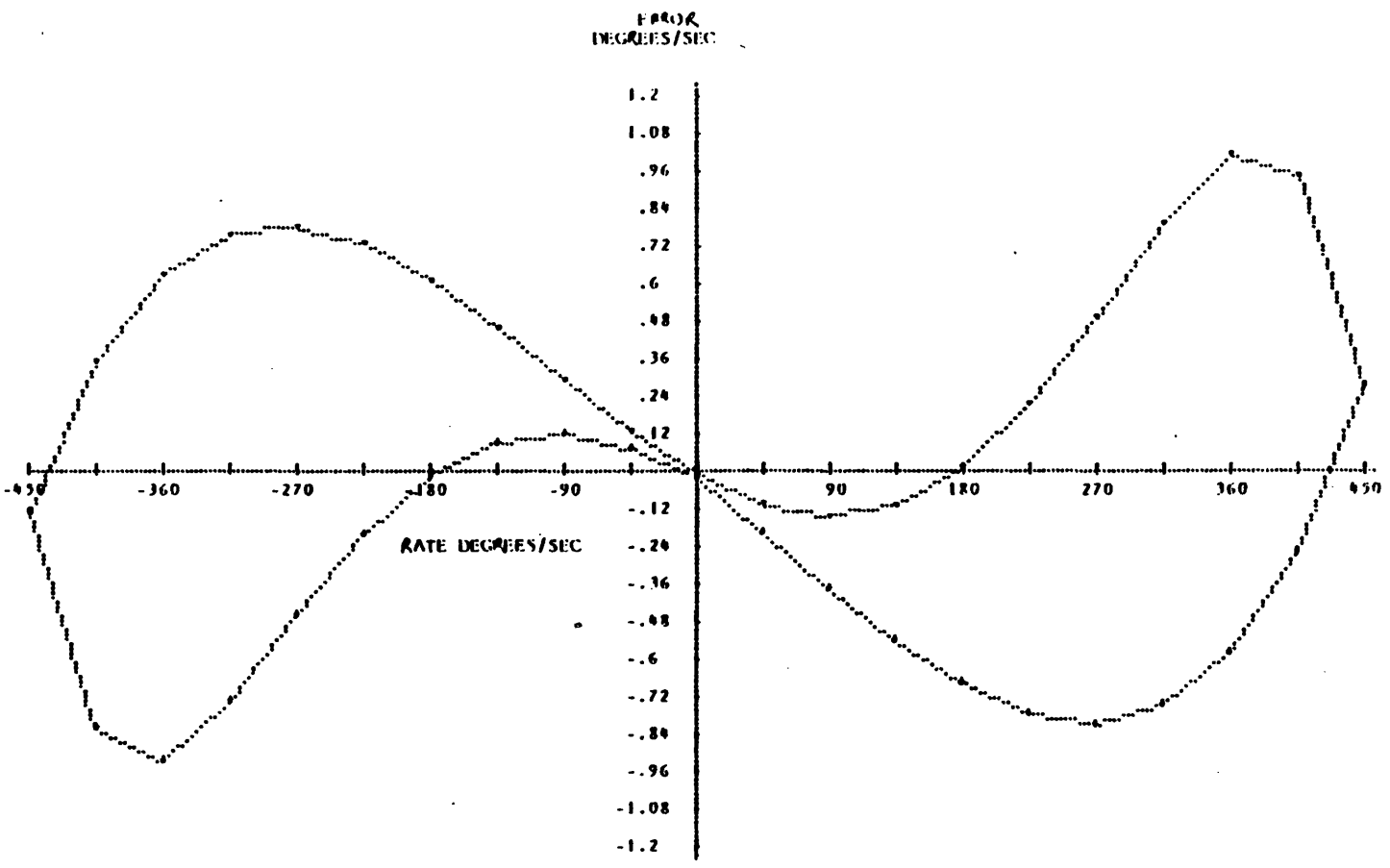
RATE TANSFER TEST M307-132 ERROR PLOT
ERROR
DEGREES/SEC
1.2
1.08
.96
.84
.72
.6
.48
.36
.24
.12
-.12
-.24
-.36
-.48
-.6
-.72
-.84
-.96
-1.08
-1.2
-450
-360
-270
-180
-90
90
180
270
360
450
RATE DEGREES/SEC

TABLE 6.4

RATE TANSFER TEST M507-132 ANALYSIS

GYRO TYPE:-M507 SERIAL NUMBER:-L103 TEST NUMBER:-132 DATE OF TEST:-3/3/83
INPUT AXIS:-Y-DOWN OUTPUT AXIS:-Y-UNCOMP ENGINEER:-DGH/DK TIME OF TEST:-01HRS 01MINS 56SEC

INITIAL TEMP:- 23 MID TEMP:- 23 FINAL TEMP:- 23

ERROR LIST

RATE INPUT (DEG/SEC)	SENSOR OUTPUT (VOLTS)	ERROR (DEG/SEC)	ERROR %
-.0049	-.00522	-.01800	
44.9583	.44828	-.20779	-.46219
89.915	.90177	-.39220	-.43619
134.8723	1.35538	-.56576	-.41948
179.8123	1.80909	-.71185	-.39588
224.7863	2.26361	-.81197	-.36122
269.7402	2.71857	-.84854	-.31458
314.7177	3.17473	-.79025	-.25110
359.673	3.63188	-.61201	-.17016
404.6223	4.09058	-.27475	-.06790
449.5829	4.55158	.27829	.06190
404.6294	4.10339	.98286	.24290
359.6827	3.64883	1.05173	.29240
314.7295	3.19123	.82696	.26275
269.7542	2.73254	.51669	.19154
224.801	2.27424	.22281	.09912
179.8249	1.81633	.01009	.00561
134.8811	1.36002	-.11646	-.08634
89.922	.90430	-.14981	-.16661
44.9637	.44931	-.11190	-.24886
-.005	-.00516	-.01195	
-44.9497	-.45894	.13243	-.29461
-89.8946	-.91249	.29852	-.33208
-134.8514	-1.36604	.47740	-.35402
-179.7802	-1.81954	.63302	-.35211
-224.7388	-2.27367	.75625	-.33650
-269.679	-2.72826	.81565	-.30245
-314.6375	-3.18388	.79167	-.25161
-359.575	-3.64043	.65487	-.18212
-404.5051	-4.09845	.36554	-.09037
-449.4503	-4.55882	-.14070	.03130
-404.5151	-4.11098	-.86152	.21298
-359.5818	-3.65691	-.96537	.26847
-314.6465	-3.19978	-.76910	.24443
-269.6851	-2.74146	-.48146	.17853
-224.743	-2.28354	-.21400	.09522
-179.7824	-1.82614	-.01638	.00911
-134.8538	-1.36996	.09279	-.06881
-89.8982	-.91434	.12007	-.13356
-44.9509	-.45956	.07192	-.16000
-.005	-.00532	-.02780	

ANALYSIS

MEAN TEMP:- 23 DEGc

SCALE FACTOR:-	10.12883	mV/DEG/SEC
NON-LINEARITY,MAX:-	1.05173	DEG/SEC
OCCURING A :-	359.6827	DEG/SEC
EQUIVALENT 0:-	.23372%	OF MAXIMUM RATE
S D. DEVIATION:-	.55063	DEG/SEC
ZERO CROSSING:-	-.49249	DEG/SEC
ZERO OFFSET:-	-.50992	DEG/SEC
ZERO HYSTERESIS:-	.00011	DEG/SEC

RATE I/P (DEG/SEC)	HYSTERESIS (DEG/SEC)
45	.10129
90	.24939
135	.45810
180	.73458
225	1.04948
270	1.37923
315	1.62901
360	1.67344
405	1.26871
450	
-45	.06171
-90	.18205
-135	.38701
-180	.65161
-225	.97445
-270	1.30321
-315	1.56978
-360	1.62704
-405	1.23706
-450	

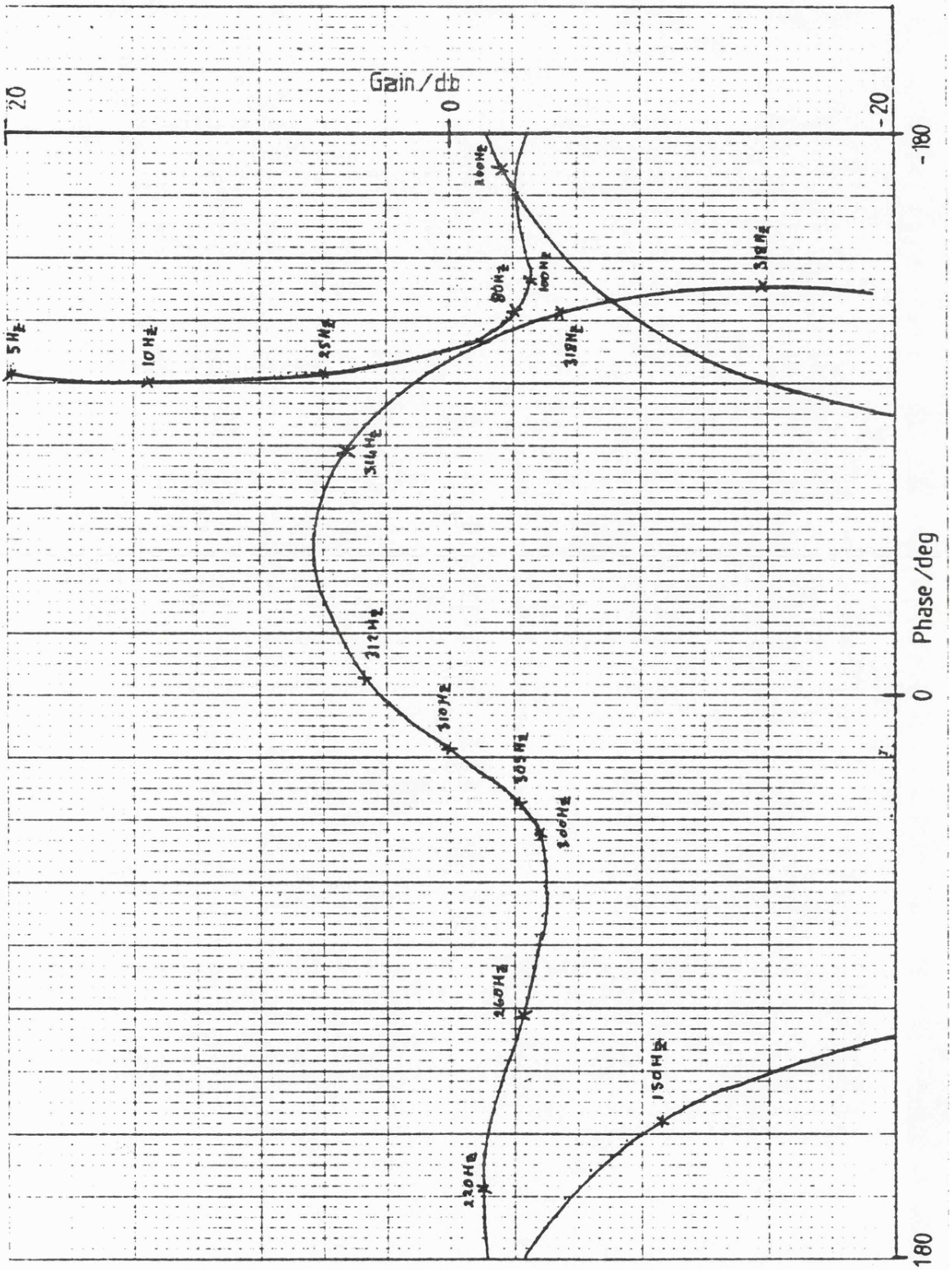

Figure 6.9 The SPT Gyroscope (Analogue) Open Loop Response

120Hz. Apart from this the responses agree well and the actual response obtained is within the design aims of a loop ripple of less than 3dbs within the passband.

6.5 Results for the SPT Gyroscope Digital Controller

The hardware which was produced to demonstrate the digital controller feasibility has not yet been developed to the stage where the system is portable. This has restricted the extent of the testing of the system. However, it has been possible to measure the open loop and closed loop responses of the system and confirm the operation of the controller and the stability of the resulting rate gyroscope. These responses are shown in Figures 6.11 and 6.12 respectively. From these it can be seen at low frequencies, ie. below 200Hz, the responses are almost indistinguishable from the responses of the analogue system. Above 200Hz the responses are similar to the modelled open and closed loop response of figures 5.7 and 5.10. The comments and observations which apply to the analogue controller apply equally to the digital controller. Again these results demonstrate that the models developed, although not perfect, are adequate tools to design the rate system. The loop is stable, does not excite nutation and does not exhibit any limit cycles. Further work is required to assess in greater detail the other aspects of the digitally controlled gyroscopes performance.

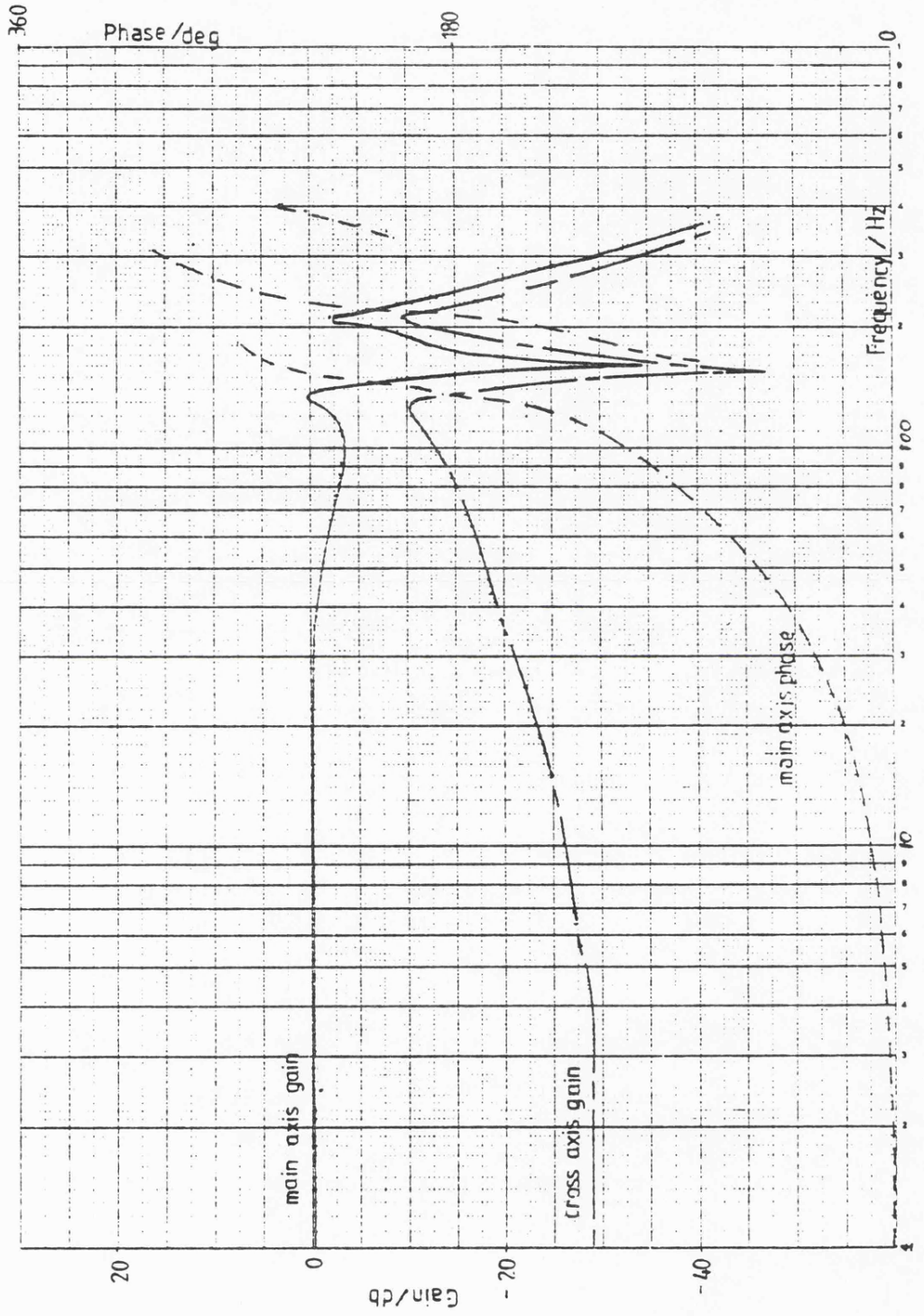

Figure 6.10 SPT Gyroscope Closed Loop Response

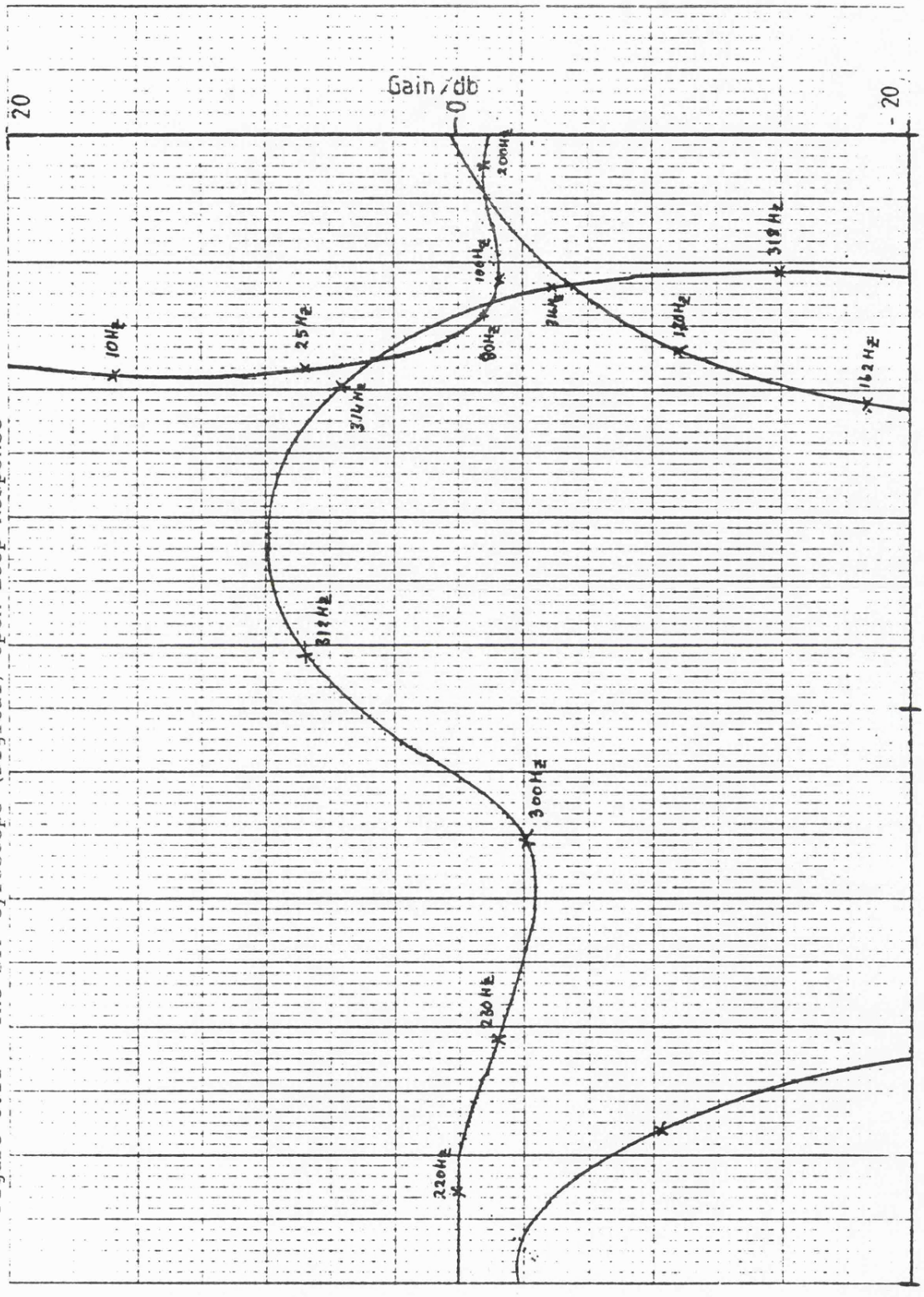

Figure 6.11 The STP Gyroscope (Digital) Open Loop Response

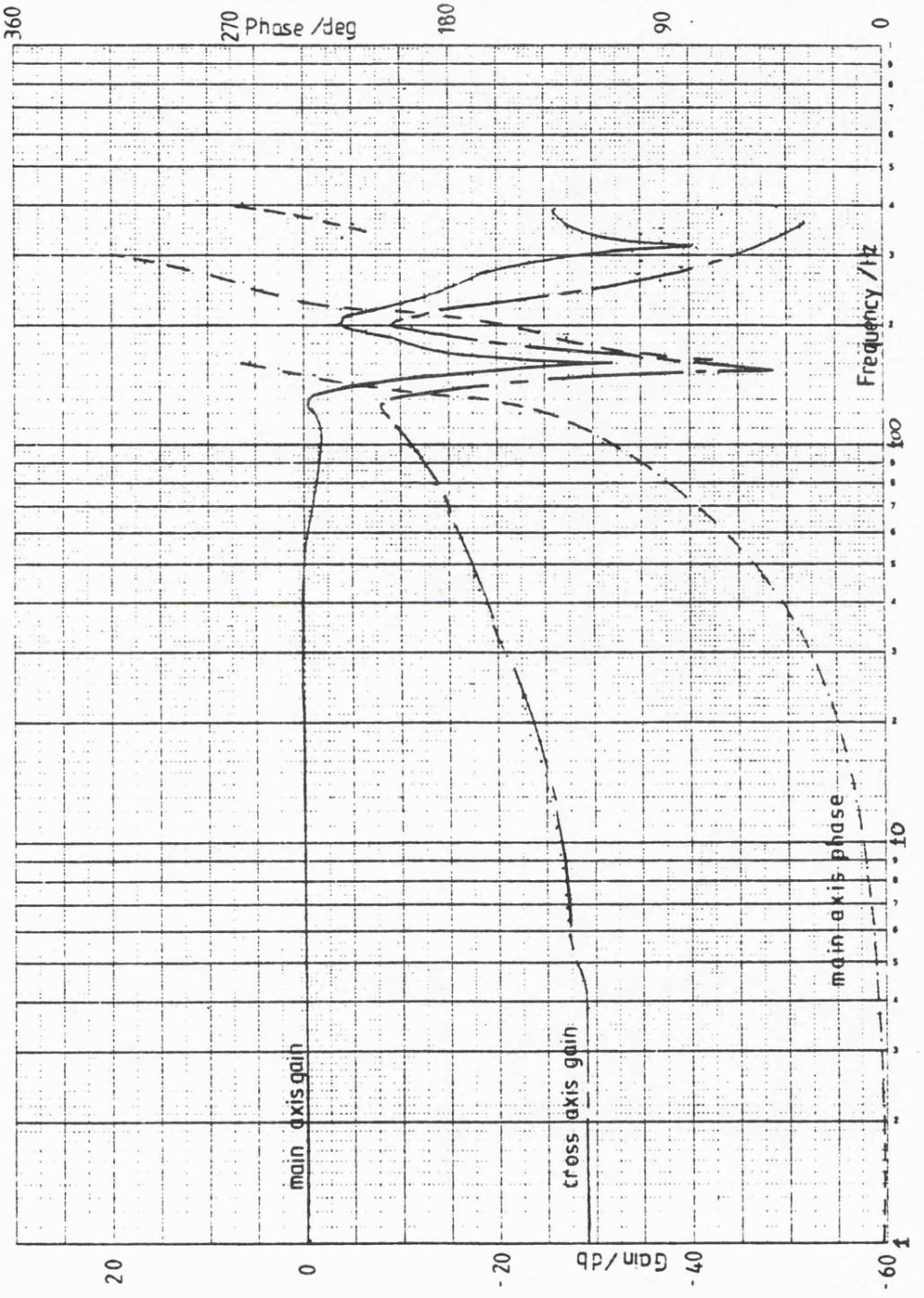

Figure 6.12 SPT Gyroscope (Digital) Closed Loop Response

CHAPTER VII

CONCLUSIONS AND RECOMMENDATIONS

The work detailed in this thesis describes how an angular limited two degree of freedom gyroscope can be controlled by the application of feedback. The feedback has been configured to implement a type II servo system and provide an output which is the first derivative of the angular displacement applied to the gyroscope. The thesis traces the development of an analogue controller for the combined pickoff and torquer variant of the Microflex gyroscope, on through the development of an analogue controller for the separate pickoff and torquer gyroscope, to the development of a digital controller for the gyroscope.

A simple set of design rules has been established. These allow the controller to be implemented without the need to compensate for nutation interactions between the two gyroscope axes. The design rules which are set out in Chapter IV show that the low frequency response can be controlled using an integral plus proportional term. Also, provided that the filtering introduced to attenuate the unwanted demodulation products (and in the case of the CPT the 'figure of eight' loop) is selected such that the phase of the open loop response is determined by the criteria given in Chapter IV, paragraph 4.1.2, equation 4.5, nutation will be stable. Meeting the criteria of equation 4.5 also provides some limited damping of nutation.

The use of the SPT gyroscope as opposed to the CPT gyroscope simplifies the design as the restrictions of the 'figure of eight' loop are removed. This allows a higher proportion of the wheel speed to be achieved as a working bandwidth. The major limiting factor in the case of the SPT gyroscope is the need to attenuate the wheel speed component. Also because the loop has a higher bandwidth, any future work should consider introducing elements to reduce the nutation coupling. The ability to achieve a higher precentage of wheel rotation frequency as bandwidth, for most applications, allows the gyroscope to be operated at a lower rotationsl frequency, thus extending the gyroscopes ability to sustain higher angular rates. It is the advantages achieved by using the SPT gyroscope which allow a digital controller to be used. The restrictions imposed by the 'figure of eight' loop affect the use of a digital controller in two ways: first the presence of the 'figure of eight' loop seriously compromises the stability of the design and second, the extra complexity of the design needed to suppress it, increases the demands and complexity of the signal processor which is required.

Chapter V shows how the simple design rules established for the analogue controller can be applied to the digital controller. Chapter V also examines the effects of quantisation, examining limit cycling, using a graphical technique to determine the frequency and amplitude of any possible limit cycle modes. In Chapter V it is also shown

that the presence of pickoff noise has a beneficial effect in that it can destroy limit cycles and because of the nature of the control loop enhance the resolution of the system. The effects of quantisation are also examined with respect to sampling frequency.

Throughout the thesis several areas needing further investigation have been highlighted. Some work is needed to establish the mechanisms which lead to the minor differences between the modelled and practical responses in the region 50 to 200Hz. In addition more detailed testing of the digital control loop is required to fully determine its system performance, and the effects of noise enhancement should be subject to practical investigation.

To fully take advantage of digital control, further work is required to incorporate more of the filtering terms in the controller and integrate this with a pulse torquing scheme. The design could then be ultimately developed to be implemented using a single substrate silicon circuit.

APPENDIX I

The Gyroscope's Equations of Motion

The gyroscope's equation of motion can be derived from the fundamental equations which represent Newton Laws of Motion, with respect to a rotating body.

The total angular momentum $\underline{L}$ of any system is given by:-

$$\underline{L} = \sum m(\underline{r} \wedge \dot{\underline{r}})$$

Where m is an elemental mass rotating about a point at distance $\underline{r}$. Also torque $\underline{M}$ is defined as the rate of change of angular momentum, thus

$$\underline{M} = \frac{d\underline{L}}{dt}$$

Now, $\underline{M} = \frac{d}{dt}\left\{\sum m(\underline{r} \wedge \dot{\underline{r}})\right\}$

$$\underline{M} = \sum m\,(\underline{r} \wedge \ddot{\underline{r}} + \dot{\underline{r}} \wedge \dot{\underline{r}})$$

but, $\dot{\underline{r}} \wedge \dot{\underline{r}} = 0$

so, $\underline{M} = \sum m(\underline{r} \wedge \ddot{\underline{r}})$

Now let r be a vector in an orthogonal right handed set fixed to the gyro rotor such as defined in the Figure A-1

Figure A1-1

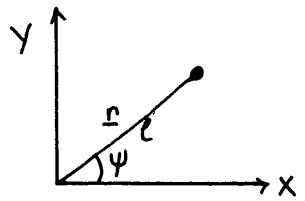

$$r = \ell\cos\psi\ \underline{x} + \ell\sin\psi\underline{y}$$

Consider the case of the gyroscope's rotor axes X, Y and Z initially aligned to a right handed set of orthogonal axes X_c, Y_c and Z_c fixed to the gyroscopes case. If the gyro case is fixed and the wheel rotated through, an angle α about X_c, an angle β about Y_c and an angle γ about Z_c, now

$$\underline{r}_c = [\alpha][\beta][\gamma]\ \underline{r}$$

where $\alpha = \begin{bmatrix} 1 & 0 & 0 \\ 0 & \cos\alpha & -\sin\alpha \\ 0 & \sin\alpha & \cos\alpha \end{bmatrix}$ $\beta = \begin{bmatrix} \cos\beta & 0 & \sin\beta \\ 0 & 1 & 0 \\ -\sin\beta & 0 & \cos\beta \end{bmatrix}$

$$\gamma = \begin{bmatrix} \cos\gamma & -\sin\gamma & 0 \\ \sin\gamma & \cos\gamma & 0 \\ 0 & 0 & 1 \end{bmatrix}$$

hence for a particle whose position is defined as in figure A-1, in the rotor coordinates can be transferred to a position in the case coordinate. Now if we make the approximation that α and β are small and γ is constant it can be shown that

$$r_c = \begin{bmatrix} 1 & 0 & \beta \\ (\alpha\beta) & 1 & -\alpha \\ -\beta & \alpha & 1 \end{bmatrix} \begin{bmatrix} \ell[\cos\gamma\cos\psi - \sin\gamma\sin\psi] \\ \ell[\sin\gamma\cos\psi + \cos\gamma\sin\psi] \\ 0 \end{bmatrix} [X, Y, Z]$$

As the quantities α and β are small their product terms may be neglected. If this approximation is made, and the necessary differentials taken it can be shown that:

$$\underline{r}_c \hat{\wedge} \ddot{\underline{r}}_c = \begin{vmatrix} \underline{i} & \underline{j} & \underline{k} \\ \ell\cos(\psi+\gamma) & \ell\sin(\psi+\gamma) & -\ell\beta\cos(\psi+\gamma) + \alpha\ell\sin(\psi+\gamma) \\ -\gamma^2\ell\cos(\psi+\gamma) & -\ell\gamma^2\sin(\psi+\gamma) & -\beta\ell\cos(\psi+\gamma)+2\beta\gamma\ell\sin(\psi+\gamma) \\ & & +\beta\gamma^2\ell\cos(\psi+\gamma)+\alpha\ell\sin(\psi+\gamma) \\ & & -2\alpha\gamma\ell\cos(\psi+\gamma)-\alpha\gamma^2\ell\sin(\psi+\gamma) \end{vmatrix}$$

where $\underline{i}$, $\underline{j}$ and $\underline{k}$ are unit vectors in the axes X_c, Y_c and Z_c respectively.

Collecting the terms we have:-

for the i^{th} component

$= (2\beta\gamma+\alpha)\sin^2(\psi+\gamma)\ell^2 + (2\alpha\gamma-\beta)\ell^2\cos(\psi+\gamma)\sin(\psi+\gamma)$

for the j^{th} component

$= \ell^2\cos^2(\psi+\gamma)(\beta-2\alpha\gamma) - \ell^2\cos(\psi+\gamma)\sin(\psi+\gamma)(2\beta\gamma+\alpha)$

for k^{th} component

$= 0$

Recalling that the torque is given by:-

$$\underline{M} = \Sigma\, m(\underline{r} \wedge \ddot{\underline{r}})$$

if we now apply this to the particular case of the microflex gyroscope. The inertial element of the microflex gyroscope can be approximated as an anular ring as shown in figure A1-2.

Figure A1-2 Approximation to microflex wheel

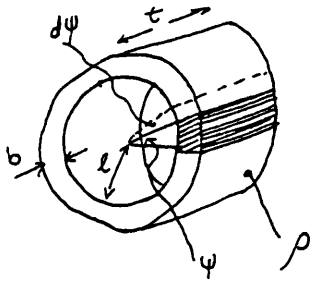

from this dm can be approximated to be equal to

$$m = \ell.t.b.\rho\ d\psi$$

Now the torque equation can be approximated to:-

$$\underline{M} = \int_0^{2\pi} \ell.t.b.\rho\{\underline{r_c} \wedge \ddot{\underline{r}}_c\}\ d\psi$$

Substituting the equation for the vector product $(\underline{r_c} \wedge \ddot{\underline{r}}_c)$ and completing the integration give the equation of motion for the gyroscope:-

$$\underline{M} = \underline{i}(2\beta\gamma+\alpha)\pi\ell^3 tb\rho + \underline{j}(\beta - 2\alpha\gamma)\pi\ell^3 tb\rho$$

Noting that for an annular ring that the moment of inertia about its axial axis $I_z = 2bt\rho\ell^3\pi$ and the moment of inertia about a diameter $I_x = bt\rho\ell^3\pi$.

Also that γ is the angular rotational frequency of wheel (ω) and α and β are prcession rates $\dot{\theta}_x$ and $\dot{\theta}_y$. Thus the equation of motion can be resolved into two components.

$$\begin{bmatrix} \bar{M}_x \\ \bar{M}_y \end{bmatrix} = \begin{bmatrix} sI_x & I_z\omega \\ -I_z\omega & sI_x \end{bmatrix} \begin{bmatrix} \dot{\theta}_x \\ \dot{\theta}_y \end{bmatrix}$$

APPENDIX II

ORDER OF MAGNITUDE CALCULATION OF THE CPT GYROSCOPE PARAMETERS

A.2.1 Moments of Inertia

Table A2.1

Wheel Element Moments of Inertia

	Iz	Ix
Element 1	$M_1 r_1^2$	$M_1[\frac{r_1^2}{2} + \frac{\ell^2}{12} + (\frac{\ell}{2}-h)^2]$
Element 2	$M_2 r_2^2$	$M_2[\frac{r_2^2}{2} + \frac{\ell^2}{12} + (\frac{\ell}{2}-h)^2]$
Element 3	$\frac{M_3(r_1^2 + r_2^2)}{2}$	$\frac{M_3(r_1^2 + r_2^2)}{4} + M_3h^2$

Referring to Table A2.1. These values refer to Figure A2.1 wheel element moment of inertia for the Microflex gyroscope: r_1 = 0.861cm, r_2 = 0.607cm, t = 0.038cm, ℓ = 0.216cm and the density of the material = 8800 kg/m³. Using these values the moments of inertia of each element have been calculated and are given in Table A2.2. (The mass of the magnets 0.20gms has been assumed to be distributed about the outer rim of wheel).

Table A2.2

Moment of Inertia

ELEMENT	I_z/gmcm²	I_x/gmcm²
1	0.438	0.223
2	0.101	0.051
3	0.185	0.101

$$I_z(\text{total}) = I_{z1} + I_{z2} + I_{z3} = 0.724\text{gmcm}^2$$

Figure A2.1

The Elements of the Gyroscope Wheel

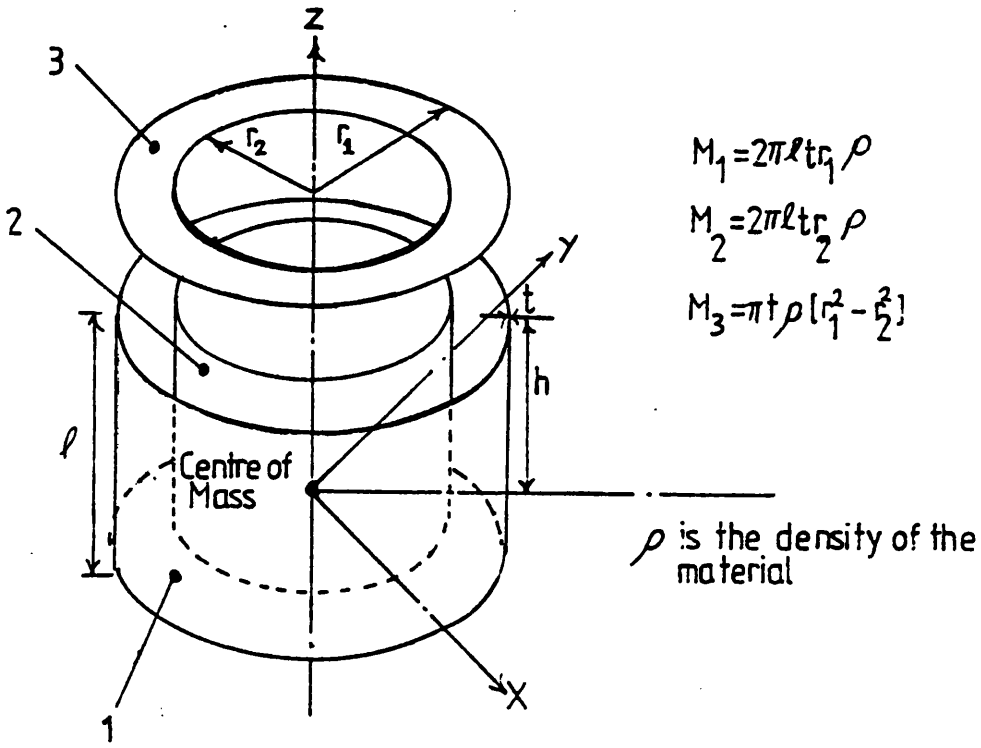

$$I_x(\text{total}) = I_{x1} + I_{x2} + I_{x3} + (M_1 + M_2)\ (\tfrac{\ell}{2}-h)^2 + M_2h^2 = 0.383\text{gmcm}^2$$

(using parallel axis theorem).

Where h is as defined in Figure A2.1 and is given by:

$$h = \left[\frac{M_1 + M_2}{M_1 + M_2 + M_3}\right] \quad \ell = 0.149\text{cm}$$

A2.2 Magnetic Field in the Wheel Channel

The magnetic circuit is shown in Figure A2.2, the magnetic field can be split into 3 separate areas which can be evaluated separately.

Figure A2.2

The Magnetic Circuit

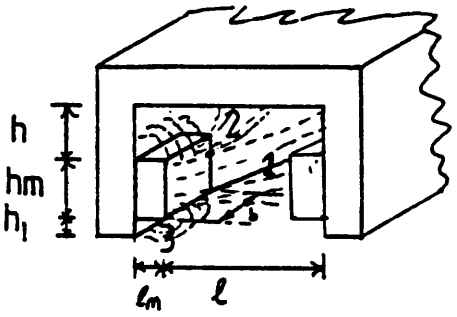

b = 3mm

ℓ_m = 0.5mm

ℓ = 1.27mm

hm = 1.127mm

h = 0.635mm

h_1 = 0.254mm

Surface area of magnet = Am

In the calculations the wheel is assumed to have a very high permeability.

For permanent magnet system it can be shown that:

$$\frac{Bm}{\mu_o Hm} = \frac{\ell n}{Am\mu_o R} \qquad \text{A2.1}$$

Where Hm is the magnetic field strength of magnets, Bm is the flux of the magnets, R is the reluctance of the three flux paths (Crangle, 1977).

Where R the reluctance, is given by:

$$R = \Sigma \frac{\ell_i}{\mu_i A_i}$$

Where ℓi is the length of the fluxpath, μi is the permeability of the path and Ai is the area of the path.

The reluctance of the path labelled (1) in Figure A2.2 can be estimated, with recourse to Figure A2.3.

Figure A2.3

Reluctance of Path (1)

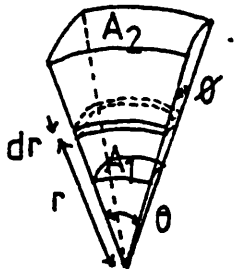

A_2 represents the area of the rim of the wheel

A_1 represents the area of the magnets front face

μo is the permeability of free space

Referring to Figure A2.3, the reluctance (dR) of an elemental section of the fluxpath is given by:

$$dR = \frac{dr}{\mu o\ r^2}\ \sin\theta\ \sin\phi$$

The total reluctance of the path is given by integrating from r_1 to r_2, with respect to r. This gives the total reluctance R as:

$$R = \frac{r_2 - r_1}{\mu o\ r_1 r_2}\ \sin\theta\ \sin\phi$$

However, it can be shown that $r_1 r_2 \sin\theta \sin\phi = \sqrt{a_1 a_2}$ and $\ell = r_2 - r_1$ thus:

$$R = \frac{1}{\mu o}\ \frac{\ell}{\sqrt{a_1 a_2}}$$

If the areas are assumed to have the same aspect ratio, for the dimensions shown in Figure A2.2 the value for the reluctance of this path is $\frac{196.}{\mu o}$.

The reluctance of path 2 can be estimated with recourse to Figure A2.4.

Figure A2.4

Reluctance of Path 2

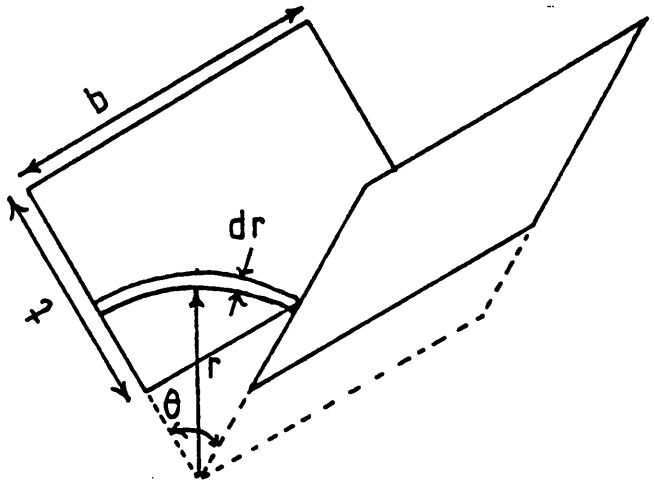

Referring to Figure A2.4 the elemental reluctance is given by:

$$dR = \frac{r\theta}{\mu o\ bdr}$$

The inverse of the reluctance is called the permanence (P) thus integrating from $\frac{\ell}{2 \sin \frac{1}{2}\theta}$ to $t + \frac{\ell}{2 \sin \frac{1}{2}\theta}$ gives the total permanence P,

$$P = \frac{b}{\theta} \log_e \left(1 + \frac{2t}{e} \sin \frac{\theta}{2}\right)$$

Thus for the case of $\theta = \frac{\pi}{2}$ rads the reluctance is given by:

$$R = \frac{\pi}{2\mu ob \log_e \left(1+\frac{2t}{e}\right)} = \frac{477}{\mu o} \quad \text{(for the Microflex gyroscope)}$$

The reluctance of the flux path from the magnet back to the outer wheel rim (path 3) can be estimated with recourse to Figure A2.5.

Figure A2.5

Reluctance Path 3

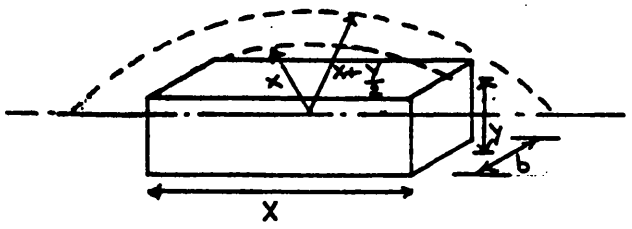

The reluctance of path 3 can be split into 4 separate paths. However, proceeding as for the two other paths, and noting that for parallel path the permenance may be added it can be shown that the reluctance is given by:

$$R = \frac{\pi}{2\mu o}\left[\frac{1}{Y \log_e (1+\frac{b}{y})} + \frac{1}{b \log_e (1+\frac{Y}{X})}\right]$$

$R = \frac{253}{\mu o}$ for the Microflex gyroscope

The total reluctance of the flux path is given by:

$$R = \frac{1}{\frac{\mu o}{196} + \frac{\mu o}{477} + \frac{\mu o}{253}} = \frac{89.6}{\mu o}$$

Recalling Equation 2.17 we have:

$$\frac{Bm}{\mu oHm} = \frac{\ell m}{Am}\frac{1}{\mu oR} = 1.48$$

From the demagnetising curve from samarium cobalt, using this figure, we determine:

$$B_m = 0.46 \text{ Tesla}$$

The actual flux in the vicinity of the gyro coils, is the flux between the magnet and the inner rim of the wheel. The proportion of flux in this region is determined by the ratio of the reluctance thus, the coil flux (B_c) is given by:

$$B_c = \frac{BmAm}{Ac}\frac{R}{Rc}$$

Where R is the total reluctance

Rc is the reluctance of the coil flux path

Ac is the area of the coil flux

For Am = Ac, $Rc = \frac{\ell}{\mu oAm} = \frac{333.6}{\mu o}$, $R = \frac{89.6}{\mu o}$

Gives Bc = 0.12 Tesla/magnet

A2.3 Pick-off Scale Factor

This can be calculated by equation (note the modulated flux pattern which generates the pick off depends on only one magnet).

$$\varepsilon_p = 2r\varepsilon o\theta o \cos(8\omega t) \cos(\omega mt)$$

The term Cos(8ωt) is the modulation carrier frequency and can be assumed to be unity when the signal is demodulated. To obtain the scale factor consider a fixed offset θ_o(ωm = 0) thus:

$$\frac{\varepsilon_p}{\theta_o} = 2\varepsilon or = 2r^2\omega B_c n$$

For the Microflex gyroscope r = 6.5mm, ω = 2π x 200 rads Bc = 0.8 tesla and n = 50. For 1 min of arc:

(Note Bc is reduced by 40% as the pick off work on the average ripple).

$$\varepsilon_p = 2 \times (6.5 \times 10^{-3})^2 \times 2\pi \times 200 \times 0.08 \times 2.9 \times 10^{-4} \times 50$$

$$\frac{\varepsilon_p}{\vartheta_o} = 123\mu V/\text{arc min}$$

However, overlap of the coils causes a reduction in this voltage. This can be estimated by subtracting a portion scaled by the ratio of the thickness of the coil (0.6mm) and half the length of the coil (3.8mm) thus:

$$\frac{\varepsilon_p}{\theta_o} = 123 \left(1 - \frac{0.6}{3.8}\right) = 103\mu V/\text{min arc}$$

The average pick-off scale factor measured on 5 gyroscopes 100μV/arc min.

A2.4 Torquer Scale Factor

This can be calculated directly from the following equation:

$$\frac{\dot{\theta}}{i} = \frac{nr^2\, Bm(ave)(\phi + \frac{\sin 8\phi}{8})}{I_z \omega}$$

$n = 95$, $r = 7 \times 10^{-3}$m, $\phi = \frac{3}{8}\pi$ rads, $\omega = 200 \times 2\pi$ rads/sec,

$Iz = 0.724 \times 10^{-7}$kgm^2 Bm (ave) = 0.18 Tesla

$\frac{\dot{\theta}}{i} = 7.23$ rad/sec/Ampere $\equiv$ 2254 deg/hr/mA

The average torquer scale factor measured for 5 gyroscopes 2200 deg/hr/mA.

A2.5 The Gyroscope Gain

In all the models used the gyroscope gain includes the torquer amplifier of transconductance 65mA/V, and the preamplifier and demodulator with volt rms peak to dc gain of 90.

Figure A2.6 shows in block diagram form how the gain is calculated.

Figure A2.6

Gyroscope Gain

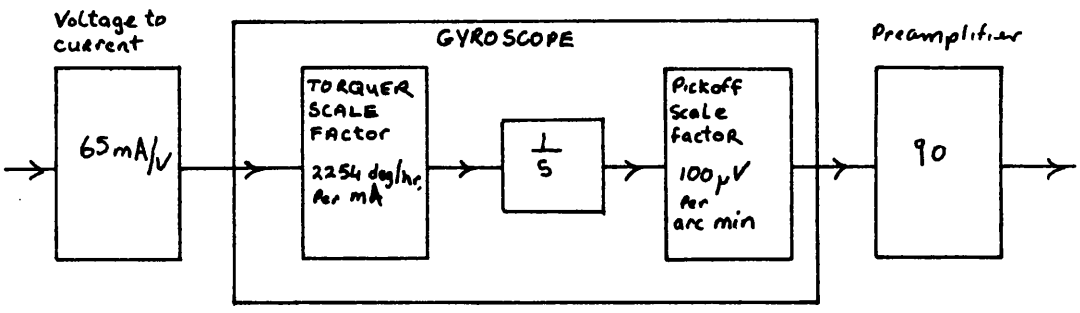

Hence torquer gain:

$$1V_{in} \text{ produce} = 65 \times \frac{2254}{3600} \times \frac{1}{s} \times \quad \text{deg}$$

$$= 100 \times 60 \times 65 \times \frac{2254}{3600} \times \frac{1}{s} \times 10^{-6} = 14.6 \text{ volts}$$

Thus V_{in} to V_{out} the gain is $\frac{14.6}{s}$

APPENDIX III

ORGANON MODELS

```
LOOP  MODEL

  2   @   MICROFLEX GYRO MODEL  M TAYLOR/B JOHNSON   16/05/85
  4   @             COMPLETE C.A.T. CLOSED LOOP
  6   @             ANALOGUE ELECTRONICS
  8   @-----------------------------------------------------------------
 10   @   REAL LABEL DECLARATIONS
 12   @
 14   REAL GKN2 GKN1 GKN0 GKD2 GKD1 GKD0 GFN1 GFN0 GFD1 GFD0
 16   REAL GCN1 GCN0 GCD1 GCD0 INLN1 INLN0 INLD1 INLD0
 18   REAL SG ONE
 20   REAL SHAN2 SHAN1 SHAN0 SHAD2 SHAD1 SHAD0
 22   REAL SHBN2 SHBN1 SHBN0 SHBD2 SHBD1 SHBD0
 24   REAL SHCN2 SHCN1 SHCN0 SHCD2 SHCD1 SHCD0
 26   REAL SHDN1 SHDN0 SHDD1 SHDD0 INTN1 INTN0 INTD1 INTD0
 28   REAL SHEN2 SHEN1 SHEN0 SHED2 SHED1 SHED0
 30   REAL SHFN2 SHFN1 SHFN0 SHFD2 SHFD1 SHFD0
 32   REAL GM2[2,2] GM1[2,2] GM0[2,2] ZERO ORIGIN[2]
 34   REAL RANGE[3] STOP[3] OUTPUT[2] FLIST[200]
 36   @-----------------------------------------------------------------
 38   @   COMPLEX LABEL DECLARITIONS
 40   @
 42   COMPLEX GKN GKD GKK GFN GFD GFF GCN GCD GCC INLN INLD INL
 44   COMPLEX SHAN SHAD SHA SHBN SHBD SHB SHCN SHCD SHC SHDN SHDD SHD
 46 COMPLEX SHP SHEN SHED SHF SHFN SHFD
 48   COMPLEX INTN INTD INT[2,2] SHAPER[2,2] GMAT[2,2] GYRO[2,2]
 50   COMPLEX SHAPE SHAPE1[2,2]
 52   RRM=ZERO
 54   FLIST=FRQL[RANGE]
 56   ORIGIN
 58   @--------------------------------    GYRO CONSTANT EVALUATION
 60     GKN=FNS[GKN2,GKN1,GKN0]
 62     GKD=FNS[GKD2,GKD1,GKD0]
 64   GKK=GKN/GKD
 66   @--------------------------------    GYRO INTEGRATOR EVALUATION
 68     GFN=FNS[GFN1,GFN0]
 70     GFD=FNS[GFD1,GFD0]
 72   GFF=GFN/GFD
 74   @--------------------------------    GYRO TORQUER POLE EVALUATION
 76     GCN=FNS[GCN1,GCN0]
 78     GCD=FNS[GCD1,GCD0]
 80   GCC=GCN/GCD
 82   @--------------------------------    GYRO MATRIX DEFINITION
 84   GMAT=FNS[GM2,GM1,GM0]
 86   @--------------------------------    208HZ/0.767 LOWPASS
 88     SHAN=FNS[SHAN2,SHAN1,SHAN0]
 90     SHAD=FNS[SHAD2,SHAD1,SHAD0]
 92   SHA=SHAN/SHAD
 94   @--------------------------------    200HZ NOTCH
 96     SHBN=FNS[SHBN2,SHBN1,SHBN0]
 98     SHBD=FNS[SHBD2,SHBD1,SHBD0]
100   SHB=SHBN/SHBD
102   @--------------------------------    512HZ/1.27/X5 LOWPASS
104     SHCN=FNS[SHCN2,SHCN1,SHCN0]
106     SHCD=FNS[SHCD2,SHCD1,SHCD0]
108   SHC=SHCN/SHCD
```

```
110   @--------------------------------    SHAPER POLE EVALUATION
112     SHDN=FNS[SHDN1,SHDN0]
114     SHDD=FNS[SHDD1,SHDD0]
116   SHD=SHDN/SHDD
118   @--------------------------------    244HZ/0.84 LOWPASS
120     SHEN=FNS[SHEN2,SHEN1,SHEN0]
122     SHED=FNS[SHED2,SHED1,SHED0]
124   SHP=SHEN/SHED
126   @--------------------------------    312HZ/0.767 LOWPASS
128     SHFN=FNS[SHFN2,SHFN1,SHFN0]
130     SHFD=FNS[SHFD2,SHFD1,SHFD0]
132   SHF=SHFN/SHFD
134   @--------------------------------    INTEGRATOR MATRIX EVALULATION
136     INTN=FNS[INTN1,INTN0]
138     INTD=FNS[INTD1,INTD0]
140   INT[1,1]=ONE
142   INT[1,2]=ZERO
144   INT[2,1]=ZERO
146   INT[2,2]=ONE
148   @--------------------------------    INTEGRATOR & LEAD
150     INLN=FNS[INLN1,INLN0]
152     INLD=FNS[INLD1,INLD0]
154   INL=INLN/INLD
156   @--------------------------------    GYRO TRANSFER FUNCTION
158   GYRO=[GKK*GFF*GMAT]
160   @--------------------------------    SHAPER TRANSFER FUNCTION
162   SHAPE=SHA*SHB*SHC*SHD*SHP*SHF*SG
164   SHAPER[1,1]=ZERO
166   SHAPER[1,2]=SHAPE
168   SHAPER[2,1]=-SHAPE
170   SHAPER[2,2]=ZERO
172   SHAPE1=INL*SHAPER*GCC
174   @--------------------------------    OPEN LOOP TRANSFER FUNCTION
176   LOOP=INL*SHAPER*[GFF*GMAT*GKK]*GCC
178   @--------------------------------    RRM EVALUATION
180   RRM[1,1]=-LOOP
182     RRM[3,1]=-LOOP
184   RRM[1,3]=-INT
186   @--------------------------------    OUTPUT
188   OUTPUT RRM
190 STOP FLIST
```

```
TIME  MODEL

100    @-------------------------------------------------------------
110    @
120    @                    CPT GYRO
130    @                 SIMULATION MODEL
140    @                 M.TAYLOR/B.JOHNSON 09/09/85
150    @
160    @-------------------------------------------------------------
170    REAL RDTN1[2] RDTN0[2] RDTD1[2] RDTD0[2]
180    REAL INLN1[2] INLN0[2] INLD1[2] INLD0[2]
190    REAL SHAN2[2] SHAN1[2] SHAN0[2] SHAD2[2] SHAD1[2] SHAD0[2]
200    REAL SHBN2[2] SHBN1[2] SHBN0[2] SHBD2[2] SHBD1[2] SHBD0[2]
210    REAL SHCN1[2] SHCN0[2] SHCD1[2] SHCD0[2]
220    REAL SHDN2[2] SHDN1[2] SHDN0[2] SHDD2[2] SHDD1[2] SHDD0[2]
230    REAL SHFN2[2] SHFN1[2] SHFN0[2] SHFD2[2] SHFD1[2] SHFD0[2]
240    REAL SHGN2[2] SHGN1[2] SHGN0[2] SHGD2[2] SHGD1[2] SHGD0[2]
250    REAL SHA[2,1] SHB[2,1] SHC[2,1] SHD[2,1] SHF[2,1] SHG[2,1]
260    REAL XOVER[2,1] CROSS[2,2]
270    REAL READOUT[2,1] CONTROL[2,1] SG
280    REAL GINO[2,1] GOUT[2,1]
290    REAL GINT1[2,2] GINT0[2,2] GIDT1[2,2] GIDT0[2,2]
300    REAL GMN2[2] GMN1[2] GMN0[2]
310    REAL GMD2[2] GMD1[2] GMD0[2]
320    REAL LOOPSUM1[2,1] LOOPSUM2[2,1] SUM[2,1]
330    REAL INPUT[2,1]
331    REAL SCOUTPUT[2,1] SF
340
350    REAL ORIGIN[2] STOP[3] OUTPUT[2] DIGITAL[2]
360
370    ORIGIN
380   LOOPSUM2=INPUT*SF
400      SUM=LOOPSUM2-LOOPSUM1
410      GINO=RFS[GINT1,GINT0/GIDT1,GIDT0]*SUM
420      GOUT=RFS[GMN2,GMN1,GMN0/GMD2,GMD1,GMD0]*GINO
430      READOUT=RFS[RDTN1,RDTN0/RDTD1,RDTD0]*GOUT
440      CONTROL=SG*RFS[INLN1,INLN0/INLD1,INLD0]*READOUT
450      SHA=RFS[SHAN2,SHAN1,SHAN0/SHAD2,SHAD1,SHAD0]*CONTROL
460      SHB=RFS[SHBN2,SHBN1,SHBN0/SHBD2,SHBD1,SHBD0]*SHA
470      SHC=RFS[SHCN1,SHCN0/SHCD1,SHCD0]*SHB
480      SHD=RFS[SHDN2,SHDN1,SHDN0/SHDD2,SHDD1,SHDD0]*SHC
490      SHF=RFS[SHFN2,SHFN1,SHFN0/SHFD2,SHFD1,SHFD0]*SHD
500      SHG=RFS[SHGN2,SHGN1,SHGN0/SHGD2,SHGD1,SHGD0]*SHF
510      XOVER=CROSS*SHG
520      LOOPSUM1=XOVER
521      SCOUTPUT=LOOPSUM1/SF
530   OUTPUT INPUT SCOUTPUT REA
540 STOP
```

```
LOOP  MODEL

100   @   MICROFLEX GYRO MODEL  M TAYLOR/B JOHNSON   16/05/85
110   @             COMPLETE CLOSED LOOP SYSTEM (S.P.T.)
111   @             ANALOGUE ELECTRONICS
120   @-------------------------------------------------------------
130   @   REAL LABEL DECLARATIONS
140   @
150   REAL GKN2 GKN1 GKN0 GKD2 GKD1 GKD0 GFN1 GFN0 GFD1 GFD0
160   REAL GCN1 GCN0 GCD1 GCD0 INLN1 INLN0 INLD1 INLD0
170   REAL SHAN2 SHAN1 SHAN0 SHAD2 SHAD1 SHAD0
180   REAL SHBN2 SHBN1 SHBN0 SHBD2 SHBD1 SHBD0
190   REAL SHCN2 SHCN1 SHCN0 SHCD2 SHCD1 SHCD0
200   REAL SHDN1 SHDN0 SHDD1 SHDD0
201   REAL IDENTITY[2,2]
210   REAL GM2[2,2] GM1[2,2] GM0[2,2] ZERO ORIGIN[2]
220   REAL RANGE[3] STOP[3] OUTPUT[2] FLIST[200]
230   @-------------------------------------------------------------
240   @   COMPLEX LABEL DECLARITIONS
250   @
260   COMPLEX GKN GKD GKK GFN GFD GFF GCN GCD GCC INLN INLD INL
270   COMPLEX SHAN SHAD SHA SHBN SHBD SHB SHCN SHCD SHC SHDN SHDD SHD
280   COMPLEX SHAPER[2,2] GMAT[2,2] GYRO[2,2]
290   COMPLEX SHAPE SHAPE1[2,2]
300   RRM=ZERO
310 FLIST=FRQR[RANGE]
320   ORIGIN
330   @-------------------------------    GYRO CONSTANT EVALUATION
340     GKN=FNS[GKN2,GKN1,GKN0]
350     GKD=FNS[GKD2,GKD1,GKD0]
360   GKK=GKN/GKD
370   @-------------------------------    GYRO INTEGRATOR EVALUATION
380     GFN=FNS[GFN1,GFN0]
390     GFD=FNS[GFD1,GFD0]
400   GFF=GFN/GFD
410   @-------------------------------    GYRO TORQUER POLE EVALUATION
420     GCN=FNS[GCN1,GCN0]
430     GCD=FNS[GCD1,GCD0]
440   GCC=GCN/GCD
450   @-------------------------------    GYRO MATRIX DEFINITION
460   GMAT=FNS[GM2,GM1,GM0]
470   @-------------------------------    SHAPER LOWPASS EVALUATION
480     SHAN=FNS[SHAN2,SHAN1,SHAN0]
490     SHAD=FNS[SHAD2,SHAD1,SHAD0]
500   SHA=SHAN/SHAD
510   @-------------------------------    320 HZ NOTCH EVALUATION
520     SHBN=FNS[SHBN2,SHBN1,SHBN0]
530     SHBD=FNS[SHBD2,SHBD1,SHBD0]
540   SHB=SHBN/SHBD
550   @-------------------------------    160 HZ NOTCH EVALUATION
560     SHCN=FNS[SHCN2,SHCN1,SHCN0]
570     SHCD=FNS[SHCD2,SHCD1,SHCD0]
580   SHC=SHCN/SHCD
590   @-------------------------------    SHAPER POLE EVALUATION
600     SHDN=FNS[SHDN1,SHDN0]
610     SHDD=FNS[SHDD1,SHDD0]
620   SHD=SHDN/SHDD
```

```
630   @--------------------------------    INTEGRATOR MATRIX EVALUATION
640     INTN=FNS[INTN1,INTN0]
650     INTD=FNS[INTD1,INTD0]
660   INT[1,1]=INTN/INTD
670   INT[1,2]=ZERO
680   INT[2,1]=ZERO
690   INT[2,2]=INTN/INTD
700   @--------------------------------    INTEGRATOR & LEAD
710     INLN=FNS[INLN1,INLN0]
720     INLD=FNS[INLD1,INLD0]
730   INL=INLN/INLD
740   @--------------------------------    GYRO TRANSFER FUNCTION
750   GYRO=[GKK*GFF*GMAT]
760   @--------------------------------    SHAPER TRANSFER FUNCTION
770   SHAPE=SHA*SHB*SHC*SHD
780   SHAPER[1,1]=ZERO
790   SHAPER[1,2]=SHAPE
800   SHAPER[2,1]=-SHAPE
810   SHAPER[2,2]=ZERO
820   @--------------------------------    OPEN LOOP TRANSFER FUNCTION
830   LOOP=INL*SHAPER*[GFF*GMAT*GKK]*GCC
840   @--------------------------------    RRM EVALUATION
850   RRM[1,1]=-LCOP
860   RRM[3,1]=-LOOP
870   RRM[1,3]=-IDENTITY
880   @--------------------------------    OUTPUT
890   OUTPUT RRM
900  STOP FLIST
```

```
LOOP  MODEL

100   @   MICROFLEX GYRO MODEL  M TAYLOR/B JOHNSON   21/05/85
102   @             COMPLETE CLOSED LOOP SYSTEM (S.P.T.)
104   @             DIGITAL INTEGRATOR AND LEAD
106   @             INCLUDING DELAY (10KHZ SAMPLING)
108   @             (MULTIPASSED ANALOGUE SECTORS)
110   @-----------------------------------------------------------------
112   @   REAL LABEL DECLARATIONS
114   @
116   REAL GKN2 GKN1 GKN0 GKD2 GKD1 GKD0 GFN1 GFN0 GFD1 GFD0
118   REAL GCN1 GCN0 GCD1 GCD0 INLN1 INLN0 INLD1 INLD0
120   REAL SHAN2 SHAN1 SHAN0 SHAD2 SHAD1 SHAD0
122   REAL SHBN2 SHBN1 SHBN0 SHBD2 SHBD1 SHBD0
124   REAL SHCN2 SHCN1 SHCN0 SHCD2 SHCD1 SHCD0
126   REAL SHDN1 SHDN0 SHDD1 SHDD0
128   REAL DLZN1 DLZN0 DLZD1 DLZD0 KG
130   REAL MLTIPSS[2] SUM[2]
132   REAL IDENTITY[2,2]
134   REAL PERIOD[2] DELAY[2] SCALAR
136   REAL GM2[2,2] GM1[2,2] GM0[2,2] ZERO ORIGIN[2]
138   REAL RANGE[3] STOP[3] OUTPUT[2] FLIST[200]
140   @-----------------------------------------------------------------
142   @   COMPLEX LABEL DECLARITIONS
144   @
146   COMPLEX GKN GKD GKK GFN GFD GFF GCN GCD GCC INLN INLD INL
148   COMPLEX SHAN SHAD SHA SHBN SHBD SHB SHCN SHCD SHC SHDN SHDD SHD
150   COMPLEX SHAPER[2,2] GMAT[2,2] GYRO[2,2]
152   COMPLEX DLZN DLZD DLZ SHAPE
154   COMPLEX SHAPING[2,2] OPENLOOP[2,2]
156   RRM=ZERO
158   FLIST=FRQL[RANGE]
160   ORIGIN
162   @---------------------------------  DISCRETE INTEGRATOR & LEAD
164     DLZN=FNZ[DLZN1,DLZN0]
166     DLZD=FNZ[DLZD1,DLZD0]
168   DLZ=KG*DLZN/DLZD
170   GYRO=ZERO
172   SHAPING=ZERO
174   OPENLOOP=ZERO
176   SHAPE=ZERO
178 MLTIPSS
180   @---------------------------------  SHAPER LOWPASS
182     SHAN=FNS[SHAN2,SHAN1,SHAN0]
184     SHAD=FNS[SHAD2,SHAD1,SHAD0]
186   SHA=SHAN/SHAD
188   @---------------------------------  320 HZ NOTCH
190     SHBN=FNS[SHBN2,SHBN1,SHBN0]
192     SHBD=FNS[SHBD2,SHBD1,SHBD0]
194   SHB=SHBN/SHBD
196   @---------------------------------  160 HZ NOTCH
198     SHCN=FNS[SHCN2,SHCN1,SHCN0]
200     SHCD=FNS[SHCD2,SHCD1,SHCD0]
202   SHC=SHCN/SHCD
204   @---------------------------------  SHAPER POLE
206     SHDN=FNS[SHDN1,SHDN0]
208     SHDD=FNS[SHDD1,SHDD0]
210   SHD=SHDN/SHDD
```

```
@---------------------------------  GYRO TRANSFER FUNCTION
@                                   GYRO CONSTANT
   GKN=FNS[GKN2,GKN1,GKN0]
   GKD=FNS[GKD2,GKD1,GKD0]
 GKK=GKN/GKD
@                                   GYRO INTEGRATOR
   GFN=FNS[GFN1,GFN0]
   GFD=FNS[GFD1,GFD0]
 GFF=GFN/GFD
@                                   GYRO TORQUER POLE
   GCN=FNS[GCN1,GCN0]
   GCD=FNS[GCD1,GCD0]
 GCC=GCN/GCD
@                                   GYRO CROSS COUPLING
@                                   MATRIX DEFINITION
 GMAT=FNS[GM2,GM1,GM0]
@                                   GYRO TRANSFER FUNCTION
 GYROSUB=GKK*GFF*GMAT*GCC
 GYRO=GYRO+GYROSUB
 @                                 SHAPER MATRIX DEFINITION
 SHAPSUB=SHA*SHB*SHC*SHD
 SHAPE=SHAPE+SHAPSUB
 SHAPE=SHAPE+SHAPSUB
 SHAPER[1,1]=ZERO
 SHAPER[1,2]=SHAPE
 SHAPER[2,1]=-SHAPE
 SHAPER[2,2]=ZERO
@
 SHAPING=SHAPING+SHAPER*DLS[DELAY]*SHS[PERIOD]
 OPENLOOP=OPENLOOP+GYRO*SHAPER*DLS[DELAY]*SHS[PERIOD]
SUM
@---------------------------------  OPEN LOOP TRANSFER FUNCTION
 LOOP=OPENLOOP*DLZ
@---------------------------------  RRM EVALUATION
 SHAPE1=DLZ*SHAPING
 RRM[1,1]=-LOOP
 RRM[3,1]=-LOOP
 RRM[1,3]=-IDENTITY


 OUTPUT RRM
STOP FLIST
```

```
TIME  MODEL

100    @-------------------------------------------------------------
110    @
120    @                    SRT GYRO
130    @                 SIMULATION MODEL
140    @                 M.TAYLOR/B.JOHNSON 05/09/85
150    @
160    @-------------------------------------------------------------
170    REAL RDTN1[2] RDTN0[2] RDTD1[2] RDTD0[2]
180    REAL INLN1[2] INLN0[2] INLD1[2] INLD0[2]
190    REAL SHAN2[2] SHAN1[2] SHAN0[2] SHAD2[2] SHAD1[2] SHAD0[2]
200    REAL SHBN2[2] SHBN1[2] SHBN0[2] SHBD2[2] SHBD1[2] SHBD0[2]
210    REAL SHCN1[2] SHCN0[2] SHCD1[2] SHCD0[2]
220    REAL SHDN2[2] SHDN1[2] SHDN0[2] SHDD2[2] SHDD1[2] SHDD0[2]
250    REAL SHA[2,1] SHB[2,1] SHC[2,1] SHD[2,1] SHF[2,1] SHG[2,1]
260    REAL XOVER[2,1] CROSS[2,2]
270    REAL READOUT[2,1] CONTROL[2,1] SG
280    REAL GIN0[2,1] GOUT[2,1]
290    REAL GINT1[2,2] GINT0[2,2] GIDT1[2,2] GIDT0[2,2]
300    REAL GMN2[2] GMN1[2] GMN0[2]
310    REAL GMD2[2] GMD1[2] GMD0[2]
320    REAL LOOPSUM1[2,1] LOOPSUM2[2,1] SUM[2,1]
330    REAL INPUT[2,1] SCINPUT[2,1]
331    REAL 0 1 VECTOR[2,1]
332    REAL TIME SF SCOUTPUT[2,1]
333    REAL XBREAKS[5,2] YBREAKS[5,2]
334    REAL RAMP[2,1] SCRAMP[2,1]
335    REAL TINPUT[2,1] SCTINPUT[2,1]
340
350    REAL ORIGIN[2] STOP[3] OUTPUT[2] DIGITAL[2]
360
370    ORIGIN
380      TIME=RFS[1/1,0]*1
390      RAMP=TIME*VECTOR
400      TINPUT=ABFG[XBREAKS,YBREAKS]*RAMP
410      SCTINPUT=SF*TINPUT
415      SCINPUT=SF*INPUT
420 LOOPSUM2=SCINPUT
430      SUM=LOOPSUM2-LOOPSUM1
440      GIN0=RFS[GINT1,GINT0/GIDT1,GIDT0]*SUM
450      GOUT=RFS[GMN2,GMN1,GMN0/GMD2,GMD1,GMD0]*GIN0
460      READOUT=RFS[RDTN1,RDTN0/RDTD1,RDTD0]*GOUT
480      SHA=RFS[SHAN2,SHAN1,SHAN0/SHAD2,SHAD1,SHAD0]*READOUT
490      SHB=RFS[SHBN2,SHBN1,SHBN0/SHBD2,SHBD1,SHBD0]*SHA
500      SHC=RFS[SHCN1,SHCN0/SHCD1,SHCD0]*SHB
510      SHD=RFS[SHDN2,SHDN1,SHDN0/SHDD2,SHDD1,SHDD0]*SHC
511      CONTROL=SG*RFS[INLN1,INLN0/INLD1,INLD0]*SHD
540      XOVER=CROSS*CONTROL
550      LOOPSUM1=XOVER
560      SCOUTPUT=LOOPSUM1/SF
570 OUTPUT INPUT SCOUTPUT GOUT
580 STOP
```

```
TIME  MODEL

100    @-------------------------------------------------------------
110    @
120    @                    S.P.T. GYRO
130    @                   SIMULATION MODEL
140    @                   DIGITAL INT & LEAD
145    @                   M.TAYLOR/B.JOHNSON 05/09/85
150    @
160    @-------------------------------------------------------------
170    REAL RDTN1[2] RDTN0[2] RDTD1[2] RDTD0[2]
180    REAL INLN1[2] INLN0[2] INLD1[2] INLD0[2]
190    REAL SHAN2[2] SHAN1[2] SHAN0[2] SHAD2[2] SHAD1[2] SHAD0[2]
200    REAL SHBN2[2] SHBN1[2] SHBN0[2] SHBD2[2] SHBD1[2] SHBD0[2]
210    REAL SHCN1[2] SHCN0[2] SHCD1[2] SHCD0[2]
220    REAL SHDN2[2] SHDN1[2] SHDN0[2] SHDD2[2] SHDD1[2] SHDD0[2]
230    REAL SHA[2,1] SHB[2,1] SHC[2,1] SHD[2,1] SHF[2,1] SHG[2,1]
240    REAL XOVER[2,1] CROSS[2,2]
250    REAL READOUT[2,1] CONTROL[2,1] SG
260    REAL GINO[2,1] GOUT[2,1]
270    REAL GINT1[2,2] GINT0[2,2] GIDT1[2,2] GIDT0[2,2]
280    REAL GMN2[2] GMN1[2] GMN0[2]
290    REAL GMD2[2] GMD1[2] GMD0[2]
300    REAL LOOPSUM1[2,1] LOOPSUM2[2,1] SUM[2,1]
310    REAL INPUT[2,1] SCINPUT[2,1]
320    REAL 0 1 VECTOR[2,1]
330    REAL TIME SF SCOUTPUT[2,1]
340    REAL XBREAKS[5,2] YBREAKS[5,2]
350    REAL RAMP[2,1] SCRAMP[2,1]
360    REAL TINPUT[2,1] SCTINPUT[2,1]
361    REAL SAMPLED[2,1] PERIOD[2] HELD[2,1]
370
380    REAL ORIGIN[2] STOP[3] OUTPUT[2] DIGITAL[2]
390
400    ORIGIN
410      TIME=RFS[1/1,0]*1
420      RAMP=TIME*VECTOR
430      TINPUT=ABFG[XBREAKS,YBREAKS]*RAMP
440      SCTINPUT=SF*TINPUT
450      SCINPUT=SF*INPUT
460 LOOPSUM2=SCINPUT
470      SUM=LOOPSUM2-LOOPSUM1
480      GINO=RFS[GINT1,GINT0/GIDT1,GIDT0]*SUM
490      GOUT=RFS[GMN2,GMN1,GMN0/GMD2,GMD1,GMD0]*GINO
500      READOUT=RFS[RDTN1,RDTN0/RDTD1,RDTD0]*GOUT
510      SHA=RFS[SHAN2,SHAN1,SHAN0/SHAD2,SHAD1,SHAD0]*READOUT
520      SHB=RFS[SHBN2,SHBN1,SHBN0/SHBD2,SHBD1,SHBD0]*SHA
530      SHC=RFS[SHCN1,SHCN0/SHCD1,SHCD0]*SHB
540      SHD=RFS[SHDN2,SHDN1,SHDN0/SHDD2,SHDD1,SHDD0]*SHC
550      SAMPLED=SHS[PERIOD]*SHD
560       DIGITAL
570        CONTROL=SG*RFZ[INLN1,INLN0/INLD1,INLD0]*SAMPLED
580       ORIGIN
581      HELD=SHS[PERIOD]*CONTROL
590      XOVER=CROSS*HELD
600      LOOPSUM1=XOVER
610      SCOUTPUT=LOOPSUM1/SF
620 OUTPUT INPUT SCOUTPUT GOUT
630 STOP
```

APPENDIX IV

THE EFFECTS OF FILTERING AMPLITUDE MODULATED SIGNALS PRIOR TO SYNCHRONOUS DEMODULATION

This discussion deals with signals which are of the form of double side-band suppressed carriers, and examines the effect of filtering these signals on subsequent demodulation.

Consider the following situation:- our DSBSC carrier signal may be represented by;

$$V_m = [\cos(\omega_c - \omega_m)t + \cos(\omega_c + \omega_m)t]m$$

Where ω_m is the modulation frequency (rad/sec)

m is the amplitude of modulation

ω_c is the carrier frequency (rad/sec)

This signal is to be filtered with the filter shown below.

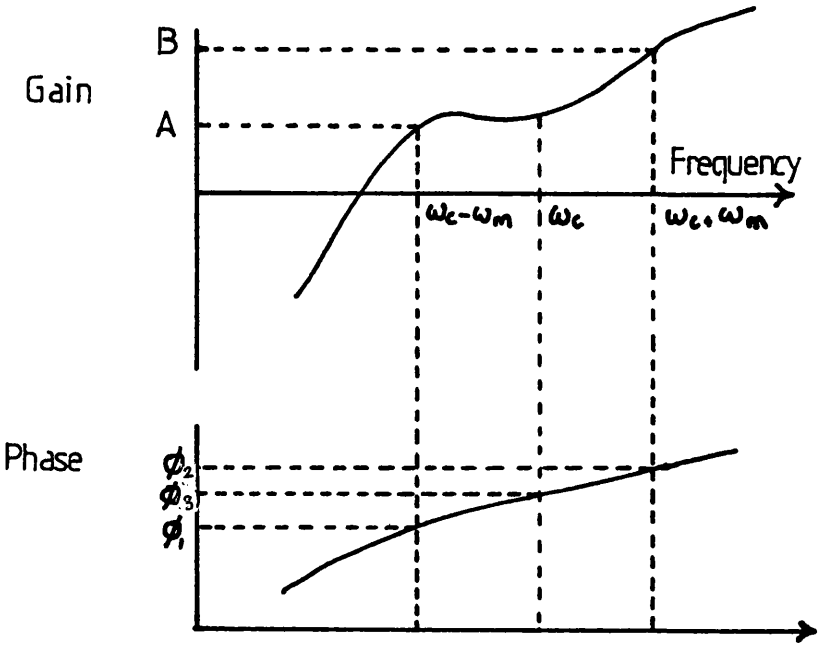

So our double side-band suppressed carrier signal is now:

$$V_m' = A_m \cos [(\omega_c - \omega_m)t + \phi_1] + B_m \cos [(\omega_c + \omega_m)t + \phi_2$$

For synchronous demodulation we must multiply by a phase locked carrier frequency. So we multiply by:

$$\cos (\omega_c t + \phi_3)$$

If we assume good lowpass filtering after demodulation, ie. all terms involving cos $2\omega_c$ are completely attenuated, then using the identity

$$\cos A \cos B = \tfrac{1}{2} \cos (A + B) + \tfrac{1}{2} \cos (A - B)$$

we obtain

$$(V_m')_{\text{demodulated}} = m(t) = \frac{A_m}{2} \cos (-\omega_m t + \phi_1 - \phi_3) + \frac{B_m}{2} \cos (\omega_m t + \phi_2 - \phi_3)$$

For the special case of $\frac{A_m}{2} = \frac{B_m}{2} = C$

we have

$$m(t) = C[\cos (-\omega_m t + \phi_1 - \phi_3) + \cos (\omega_m t + \phi_2 - \phi_3)]$$

Now using

$$\cos A + \cos B = 2 \cos \tfrac{1}{2} (A + B) \cos \tfrac{1}{2} (A - B)$$

we obtain

$$m(t) = 2C \left[\cos \tfrac{1}{2} (\phi_1 + \phi_2 - 2\phi_3) \cos \tfrac{1}{2} (2\omega_m t + \phi_2 - \phi_1)\right]$$

$$m(t) = 2C \left[\cos \frac{(\phi_1 + \phi_2 - \phi_3)}{2} \cos \left(\omega_m t + \frac{\phi_2 - \phi_1}{2}\right)\right]$$

Hence gain corruption is $C \cos \frac{(\phi_1 + \phi_2 - \phi_3)}{2}$

and resulting phase $\frac{\phi_2 - \phi_1}{2}$

Hence for minimum phase $\phi_2 = \phi_1$

and ideally $\phi_1 = \phi_2 = \phi_3$

APPENDIX V

HIGH PASS FILTER DESIGN

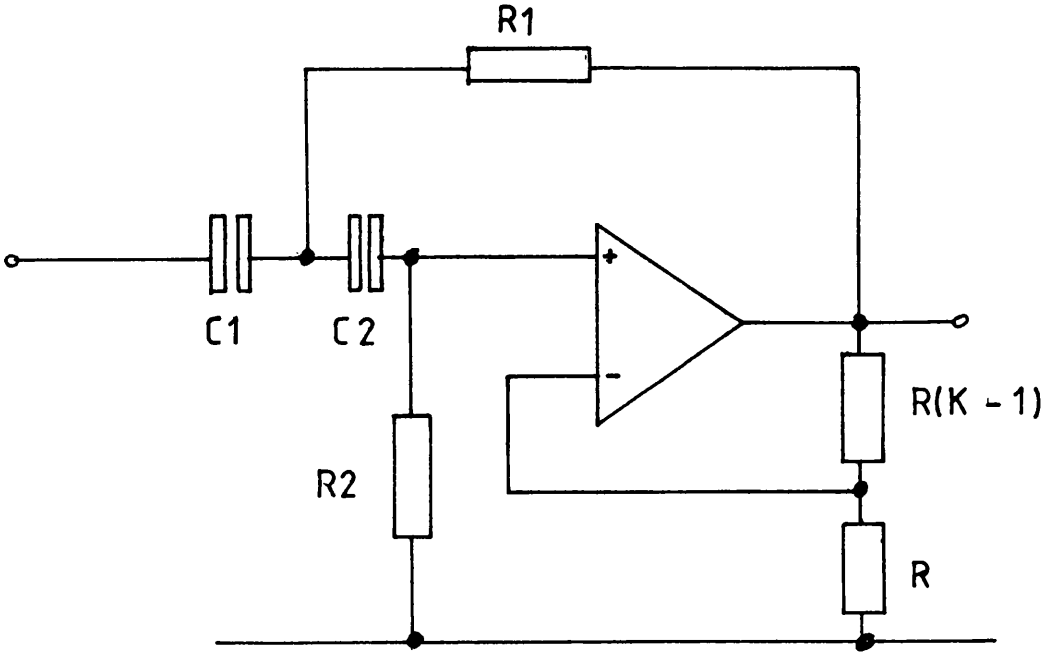

$$T(s) = \frac{K s^2}{s^2 + a\omega_o s + \omega_o^2}$$

Where K is the gain of the stage, ω_o is the break frequency of the filter (rad/sec) while a is the damping factor.

Design Equations

$$\omega_o = \frac{1}{\sqrt{C_1 C_2 R_1 R_2}}$$

$$a = [R_1(C_2 + C_1) + (1 - K)\, C_2 R_2]\omega_o$$

To simplify the design put $C_1 = C_2 = C$, and to minimise bias current offsets

$$R = \frac{KR_2}{K-1}$$

Sensitivity Analysis

Using partial differentiation it can be shown for small perturbations that:

$$\Delta|T(s)| = \frac{\partial|T(s)|}{\partial H}\Delta K + \frac{\partial|T(s)|}{\partial \omega_o}\Delta\omega_o + \frac{\partial|T(s)|}{\partial a}\Delta a$$

and that:

$$\Delta K = \pm (K-1)\, 2\, \frac{\Delta R}{R}$$

$$\Delta\omega_o = \omega_o\{\pm \frac{\Delta C}{C} \pm \frac{1}{2}\frac{\Delta R_1}{R_1} \pm \frac{\Delta R_2}{R_2}\}$$

$$\Delta a = \Delta C(2R_1 + (1-K)R_2)\omega_o + 2\Delta R_1 C\, \omega_o + (1-K)C\, \omega_o\, \Delta R_2$$

Noise Analysis

The sources of noise within this circuit are the thermal noise generated by the resistors, and the current noise due to the transistors within the operational amplifier. The total figure for "noise" (V_m) is given by the square root of the sum of each noise contribution squared.

$$V_{nT} = \sqrt{\Sigma\, V_n^2}$$

The noise contribution of each source is modified by the transfer function of its origin to the filler output (F(s)). The contribution is determined by:

$$V_o^2 = \int_{f_1}^{f_2} V_n^2\, F(s)^2$$

Where f_1 and f_2 define the frequency bond.

Table A5.1 gives the transfer function F(s) for each component.

TABLE A5.1

NOISE TRANSFER FUNCTIONS

SOURCE	TRANSFER FUNCTION F(s)
Amplifier offset noise	$\frac{L(s)\ \omega_o^2\ T(s)}{S^2}$
R_1	$\frac{1}{SCR_1}\ .\ T(s)$
R_2	$\frac{\omega_o^2\ (2sCR_1 + 1)\ .\ T(s)}{S^2}$
Amplifier current noise	$= \frac{R_2\ \omega_o^2\ (2sCR_1 + 1)\ T(s)}{s^2}$
R	$\frac{L(s)\ \omega_o^2}{S^2}\ \frac{K-1}{K}\ T(s)$
R(K-1)	$\frac{L(s)}{S^2}\ \omega_o^2\ T(s)$

Where $L(s) = s^2C^2R_1R_2 + sC(2R_1 + R_2) + 1$

The current and offset noise for the amplifier is obtained from the manufacturers data book, while the resistor, or Johnson noise is obtained by:

$V_n^2 = 4KT\ R\ df$

Where K = Boltzman constant

T = Absolute temperature

R = Resistance

df = The bandwidth of the noise

APPENDIX VI

REFERENCE AMPLIFIER

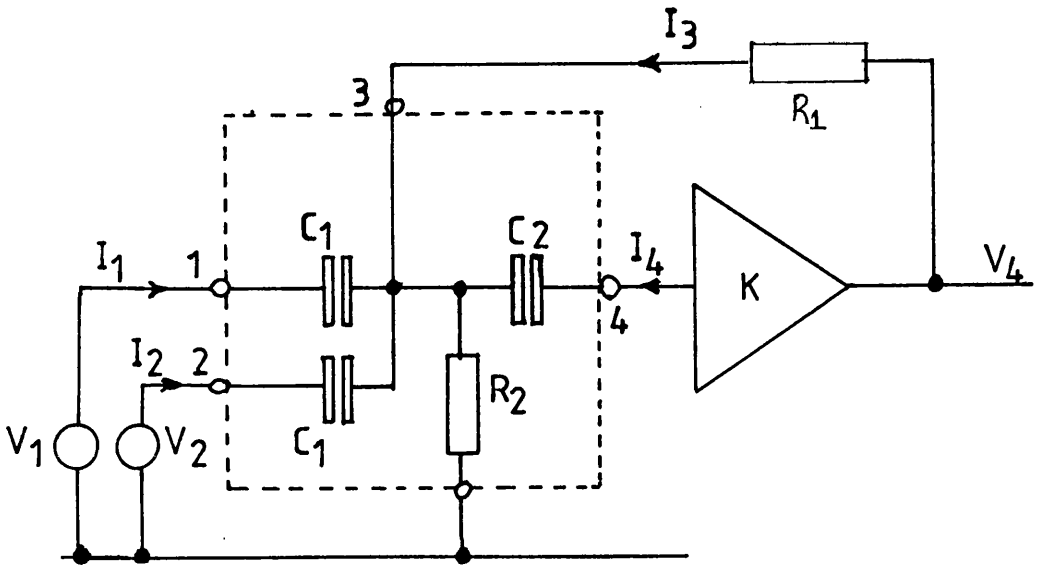

Using Y parameter to describe the circuit within the dotted box it can be shown that for an ideal amplifier:

$$i_4 = Y_{41}V_1 + Y_{42}V_2 + Y_{43}V_3 + Y_{44}V_4$$

Where Y_{nm} is given by $\left.\frac{i_n}{V_m}\right|_{V_{(x)} = 0}$

Where x all value $\neq$ m

Noting that for an ideal amplifier $i_4 = 0$ and $V_3 = V_4K$, it can be shown that:

$$\frac{V_3}{V_1 + V_2} = \frac{-Y_{41}K}{Y_{43}K + Y_{44}}$$

Now $Y_{41} = \dfrac{-s^2C_1C_2R_1}{1 + s\,R_1(2C_1 + C_2)}$, $Y_{43} = \dfrac{-sC_2}{1 + s\,R_1(2C_1 + C_2)}$

$$Y_{44} = 2s^2C_1C_2R_1R_2 + s(C_2R_2 + 2C_1R_1 + C_2R_1) + 1$$

Hence $$\frac{V_3}{V_1 + V_2} = \frac{Ks^2C_1C_2R_1R_2}{s^2 2C_1C_2R_1R_2 + s(R_1(2C_1 + C_2) + C_2R_2(1-K) + 1}$$

Matching to standard form:

$$\frac{H\,\dfrac{s^2}{\omega_o^{\,2}}}{\dfrac{s^2}{\omega_o^{\,2}} + \dfrac{as}{\omega_o} + 1}$$

Gives:

$$\omega_o = \frac{1}{\sqrt{2C_1C_2R_1R_2}} \quad , \quad H = \frac{K}{2}$$

$$a = \frac{2R_1C_1 + C_2R_2 + C_2R_2\,(1-K)}{\sqrt{2C_1C_2R_1R_2}}$$

APPENDIX VII

THE DEMODULATOR

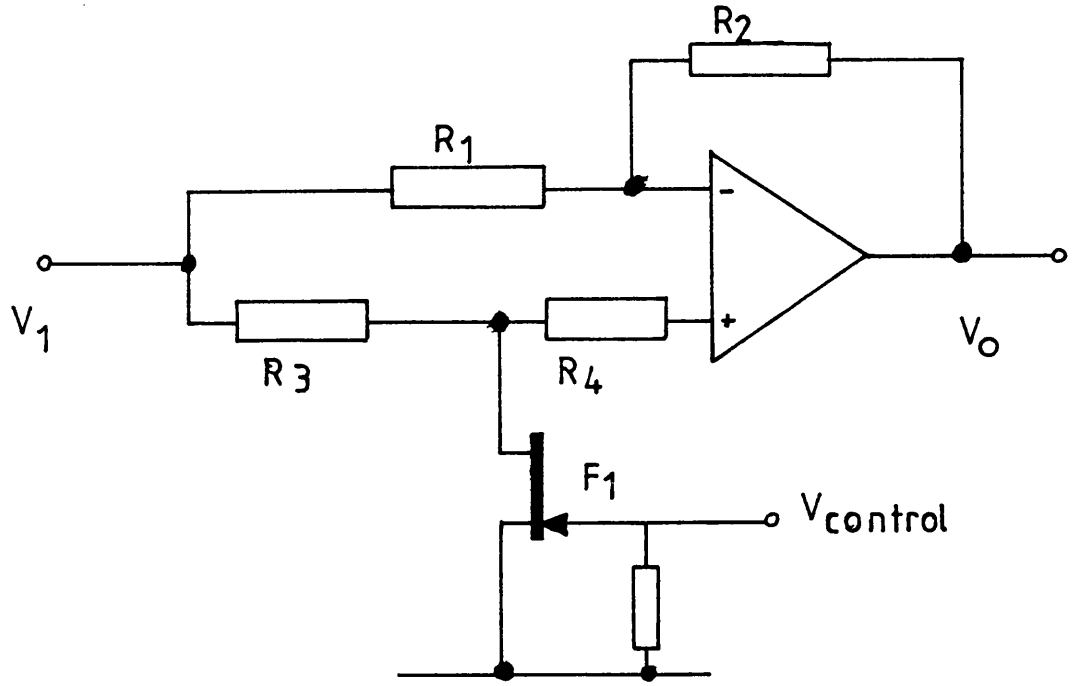

F_1 acts as a switch and is either on or off with resistance Rds(on) or Rds(off) respectively. With F_1 switched on it can be shown that the transfer function of the circuit $V_{T(on)}$ is:

$$V_{T(on)} = \frac{V_0}{V_1} = \frac{Rds(on)}{Rds(on) + R_3} \left(1 + \frac{R_2}{R_1} \right) - \frac{R_2}{R_1}$$

Provided $Rds(on) << R_3$ then $V_{T(on)} = -\frac{R_2}{R_1}$

(note the circuit is designed such that the effect of Rds(on) on the d.c. gain is less than -40db).

With F_1 switched off it can be shown that the transfer function $V_{T(off)}$ is:

$$V_{T(off)} = \frac{V_0}{V_1} = \frac{Rds(off)}{Rds(off) + R_3} \left(1 + \frac{R_2}{R_1} \right) - \frac{R_2}{R_1}$$

Provided that $Rds(off) >> R_3$

then $V_{T(off)} = +1$

Hence if $R_2 = R_1$ then the circuit can be made to multiply by + or -1 by switching F_1 off and on. Thus a synchronous squarewave voltage applied to the input V_C will demodulate the input signal. The value for R_4 is chosen to minimise the effects due to the amplifiers bias current.

APPENDIX VIII

THE INTEGRATOR

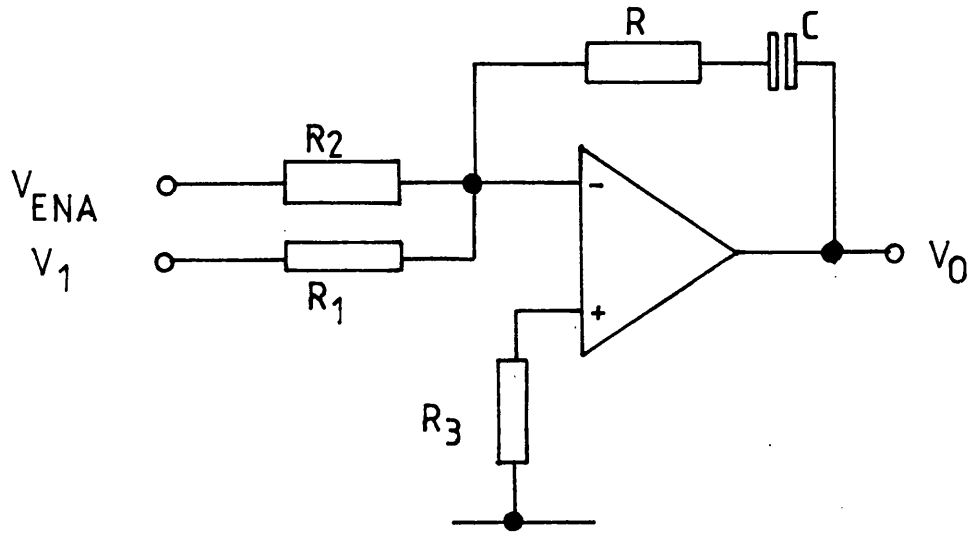

DESIGN EQUATIONS

$$V_0 = -\left[\frac{V_{ENA}}{R_2} + \frac{V_1}{R_1}\right] \frac{sCR + 1}{sC}$$

$R_3 = R_1R_2/(R_1 + R_2)$ to minimise bias current errors

INTEGRATOR ERRORS

Input offset errors appear as angular displacements. These are converted to drift via the auto erection and residual stiffness mechanism. The quality of the integrator is of only minor importance as the gyroscope loop acts to work about a null position. However the stability of the transfer function is of importance in maintaining the stability and transfer function of the closed loop system.

APPENDIX IX

LOWPASS FILTER SECTION

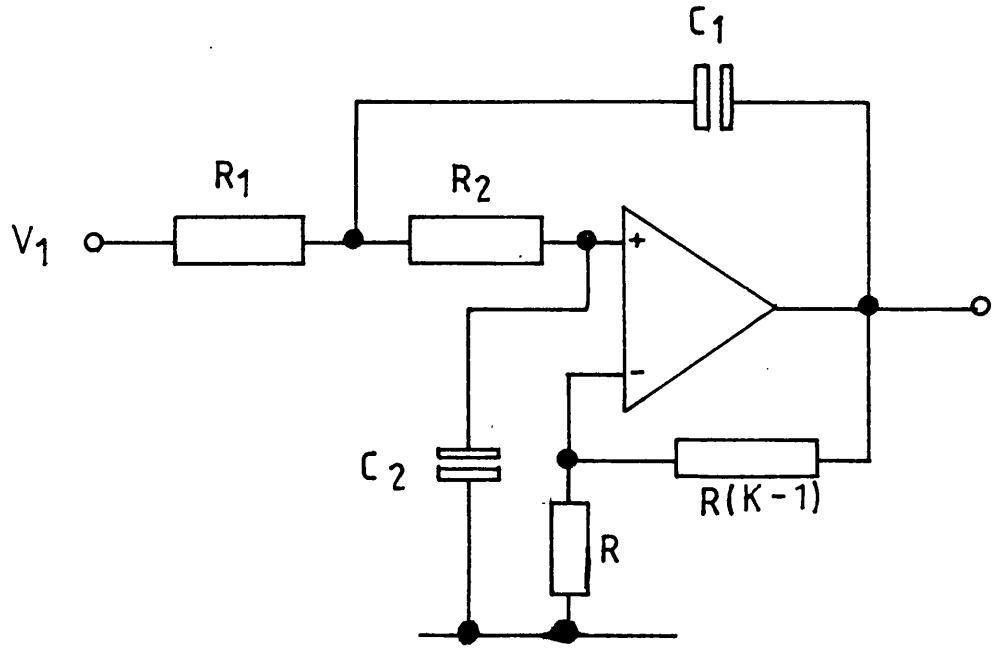

In the case of the design of the filter with unity gain (K=1), R(K-1) is a short circuit, and R is an open circuit. The transfer function of this circuit is:

$$T(s) = \frac{V_{0(s)}}{V_{1(s)}} = \frac{K}{\frac{s^2}{\omega_o^2} + \frac{2\zeta s}{\omega_o} + 1}$$

Where K is the gain of the stage, ω_o is the break frequency (rad/sec) while ζ is the damping factor.

Design Equations

$$\omega_o = \frac{1}{\sqrt{C_1 C_2 R_1 R_2}}$$

$$\zeta = [C_2(R_2+R_1) + (1-K)R_1C_1] \frac{\omega_o}{2}$$

To simplify the design equations, put $R_1 = R_2$. Hence for K = 1

$$\omega_o = \frac{1}{R\sqrt{C_1 C_2}}$$

and $$\zeta = \sqrt{\frac{C_2}{C_1}}$$

To minimise the bais current offsets

$$R = \frac{K}{(K-1)} (R_1 + R_2)$$

APPENDIX X

ACTIVE NOTCH FILTER

The general transfer function for a notch is:

$$T_{(s)\ \text{notch}} = \frac{s^2 + 2\zeta_1\omega_o s + \omega_o^2}{s^2 + 2\zeta_2\omega_o s + \omega_o^2}$$

ω_o is the notch frequency in rads/sec.

The notch depth is given by $20 \log_{10} \frac{\zeta_1}{\zeta_2}$ db

The Q is given by $\frac{1}{\zeta_1+\zeta_2}$

The above transfer function can be realised using an active bridge network the following configuration

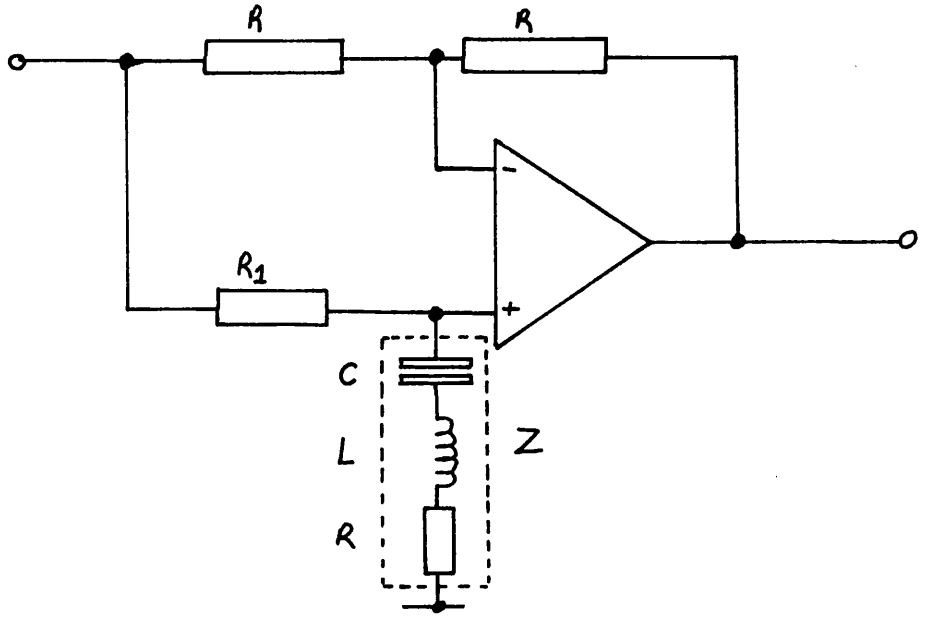

Using super position, it can easily be shown for a perfect amplifier that the transfer function is $\frac{Z - R_1}{Z + R_1}$

But $Z = R + s\ell + \frac{1}{sC}$

$$= \frac{sRs + s^2\ell C + 1}{sC}$$

Gives $T_{(s)} = \frac{s^2C\ell + sC\ (R-R_1) + 1}{s^2C\ell + sC\ (R+R_1) + 1}$

To avoid using an inductor, an active gyrator circuit is used to simulate the inductor

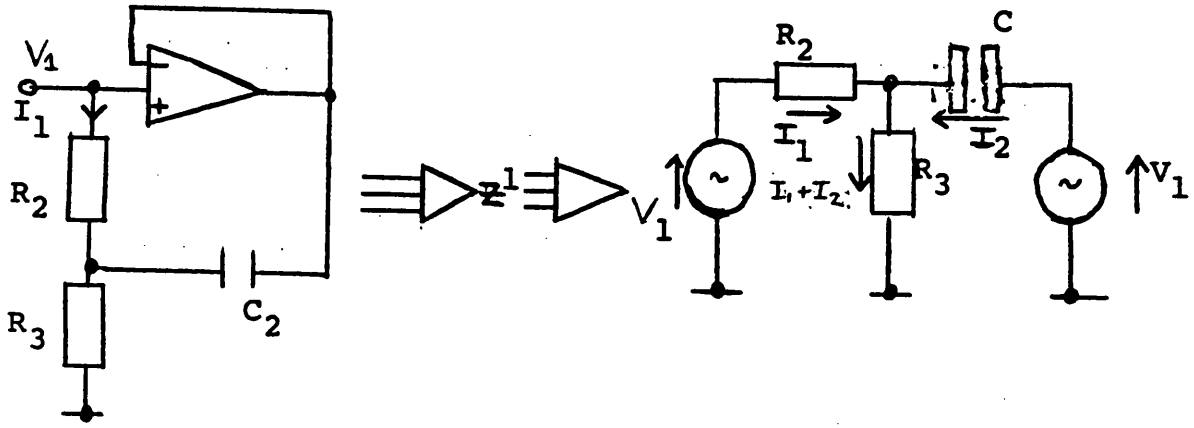

$V_1 = I_1R_2 + I_1R_3 + I_2R_3$

$V_1 = \frac{I_2}{j\omega C_2} + I_1R_3 + I_2R_3$

Give $V_1 = I_1\ (R_3+R_2) + I_1\ (j\omega C_2R_3R_2)$

Hence $\frac{V_1}{I_1} = Z^1 = (R_3+R_2) + j\omega C_2R_3R_2$

This is equivalent to inductance of $C_2R_3R_2$ with series resistance R_3+R_2.

Thus notch circuit becomes:

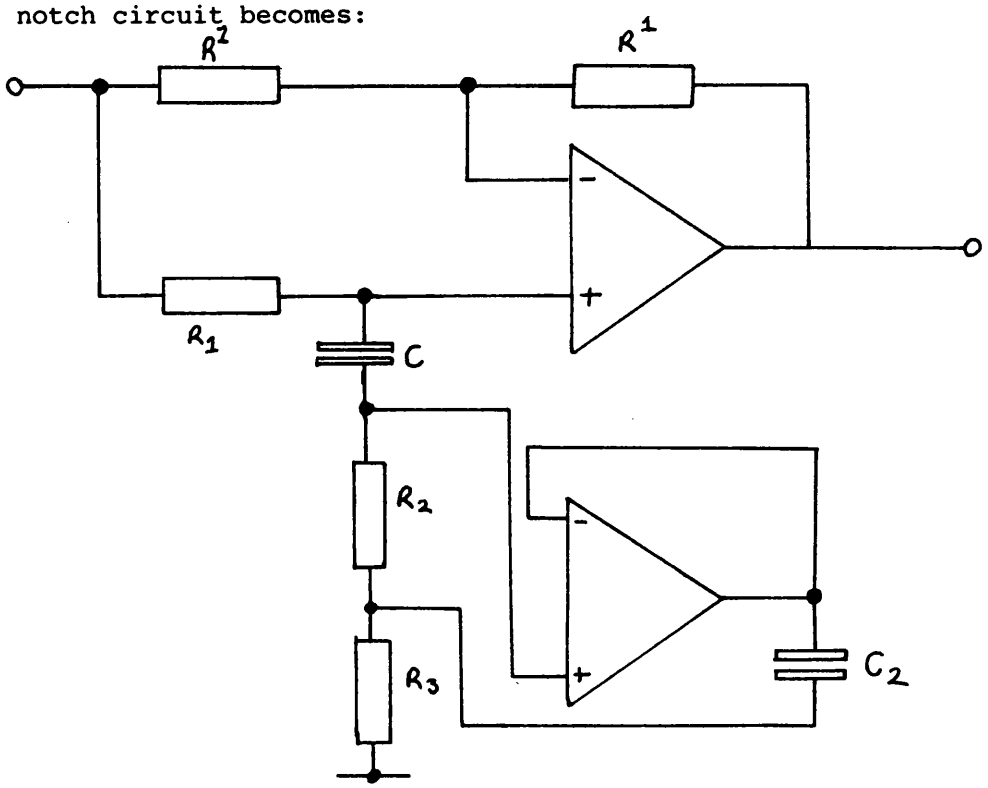

$$T_{(s)} = \frac{s^2CC_2R_2R_3 + sC(R_2+R_3-R_1)+1}{s^2CC_2R_2R_3 + sC(R_2+R_3+R_1)+1}$$

Design Equations

For good bias matching $R^1 = 2R_1$

Note trimming the ratio R_2 to R_3 changes the inductance hence max inductance is when $R_2 = R_3 = R_s$.

Choose C_2

Hence $\omega_o^2 = \frac{1}{CC_2R_3R_2} = \frac{1}{CC_2R_s^2}$

$$\zeta_1 = \frac{(C(2R_s-R_1))\ \omega_o}{2}$$

$$\zeta_2 = \frac{C(2R_s+R_1)\ \omega_o}{2}$$

Practical Limitations

The first major limitation of the design is the operation of the gyrator. The capacitor C_2 has associated series resistance, this causes considerable changes to the series resistance of the simulated inductor. The inclusion of the series resistance of the capacitor in fact gives rise to an impedance of Z.

$$Z_{(s)} = \frac{(R_2+R_3)\ \omega^2C_2^2R^2 + (R_2+R_3) + R_3R_2\omega^2C_2^2R^2 + R_1R_2sC_2}{\omega^2C_2^2R_C^2 + 1}$$

Where R_c is a series resistance.

However, as $\omega^2C_2^2R_C^2 << 1$

$$Z(s) \simeq R_3+R_2 + (R_3+R_2)\ \omega^2C^2R_C^2 + R_3R_2\omega_2C_2R_C^2 + R_1R_2sC_2$$

This has the effect of modifying the design equations thus:

$$\omega_o^2 = \frac{1}{CC_2\ \{(R_2+R_3)R_C+R_2R_3-R_1R_C\}S}$$

As $R_C << R_2 = R_3$

$$\omega_o^2 \quad \frac{1}{CC_2R_2R_3}$$

$$\zeta_1 = \frac{[C_1(R_2+R_3) + C_2R_C - C_2R_1]}{2}\ \omega_o$$

$$\zeta_2 = \frac{[C_1(R_2+R_3) + C_2R_C + CR_1]}{2}\ \omega_o$$

However the series resistance of the capacitor is dependent upon temperature, so to offset the effects of this the stability of the notch depth may be improved by increasing the series resistance by connecting a resistor in series with the capacitor.

The other main practical problem is caused by using a simulated inductor. When the arm of the bridge resonates, the voltage across the inductor can be much greater than the voltage applied to the input. This means that for high Q notches, the amplifier which is used to simulate the inductor may saturate for quite small input signals.

APPENDIX XI

THE DESIGN OF THE OSCILLATOR FOR THE GYRO MOTOR DRIVE

INTRODUCTION

The Microflex gyro's inertial element is driven by a four pole hysteresis motor, which is run at synchronous speed. The hysteresis motor requires a two phase sinusoidal supply, at a frequency of twice the rotation frequency of the motor. The two phases of the drive frequency must be at a phase angle of 90° to each other, ie. cosine and sine.

The motor supply is provided by a phase shift oscillator, which has sine and cosine outputs. These outputs are buffered by two power amplifiers, which correct the magnitude of the signals and drive the motor.

DESIGN REQUIREMENTS

The oscillator must provide a signal of stable amplitude and frequency, and the phase of the two outputs with respect to each other should also be stable. The oscillator must operate over a temperature range -40°C to +70°C. The motor supply plays a major part in the stability of the gyro. The dynamic properties relate directly to the rotation frequency of the gyro, hence any instability in the supply frequency will affect the performance of the gyro. In addition to this the angular pickoff system relies upon the frequency of the wheel rotation frequency, any perturbation in the wheel speed will both amplitude modulate and frequency modulate the pickoff signal. The phase angle

between the two outputs relates to the amount of torque which is applied to the motor rotor. Variation of the phase angle may cause the hysteresis motor to hunt and modulate the rotation frequency. The amplitude of the oscillation controls the amount of power which is applied to the motor. The amount of power applied to motor also to some extent affects the torque applied to the wheel. Also the amount of power applied to the wheel is related to the magnetic field of the motor, variations in the stray magnetic fields within the gyro affect the random drift of the gyro.

OSCILLATOR DESIGN

The oscillator is a closed loop containing three lags, the total phase lag around the loop tends to 270° as the frequency tends to infinity. While at some finite frequency the phase shift will reach 180° and hence the loop will exhibit positive feedback, and the possibility for complete instability exists.

FIGURE A11-1

WHEEL SUPPLY OSCILLATOR LOOP

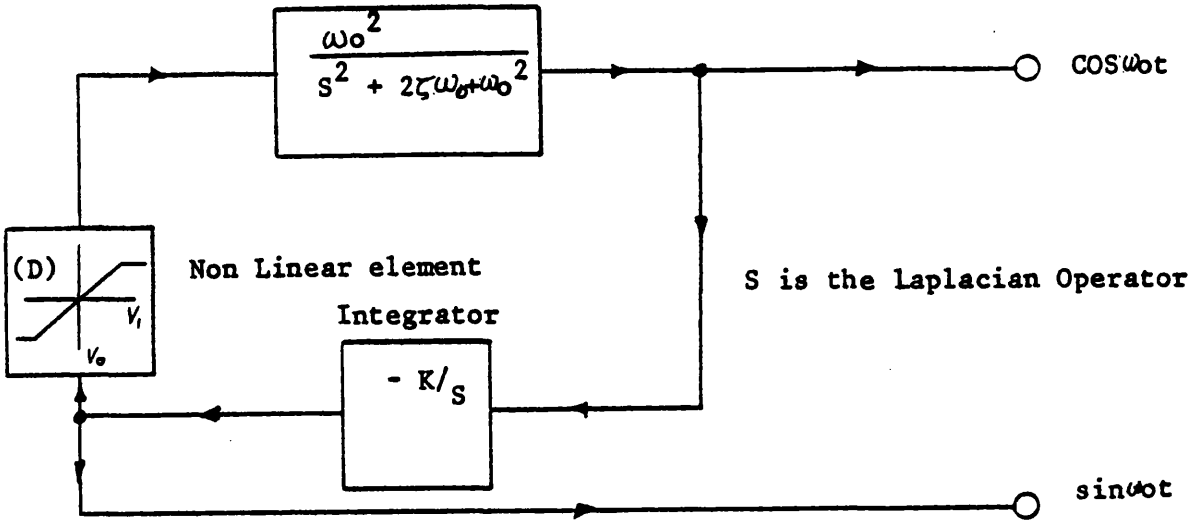

The oscillator loop is shown in Figure A11.1. This comprises of an integrator with a single pole and multiplier K, a second order low pass filter and a non-linear element. The non linear element has unity gain up to a fixed magnitude of input voltage then clips at this level. This has been included to control the magnitude of oscillation.

The open loop gain for the oscillator is:

$$T(s)_{OL} = \frac{-\omega_o^2 K(D)}{(s^2 + 2\zeta\omega_o s + 1)\, s}$$

Where (D) is the describing function of the non-linear element.

Hence for unity gain feedback the closed loop transfer function is:

$$T(s)_{CL} \quad \frac{1}{1 + \dfrac{\omega_o^2 K(D)}{(s^2 + 2\zeta\omega_o s + 1)s}}$$

Using the Nyquist criteria for instability

$$\frac{\omega_o^2 K(D)}{(s^2 + 2\zeta\omega_o s + \omega_o^2)s} = -1$$

Hence for oscillation:

$$\frac{\omega_o^2 K}{(s^2 + 2\zeta\omega_o s + \omega_o^2)s} = \frac{-1}{(D)}$$

To obtain the conditions for oscillation at ω_o, we shall assume (D) to be unity and put $\omega = \omega_o$ and $s = j\omega$

$$\frac{\omega_o^2 K}{(j^2\omega_o^2 + 2\zeta j\omega_o^2 + \omega_o^2)\, j\omega_o} = -1$$

Hence $K = 2\zeta\omega_o$

If $\zeta = 0.707$ and $\omega_o = 2\pi \times 400$ } Then K = 3553.5

These are the conditions for oscillation at 400Hz in the linear region of (D). However the complete condition for oscillation is:

$$\frac{\omega_o^2 K}{(s^2 + 2\zeta\omega_o s + \omega_o^2)\, s} = \frac{-1}{(D)}$$

The non-linear element used in the oscillator circuit is a pair of zener diodes. When the amplitude of the signal applied to the zener diodes is below the zener voltage the gain of the diode block is unity. When the amplitude of the oscillation exceeds the zener voltage, the gain of the diodes is reduced, and tends to zero as the amplitude of the oscillation tend to infinity. Hence describing function of the diode is a vertical line, starting at 0dbs, with 180 deg phase.

RUN UP TIME OF THE OSCILLATOR

The run up time is determined by the impulse response of the oscillator loop, and the impulse which stimulates it. The closed loop transfer function for the oscillator without the non-linear element is:

$$T(s)_{CL} = \frac{K}{(s^3/\omega_o^2 + 2\zeta s^2/\omega_o + s + K}$$

This can be represented in a standard form:

$$T(s)_{CL} = \frac{\omega_o^2}{(sT + 1)(s^2 - 2Z\omega_o^2 + \omega_o^2)}$$

Where $Z = \dfrac{1}{2 \times (\text{closed loop gain at } \omega_o) \times \sqrt{2}}$

To determine the attack time of the oscillator, we must find the impulse response to the stimulus which starts the oscillation. To do this we must find the inverse laplace transform of the product of the closed loop frequency response and the frequency response of the stimulus. As we use a short pulse to start the oscillator, we can approximate this to a weighted dirac delta function. The weighting factor being the area of the actual pulse used in volt seconds. The use of this approximation simplifies the mathematics, as the laplace transform of a weighted delta function to the weighting factor of the pulse.

Hence to find the impulse response to an input of $A\delta(t)$, where A is the weighting (VSec) and $\delta(t)$ is the dirac delta function we take the inverse laplace transform of:

$$\mathcal{L}^{-1} \frac{\omega_o^2 A}{(sT + 1)(s^2 - 2z\omega_o s + \omega_o^2)}$$

Which is given by:

$$\frac{AT\omega_o^2 e^{-t/T}}{1 - 2zT\omega_o + T^2\omega_o^2} + \frac{A\omega_o e^{Z\omega_o t} \sin(\omega_o\sqrt{1 - \zeta^2 t} - \phi)}{((1 - Z^2)(1 - 2zT\omega_o + T^2\omega_o^2))^{\frac{1}{2}}}$$

$$\phi = \tan^{-1}\left[\frac{T\omega_o\sqrt{1 - Z^2}}{1 + Tz\omega_o}\right]$$

Now $\omega_o = \frac{1}{T}$ and z is small

The impulse response is given by:

$$A\omega_o\left[\tfrac{1}{2}e^{-\omega_o t} + \frac{e^{\omega_o zt}}{\sqrt{2}} \sin(\omega t - \pi/4)\right]$$

CIRCUIT DIAGRAM

The circuit diagram for the oscillator is given in Figure A11.2. The values given are for oscillation at 400Hz.

FIGURE A11.2 The Oscillator Circuit